Computationally Driven Characterization of Magnetism, Adsorption, and Reactivity in Metal-Organic Frameworks

A THESIS
SUBMITTED TO THE FACULTY OF THE GRADUATE SCHOOL
OF THE UNIVERSITY OF MINNESOTA
BY

Joshua Borycz

IN PARTIAL FULFILLMENT OF THE REQUIREMENTS
FOR THE DEGREE OF
DOCTOR OF PHILOSOPHY

Laura Gagliardi

June, 2016

Acknowledgements

There are many people that have earned my gratitude for their contribution to my time in graduate school. Firstly, I would like to thank my advisor Prof. Laura Gagliardi. With her consistent help and support throughout my years here I was able to accomplish more that I thought possible. She has pushed me to pursue new and challenging research projects and has encouraged me when difficulties inevitably arose. With her help I have gained a great deal of knowledge and confidence as a scientist.

I also wish to thank Profs. Christopher J. Cramer, J. Ilja Siepmann, Donald G. Truhlar, and Andreas Stein for their help on our many collaborations. One of the main things that attracted me to the chemistry department of the University of Minnesota was the level of collaboration between the faculty members. I can say after my five years here that in this aspect the chemistry department has exceeded my expectations. Every collaboration in which I have been involved has been fruitful both in terms of my chemical knowledge and in terms of the outcomes of the research. The students within these groups that have helped me the most have been Emmanuel Haldoupis, Pragya Verma, Camille Malonzo, and Samat Tussupbayev.

My thanks to the many members of the Gagliardi group that have helped me with both their research experience and support during difficult phases of my graduate student career. Thank you to Alison Dzubak, Bess Vlaisavljevich, David Semrouni, Rémi Maurice, Nora Planas, Varinia Bernales, Konstantinos Vogiatzis, Samuel Odoh, Huiliang Shi, Chad Hoyer, Andrew Sands, and Dale Pahls for their mentorship, guidance, and collaboration. Without the help and support of these individuals and others I would not have been able to cope with the many difficulties of graduate school.

I owe a debt of gratitude to the many external collaborators that I have had over the years. My sincere thanks to Profs. Omar K. Farha, Joseph T. Hupp, Berend Smit,

Jeffrey R. Long, and Joachim Paier for their help with my many projects. Also thanks you to Davide Tiana, In Soo Kim, Martino Rimoldi, Li-Chiang Lin, Kyuho Lee, Roberta Poloni, and Rachel Klet.

Finally, thank you to my family for your love and support. David, Rachel, Micah, and Leah, thank you for helping me recharge when I felt overwhelmed, and thank you for tolerating my complaining and cynicism. Mom and dad, thank you for supporting me through college and graduate school. I love you and could not have done this without your help.

Abstract

Metal−organic frameworks (MOFs) are a class of nanoporous materials that are composed of metal-containing nodes connected by organic linkers. The study of MOFs has grown in importance due to the wide range of possible node and linker combinations, which allow tailoring towards specific applications. This work demonstrates that theory can complement experiment in a way that advances the chemical understanding of MOFs. This thesis contains the results of several investigations on three different areas of MOF research: 1) magnetism, 2) CO_2 adsorption, and 3) catalysis.

The calculation of magnetic properties within MOFs is quite problematic due to the weak nature of the interactions between the metal centers. The metal atoms in MOFs can be far apart due to the organic linkers and are often in unique chemical environments that are difficult to characterize. These weak interactions mean that the computational methods must be carefully selected and tested to attain adequate precision. The objective of the work in this thesis was to determine the single-ion anisotropy and magnetic ordering of Fe-MOF-74 before and after oxidation.

MOFs have desirable properties for CO_2 adsorption such as large pores and high surface areas. Accurate force fields are required in order to make predictions for adsorption interactions with the internal surface of MOFs. Therefore it is important to have computational protocols that enable the derivation of reliable interaction parameters in order to study the trends of adsorption for different metal centers. In the research herein we used *ab initio* calculations to compute parameters for classical force fields for members of the IRMOF-10 and the MOF-74 series.

MOFs have been considered for catalysis due to their thermal stability, reactive metal sites, and large diameter pores. In this thesis we report a series of studies that advance the understanding of the reactivity of MOFs containing Zr_6 and Hf_6 polyoxometalate nodes. In the first study the proton topology of the nodes within NU-1000 was determined. Several other studies that make use of these MOFs as supports for single-site metal catalysts are also reported. Finally, research where NU-1000 serves as a template for a thermally stable nanocasted material used for high temperature Lewis acid catalysis is also discussed.

Contents

List of Tables

List of Figures

Preface

Citations from previously published work in thesis are as follows:

Chapter 2: Theoretical and Experimental Studies of Magnetic Properties of Fe_2(dobdc) before and After Oxidation

2.1 Single-Ion Magnetic Anisotropy and Isotropic Magnetic Couplings in the Metal-Organic Framework Fe_2(dobdc)

Reproduced with permission from:

Rémi Maurice, Pragya Verma, Joseph M. Zadrozny, Sijie Luo, Joshua Borycz, Jeffrey R. Long, Donald G. Truhlar, Laura Gagliardi *Inorg. Chem.* **2013**, 52, 16, 9379-9389.

Link: http://pubs.acs.org/doi/abs/10.1021/ic400953e

2.2 Structural and Electronic Effects on the Properties of Fe_2(dobdc) upon Oxidation with N_2O

Reproduced with permission from:

Joshua Borycz, Joachim Paier, Pragya Verma, Lucy E. Darago, Dianne J. Xiao, Donald G. Truhlar, Jeffrey R. Long, Laura Gagliardi, *Inorg. Chem.* **2016**, 55, 10, 4924-4934.

Link: http://pubs.acs.org/doi/abs/10.1021/acs.inorgchem.6b00467

Chapter 3: *Ab Initio* Parameterized Forces Fields for Carbon Dioxide Adsorption in $M_4(O)(bdc)_3$ and M_2(dobdc)

3.1 CO_2 Adsorption in M-IRMOF-10 (M = Mg, Ca, Fe, Cu, Zn, Ge, Sr, Cd, Sn, Ba)

Reproduced with permission from:

Joshua Borycz, Davide Tiana, Emmanuel Haldoupis, Jeffrey C. Sung, Omar K. Farha, J. Ilja Siepmann, Laura Gagliardi, *J. Phys. Chem. C* **2016**, accepted.

Link: http://pubs.acs.org/doi/10.1021/acs.jpcc.6b02235

3.2 CO_2 Adsorption in Fe_2(dobdc): A Classical Force Field Parameterized from Quantum Mechanical Calculations

Reproduced with permission from:

Joshua Borycz, Li-Chiang Lin, Eric D. Bloch, Jihan Kim, Allison L. Dzubak, Rémi Maurice, David Semrouni, Kyuho Lee, Berend Smit, Laura Gagliardi, *J. Phys. Chem. C* **2014**, 118, 23, 12230-12240.

Link: http://pubs.acs.org/doi/abs/10.1021/jp500313j

3.3 Ab Initio Derived Force Fields for Predicting CO_2 Adsorption and Accessibility of Metal Sites in the Metal−Organic Frameworks M-MOF-74 (M = Mn, Co, Ni, Cu)

Reproduced with permission from:

Emmanuel Haldoupis, Joshua Borycz, Huiliang Shi, Konstantinos D. Vogiatzis, Peng Bai, Wendy L. Queen, Laura Gagliardi, J. Ilja Siepmann, *J. Phys. Chem. C* **2015**, 119, 28, 16058-16071.

Link: http://pubs.acs.org/doi/abs/10.1021/acs.jpcc.5b03700

Chapter 4: Experimental and Computational Characterization of Zr_6 and Hf_6 Based MOFs for Catalysis

4.1 Defining the Proton Topology of the Zr_6-Based Metal-Organic Framework NU-1000

Reproduced with permission from:

Nora Planas, Joseph E. Mondloch, Samat Tussupbayev, Joshua Borycz, Laura Gagliardi, Joseph T. Hupp, Omar K. Farha, Christopher J. Cramer, *J. Phys. Chem. Lett.* **2014**, 5, 21, 3716-3723.

Link: http://pubs.acs.org/doi/abs/10.1021/jz501899j

4.2 A Hafnium-Based Metal-Organic Framework as an Efficient and Multifunctional Catalyst for Facile CO_2 Fixation and Regioselective and Enantioretentive Epoxide Activation

Reproduced with permission from:

M. Hassan Beyzavi, Rachel C. Klet, Samat Tussupbayev, Joshua Borycz, Nicolaas A. Vermeulen, Christopher J. Cramer, J. Fraser Stoddart, Joseph T. Hupp, Omar K. Farha, *J. Am. Chem. Soc.* **2014**, 136, 45, 15861-15864.

Link: http://pubs.acs.org/doi/abs/10.1021/ja508626n

4.3 Targeted Single-Site MOF Node Modification: Trivalent Metal Loading via Atomic Layer Deposition

Reproduced with permission from:

In Soo Kim, Joshua Borycz, Ana E. Platero-Prats, Samat Tussupbayev, Timothy C. Wang, Omar K. Farha, Joseph T. Hupp, Laura Gagliardi, Karena W. Chapman, Christopher J. Cramer, Alex B. F. Martinson, *Chem. Mater.* **2015**, 27, 13, 4772-4778.

Link: http://pubs.acs.org/doi/abs/10.1021/acs.chemmater.5b01560

4.4 Tuning Zr_6 Metal-Organic Framework (MOF) Nodes as Catalyst Supports: Site Densities and Electron-Donor Properties Influence Molecular Iridium Complexes as Ethylene Conversion Catalysts

Reproduced with permission from:

Dong Yang, Samuel O. Odoh, Joshua Borycz, Timothy C. Wang, Omar K. Farha, Joseph T. Hupp, Christopher J. Cramer, Laura Gagliardi, Bruce C. Gates, *ACS Catal.* **2016**, 6, 13, 235-247.

Link: http://pubs.acs.org/doi/abs/10.1021/acscatal.5b02243

4.5 Single-Site Organozirconium Catalyst Embedded in a Metal-Organic Framework

Reproduced with permission from:

Rachel C. Klet, Samat Tussupbayev, Joshua Borycz, James R. Gallagher, Madelyn M. Stalzer, Jeffrey T. Miller, Laura Gagliardi, Joseph T. Hupp, Tobin J. Marks, Christopher J. Cramer, Massimiliano Delferro, Omar K. Farha, *J. Am. Chem. Soc.* **2015**, 137, 50, 15680-15683.

Link: http://pubs.acs.org/doi/abs/10.1021/jacs.5b11350

4.6 Thermal Stabilization of Metal−Organic Framework-Derived Single-Site Catalytic Clusters through Nanocasting

Reproduced with permission from:

Camille D. Malonzo, Sammy M. Shaker, Limin Ren, Steven D. Prinslow, Ana E.

Platero-Prats, Leighanne C. Gallington, Joshua Borycz, Anthony B. Thompson, Timothy C. Wang, Omar K. Farha, Joseph T. Hupp, Connie C. Lu, Karena W. Chapman, Jason C. Myers, R. Lee Penn, Laura Gagliardi, Michael Tsapatsis, Andreas Stein, *J. Am. Chem. Soc.* **2016**, 138, 8, 2739-2748.

Link: http://pubs.acs.org/doi/abs/10.1021/jacs.5b12688

Chapter 1

Introduction

1.1 Introduction

Metal−organic frameworks (MOFs) are a class of nanoporous materials that are composed of metal-containing nodes connected by organic linkers. These materials have been studied extensively due to the wide array of possible structures,[1,2] tunability of the metal/organic linker combination,[3,4,5] and the high surface area of many of the materials.[6,7] MOFs have been utilized for many applications, which include chemical sensing,[8,9] gas separation,[10,11] and catalysis.[9,12,13] Much of the early work on MOFs was performed by Profs. Susumu Kitagawa[14] and Gérard Férey[15] when they were called porous coordination polymers (PCPs). The term metal-organic frameworks was coined by Prof. Omar M. Yaghi,[16,17] who performed some of the first work[18] on one of the most widely studied MOFs, $Zn_4(O)(bdc)_3$ (bdc=1,4-benzenedicarboxylate, also called MOF-5 and IRMOF-1) (Figure 1.1),[19,20,21,22] and has worked to define much of the modern terminology used with MOFs.[23] Since these efforts, thousands of MOFs with unique properties[24,25] have been synthesized, and these MOFs represent a small proportion of the millions of possible theoretical structures.[26] To narrow down the number of MOF structures that are studied it helps to systematically research specific families of MOFs that have desirable properties for chosen applications. The research contained in this thesis has mainly focused on three applications for MOFs: (1) magnetic properties, (2) CO_2 capture, and (3) catalysis.

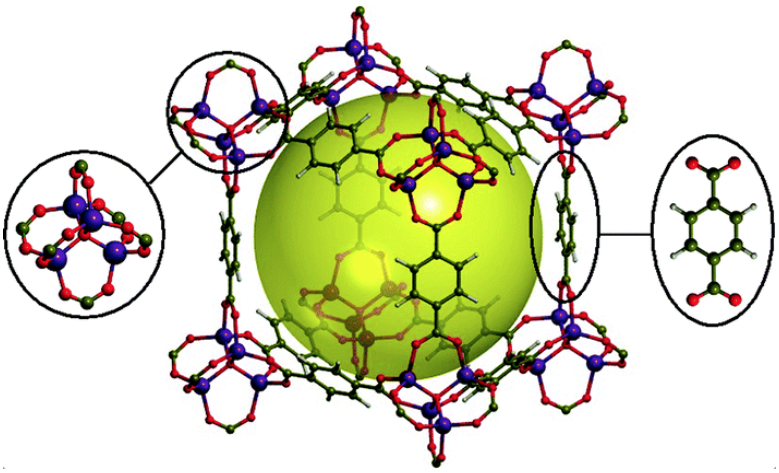

Figure 1.1: Structure of MOF-5 showing the cubic crystallographic cell. The octahedral inorganic units (left) are located at the corner of the cell (nodes) while the organic units (right) act as linkers (spacers). The large sphere highlights the cavity inside the structure. (Atom legend: violet = Zn and red = O, yellow = C, and gray = H). Reprinted with permission from ref 27. Copyright 2006 The Royal Society of Chemistry.

Magnetic materials require the presence of cooperative exchange interaction between paramagnetic metal ions and/or organic radicals through diamagnetic linkers. One paradoxical relationship between MOFs and magnets is that strong magnetic exchange generally requires short bridges between the spin carriers, but MOF porosity is increased by increasing the length of the organic linkers. These properties make the discovery of MOFs with strong magnetic exchange unlikely, but this unique combination of high-porosity with the presence of complex, metal-containing nodes has lead to many interesting and useful discoveries. For example, Fe_2(dobdc) (dobdc^{4-}=2,5-dioxodo-1,4-benzenedicarboxylate) (Figure 1.2) has chains of open-site, high-spin iron centers bridged by oxygen atoms.[28,10] Open-site metals are those with one or more ligands missing from their typical coordination environment, which leads to exposed electron density in the MOF pores and novel electronic structures.[29] Each chain is separated by ∼8 Å due to the length of the linker, which leads to separated chains with linear magnetic exchange. Spin-crossover can also result in changes in the magnetic moment of MOFs upon temperature change or adsorption of certain guests.[30] One possible application for such a MOF could be in the field of chemical sensors, since recent

work indicated that the magnetic ordering of Fe_2(dobdc) changes when olefins were adsorbed to the surface.[31] Accurately computing the interaction of adsorbants with the pore surface of MOFs is another active area of research due to ability of certain MOFs to selectively adsorb and desorb guests.

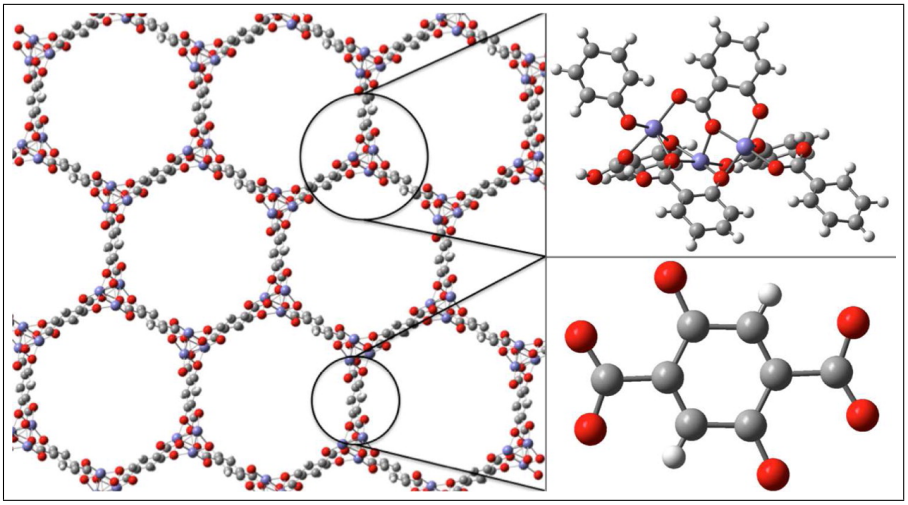

Figure 1.2: Crystal structure of Fe_2(dobdc) (dobdc^{4-} = 2,5-dioxido-1,4-benzenedicarboxylate) (left), structure of the 88-atom cluster used for computation (top right) and of the dobdc^{4-} ligand (bottom right). (Atom legend: blue = Fe and red = O, gray = C, and white = H).

One of the primary focuses of the MOF research community is to address the impending issue of anthropogenic global climate change. As such, gas separation in MOFs is one of the most popular areas of study. Currently, one of the most prominent sources of energy in the United States is coal, which produces large amounts of CO_2 when burned. Amine scrubbers represent the most mature method for carbon capture. Monoethanolamine (MEA) is used to perform a nucleophilic attack on CO_2 to form a carbon-nitrogen bond that falls in the chemisorptive range of -50 to -100 kJ/mol.[32] The amine solution is typically packed into an absorber column for the CO_2 to be passed through. Steam is then passed through the solvent to release the CO_2 and then the water vapor is condensed. This process leaves a highly concentrated CO_2 stream for compression and storage.[33] The main disadvantages of this method are the low loading capacity of MEA, the quick corrosion of equipment, and the substantial energy requirement.[34,35] Since materials do not need to be dissolved in water, the energy input of this

process might be decreased by introducing MOF filtration. Nanoporous materials have already been used for other gas separations and storage in industrial processes. For example, MOFs have been used to increase the volumetric density of methane, making it a more practical fuel source.[36] They have also been demonstrated to efficiently store hydrogen for use as a clean fuel source, and CO_2 can be stored as well.[37,38] With regard to CO_2 adsorption, Mg_2(dobdc) has a very high CO_2 binding energy due to the presence of open-site metal atoms that interact strongly with the oxygen of CO_2.[39]

MOFs with large pores allow for high diffusion rates which, when combined presence of metal atoms on the inner surface, have lead to MOFs being used at catalysts[40,12] and catalyst supports.[40,41] Although MOFs themselves have been utilized as catalysts, there are some inherent downsides that must be taken into account. One such problem is that synthesizing MOFs that contain large enough pores and metal sites of a specific element that are close enough to the surface to interact with guests can be difficult. As such, using MOFs as supports for catalytic sites has arisen as a recent area of study due to past success with zeolites[42,43] and surfaces.[44] In particular, $Zr_6(\mu_3{-}OH)_8(OH)_8(TBAPy)_2$ ($TBAPy^{4-}$=1,3,6,8-tetrakis(*p*-benzoic acid)pyrene), referred to as NU-1000, has $\sim$30 Å pores that allow quick diffusion of metal guests throughout the material and reactive Zr_6-nodes on which metal atoms can be deposited via atomic layer deposition (ALD)[45] (Figure 1.3) or solvothermal deposition. To deposit metal atoms onto the surface of MOFs, metal-organic precursors are flowed through the MOF in the gas phase,[45] in the case of ALD, or the solution phase, in the case of solvothermal deposition. Several metals have been deposited successfully on the surface of MOFs with ALD[45,46] and solvothermal deposition,[47] and in some cases have produced viable catalysts.[46,48]

Some catalytic reactions require or produce high temperatures that often lead to MOF degradation. For example, one of the most conceptually simplistic catalytic reactions is dehydrogenation, which is commonly used to produce styrene from ethylbenzene.[49] Dehydrogenation requires heating to temperatures near 500 °C,[50] while MOFs have fairly low thermal stability (150$-$350 °C).[51,52,52] Since MOFs are not viable candidates for these reactions, post-synthetic methods than can produce materials with high thermal stability are necessary. The process of nanocasting[53] can be used to stabilize the MOF metal clusters with a secondary, amorphous, porous skeleton that can withstand much higher temperatures. The organic linkers of the MOF template can then

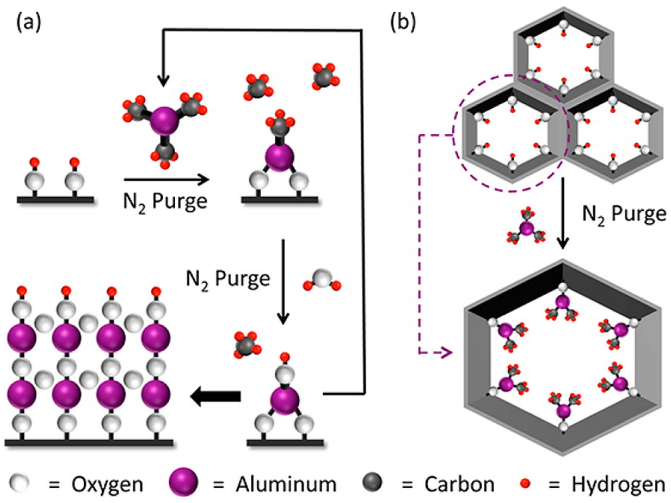

Figure 1.3: Illustration of (a) Thin film ALD on a surface and (b) Metalation by ALD in a MOF (AIM). Reprinted with permission from ref 45. Copyright 2013 American Chemical Society.

be removed, while the porous structure is maintained. Nanocasted materials have been used for catalytic reactions previously,[54,55] such as the oxidation of polycyclic aromatic hydrocarbons, which is an environmental pollutant resulting from fuel combustion.[56] One of the potential applications for nanocasted materials could be methane to methanol conversion, which has historically required very high temperatures.[57]

Herein, computational work that we have performed on MOFs is presented. Studies about magnetism, CO_2 capture, and catalysis within MOFs will be described briefly in three different sections. In each section the main goal of the studies, a discussion of how the problems were addressed, and the primary results will be provided.

1.1.1 Theoretical and Experimental Studies of Magnetic Properties of Fe_2(dobdc) Before and After Oxidation

This section contains a description of the materials and computational methods that we used in our magnetic studies. As mentioned previously, Fe_2(dobdc) is a material that contains open-metal sites, which means that upon synthesis the iron centers within Fe_2(dobdc) are hexacoordinate. Five of the sites are occupied by the oxygens within the organic linkers, and the remaining site, which points into the hexagonal pores is

occupied by a solvent molecule. The coordinating solvent molecule can be removed to leave behind helical chains of pentacoordinate Fe(II) ions. To understand the nature of the magnetism within Fe_2(dobdc), two sets of interactions must be computed, (1) the single-ion anisotropy, which represents the interactions between the spins on a single metal center due to the ligand field and spin-orbit interactions, and (2) the isotropic coupling between the metal centers, which is a measure of the energy necessary to flip the spin of a single metal center from up to down. Previous work has already demonstrated that the d^6 Fe(II) ions within this MOF are in the quintet state (four unpaired electrons),[8] but these measurements did not indicate whether or not the metal centers have multiconfigurational character, which occurs when there are near degenerate electron configurations. The isotropic coupling between the metal centers within Fe_2(dobdc) was determined via magnetic susceptibility measurements in previous work.[10] The primary goals of these works were to determine the potential utility of Fe_2(dobdc) as a magnet or magnetic sensor, and predict the magnetic ordering of isotopological structures oxidized with N_2O [$Fe_2(OH)_2$(dobdc) and $Fe_2(O)_2$(dobdc)].

The intra-ion ligand field and spin-orbit interactions can be described by the effective second-order perturbation theory parameters D and E, which represent the axial and rhombic zero-field splitting parameters, respectively. These parameters represent the definition of single-ion anisotropy, which is the directional dependence of the spin within a molecule or material. Accurately computing D and E often requires methods that explicitly compute multiple electron configurations. As such multiconfigurational wave function theory (WFT) methods have often resulted in parameters in good agreement with experiment,[58,59,60,61,62,63] and sometimes in better agreement than those computed with density functional theory (DFT).[64,65,66] As such, complete active space self-consistent field (CASSCF) that averaged over the (i) M_s=0 quintet states on Fe(II) that would be degenerate in the absence of a ligand field and (ii) the 100 M_s=0 states (5 quintet, 45 triplets, and 50 singlets) arising from the d^6 configuration of Fe(II). CASSCF is a wave function based method in which all possible electron configurations for a selected group of the molecular orbitals (known as the active space) of the system in question are computed. In CASSCF, all orbitals lower in energy than the active space are doubly occupied and all those higher in energy than the active space are empty. The selected set of molecular orbitals is referred to as the active space. This method is

not black-box and requires that a reasonable set of orbitals is chosen to yield accurate results. Although this method does provide a more accurate representation of multiconfigurational systems, it does not capture the dynamic correlation, interaction resulting from the motion of electrons, present within chemical systems. To compute this contribution the n-electron valence state perturbation theory (NEVPT2)[67] was employed. To make use of these rather computationally expensive methods, it was necessary to design cluster models. These models had to be small enough to allow the calculations to finish in relatively short order but large enough to properly represent the chemical environment of the metal centers within Fe_2(dobdc). The results of the CASSCF and NEVPT2 calculations showed that the five quintet states of the Fe(II) centers within Fe_2(dobdc) account for $\sim$90% of the contribution to the D and E parameters. This indicated that the Fe(II) ions in Fe_2(dobdc) are in the weak ligand field regime, i.e. the dobdc^{4-} ligands do not separate the orbital energies of the Fe(II) ions significantly, which allows these ions to exist in the high spin state (Figure 2.8). This leads to a large single-ion anisotropy, which is a measure of the directional preference of the spin of the Fe(II) centers. Finally, the isotropic coupling energies computed with DFT showed weak ferromagnetic interaction along the metal chains of Fe_2(dobdc)

In an extension of the work on Fe_2(dobdc), we made use of a combination of periodic and molecular DFT to compute the isotropic coupling energies in Fe_2(dobdc), and versions of this MOF oxidized with N_2O.[68] Periodic DFT was utilized to more accurately model the long range magnetic interactions in the extended MOF crystals. Molecular DFT was used with the cluster model from our previous work[69] to compare more modern DFT methods with the periodic results and to isolate the variables that result in the observed magnetic ordering within these MOFs. Periodic DFT models materials by employing periodic boundary conditions, which replicate a chosen unit cell in three dimensions to represent the full crystal. To ensure the accuracy of our computed crystal structures and isotropic coupling values it was necessary to compare to available experimental data. As such we compared to experimental crystal structures of Fe_2(dobdc) and $Fe_2(OH)_2$(dobdc), infrared spectra of Fe_2(dobdc) and $Fe_2(OH)_2$(dobdc), isotropic coupling values derived from magnetic susceptibility measurement of Fe_2(dobdc),[10] and newly measured magnetic susceptibility measurements of $Fe_2(OH)_2$(dobdc). We also

tested a wide array of functionals at the periodic level. We included generalized gradient approximation (GGA),[70] nonseparable gradient approximation (NGA),[71,72] hybrid type functionals,[73,74,75,76] and we tried the GGA and NGA types with and without empirical corrections[77] to the Coulomb and exchange integrals accounting for the over delocalization of electrons common in DFT[78,79,80,81] and dispersion corrections to capture the long range interactions present within materials.[82] These periodic calculations allowed us to compute both the interactions of the metals centers down the chains of metals and across the linkers with high levels of accuracy. The cluster models were used to isolate the effect that changing the Fe−Fe distances and Fe−O−Fe angles has on the isotropic coupling values. From these calculations we were able to accurately compute the structures of these MOFs, reproduce and improve upon previous results[31,28] that predicted the magnetic alignment of the metal centers within Fe_2(dobdc) and predict the magnetic ordering of $Fe_2(OH)_2$(dobdc), which had not been measured previously. We also determined that the shift in magnetic ordering from ferromagnetic to antiferromagnetic (Figure 2.18) upon oxidation is the result of both structural changes in the MOFs and changes in the electronic structure resulting from the presence of the O^{2-} and $(OH)^-$ ligands.

The complete details of the aforementioned works on magnetism are provided in Chapter 2. In Section 2.1, the computations and experimental work performed to elucidate the magnetic behavior of Fe_2(dobdc) are provided. First, we introduce the importance of this material and its relation to similar studies in molecular magnetism. Second, we describe the computational methods and phenomenological Hamiltionians that were utilized to extract the magnetic data. Also provided here are descriptions of the alternating current and direct current magnetic susceptibility measurements that were used to compare to the computational results. Lastly, we provide an interpretation of the magnetic data that suggests that Fe_2(dobdc)has unique metamagnetic behavior that is dependent on temperature due to the high single-ion anisotropy and weak isotropic coupling down the metal chains. In Section 2.2, the study of the oxidized version of Fe_2(dobdc), namely $Fe_2(O)_2$(dobdc) and $Fe_2(OH)_2$(dobdc) is discussed. The parameters used in the periodic and molecular DFT calculations are described along with the procedure utilized to measure the direct current magnetic susceptibility of $Fe_2(OH)_2$(dobdc). Finally, an explanation for the change in isotropic coupling values

upon oxidation is described.

1.1.2 *Ab Initio* Parameterized Forces Fields for Carbon Dioxide Adsorption in $M_4(O)(bdc)_3$ and $M_2(dobdc)$

Electronic structure calculations are extremely useful for understanding the details of interactions between small numbers of atoms. However, many of the applications for which MOFs are considered require understanding the behavior of molecules in the bulk phase. A great deal of effort has been devoted to obtaining force fields that can reasonably model the interactions of liquids and gasses.[83,84,85,86,87,88] These force fields simplify complex chemical relationships by separating them into sums of different types of empirical interactions. Much of the work involves structural force fields that include terms for angles and torsions,[89] but for work involving adsorption, the most important interactions are the non-bonding interactions of gasses with other gasses and with surfaces. This is because the interatomic interactions within MOFs are typically strong enough that the structures can be considered rigid, although this is not true in the case of flexible MOFs such as MIL-53.[90,91] One of the most common methods used to compute non-bonding interactions is to sum contributions from the point charges of the atoms present with the dispersion interaction that occurs from the long-range, instantaneous interaction of electrons. This force field typically takes the form of the Lennard-Jones potential,

$$E_{ij} = \frac{q_i q_j}{4\pi\epsilon_0 r_{ij}} + 4\epsilon_{ij}\left[\left(\frac{\sigma_{ij}^{12}}{r_{ij}^{12}}\right) - \left(\frac{\sigma_{ij}^{6}}{r_{ij}^{6}}\right)\right] \tag{1.1}$$

where r_{ij} is the distance between the interaction sites, σ_{ij} is related to atom size, ϵ_{ij} is related to the strength of the disperson interaction, q_i and q_j are the partial atomic charges for sites i and j, respectively, and ϵ_0 is the vacuum permittivity. There are many assumptions that must be made to simplify complex interactions into this form. For example, interactions involving three or more atoms as well as interactions between dipoles, quadrupoles, and higher degree terms of the Taylor series that describe electrostatic interactions are not explicitly described. Note that the summation over point charges does indirectly capture some of the higher order electrostatic terms, and that there are force fields that do explicitly compute these more complex contributions, but

they tend to be quite memory intensive and less general.[92] Despite all of these assumptions, eq 1.1 has proven invaluable for describing weak, non-bonding interactions. This success is due to the fact that the contributions from the aforementioned interactions are generally quite small, and can often be partially represented by choosing the right values for the Lennard-Jones terms (σ_{ij}, ϵ_{ij}), and the point charges (q_i) for each atom.

The transferable potentials for phase equilibria (TraPPE) force field[93,87,94,95,96,97,98] is one of the most accurate and widely used empirical force fields in the world due to its highly accurate description of bulk phase interactions between molecules. TraPPE parameters are computed by fitting σ_{ij} and ϵ_{ij} such that they reproduce the vapor-liquid coexistence curve of the gas in question. This is because vapor-liquid equilibria (VLE) are highly sensitive to many types of interactions that can occur in the bulk phase. Hence, if the VLE is well described, these interactions are likely to be well described. One of the issues with using general force fields such as the universal force field (UFF)[84,85] for MOFs, is that the parameters were not optimized to model the strong non-bonding interactions that can occur with the metal centers. Hence, they often underestimate adsorption within these materials.[39] Since strong non-bonding metal interactions are some of the reasons that MOFs have been considered for application to gas separations, it is vitally important to describe these interactions accurately. Electronic structure calculations can model the behavior of metal atoms quite well, as evidenced by Chapter 2, as such they can be used to supplement the calculation of gas separations in MOFs.

In the first section of Chapter 3, work describing the interaction of CO_2 with $M_4(O)(bdc)_3$, also called M-IRMOF-10 (where M = Mg, Ca, Fe, Cu, Zn, Ge, Sr, Cd, Sn, Ba) is provided. The metal atoms present in members of the IRMOF-10 series are coordinatively saturated, meaning that each of the bonding positions of the metal atoms is filled by a ligand. This typically would mean that interactions between the metal atoms and CO_2 would be quite weak. But in this work we tested the hypothesis that when atoms with larger ionic radii were used to replace the Zn^{2+} ions typically present within IRMOF-10, the metal$-CO_2$ interaction would become stronger. To make sure that we were describing all of non-metal interactions correctly we tested both the universal force field (UFF) and TraPPE, and two sets of points charges (q) that were derived in different ways [charge model 5 (CM5)[99] and density derived electrostatic and chemical

charges (DDEC)[100]]. To compute our force field we assumed that the CO_2-CO_2 interactions could be described by TraPPE inside the MOF,[98] that the MOF would remain rigid at all studied pressures, and that the metal$-CO_2$ dispersion interactions could be represented by using DFT to compute interaction energies between a cluster cut from IRMOF-10 and CO_2. To compute the dispersion energy contribution from eq 1.1, we subtracted the point charge interaction from the potential energy curves computed with DFT and fit σ_{ij} and ϵ_{ij} to the remaining interaction energy. By doing so we were able to demonstrate that when metal ions with larger ionic radii, e.g. Ba^{2+} and Sn^{2+}, are placed within the IRMOF-10 framework, the low pressure CO_2 affinity increases significantly and the CO_2 molecules bind more strongly to the metal containing nodes.

In Section 3.2, a force field modelling the interaction of CO_2 with Fe_2(dobdc) is described. The exposed electron density on the open-metal sites within the M_2(dobdc) series have been shown to result in very strong non-bonding interactions with CO_2 in previous work on Mg_2(dobdc),[39] but a force field had not yet been developed for a MOF containing an open-shell metal. In the work on Mg_2(dobdc) calculations were performed to parameterize the interaction between CO_2 and every atom type present within the MOF. This meant that clusters had to be designed and potential energy curves had to be computed for CO_2 as it approached each of the seven atoms types. Since the work of Dzubak et al.[39] demonstrated that the primary binding site for CO_2 was the metal center, we decided to utilize a general force field to model the interaction with all non-metal atoms, and focus only on parameterizing the interaction with the unique, open-shell, open-metal Fe(II) sites present within Fe_2(dobdc). To parameterize for this more complex interaction, interaction energies were computed by using complete active space self-consistent field (CASSCF) calculations to account for the potentially multiconfigurational nature of this interaction and second-order perturbation theory (CASPT2)[101] to account for the dynamic correlation necessary to describe CO_2 binding. To do so it was necessary to utilize a model cluster cut from periodically optimized DFT structures, due to the expensive nature of WFT calculations. From these calculations we were able to ascertain that the the MOF$-CO_2$ can be easily described by a single electron configuration, which was in the quintet spin state. Hence the method of calculation was simplified to restricted open-shell Møller-Plesset second-order perturbation theory (ROMP2).[102] We discovered in this work that parameterizing only the

interaction of CO_2 with the metal center of Fe_2(dobdc) and modeling all non-metal interactions with an established force field[83,84] yielded CO_2 isotherms that were quite close to experimental values, and confirmed that the primary site of interaction within Fe_2(dobdc) is near the metal center as in Mg_2(dobdc).

The question remains as to how other 3d metal atoms within the M_2(dobdc) framework interact with CO_2. This is why in Section 3.3 we extended our study to include Mn^{2+}, Co^{2+}, Ni^{2+}, and Cu^{2+}, which were the only metals for which CO_2 force fields in M_2(dobdc) had not yet been developed. Since in our previous work,[103] discussed in Section 3.2, we discovered that the metal centers within Fe_2(dobdc) were single configurational and high-spin, we decided to test the efficacy of using DFT calculations to parameterize the interaction of CO_2 with these metal centers. As such we computed the interaction energies with ROMP2, as well as two commonly used density functionals[70,104] with dispersion corrections added.[105] Furthermore, we decided to explicitly test the effect that remaining solvent molecules (methanol and water), which bind strongly to the metal centers, might have on the CO_2 isotherms simulated within these MOFs. In the work described in Section 3.2, the computed isotherms had to be scaled to account for impurities in the experimental structures when the measurements were taken. In this work we sought to see if we could quantify the extent to which strongly bound solvent molecules and void space resulting from framework distortions would affect the isotherms. We did so by computing isotherms for each metal with different proportions of the metal centers saturated by methanol or water, and by also computing isotherms with portions of the pores clogged by artificial void spaces. We discovered in this work that we could predict approximate proportions of remaining solvent bound to the metal centers, which may help experimentalists to determine which solvents are most difficult to remove. We also discovered by comparing the CO_2 interaction with each of the aforementioned metal centers that Mn_2(dobdc) had the strongest interaction with CO_2 of those tested, and that Cu_2(dobdc) had a very weak affinity for CO_2, methanol, and water. Electronic structure calculations helped us to determine that this was because the d^9 electron configuration of the Cu^{2+} ion had electrons present in anti-bonding orbitals that prevented back bonding with the guest molecules.

In summary, the entirety of these articles on CO_2 adsorption are provided in Chapter 3. Section 3.1 describes the work performed on the M-IRMOF-10 series (M = Mg, Ca,

Fe, Cu, Zn, Ge, Sr, Cd, Sn, Ba), in which we discovered that CO_2 bound more strongly to metal centers that had larger ionic radii due to the increase in the exposure of the electron density of metal atoms to the pore. In Section 3.2, the work is extend to include an open-metal site MOF containing iron known as Fe_2(dobdc). This work demonstrated that by parameterizing only the metal-CO_2 interaction with *ab initio* calculations, we could described even the complex interactions that occur within MOFs containing open-shell, open-metal sites. Finally, in Section 3.3 the computation of isotherms is extended to other members of the M_2(dobdc) series (M = Mn, Co, Ni, Cu) that contain metal atoms in the 3d block of the periodic table. A comparison of the CO_2 affinity of these metal centers and the effect that strongly bound solvent and defects present have on CO_2 adsorption are discussed in this section.

1.1.3 Experimental and Computational Characterization of Zr_6 and Hf_6 Based Metal-Organic Frameworks for Catalysis

The search for efficient catalysts has been one of the primary efforts in chemistry for quite some time. Materials such as zeolites have been used for catalysis in the petroleum industry for over 60 years.[106] Recent work has shown that by attaching metals to the surfaces of zeolites, new catalytic activity can be observed.[107] Similar procedures have also been applied to NU-1000 due to its high thermal stability and large pore diameter.[108,109,13,45] To improve upon the understanding of catalysis within modified NU-1000, it is first necessary to understand the structure of the reactive Zr_6-nodes.

In Section 4.1, the first computational study that we performed on NU-1000 was done in collaboration with experimentalists to determine the proton topology of the Zr_6-nodes. The exact structure of the Zr_6-nodes was in contention at the time of this study. In work by Morris et al. on MOF-545, which contain Zr_6-nodes that are isostructural to those in NU-1000 (Figure 1.4), X-ray diffraction data suggested that the eight terminating oxygen groups were water molecules ($[Zr_6(\mu_3\text{-}O)_8(H_2O)_8]^{8+}$).[110] In PCN-222, which also contains these nodes, Feng et al. assigned single protons to all of the oxygens within the node ($[Zr_6(\mu_3{-}OH)_8(OH)_8]^{8+}$).[111] Due to the ambiguities that result from the interpretation of X-ray diffraction data, in our work we combined experiment and computation to obtain structures and infrared (IR) spectra of NU-1000 to determine the most likely proton topology. In this work we computed the energies

of different proton topologies with both periodic and molecular DFT and compared the results to find the lowest energy structure. With cluster calculations we also computed IR spectra and compared to experimental values to find the closest match. We discovered in this work that the most likely proton topology was a mix of those predicted previously ($[Zr_6(\mu_3\text{-}O)_4(\mu_3\text{-}OH)_4(OH)_4(H_2O)_4]^{8+}$).

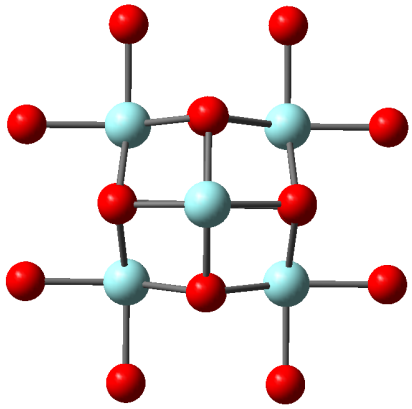

Figure 1.4: Zr_6-nodes present within NU-1000 (MOF-545 and PCN-222) with protons removed. (Atom legend: light blue = Zr and red = O).

Section 4.2 describes a study performed on an isotopological version of NU-1000 containing Hf_6 nodes (Hf-NU-1000). The catalytic efficiency of this MOF for epoxide activation was examined both experimentally and computationally. Periodic DFT was used to optimize the structure of Hf-NU-1000 with the lowest energy proton topology determined in Section 4.1 to compare the X-ray diffraction data. We were able to determine that the proton topology of Hf-NU-1000 is the same as the one predicted for zirconium analogue. Experimental results showed that Hf-NU-1000 readily reacts with styrene oxide and trimethylsilyl-azide ($TMS{-}N_3$) to selectively form β-azidohydrin which resulted in a significantly higher yield of the cyclic carbonate final product than when NU-1000 was used. This computational work on the mechanism of the epoxide activation showed that the epoxide bound more strongly to the $-OH$ sites of Hf_6 than those of Zr_6 and that the epoxide ring preferred to open such that the azide would attack at the benzylic position by $\sim$12 kJ/mol when reacting with Hf_6. This difference in energy accounts for the selectivity of the β-azidohydrin formation and suggests that it is promising candidate for enantioselective catalysis.

Since the structure of the catalytically active sites in NU-1000 is now understood, we can now study the modification of this MOF via ALD. Since the ALD process often results in the formation of nanoparticles,[112,113] the reactivity of these species can be quite difficult to characterize both experimentally and computationally due to the large size and complexity of the structures.[114,115] As such, in the work in Section 4.3 we sought to use ALD to deposit single-site catalysts on the surface of NU-1000. This procedure would allow a more precise understanding of the reactivity taking place within the MOF. Many metals have been considered for functionalization[116,48] of NU-1000, but we decided to focus on aluminum and indium first due to the simplicity of their electronic structures and precursors [trimethyl aluminum ($AlMe_3$) and trimethyl indium ($InMe_3$)]. $InMe_3$ and $AlMe_3$ were each reacted with NU-1000 under vacuum at 125 °C until the protons on the surface of the MOF had all reacted with the precursors. At high concentrations $AlMe_3$ caused NU-1000 to lose its porosity. $InMe_3$ did not cause the MOF to degrade. X-ray pair distribution function (PDF) measurements were performed and compared to DFT optimized structures of the indium loaded MOF. Cluster DFT calculations were used to optimize the structures resulting from the reaction of $AlMe_3$ and $InMe_3$ with the Zr_6-nodes. The full mechanism of the reaction with each species was computed and it was determined that two metal atoms could be added to each face of the Zr_6-nodes for a total of eight metal atoms per node, which aligned reasonably well with experimental predictions of the total metal loading and the PDF measurements.

Another metal that was considered as a possibility for single-site catalysis within MOFs was iridium. The work described in Section 4.4 was inspired by work with iridium catalysts in zeolites.[107,117] The HY zeolite contains Al−O sites that form strong bonds with iridium. These iridium sites decrease the reaction barrier for the dimerization of ethylene significantly. The goal of this work was to see if the Zr_6-based MOFs UiO-66, UiO-67, and NU-1000 would result in comparable catalytic efficiency for this reaction. Since the Zr_6-nodes in UiO-66 and UiO-67 are saturated with linkers, it was necessary to remove some of the linkers from these materials to create $-OH/-OH_2$ active sites similar to those in NU-1000. Cluster DFT calculations were used to model the reactive iridium sites present within the HY zeolite, and the MOFs UiO-66, UiO-67, and NU-1000. Extended X-ray adsorption fine structure (EXAFS) spectra were measured for each experimental structure and compared to the DFT optimized cluster models for

validation. Carbon monoxide molecules were then attached to the iridium atom sites and the frequencies of the dicarbonyl bands in the IR spectra were plotted against the selectivity of each structure for the dimerization of ethylene. Previous work had already shown that, like the HY zeolite, the Zr_6-nodes in these MOFs could be used to catalyze ethylene dimerization.[48] In this work we compared the efficiency of each of these MOFs as catalysts for this reaction and determined that the efficiency is dependent upon the electron withdrawing properties of the surface. If the surface withdraws electron density from the reactive iridium sites then they are more likely to react with ethylene. The Al−O sites within the HY zeolite withdraw more electron density than the sites on the Zr_6-nodes. This research suggests that the catalytic efficiency of these MOFs might be improved by depositing aluminum on the surface before adding iridium.

The Hf_6 based version of NU-1000 can also be used as a support for single-site catalysts. In Section 4.5, tetrabenzylzirconium ($ZrBn_4$) was reacted with Hf-NU-1000 to create single-site catalysts for alkene polymerization. ZrBn sites on silica surfaces have been used with some success for alkane metathesis.[118] In this work both cluster and periodic DFT calculations were used to determine the chemical structure of the ZrBn sites on the Hf_6-nodes. With the final structure of Hf-NU-1000-ZrBn determined we were then able to compute the mechanism of 1-hexene polymerization within this MOF. The final mechanism for this polymerization had fairly low (∼100 kJ/mol) reaction barriers, which aligned quite well with experimental results.

Another application of MOFs for catalysis is as templates to synthesize materials with high thermal stability through nanocasting. Section 4.6 contains an article that describes a nanocasting procedure which uses NU-1000 as a template. NU-1000 was reacted with tetramethyl orthosilicate (TMOS) to form an amorphous material that retained the porosity of a MOF. The organic linkers of NU-1000 were then removed via calcination so that only the Zr_6 clusters within amorphous silica (SiO_2@NU-1000) were left behind. This new material was heated to 600 °C and maintained its porosity. Furthermore, the dehydrated Zr_6 clusters within SiO_2@NU-1000 retained their catalytic activity. The isomerization of glucose to fructose was successfully catalyzed within this material even after heating to exteme temperatures. Note that when Zr_6 clusters were directly reacted with TMOS, and not contained within the NU-1000 framework, the final structure was not reactive with glucose due to the lack of porosity of the resulting

material. Computational results were able to confirm that the dehydrated Zr_6 clusters were highly efficient Lewis acid catalysts that lowered to barrier for glucose isomerization to a point where the reaction could easily occur at room temperature (86.2 kJ/mol).

In summary, Chapter 4 contains descriptions of combined experimental and computational studies that helped to determine the structure of NU-1000 and Hf-NU-1000 as well as predict the structure and catalytic activity of aluminum, indium, iridium, and zirconium sites attached the surface of Hf_6 and Zr_6 based MOFs. Section 4.1, describes a study that determined the proton topology of the Zr_6-nodes that were used for catalysis in subsequent works. Section 4.2, contains an article about epoxide activiation within Hf-NU-1000. In Section 4.3, the structure of NU-1000 modified through ALD with aluminum and indium precursors is provided. Section 4.4 contains a study comparing the catalytic efficiency of iridium sites within UiO-66, UiO-67, and NU-1000 to similar sites within a zeolite. In Section 4.5 ZrBn sites were place on the surface of Hf-NU1000 and the final structure was characterized and its catalytic efficiency for alkene polymerization was computed and compared to experiment. Finally, Section 4.6 outlines research on the activity of dehydrated Zr_6 clusters for Lewis acid catalysis within a nanocasted materials that was templated with NU-1000.

1.1.4 Organization of the Thesis

The purpose of this thesis is to report work that analyzes MOFs magnetic characteristics, their capability as CO_2 adsorbers, and several possible methods for utilizing the porosity and reactivity of MOFs to improve catalytic techniques for many different reactions. To this end, this thesis is separated into three chapters based on these application.

Chapter 2: Theoretical and Experimental Studies of Magnetic Properties of Fe_2(dobdc) Before and After Oxidation

This chapter contains two studies on the magnetic characteristic of MOFs. The first section involves the computation of the single-ion anisotropy and isotropic coupling values within Fe_2(dobdc). The next section extends this study to oxidized version of this MOF ($Fe_2(O)_2$(dobdc) and $Fe_2(OH)_2$(dobdc)). We show here that the Fe(II) sites within Fe_2(dobdc) have high single-ion anisotropy, which is why they are in the quintet state, and that the isotropic coupling between the metal centers is weakly ferromagnetic

going down the chains of metals, but that this MOF is unlikely to be a magnet due to the noncollinearity of the spin centers. The second study shows that the magnetic ordering of this MOF changes from ferromagnetic to antiferromagnetic upon oxidation due to the presence of the newly added O^{2-} and $(OH)^{-}$ ligands and the elongated Fe−Fe bond and Fe−O−Fe angles.

Chapter 3: *Ab Initio* Parameterized Forces Fields for Carbon Dioxide Adsorption in $M_4(O)(bdc)_3$ and $M_2(dobdc)$

This chapter follows a series of studies that involve various computational approaches to compute force field parameters that describe the adsorption of CO_2 to the surface of MOFs. The first section describes the parameterization of force fields for the interaction of CO_2 with members of the M-IRMOF-10 series with various metals. In this section we demonstrate that metals with larger ionic radii could adsorb CO_2 more strongly in this MOF topology. The next two sections involve the simulation of CO_2 isotherms within members of the open-metal site containing M_2(dobdc) series (M = Fe, Mn, Co, Ni, Cu). We also examine the effect that leftover solvent molecules bound the metal centers have on the final computed CO_2 isotherms.

Chapter 4: Experimental and Computational Characterization of Zr_6 and Hf_6 Based MOFs for Catalysis

This chapter contains one study that characterized the structure of the Zr_6 based MOF NU-1000, since this study was necessary to understand the reactivity of this and other similar MOFs, three studies about catalytic reactions that can be performed within Zr_6 and Hf_6 MOFs that have various metals deposited on their surfaces, and one study that makes use of NU-1000 as a template to make a material that can withstand high temperature catalysis through nanocasting. In Section 4.1, the structural characterization of NU-1000 is described. Sections 4.3 through 4.5 contain studies about aluminum and indium deposition on the surface of NU-1000, the efficacy of single-site iridium catalysis within Zr_6 based MOFs compared to the HY zeolite, and enantioselective epoxide activation due to ZrBn sites added to the surface of Hf-NU-1000. Finally, the study of a nanocasted material that used NU-1000 as a template to create a thermally stable Lewis acid catalyst is described in Section 4.6.

Chapter 2

Theoretical and Experimental Studies of Magnetic Properties of Fe_2(dobdc) Before and After Oxidation

2.1 Single-Ion Magnetic Anisotropy and Isotropic Magnetic Couplings in the Metal-Organic Framework Fe_2(dobdc)

2.1.1 Introduction

Transition metal based nanoporous materials are attracting the attention of many scientists because of their high selectivity in gas separations,[119,10,120,121,122,123] catalytic activity,[124,125] and magnetic properties.[2,126,127] Many of their properties are linked to the presence of open-site transition metal ions, which may have open shells depending on their d^n configuration and their coordination environments inside the framework. If the metal ions are connected by organic linkers, one may refer to such materials as metal-organic frameworks (MOFs), coordination polymers, or coordination networks.

Among this newly popular class of materials, the Fe_2(dobdc) (dobdc^{4-} = 2,5-dioxido-1,4-benzenedicarboxylate) system, referred to as Fe-MOF-74, is particularly noteworthy. It exhibits very high performance for the separation of methane/ethane/ethylene/acetylene mixtures[10,128,11] and can selectively bind O_2 over N_2.[8] The structure of this compound consists of high-spin Fe^{II} ions arranged in a helical pattern along columns at the intersection of three hexagonal pores. As synthesized, each Fe^{II} ion is hexacoordinate; five coordination sites occupied by dobdc^{4-} ligands and one by solvent. Upon activation, however, the coordinating solvent is removed, leaving the Fe^{II} ion in a pentacoordinate environment. The first coordination sphere around each Fe^{II} ion is a distorted square pyramid (SPy), with the oxygen atoms of the dobdc^{4-} ligands bridging to other Fe^{II} ions along the same or other helical chains (see Figure 2.1).

A detailed analysis of the magnetic properties of Fe_2(dobdc) by the spin Hamiltonian approach can be problematic. The universal starting point of representing the system by a phenomenological spin Hamiltonian[129] involves exchange integrals J_{ab} and effective local spins $\hat{S}_a$, sometimes called fictitious spins. These exchange integrals, which describe the interactions of spins on magnetic centers a and b, are called isotropic magnetic couplings. Interactions can also occur between spins on the same metal center

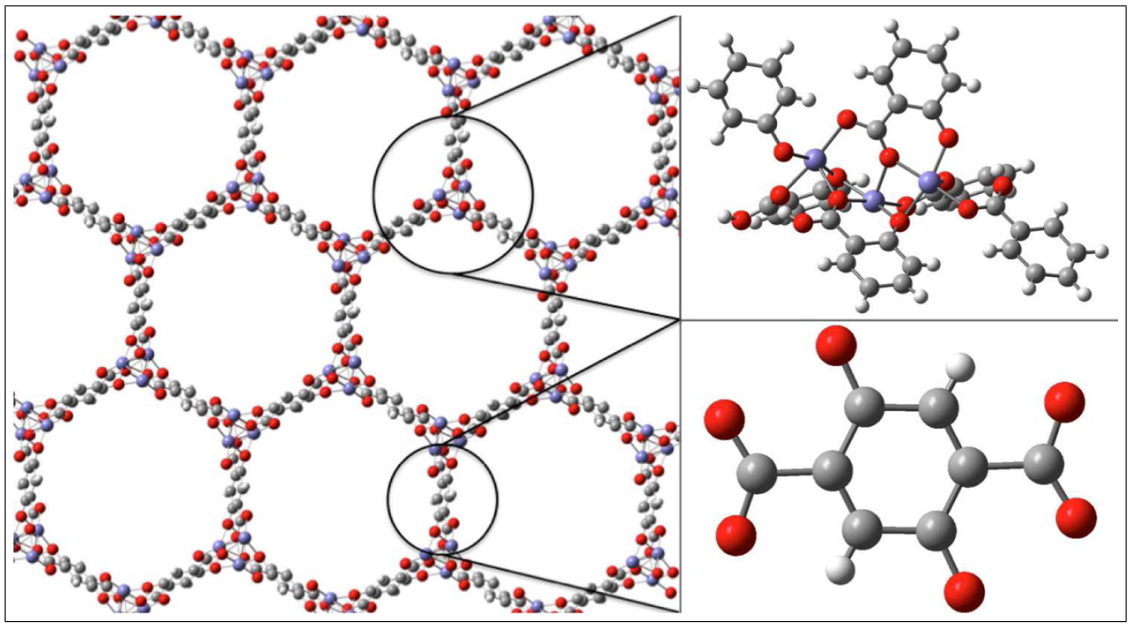

Figure 2.1: Crystal structure of Fe_2(dobdc) (dobdc^{4-} = 2,5-dioxido-1,4-benzenedicarboxylate) (left), structure of the 88-atom cluster used for computation (top right) and of the dobdc^{4-} ligand (bottom right), where Fe atoms are represented in purple, O atoms in red, C atoms in dark gray, and H atoms in light gray.

because of ligand field and spin-orbit interactions. These intra-ion interactions are usually described by the effective second-order perturbation theory parameters D and E, which correspond to the axial and rhombic zero-field splitting parameters, respectively. As given, this picture of the magnetic interactions is simple, yet it is nearly impossible to simultaneously extract the magnitudes of all the spin Hamiltonian parameters present in a system (i.e., J_{ab}, D, and E) from one measurement technique without approaching overparameterization. A previous analysis of the magnetic susceptibility data of Fe_2(dobdc) attempted to avoid the overparameterization problem by using a model that only included inter- and intrachain isotropic magnetic couplings.[10] Note that, though the quality of the fit was good, the model did not address the probability that the Fe^{II} spin centers are appreciably anisotropic. Recent work has demonstrated that coordinatively saturated and unsaturated Fe^{II} ions can possess very large magnetic anisotropies.[130,131,132,133,134] Furthermore, the previous analysis did not account for intrachain next-nearest neighbor interactions, which can in some systems compete with nearest neighbor interactions[135,136] and lead to spiral spin orderings (and we note that some omitted intrachain interactions involve Fe atoms closer than those involved in the included interchain interactions). Here we revisit this problem via quantum mechanical electronic structure calculations. We use a cluster approach, and effective interactions are addressed by choosing a given level of electronic structure theory and basis set and by selecting the ions to be explicitly treated. For instance, the calculation of the single-ion anisotropy parameters requires one to treat explicitly (at least) one magnetic center, while the calculation of isotropic magnetic couplings requires at least two. With these considerations in mind, the choice of clusters is not unique, and one has to catch in them the most important electronic effects present in the real material. Note that the isotropic interactions addressed in the present work have been obtained from periodic calculations by Canepa et al.[28]

Several methods are now available for the computation of single-ion anisotropies, based on both density functional theory (DFT)[137,138,58,139,140] and wave function theory (WFT).[64,141,59,142,60] The interpretation and analysis of magnetic data of transition metal complexes is a very active field, and computational and theoretical studies can play a useful role in interpreting experiments.[143,144,145,61,146] With these methods, valuable information can be obtained on the anisotropy of metal ions even in non-standard

coordination environments, for example, distorted pentacoordinate and heptacoordinate environments.[62,63,147] In cases closer to ideal geometries, the results of quantum chemical calculations can also be connected to crystal-field theory to gain further insights into the factors governing the anisotropy.[148,149,150,151,152] Since MOFs can present transition metal ions in unprecedented coordination environments, the theoretical determination of the single-ion anisotropies is particularly important. Part of the present paper is therefore devoted to the determination of the single-ion anisotropy in Fe_2(dobdc), which is expected to be large, as in mononuclear heptacoordinate Fe^{II} complexes.[132,63] Indeed, in a ligand field picture, both situations show near degeneracy of orbital configurations that can be coupled via the spin-orbit operator once the spin is introduced, resulting in large zero-field splittings. In many cases, WFT approaches have led to single-ion anisotropic parameters in good agreement with experimental values,[58,59,60,61,62,63] and sometimes in better agreement than those obtained by DFT.[64,65,66] Therefore, we will use WFT to predict the values of the single-ion magnetic anisotropy parameters in Fe_2(dobdc).

Isotropic magnetic couplings can be extracted from computed energies of spin-adapted wavefunctions or broken-spin-symmetry solutions, which can be obtained from either WFT or DFT calculations.[153] Within the cluster approach, a wide choice of methods based on WFT and/or DFT is available. WFT studies usually involve a complete active space self-consistent field (CASSCF) calculation where the active space includes the magnetic electrons and orbitals, followed by a perturbative and/or variational treatment of the most important remaining electron correlation effects. As shown in a series of papers by Calzado et al.,[154,155,156] a careful treatment of the dynamic correlation is required to obtain accurate couplings; in particular, in a WFT approach, all the excited determinants contributing to the magnetic coupling at second order of perturbation have to be treated variationally. This leads to very expensive multi-reference configuration interaction (MRCI) calculations, which become impractical when several magnetic centers are considered. Alternatively, DFT studies only require the treatment of single Slater determinants, but the results may be strongly dependent on the exchange-correlation functional. It is therefore necessary to check the accuracy of the functionals to treat magnetic couplings. We note, however, that newly developed functionals appear to be particularly accurate,[157,76] thus simplifying the process of functional selection. Given

this fact, and the relative computational ease with respect to WFT methods, we chose DFT as the preferred method for determination of the isotropic coupling constants for Fe_2(dobdc).

Herein, we present a detailed theoretical and experimental analysis of the single-ion magnetic anisotropy and isotropic magnetic couplings in Fe_2(dobdc). The choice of the cluster will be described, as well as the phenomenological Hamiltonians, the computational details, and information concerning the extraction of the relevant effective parameters. Then, results for the single-ion anisotropy and magnetic couplings will be presented, as well as additional magnetic data analysis, followed by a discussion.

2.1.2 Methods

Magnetic Measurements

Fe_2(dobdc) was prepared according to the published procedures.[8] All handling of the compound during sample preparation was performed under an inert atmosphere. Powdered samples of Fe_2(dobdc) were restrained with a plug of glass wool within a sealed quartz tube for measurement. Magnetic data were collected using a Quantum Design MPMS-XL SQUID magnetometer at temperatures from 1.8 to 300 K and applied direct current (DC) fields from 0 to 7 T. Alternating current (AC) susceptibility measurements were performed with a 4 Oe applied switching field. No effects of crystallite torquing were observed during any measurement. AC and DC magnetic susceptibility data were corrected for diamagnetic contributions from the sample holder and glass wool, as well as for the core diamagnetism of each sample (estimated using Pascals constants).[158]

Theoretical and Computational Study

Model for the Isotropic Coupling Calculations

The isotropic magnetic couplings are calculated for an 88-atom model[159] of Fe_2(dobdc) (as shown in Figure 2.2) that contains three pentacoordinate Fe^{II} centers and six organic linkers. Four of the six organic linkers coordinate the central iron ion, and the 88-atom cluster has been designed in such a way that the overall charge on the model is zero and the first coordination sphere of the central iron ion is unmodified from the crystal, whereas the structural features farther away from the central iron ion are truncated to

terminate the cluster. Note that the charge of the model has been set to zero by a judicious addition of protons. In the extended structure, all Fe^{II} centers are symmetry equivalent; however, in our truncated model cluster, for which we have ensured a neutral charge, they have slightly different coordination environments. We assume that the Madelung field does not affect significantly the computed energy differences, that is, it is expected to have a minor effect on these energy differences compared to the local bonding, electrostatic, and correlation effects that are explicitly treated in the 88-atom model.

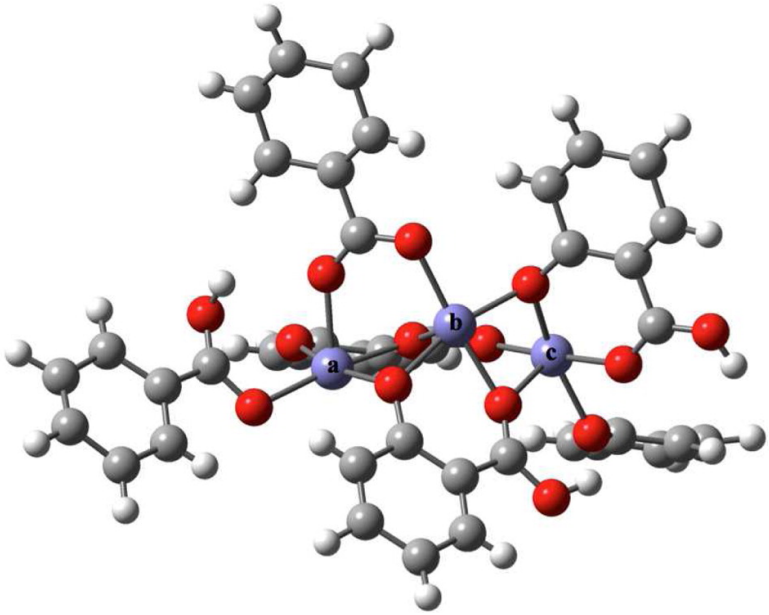

Figure 2.2: Eighty-eight atom model of Fe_2(dobdc) designed from its crystal structure as viewed along an axis perpendicular to the c axis, which is the axis through the helical column of Fe atoms. The three iron ions within the structure are labeled as a, b, and c from left to right. The Fe atoms are represented in purple, O atoms in red, C atoms in dark gray, and H atoms in light gray.

Each of the Fe^{II} centers is in a high spin state ($S = 2$, $M_S = 2$). For the purpose of calculating isotropic coupling constants between the three iron centers, a value of M_S of either 2 or -2 is assigned to each of the iron centers. We have considered four possible ways to assign these M_S values (spin states) in the four Slater determinants studied using density functional calculations. In the first case, a local spin component of 2 is

assigned to all the three iron centers, labeled a, b, and c in Figure 2.2, making the total spin of the model equal to $S = 6$. In the second case, a local spin component of 2 is assigned to both the leftmost and the central iron centers (a and b, respectively) and a -2 spin component is assigned to the rightmost iron center (c) leading to the overall spin component of the model being $M_S = 2$. In the third case, both the peripheral iron centers (a and c) are assigned a local spin component of 2 while the central iron ion has a local spin component of -2 which also results in the total spin of the model being $M_S = 2$. In the fourth case, a local spin component of -2 is assigned to the leftmost iron center (a) and a spin component of 2 to the central and the rightmost iron centers (b and c, respectively) leading to the overall spin component of the model being $M_S = 2$. Although the Slater determinants of the second through fourth states do not correspond to a definite value of the spin quantum number S, these four states can be used in a straightforward way for calculating the coupling constants. All four possibilities are shown schematically in Figure 2.3.

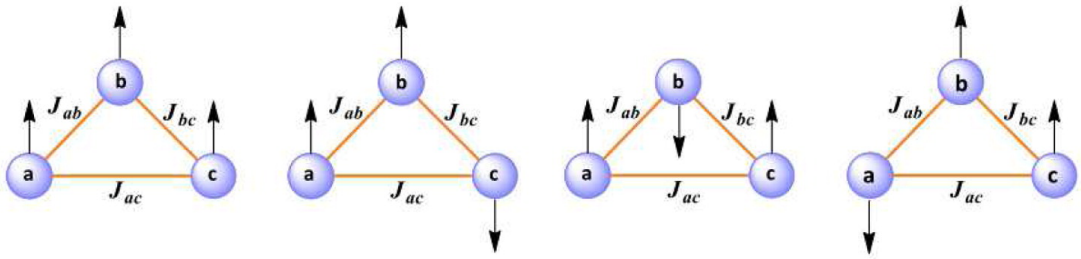

Figure 2.3: Schematic representation of all four cases of spin states considered on the three iron centers of the 88-atom model. The arrows denote the direction of the local spins at the quintet Fe^{II} centers.

Model for the Single-Ion Anisotropy Calculations

The single-ion anisotropy arises from the joint effects of the ligand field and spin-orbit coupling (SOC); these effects are mainly determined by the metal center and its first coordination sphere. Note, however, that the extreme sensitivity of the magnetic anisotropy of transition metal ions to their surroundings leads to a significant influence upon D from metal ions immediately outside the first coordination sphere.[61,160] Hence, we also include the effect of the two nearest-neighbor Fe^{II} ions, and more specifically

their influence on the crystal field felt by the central one. Since an explicit treatment of these additional Fe^{II} ions would dramatically complicate the analysis, we model them in the anisotropy calculations by closed-shell ions with the same nominal charge and a similar ionic radius, in particular by Zn^{II} ions. The cluster considered for these calculations is the 88-atom cluster described previously[159] and above, where two of the three Fe^{II} ions, in particular the peripherical ones, have been replaced by Zn^{II} ions, while all the atomic positions remain the same.

Phenomenological Hamiltonians

In general permanent magnetization in a system like Fe_2(dobdc) can be caused in three possible ways:[161,162,163] (i) ferromagnetic exchange interactions of directly interacting metal ions or superexchange of metal ions by bridging ligands within a chain of iron ions, (ii) single-ion anisotropy because of lower than cubic symmetry at the spin center, or (iii) magnetic dipole coupling between the one-dimensional chains of iron ions. The third contribution is typically the least important although it could become important at low temperature. Nevertheless the present article considers only (i) and (ii).

In keeping with the previous paragraph, we employ two phenomenological Hamiltonians, one to determine the single-ion magnetic anisotropy parameters and one to model the exchange and superexchange coupling of magnetic sites along the chains of iron ions.

Single-Ion Hamiltonian

The effective Hamiltonian operator for single-ion anisotropy is sometimes called the zero-field splitting (ZFS) Hamiltonian or the fine structure Hamiltonian. It is given by[59,150,164,165,166,166]

$$\hat{H}_{\mathrm{ZFS}} = \hat{\mathbf{S}}_b \cdot \mathbf{D} \cdot \hat{\mathbf{S}}_b \tag{2.1}$$

where $\hat{\mathbf{S}}_b$ is the vector operator for the effective spin of center b, and $\mathbf{D}$ is the second-order anisotropy tensor. The coordinate system that diagonalizes $\mathbf{D}$ is called the magnetic axis frame. In this frame, the Hamiltonian becomes

$$\hat{H}_{\mathrm{ZFS}} = D\hat{S}_z^2 + E(\hat{S}_x^2 - \hat{S}_y^2) \tag{2.2}$$

where z is the highest-symmetry axis, and

$$D = D_{zz} - \frac{1}{2}(D_{xx} + D_{yy}) \tag{2.3}$$

and

$$E = \frac{1}{2}(D_{xx} + D_{yy}) \tag{2.4}$$

$\hat{H}_{\mathrm{ZFS}}$ splits the states of the ion when $S > 1/2$. The parameter D is called the axial ZFS parameter because E, which is called the rhombic ZFS parameter, vanishes for a system with a 3-fold or higher axis of symmetry. D is nonzero only if the symmetry is less than cubic or octahedral. D may have either sign, but E is here chosen positive by convention, and $E/|D|$ ranges from 0 (the axial limit) to 1/3 (the rhombic limit). Negative D is necessary for the magnetic bistability associated with single-molecule magnets.[167] When D is negative, z is the easy axis of magnetization. Note that the D and E parameters have units of energy.

Both first-order spin-spin interactions and second-order spin-orbit coupling (SOC) contribute to the anisotropy; for transition metals the latter usually dominates.(18, 68) Several studies concerning single-ion anisotropy[58,65,168,169] or intersite magnetic anisotropy[170] showed that the first-order spin-spin contribution becomes non-negligible in the case of small to moderate zero field splitting. When the SOC contribution to the anisotropy is large, however, the spin-spin interactions become negligible. As we will show later, this situation occurs in Fe_2(dobdc), and therefore only SOC is included in the present study. We will calculate the phenomenological parameters D and E by carrying out electronic structure calculations including SOC and calculating the parameters either directly by second-order perturbation theory or, for higher accuracy, by fitting variationally calculated energy levels to eq 2.2.

The representation of eq 2.1 in the magnetic axis frame is given in Table 2.1. The eigenvalues and eigenvectors[58,171] of this matrix are given in Table 2.2. The eigenvalue expressions in Table 2.2 are independent of the sign of D, but we have listed the states in order of increasing energy for the case where D is negative.

Table 2.1: Matrix of the single-ion model Hamiltonian in the $|S_b, M_S(b)\rangle$ basis in the magnetic axis frame.

$\hat{H}_{\mathrm{mod}}$	$\|2,-2\rangle$	$\|2,-1\rangle$	$\|2,0\rangle$	$\|2,1\rangle$	$\|2,2\rangle$
$\langle 2,-2\|$	$4D$	0	$\sqrt{6}E$	0	0
$\langle 2,-1\|$	0	D	0	$3E$	0
$\langle 2,0\|$	$\sqrt{6}E$	0	0	0	$\sqrt{6}E$
$\langle 2,1\|$	0	$3E$	0	D	0
$\langle 2,2\|$	0	0	$\sqrt{6}E$	0	$4D$

Table 2.2: Eigenvalues and eigenvectors of the single-ion model Hamiltonian of Table 2.1.

model state	model energy	model vector[a]
ϕ_1	$2D - 2\sqrt{D^2+3E^2}$	$\frac{c_1}{\sqrt{2}}\{\|2,2\rangle + \|2,-2\rangle\} - c_2\,\|2,0\rangle$
ϕ_2	$4D$	$\frac{1}{\sqrt{2}}\,\|2,2\rangle - \|2,-2\rangle$
ϕ_3	$D - 3E$	$\frac{1}{\sqrt{2}}\,\|2,1\rangle - \|2,-1\rangle$
ϕ_4	$D + 3E$	$\frac{1}{\sqrt{2}}\,\|2,1\rangle + \|2,-1\rangle$
ϕ_5	$2D + 2\sqrt{D^2+3E^2}$	$\frac{c_2}{\sqrt{2}}\{\|2,2\rangle + \|2,-2\rangle\} + c_1\,\|2,0\rangle$

[a] c_1 and c_2 are functions of the D and E parameters.

Spin Coupling Hamiltonian

The coupling of magnetic sites by exchange interactions is represented by the Heisenberg-Dirac-Van Vleck (HDV) Hamiltonian[172,173,174] for three ionic sites:

$$H_{\mathrm{HDV}} = -2J_{ab}\hat{\mathbf{S}}_a \cdot \hat{\mathbf{S}}_b - 2J_{bc}\hat{\mathbf{S}}_b \cdot \hat{\mathbf{S}}_c - 2J_{ac}\hat{\mathbf{S}}_a \cdot \hat{\mathbf{S}}_c \tag{2.5}$$

where J_{ab} is the exchange coupling between site a and site b. A positive J_{ab} corresponds to ferromagnetic coupling (as in a high-spin diradical), and negative J_{ab} corresponds to antiferromagnetic coupling (as in singlet diradicals or half-broken covalent bonds). Just as in the previous section, we will obtain the coupling constants by carrying out electronic structure calculations and fitting the resulting energies to the phenomenological Hamiltonian (in this case given by eq 2.5). Note that in a perfect periodic system, as is the reported experimental structure used to define the cluster,[8] J_{ab} and J_{bc} are equivalent. In the truncated model, these two interactions are not equivalent by symmetry, and hence it is crucial to extract both parameters to assess the magnitude of the deviation between these two extracted parameter values.

Electronic Structure Methods

The single-ion anisotropy is first computed using wave function approaches, allowing a multideterminental treatment of the ligand-field states corresponding to the d^6 manifold, and therefore a consistent treatment of the ligand field and its effect on the zero-field splitting of the ground state. For the calculation of the isotropic couplings, we will use DFT, since an explicit treatment of the spin-adapted wave functions generated with three explicitly treated Fe^{II} ions would be prohibitively expensive at a very accurate level with wave function theory.

Methods for a Single Fe^{II} Site

We will calculate D and E by two methods, perturbation theory and a variational method. The perturbation calculations proceed as follows. First we carry out SOC-free state-averaged complete active space self-consistent field[175] (SA-CASSCF) calculations, with averaging over either (i) the five $M_S = 0$ quintet states, which would form a degenerate ^{5}D state in the absence of the ligand field, or (ii) all 100 $M_S = 0$ states (five

quintets, 45 triplets, and 50 singlets) arising from the d^6 configuration. Note that S is a good quantum number for the SOC-free calculations, so the singlets, triplets, and quintets form separate blocks, but they must be solved together because we want to express all states in a common set of orbitals. Then we calculate the matrix elements of the SOC operator and evaluate the elements of the **D** tensor by second-order perturbation theory applied to the ground state; the equations for this step are eqs 2.1, 2.2, and 2.3 of ref 58, which have the form

$$D_{kl} = \sum_B \frac{\gamma_{kl}^{0B}}{\Delta_{0B}} \tag{2.6}$$

where $k, l = x, y, z, B$ is an excited state with excitation energy Δ_{0B}, and γ_{kl}^{0B} is a complicated sum specified in ref 58. Next we diagonalize **D**, which yields D and E by eqs 2.3 and 2.4 above. The eigenvectors are the principal axes (magnetic axes). To see the effect of dynamical electron correlation on the perturbation theory results, we recalculate the results by replacing the SA-CASSCF values of Δ_{0B} in eq 2.6 by more accurate excitation energies calculated by the n-electron valence states for multireference perturbation theory[67] (NEVPT2) method.

The variational calculations[176,177] begin with an SOC-free five-state SA-CASSCF calculation. We then construct the total Hamiltonian matrix

$$\mathbf{H}_{\text{total}} = \mathbf{H}_{\text{electronic}} + \mathbf{H}_{\text{SOC}} \tag{2.7}$$

in the SA-CASSCF basis, in which the SOC-free $\mathbf{H}_{\text{electronic}}$ is diagonal, and H_{SOC} is non-diagonal (with zeros on the diagonal) and is given by the expression of Neese under the mean-field approximation,[177] based on earlier work by Hess et al.[176] We consider only the quintet subspace, but because M_S is no longer a good quantum number we now must consider all 25 quintet states that correlate with the ^{5}D bare ion manifold. We diagonalize $\mathbf{H}_{total}$ and find that the five lowest states have a weight of more than 95% on the ground SOC-free state, so we are justified in considering only these states for determining D and E (under the usual assumption that the zero field splitting is smaller than the ligand field splitting).

The variational calculations with the Hamiltonian of eq 2.7 are carried out in the basis of the spin components of the SA-CASSCF eigenvectors, which is usually called the spin-orbit state interaction (SO-SI) method. While other approaches, such as the

RASSI-SO method,[178,179] do not require using a common set of molecular orbitals, the method used here, which is the one implemented in ORCA,[180] requires an orthogonal many-electron basis, which is only achieved with a common set of orbitals for all states. One should note, however, that this requirement, rather than being a limitation, may actually be beneficial for computing the effective zero-field splitting of the ground-state spin components. Indeed, by accounting for all the spin-orbit components of the ^{5}D free ion manifold within the same orbital set, one ensures that the representation of the spin-orbit excitations is well balanced for all orientations of space, which is crucial for accurate computations of this anisotropic property.

The five quintet states have four energy splittings, and we could fit the four variational energy splittings of the five lowest states to the four energy spacings of Table 2.2 by least-squares. Instead we take a simpler approach, in particular obtaining the parameters by using the second, third, and fourth energies in Table 2.2. This yields

$$D = \frac{1}{3}\left\{E(\phi_2) - \frac{E(\phi_3) + E(\phi_4)}{2}\right\} \tag{2.8}$$

and

$$E = \frac{1}{6}\left\{E(\phi_4) - E(\phi_3)\right\} \tag{2.9}$$

The model Hamiltonian of eqs 2.1 and 2.2 does not consider any anisotropic fourth-order terms, which are nonnegligible in the case of nearly degenerate same-spin states.[150,151] Because of the highly distorted environment of the Fe^{II} ion, these terms are expected to be very small, although not strictly zero. As a consequence, a reconstructed model spectrum, obtained by using the extracted D and E parameters values, is not expected to perfectly match the set of variational energies from which they were obtained by fitting. To estimate the quality of the model spectrum, a mean percentage of error δ is computed as follows

$$\delta = \frac{\sum_{i=1}^{N} |E_i^{\text{ab initio}} - E_i^{\text{model}}|}{N \times \Delta E^{\text{ab initio}}} \times 100 \tag{2.10}$$

where N is the number of roots, $\Delta E_{\text{ab initio}}$ is the ab initio spectrum width, and $E_i^{\text{ab initio}}$ and E_i^{model} are the ab initio and model energies, respectively. Note that in the present case, N is five.

To include dynamical electron correlation in the variational calculations, we replace the SA-CASSCF energies on the diagonal of $H_{\text{electronic}}$ by NEVPT2 eigenvalues, and we repeat the procedure leading to eqs 2.8 and 2.9. Such a treatment assumes that the main dynamical correlation effect is the revision of the excitation energies while the off-diagonal SOC matrix elements are almost unchanged, and was first introduced by Llusar et al. to compute spin-orbit splittings.[181]

A smaller basis set[182] is initially considered to select a small state-interaction space, accounting for the most important contributions within the d6 manifold. This basis set consists of the def2-SV(P) bases for all atoms (i.e., 5s3p2d1f for Fe and Zn, 3s2p1d for O and C, and 2s for H atoms). A larger basis set[182] is then used, in particular def2-TZVPP for Fe and Zn atoms (i.e., 6s5p4d2f1g), def2-TZVPP for O atoms (i.e., 5s3p2d1f), and def2-SV(P) for C and H atoms.

Methods for Intersite Exchange Coupling

We calculated J_{ab}, J_{bc}, and J_{ac} by Kohn-Sham DFT. We used the M06-L[183] and M06[184] exchange-correlation functionals, the def2-TZVP basis set,[182] the density fitting algorithm for Coulomb integrals to reduce computer time in M06-L calculations, and a density functional integration grid with 99 radial nodes and 590 angular nodes.

A key issue is the initial guess for orbitals to start the SCF process. We use a guess that corresponds to a local quintet on each Fe^{II} center. Then we optimize the Slater determinant by the Kohn-Sham method without any symmetry constraints and breaking all symmetries until the lowest-energy stable solution is obtained.

Although each Fe^{II} center has $|M_S| = 2$, we can arrange the centers in various combinations of spin up ($M_S = +2$) and spin down ($M_S = 2$), which generates various Slater determinants. We label the determinants corresponding to these combinations as $|M_S(a), M_S(b), M_S(c)\rangle$. Then we can obtain the exchange coupling constants from the following equations:

$$\begin{aligned}
\langle 2,2,2|\,\hat{H}_{\mathrm{HDV}}\,|2,2,2\rangle &= -8J_{ab} - 8J_{bc} - 8J_{ac} \\
\langle -2,2,2|\,\hat{H}_{\mathrm{HDV}}\,|-2,2,2\rangle &= +8J_{ab} - 8J_{bc} + 8J_{ac} \\
\langle 2,-2,2|\,\hat{H}_{\mathrm{HDV}}\,|2,-2,2\rangle &= -8J_{ab} + 8J_{bc} - 8J_{ac} \\
\langle 2,2,-2|\,\hat{H}_{\mathrm{HDV}}\,|2,2,-2\rangle &= -8J_{ab} + 8J_{bc} + 8J_{ac}
\end{aligned} \tag{2.11}$$

Solving these equations gives

$$\begin{aligned}
J_{ab} &= \frac{1}{32}\left(E_{|2,-2,2\rangle} - E_{|2,2,2\rangle} + E_{|-2,2,2\rangle} - E_{|2,2,-2\rangle}\right) \\
J_{bc} &= \frac{1}{16}\left(E_{|2,2,-2\rangle} - E_{|-2,2,2\rangle} + 16J_{ab}\right) \\
J_{ac} &= \frac{1}{16}\left(E_{|2,2,-2\rangle} - E_{|2,2,2\rangle} - 16J_{bc}\right)
\end{aligned} \tag{2.12}$$

Software

All WFT calculations were carried out with the ORCA program.[180] All DFT calculations were carried out with *Gaussian 09*.[185]

2.1.3 Results

Magnetic Data

Variable field magnetization data collected at 1.8 K reveal a sigmoidal dependence on the magnetic field, as shown in Figure 2.4. At zero field, the magnetization of the sample is zero, and it increases slowly with increasing H until a field strength of 1 T, when the magnetization sharply increases. At 7 T, the magnetization reaches 5.10 $N\beta$, far short of the expected 8 $N\beta$ for two isotropic $S = 2$ centers at saturation. The magnetization appears to be still increasing at these field magnitudes; thus saturation is not yet observed. Upon decreasing the field from 7 T, there is no observed hysteresis, and no remanent magnetization upon returning to 0 T. With increasing temperature, the profile of the M vs H curve loses its sigmoidal shape, approaching a Brillouin-like function[186] at 12 K, but still lacking clear magnetic saturation. We note that at the higher fields, no hysteretic behavior is observed, suggesting that the high-field phase of this material is paramagnetic in nature, rather than ferromagnetic. The paramagnetic

nature of the high-field phase is further corroborated by AC in phase (χ'_M) and out-of-phase (χ''_M) susceptibility studies, which revealed no slow magnetic relaxation at low temperature for either the low-field phase or the high-field phase (see Figures 2.5 and 2.6). At high fields, however, the cusp in the low temperature in-phase AC susceptibility, χ'_M, appears to move to lower temperatures. Thus, the applied DC fields appear to nullify the magnetic interactions responsible for the decrease in χ'_M at low temperature.

Single-Ion Anisotropy

Safe Reduction of the State-Interaction Space

A first choice of a state-interaction space consists of all the crystal-field states belonging to the d^n manifold. For the d^6 configuration under study, this implies the computation of five quintets (Q), forty five triplets (T), and fifty singlets (S), for a total of 210 (spin-orbit) states. Such state-interaction space is naturally well balanced in all the orientations in space, which makes it adequate for the calculation of an anisotropic property. However, since SA-CASSCF calculations are performed by optimizing democratically the orbitals on all the states, the orbitals obtained may not be optimal for the description of the ground state and of the states most contributing to the single-ion anisotropy. Hence, it is wise to try to reduce the state-interaction space to a smaller set of states to better describe the dominant contributions.[59]

To choose a smaller subset of states, we first calculate the D and E parameters with all the states belonging to the d^6 manifold and second-order perturbation theory. For this large number of states, def2-SV(P) basis sets[182] are used for all atoms to reduce computational cost. The SA-CASSCF calculations need to include only 100 of the 210 states. The SA-CASSCF excitation energies (ΔE) are presented in Table 2.3; the bottom row of the table gives the range of the 99 excitation energies and the final perturbation theory values of D and E. The three rows above give the range of excitation energies for all quintet excited states, all triplet, and all singlets. The last two columns of the table give the contributions of individual quintet states and the group of quintets, triplets, and singlets to D and E. These individual contributions are obtained by rotating the state contributions to the $\mathbf{D}$ tensor to the magnetic axis frame; the diagonal elements in this frame sum over states to the final D and E values, and

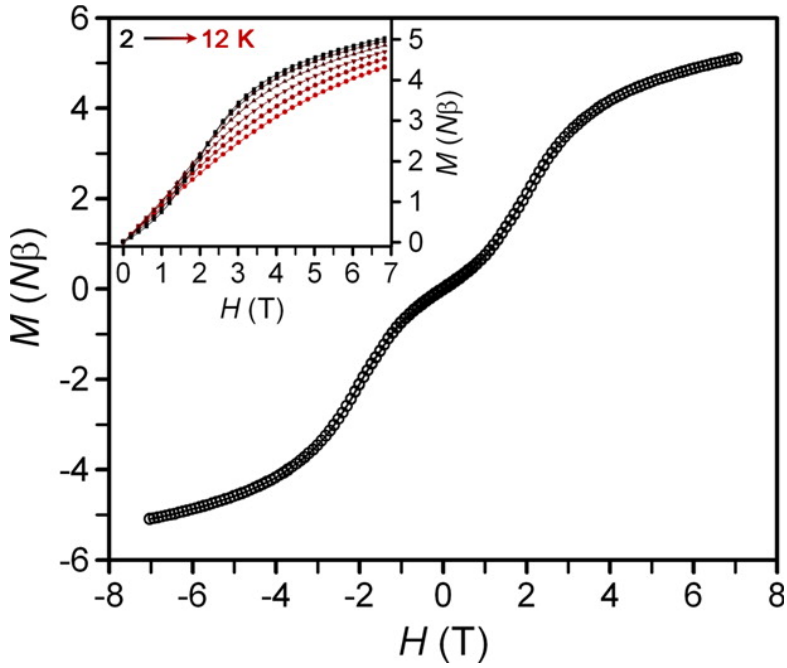

Figure 2.4: Variable-field (H) magnetization (M) data collected on a powder sample of Fe_2(dobdc) at 1.8 K and an average field sweep rate of 2 Oe/s. The magnetization is depicted per formula unit, which includes two Fe^{II} ions. Inset: Variable temperature variable field magnetization data collected from 2 to 12 K.

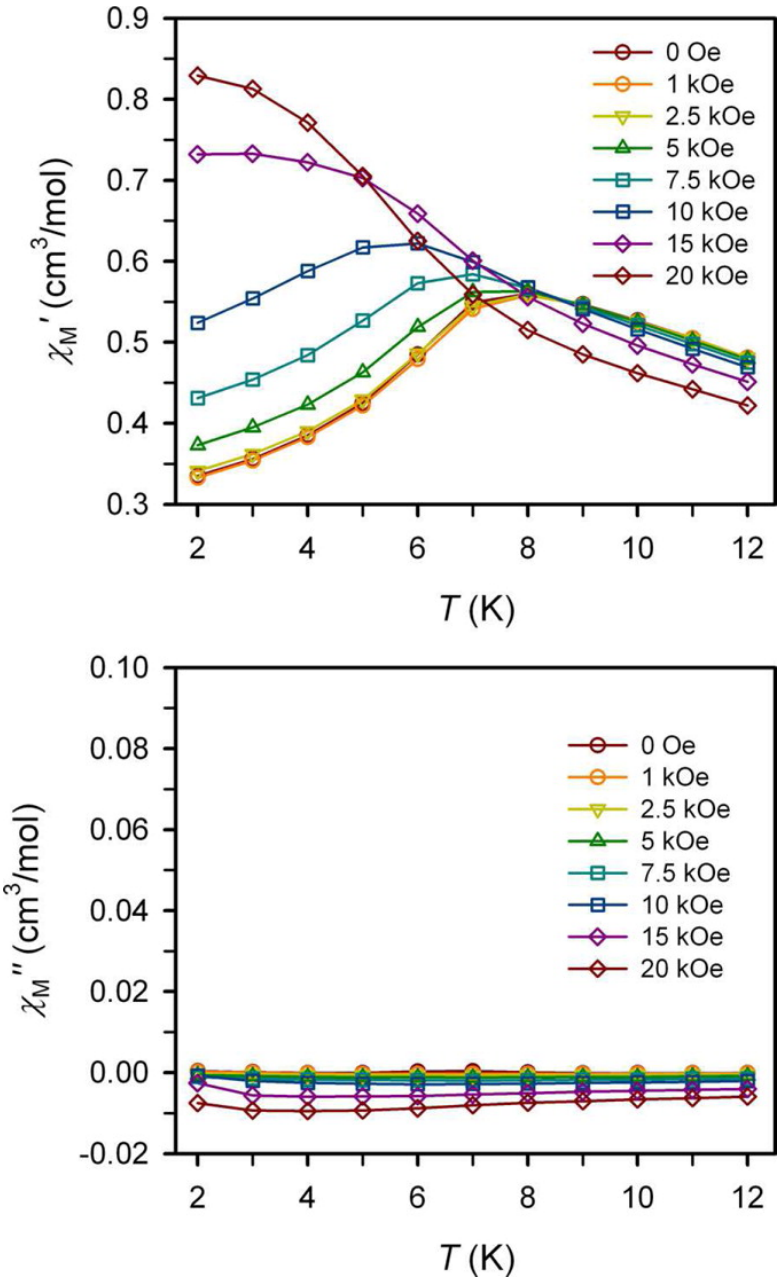

Figure 2.5: Variable temperature in-phase ($\chi_M^{'}$, top) and out-of-phase ($\chi_M^{''}$, bottom) AC susceptibility for Fe_2(dobdc) collected at an applied AC field frequency of 10 Hz and various applied DC fields, as denoted in the figure legends.

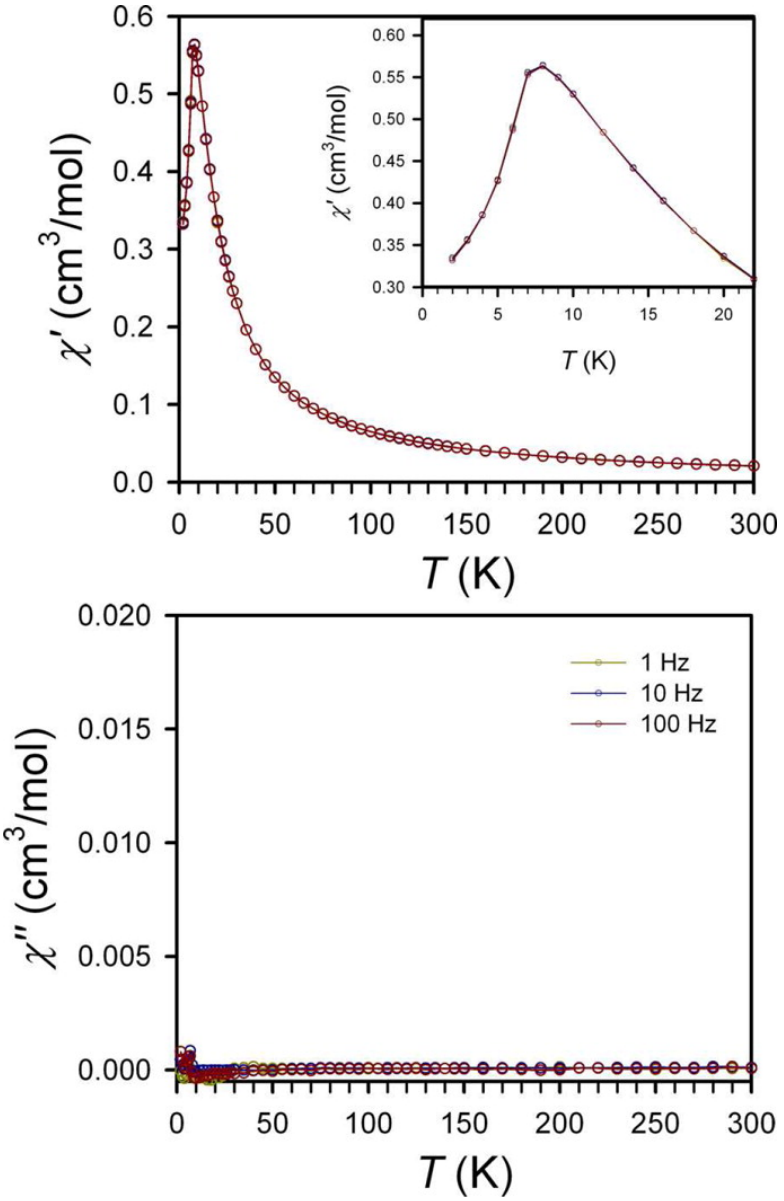

Figure 2.6: Variable temperature in-phase ($\chi_M^{'}$, top) and out-of-phase ($\chi_M^{''}$, bottom) AC susceptibility for Fe_2(dobdc) collected at AC field frequencies of 1 (yellow), 10 (blue), and 100 (red) Hz collected at zero applied DC field. Inset: Zoom in below 20 K, highlighting the cusp in $\chi_M^{'}$.

so these diagonal elements are interpreted as the individual state contributions. From these results, it is clear that the states with lower spin multiplicity than the ground Q_1 state are much higher in energy than the same-spin (i.e., quintet) states, which indicate that Fe_2(dobdc) is in a weak ligand-field regime.[187] The largest contribution from a triplet state to the D parameter in absolute value is 0.55 cm^{-1}, while the sum of all the triplet state contributions accounts for less than 10% of the total D parameter value (see Table 2.3). Moreover, the largest individual triplet contribution to E is 0.32 cm^{-1}, while the sum of the triplet contributions give 0.43 cm^{-1}, that is, less than 10% of the total parameter value (see Table 2.3). As a consequence, the single-ion anisotropy is dominated by same-spin spin-orbit interactions, and the state-interaction space can be safely reduced to the quintet spin states only. Such reduction allows efficient computations at higher levels of theory, in particular, larger basis sets and post-CASSCF levels. In all the tables after Table 2.3 we use the larger basis set described in Section 2.1.2.

Table 2.3: Excitation energies and contributions to the D and E parameters obtained at second order of perturbation with the CASSCF states[a] and energies.

state(s)	ΔE (eV)	D (cm^{-1})	E (cm^{-1})
Q_2	0.12	−7.92	+2.29
Q_3	0.30	−4.84	+1.14
Q_4	0.49	−0.98	+0.86
Q_5	1.32	+0.36	−0.16
Q states	0.00−1.32	−13.38	+4.13
T states	2.10−8.52	−1.37	+0.43
S states	3.02−14.98	0.00	0.00
d^6 manifold	0.00−14.98	−14.75	+4.56

[a]The CASSCF states were obtained by a state average calculation that includes all five quintet states of the d^6 manifold (see text).

Role of Dynamical Correlation and the Orientation of the Magnetic Axes

To assess the role of dynamical correlation on the single-ion anisotropy, the D and E parameters were determined with second-order perturbation theory as above, but

with the small state space (quintets only) and the larger basis set. Then, these results were compared to calculations employing NEVPT2 diagonal energies as explained in 2.1.2. The results are shown in Tables 2.4 and 2.5. These tables show that the use of the NEVPT2 excitation energies results in slightly lower values of the total anisotropy parameters. The ground quintet state is more stabilized by dynamical correlation than the other quintet states, which results in larger excitation energies at the NEVPT2 level for the same-spin states and weakens each individual contribution to the total anisotropy tensor.

Since the effect of the dynamical correlation on the four excited quintets is not the same, the magnetic anisotropy axes are affected by the use of the NEVPT2 excitation energies, which results in larger contributions to the D and E parameters for some excited states (here larger contributions for Q_3 and Q_4 to D, and Q_2 to E). The easy axis of magnetization (here z by convention since D is negative) is moved by 3.4° by using the NEVPT2 excitation energies instead of the CASSCF ones, while the hard axis (in this case x by convention) is moved by 1.0° and the intermediate axis by 3.4°. The magnetic anisotropy axes obtained with the NEVPT2 excitation energies and second-order perturbation theory are represented in Figure 7. These axes do not correspond to any simple orientations defined from the first coordination sphere, for example, Fe-O orientations. Although each Fe^{II} ion is equivalent in the crystal (see Figure 2.1), local anisotropy axes belonging to nearest neighbors are not collinear, owing to the helical nature of the chain. As a consequence, the local anisotropy axes depicted in Figure 2.7 do not correspond to any easy, intermediate, or hard axes of magnetization of the crystal.

Extraction of the Anisotropy Parameters by Variational Calculations

The values of the anisotropy parameters discussed so far were determined from second-order perturbation theory. To check if second-order perturbation theory is a good approximation in this case, the anisotropy parameters are also extracted by a variational method. However, as described in Section 2.1.2, the variational and model energies may not perfectly match in this case since the spin-allowed fourth-order terms are neglected in the model Hamiltonian. As a consequence, there is no unique way of extracting directly the D and E parameter values from the ab initio energies, but we extract them by a

Table 2.4: Excitation energies and contributions to the D and E parameters obtained at second order of perturbation with the CASSCF states[a] and Energies.

state(s)	ΔE (eV)	D (cm^{-1})	E (cm^{-1})
Q_2	0.12	−10.00	+1.74
Q_3	0.31	−3.60	+1.54
Q_4	0.51	−0.31	+1.09
Q_5	1.35	+0.37	−0.19
Q states	0.00−1.35	−13.54	+4.18

[a]The CASSCF states were obtained by a state average calculation that includes all five quintet states of the d^6 manifold (see text).

Table 2.5: Excitation energies and contributions to the D and E parameters obtained at second order of perturbation with the CASSCF States[a] and the NEVPT2 excitation energies.

state(s)	ΔE (eV)	D (cm^{-1})	E (cm^{-1})
Q_2	0.14	−7.56	+1.82
Q_3	0.32	−4.24	+1.29
Q_4	0.60	−0.55	+0.79
Q_5	1.49	+0.34	−0.18
Q states	0.00−1.49	−12.01	+3.72

[a]The CASSCF states were obtained by a state average calculation that includes all five quintet states of the d^6 manifold (see text).

straightforward scheme described in Section 2.1.2. As shown in Table 2.6, the resulting values are very close to the ones obtained with second-order perturbation theory (see Tables 2.4 and 2.5), validating the use of perturbation theory for determining the D and E parameters in this system.

To validate a posteriori the neglect of the fourth-order terms in the model Hamiltonian, the ab initio and reconstructed model spectrum are compared (see Tables 2.7 and 2.8). The i states correspond to either the computed spin-orbit states or the model states, belonging to the ab initio and model reconstructed spectrum, respectively. The ϕ_2 state is chosen as the zero of the energy since it is perfectly described according to the extraction scheme utilized (see Section 2.1.2). With this extraction scheme, the ϕ_3 and ϕ_4 model energies also perfectly match the variational ones, and then the mismatch between the spectra is relegated to 1 and 5. As can be seen, the model and variational energies match fairly well for both states at both levels of theory, and this results in a small error δ according to eq 2.10 (0.23% with the CASSCF excitation energies and 0.16% with the NEVPT2 ones). As a consequence, it is concluded that the fourth-order terms can be neglected in the model Hamiltonian to extract the second-order anisotropy parameters, that is, the D and E parameters. One should note that the order of the operators used in the model Hamiltonian is distinct from the order of operators used in the Hamiltonian of eq 2.7. For instance, since the parameters extracted from the variational energies differ slightly from the ones obtained with second-order perturbation theory, higher-order SOC effects affect the computed D and E parameter values.

Table 2.6: D and E parameter values (in cm^{-1}) Extracted from the ab initio energies as functions of the energies used on the diagonal elements of the SOC matrix.

parameter	CASSCF	NEVPT2
D	-11.93	-10.87
E	$+3.40$	$+3.17$

Isotropic Couplings

The relative energies of the four possible combinations of ferromagnetic or antiferromagnetic coupling of the three Fe^{II} quintet centers obtained with the M06-L and M06

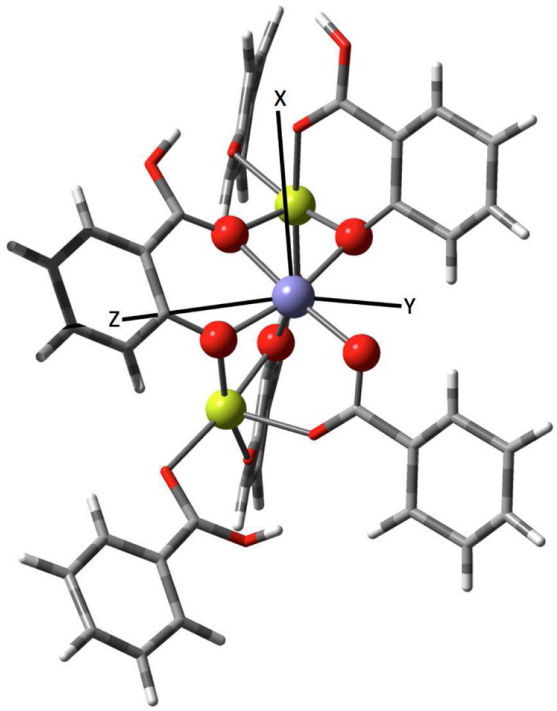

Figure 2.7: Modified 88-atom cluster and its magnetic anisotropy axes obtained with second-order perturbation theory with the NEVPT2 excitation energies, where the modification is the replacement of two Fe atoms by Zn atoms. The Zn atoms are represented in yellow, the Fe atom in purple, O atoms in red, C atoms in dark gray, and H atoms in light gray.

Table 2.7: Ab initio and model reconstructed spectrum ($\hat{H}_{\text{mod}} = D\hat{S}_z^2 + E[\hat{S}_x^2 - \hat{S}_y^2]$), where the ab initio spectrum has been obtained using the CASSCF states and energies.

state	$\text{E}^{\text{ab initio}}$ (cm^{-1})	E^{model} (cm^{-1})	model vectors
ϕ_1	-2.50	-2.75	$\approx \frac{1}{\sqrt{2}}\{\|2,2\rangle + \|2,-2\rangle\}$
ϕ_2	0.00	0.00	$\frac{1}{\sqrt{2}}\{\|2,2\rangle - \|2,-2\rangle\}$
ϕ_3	25.57	25.57	$\frac{1}{\sqrt{2}}\{\|2,1\rangle - \|2,-1\rangle\}$
ϕ_4	45.99	45.99	$\frac{1}{\sqrt{2}}\{\|2,1\rangle + \|2,-1\rangle\}$
ϕ_5	50.80	50.46	$\approx \frac{1}{\sqrt{2}}\{\|2,0\rangle\}$

Table 2.8: Ab initio and model reconstructed spectrum ($\hat{H}_{\mathrm{mod}} = D\hat{S}_z^2 + E[\hat{S}_x^2 - \hat{S}_y^2]$), where the ab initio spectrum has been obtained using the CASSCF and the NEVPT2 excitation energies.

state	$E^{\text{ab initio}}$ (cm^{-1})	E^{model} (cm^{-1})	model vectors
ϕ_1	-2.42	-2.62	$\approx \frac{1}{\sqrt{2}}\{\|2,2\rangle + \|2,-2\rangle\}$
ϕ_2	0.00	0.00	$\frac{1}{\sqrt{2}}\{\|2,2\rangle - \|2,-2\rangle\}$
ϕ_3	23.10	23.10	$\frac{1}{\sqrt{2}}\{\|2,1\rangle - \|2,-1\rangle\}$
ϕ_4	42.13	42.13	$\frac{1}{\sqrt{2}}\{\|2,1\rangle + \|2,-1\rangle\}$
ϕ_5	46.30	46.10	$\approx \frac{1}{\sqrt{2}}\{\|2,0\rangle$

exchange-correlation functionals are given in Table 2.9. Note that in a periodic treatment of the MOF crystal, $|-2,2,2\rangle$ and $|2,2,-2\rangle$ would be the same but in the 88-atom model they are slightly different. Table 10 shows the resulting exchange couplings obtained by eqs 11 and 12. Since J_{ab} differs from J_{bc} only because of truncation of the periodic crystal to 88 atoms, we may average them to obtain a nearest-neighbor (NN) coupling constant of $J_{\mathrm{NN}} = 10.3$ cm^{-1} at the M06-L level, which may be compared to the next-nearest-neighbor (NNN) value of $J_{\mathrm{NNN}} = 2.0$ cm^{-1}, while at the M06 level values of $J_{\mathrm{NN}} = 3.6$ cm^{-1} and $J_{\mathrm{NNN}} = 0.5$ cm^{-1} are obtained. Given the small magnitude of J_{NNN}, its ferromagnetic or antiferromagnetic nature cannot be unequivocally determined, but since both exchange-correlation functionals led to ferromagnetic NNN couplings, we conclude that these interactions are probably ferromagnetic, although small. Note that with both the NN and NNN interactions within a chain being ferromagnetic, no frustration would be expected within the chains. A value of $J_{\mathrm{NN}} = 4.1$ cm-1 was obtained experimentally,(2) and periodic calculations with a different functional also led to ferromagnetic J_{NN} and J_{NNN} couplings, with larger values than in the present work.[28] We conclude that both experiment and theory suggest that the NN interactions are ferromagnetic but small.

2.1.4 Discussion

Each $\mathrm{Fe}^{\mathrm{II}}$ ion in the crystal has a pentacoordinate environment in its first coordination sphere. With a perfect SPy geometry and in the absence of SOC, the ground state would be an orbital doublet, that is, two orbital configurations would be degenerate.

Table 2.9: Relative energies of selected spin broken-symmetry solutions, obtained using the M06-L and M06 exchange-correlation functionals.

$\|M_S(a), M_S(b), M_S(c)\rangle$	M06-L	M06
	E (cm^{-1})	
$\|2, 2, 2\rangle$	0.00	0.00
$\|-2, 2, 2\rangle$	222.83	97.49
$\|2, -2, 2\rangle$	330.17	115.58
$\|2, 2, -2\rangle$	170.70	34.89

Table 2.10: Isotropic Magnetic Couplings J_{ab}, J_{bc}, and J_{ac} obtained with the M06-L and M06 exchange-correlation functionals.

$\|M_S(a), M_S(b), M_S(c)\rangle$	M06-L	M06
	value (cm^{-1})	
J_{ab}	+11.9	+5.6
J_{bc}	+8.7	+1.7
J_{ac}	+2.0	+0.5

In an atomic orbital picture of the ligand field, such situation would correspond to a degeneracy between two d orbitals of the transition metal ion (see Figure 2.8). In this situation, the model space would have 10 components, the 5 spin components associated with each of the 2 degenerate orbital configurations. However, the first coordination sphere of the Fe^{II} ions is distorted, and further deviations from the ideal geometry are also related to the presence of other Fe^{II} ions in the second coordination sphere, and longer range crystalline anisotropy. As a consequence, the ground state is an orbital singlet, that is, it is non-degenerate, and the degeneracy of the (ground) quintet spin components is lifted because of the anisotropy of the ligand field and SOC, which has been effectively described in the present study by using a simple spin Hamiltonian approach accounting for only the five spin components of this ground (orbital) state. The weak ligand field imposed by the $dobdc^{4-}$ ligands results in small same-spin excitation energies and therefore the single-ion anisotropy is very large in this anisotropic system.

The single-ion anisotropy is large compared to the nearest neighbor isotropic magnetic couplings. This classifies the system as being in the weak-exchange regime.[188] Since the local anisotropy axes of the Fe^{II} ions are not collinear, the macroscopic behavior cannot be predicted from this local information. As pointed out in Section 2.1.2, negative D can lead to permanent magnetization; however, it is not sufficient, especially

if it is small. We find that D is negative and quite large. It is however probable that the mismatch between single-ion anisotropies and the weak-exchange regime opens the way for fast relaxation pathways for the macroscopic magnetization, so Fe_2(dobdc) is not expected to behave as a magnet. This is consistent with experiment, since no slow magnetic relaxation is visible in the out-of-phase AC susceptibility under zero applied DC field (see Figures 2.5 and 2.6), nor is there any observed hysteresis in the magnetization vs field curves at temperatures down to 2 K.

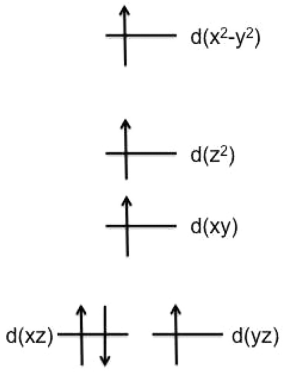

Figure 2.8: Splitting of the Fe^{2+} d orbitals under a SPy ligand field. Note that the labeling of the orbitals depends on the coordinate frame and on the ligand field strength. Electrons are displayed to illustrate one of the two degenerate high-spin configurations.

Another interesting feature of the M vs H curve is the sigmoidal shape observed at low temperature, indicating a metamagnetic behavior. This type of behavior is compatible with previous fits of the susceptibility data, which incorporated ferromagnetic chains with weak antiferromagnetic interchain interactions,[10] since the presence of these interchain interactions can explain such behavior.[161] In the field dependence of the in-phase AC susceptibility data (see Figure 2.5), the cusp, suggestive of freezing the magnetic or metamagnetic interactions, appears to be eliminated under increasingly higher DC magnetic fields. Alternatively, the combination of a weak-exchange regime and noncollinear single-ion anisotropy could also cause an abrupt change in the magnetization vs field curve at low temperature. Indeed, in such situations, the lowest-lying spin-orbit levels would show strong mixtures of different local spin configurations. By increasing the field, the spin-orbit levels would be dramatically affected, resulting in a higher spin angular momentum in the ground level, and thus in a higher magnetization.

Unfortunately, it would be a difficult task to model the complexity of such a situation, and, to the best of our knowledge, no program is able to properly model the complexity of this situation (weak exchange plus noncollinear anisotropies), although recent efforts for a 1D-exchange coupled system with noncollinear single-ion anisotropies are worth noting.[189]

Other intersite effective interactions, such as antisymmetric exchange (often referred as the Dzyaloshinskii-Moriya interaction),[190,191] biquadratic antisymmetric exchange,[192] symmetric exchange,[191] biquadratic symmetric exchange,[193] or even higher-rank anisotropic terms are spatial- and spin-symmetry allowed in Fe_2(dobdc). As shown in the literature,[191,194,195] antisymmetric interactions can be observed if the magnetic centers are connected via anisotropic superexchange(98) interactions. Symmetric exchange terms require nonzero isotropic magnetic couplings in excited states for which one electron is promoted to a combination of local ligand-field excited states.[195] Since in Fe_2(dobdc) the single-ion anisotropy is found to be very large, and since the magnetic centers are not strongly coupled, intersite anisotropic terms are expected to have a weaker influence on the magnetism of this system than the single-ion anisotropy, and therefore they were not considered in the present study. One should note, however, that these interactions may also play an important role at low temperature, as may any nonzero effective interaction present in the sample.

2.1.5 Conclusions

The further development of the utility of Fe_2(dobdc) requires a thorough understanding of the properties of the material. First and foremost, insight into the electronic structure of the compound may reveal design principles for future MOFs with improved properties. The model presented here addresses the influence of the anisotropy of the high-spin Fe^{II} centers, as well as the magnetic couplings between them, on the magnetic properties of Fe_2(dobdc). Importantly, while information about the anisotropy cannot be obtained in a straightforward way from experiment because of the mismatch between the local axes belonging to nearest and next-nearest neighbors, the electronic structure calculations can make efficient and accurate predictions within the cluster approach.

The isotropic couplings between the nearest and next-nearest neighbors, also computed within the same framework, confirm, in agreement with the experimental findings,

that the most important coupling in Fe_2(dobdc) is the ferromagnetic nearest neighbor interaction, and also show, to a lesser extent, next-nearest neighbor ferromagnetic interactions. However, the relative magnitude of the computed single-ion anisotropy places this system in the weak-exchange regime. Further, the noncollinear Fe^{II} single-ion anisotropies will partially cancel out when averaged over the crystallite. These considerations provide a reasonable explanation of the lack of an observation of bulk magnetic properties attributable to magnetocrystalline anisotropy.

Fast magnetic relaxation is demonstrated for Fe_2(dobdc), as evidenced in the featureless out-of-phase AC susceptibility data as well as the absence of hysteresis in the magnetization vs field curves down to 2 K. At low temperatures, a sigmoidal shape is observed in these curves, evidencing a metamagnetic behavior. It is hard to know at this stage which effective interactions are most responsible for the absence of hysteresis (i.e., responsible for effectively instantaneous relaxation of the magnetization), and which one is most responsible for the metamagnetic behavior (i.e., responsible for causing dramatic changes of the spin configuration of the ground state at moderate field values). Models and programs properly accounting for the complexity of the situation encountered in Fe_2(dobdc) and allowing one to simulate magnetization vs field curves, which would be a reasonable step for further understanding such magnetic data, have yet to be developed. MOFs presenting magnetic centers with large single-ion anisotropies may lead to very interesting magnetic properties. However, to limit relaxation pathways for the magnetization, it would appear more attractive to study and design MOFs with collinear single-ion magnetic anisotropy axes. Given the high number of possibilities that can be generated by combining various metal-based building blocks and organic linkers, there are numerous possibilities for new magnets that may be synthesized in the near future.

2.2 Structural and Electronic Effects on the Properties of Fe_2(dobdc) upon Oxidation with N_2O

2.2.1 Introduction

The study of magnetic porous materials is interesting because of the many possible light-weight crystalline magnets and their potential applications[2]. Porous materials have been used as molecular magnetic sponges to absorb water[196] and to improve the sensitivity and efficiency of molecular sensors[197,198]. Established theories[190] and trends[199,200] regarding magnetism within metal-oxide complexes can be used to predict magnetic behaviors of newly discovered or even as-yet unsynthesized materials through the use of quantum mechanical calculations.

One class of porous materials that has garnered considerable attention in the field of magnetism is metalorganic frameworks (MOFs), which consist of metal-containing nodes connected by organic linkers. The tunability and structural diversity of MOFs make them attractive materials for a variety of potential applications. MOFs have been synthesized with magnetically isolated nodes,[201] magnetically coupled nodes,[197,28] flexible pores,[91] very large pore diameters,[108] and combinations of these features. The M_2(dobdc) series, where M is Mg, Mn, Fe, Co, Ni, Cu, Zn, or Cd, and dobdc^4 is 2,5-dioxido-1,4-benzenedicarboxylate, has been studied extensively for its gas adsorption ability[202,203] and magnetic properties[204]. Recently, for example, it was shown that Fe_2(dobdc) can selectively adsorb olefins over paraffins[159,10]. Upon adsorption of olefins, the magnetic ordering of the Fe(II) centers changes from ferromagnetic coupling down the one-dimensional chains to antiferromagnetic exchange, which was attributed to enhanced superexchange upon olefin adsorption[10,31]. Furthermore, there is experimental and computational evidence that suggests that Fe_2(dobdc) exhibits metastable magnetic behavior that is sensitive to temperature, local coordination environment, and the type of guest molecules present in the pores of the MOF[10,69].

Four derivatives of Fe_2(dobdc), namely $Fe_2(OH)_2$(dobdc), $Fe_2(O)_2$(dobdc), $Fe_{0.1}Mg_{1.9}(OH)_2$(dobdc), and $Fe_{0.1}Mg_{1.9}(O)_2$(dobdc), were shown to be involved (in the case of the first named derivative) or postulated to be involved (in the case of the other three) in studies of the catalytic conversion of ethane to ethanol[29,12]. The compound $Fe_2(OH)_2$(dobdc) is a product of the reaction of ethane, N_2O, and

Fe_2(dobdc), which proceeds through $Fe_2(O)_2$(dobdc) as a theoretically calculated reactive intermediate[29,12]. In particular, the high-spin (S = 2) character of the Fe(IV)−oxo species contained within this intermediate was determined to be important for facilitating the ethane oxidation reaction. In order to provide insight into the tunability of the magnetic character of these MOFs, we study here the electronic structure effects resulting from differing metal oxidation states in synthesized Fe_2(dobdc) and $Fe_2(OH)_2$(dobdc) compounds, as well as the highly-reactive, and therefore fleeting, intermediate $Fe_2(O)_2$(dobdc). The parent framework, Fe_2(dobdc), contains Fe(II) centers with a quintet ground state, while $Fe_2(OH)_2$(dobdc) contains Fe(III) centers with a sextet ground state, and $Fe_2(O)_2$(dobdc) contains Fe(IV) centers with a quintet ground state[29,12].

The change in magnetic ordering upon adsorption of oxygen-containing species (e.g., H_2O) has been investigated previously for many MOFs,[2,77] and the magnetic properties of Fe_2(dobdc) with and without bound guests have previously been calculated using both cluster[69] and periodic[28,204,31] models. KohnSham density functional calculations that employ local exchange-correlation functionals (local-spin-density approximations, generalized gradient approximations (GGAs), and meta-GGAs) tend to overestimate the magnetic coupling constants between the magnetic centers within Fe_2(dobdc),[28,31,69] most likely due to over-delocalization of unpaired spins. To attempt to remediate this, one can use empirical Coulomb and exchange integrals for selected subshells (the 3d subshell of Fe in the present work), which is the GGA+U method,[205] or one can include a portion of HartreeFock exchange[69,206,207] by using hybrid exchange-correlation functionals. Guidance as to the value of the U parameter of the GGA+U method or as to a suitable amount of HartreeFock exchange for the calculation of magnetic properties can be sought from previous studies on similar materials[204,208,153] or from general parameterization of exchange-correlation functionals.

Magnetic MOFs occupy an intermediate position between molecular magnets and bulk transition metal oxide magnets. In MOFs one can, in principle, tune the magnetic coupling constants by judicious choice of metal, linker, or both during synthesis and by post-synthetic guest molecule adsorption. Quantum mechanical computations can help to understand the underlying physics behind magnetically ordered MOFs and to predict properties that may currently be inaccessible by synthetic methods. The present

work concerns magnetic exchange coupling, which tends to be quite small in MOFs, for example 110 cm^{-1}, and the prediction of such small quantities is difficult. Understanding the capabilities and/or inadequacies of various methods is indispensable when assessing the accuracy of calculations, but the calculation of trends can yield insight even when absolute values show errors. When performing these calculations on MOFs, one can use either a periodic model or a cluster model. Calculations performed with cluster models can be performed with a wider array of methods, but cluster calculations can be inaccurate if the cluster is too small or has to be too tightly constrained.

Here, we report structural and magnetic characteristics of Fe_2(dobdc), $Fe_2(O)_2$(dobdc), and $Fe_2(OH)_2$(dobdc) obtained using Kohn-Sham density functional methods with both periodic and cluster models, together with experimental magnetic susceptibility data for $Fe^{II}_{0.26}[Fe^{III}(OH)]_{1.74}$(dobdc)$(DMF)_{0.15}(THF)_{0.22}$ (where DMF denotes dimethylformamide and THF denotes tetrahydrofuran). Descriptions of the experimental and computational procedures can be found in Section 2.2.2, while Section 2.2.3 provides results and discussion, and Section 2.2.4 summarizes our conclusions.

2.2.2 Methods

Preparation and magnetic susceptibility measurements of hydroxylated Fe_2(dobdc)

The material $Fe^{II}_{0.26}[Fe^{III}(OH)]_{1.74}$(dobdc)$(DMF)_{0.15}(THF)_{0.22}$ was prepared by exposure of Fe_2(dobdc) to excess N_2O(g) at 60 °C. Mössbauer spectroscopy of the resultant material indicated that 87% of the Fe(II) sites had been oxidized to Fe(III). Full oxidation to the exact formula $Fe_2(OH)_2$(dobdc) could not be achieved without loss in crystallinity. Elemental analysis of this material indicated that residual amounts of DMF and THF were present in the material. Anal. Calcd for $C_{9.33}H_{6.55}Fe_2N_{0.15}O_{8.11}$: C, 30.94; H, 1.82; N, 0.58. Found: C, 30.90; H, 1.60; N, 0.58.

For convenience, the material $Fe^{II}_{0.26}[Fe^{III}(OH)]_{1.74}$(dobdc)$(DMF)_{0.15}(THF)_{0.22}$ will be referred to as $Fe_2(OH)_2$(dobdc). Direct current (DC) magnetic susceptibility measurements were performed on $Fe_2(OH)_2$(dobdc) under an applied magnetic field of 1,000 Oe. Magnetic samples were prepared by adding powdered crystalline compounds to a 7-mm diameter quartz tube with a raised quartz platform. Solid eicosane was added

to cover the samples to prevent crystallite torqueing and provide good thermal contact between the sample and the cryogenic bath. The tubes were fitted with Teflon sealable adapters, evacuated on a Schenk line or using a glove box vacuum pump, and sealed under vacuum using an H_2/O_2 flame. Following flame sealing, the solid eicosane was melted in a water bath at 40 °C. Data for $Fe_2(OH)_2$(dobdc) were corrected for diamagnetic contributions from the core diamagnetism estimated using Pascals constants[209] to give χ_D = 0.00027434 emu/mol and 0.00024306 emu/mol (eicosane).

In earlier work on Fe_2(dobdc),16 the temperature dependence of the magnetic susceptibility was interpreted using a two-parameter model, the Fisher model,[210,211] corresponding to a chain of Fe ions interacting with nearest neighbors in the same chain and with Fe ions in z other chains. The parameters are J_{NN} and zJ_{IC}, where J_{NN} is the magnetic coupling of nearest neighbors, and J_{IC} is the magnetic coupling of iron atoms in different chains. We also attempted to apply this to $Fe_2(OH)_2$(dobdc), and the results of this attempt are described in Section 2.2.3.

Exchange-correlation functionals

We used several exchange-correlation functionals, in particular PBE, PBE+U, HSE06, PBE-D2, PBE+U-D2, HSE06-D2, and GAM+U for periodic calculations and PBE, M06-L, PBE0, B3LYP, M06, and HSE06 for cluster calculations. The PBE[70] and GAM[71,72] exchange-correlation functionals are local gradient approximations, and M06-L[212,213] is a local meta approximation. Because local approximations tend to underestimate band gaps[208,213,214,215,216] and over delocalize charge distributions,[78,79,80,81] we also employed hybrid approximations that replace a percentage X of local exchange by nonlocal Hartree-Fock exchange. Inclusion of some Hartree-Fock exchange also affects the atomic spin distribution[217] and geometries.[217,218] B3LYP,[219,220,221,222] PBE0,[223,224] and M06[225] are global hybrids, which means that they use the same percentage X for all interelectronic separations. PBE0 and B3LYP are global-hybrid gradient approximations with X equal to 25 and 20, respectively, and M06 is a global-hybrid meta approximation with X = 27.

Periodic calculations were performed with the Vienna Ab Initio Simulation Package (VASP).[226,227] Using global-hybrid functionals for periodic calculations can very expensive. One way to cut the cost[73,228] is to decrease X to zero at large interelectronic

separations; in addition, this decrease is physically justified by the screening of nonlocal exchange by correlation effects at large interelectronic separations.[229,230] This strategy is used by the HSE06[73,74,75,76] range-separated-hybrid gradient approximation, which has X = 25 at small interelectronic separation. This decreases the cost, but it is still expensive.

An alternative strategy, with a cost almost the same as local functionals is to use rotationally invariant empirical modifications of Coulomb and exchange integrals for selected subshells;[205] calculations employing this modification with PBE are labeled PBE+U, and calculations employing this strategy with the GAM functional are called GAM+U. (The +U method of ref 77 that is used here is specified in VASP by using LDAUTYPE = 1.) For all the PBE+U and GAM+U calculations reported here, we empirically modified only the 3d subshells of the Fe centers, for which we used literature values[204,231] of 4 eV and 1 eV, respectively, for the Coulomb (U) and exchange (J) parameters.

In some calculations, a damped-dispersion molecular-mechanics term[82] was also added, and these are labeled as PBE-D2, PBE+U-D2, and HSE06-D2 calculations. The van der Waals R_0 and C_6 parameters determined by Grimme were used in the D2 terms; in particular, the global scaling parameter ($s_6 = 0.75$) fitted for PBE was used for PBE and PBE+U calculations, and the parameter ($s_6 = 0.6$) determined for the PBE0 functional was employed for the HSE06 calculations. Successful tests of these methods on extended crystalline systems are given in refs 232, 233, and 234.

Periodic Calculations

For all periodic geometries, the metal ion positions, lattice parameters, and cell volumes of the structures were optimized in the ferromagnetic (FM) spin state, which corresponds to ferromagnetic coupling both along a chain of iron centers and between the chains. These calculations employed a rhombohedral primitive cell (space group $R\bar{3}$, see Figure 2.9) containing 54, 60, and 66 atoms for Fe_2(dobdc), $Fe_2(O)_2$(dobdc), and $Fe_2(OH)_2$(dobdc), respectively.

In these calculations, projector-augmented wave[235,236] (PAW) potentials were used to describe the interaction between explicitly treated electrons and the electrons treated as core, namely the inner 10 electrons of each iron center. Two partial waves were used

for each orbital; a cutoff radius of 2.0 bohrs (a_0) was used for the 3p and 4s states, and a cutoff radius of 2.2 a_0 was used for the 3d states.

Due to the relatively small band gap and weak long-range magnetic interactions reported for Fe_2(dobdc),[204] it is especially important to converge the MOF structures and energies with respect to the number of k-points used for quadratures over the Brillouin zone. The convergence tests and final choices of grids are summarized in the supporting information (SI) of ref 9.

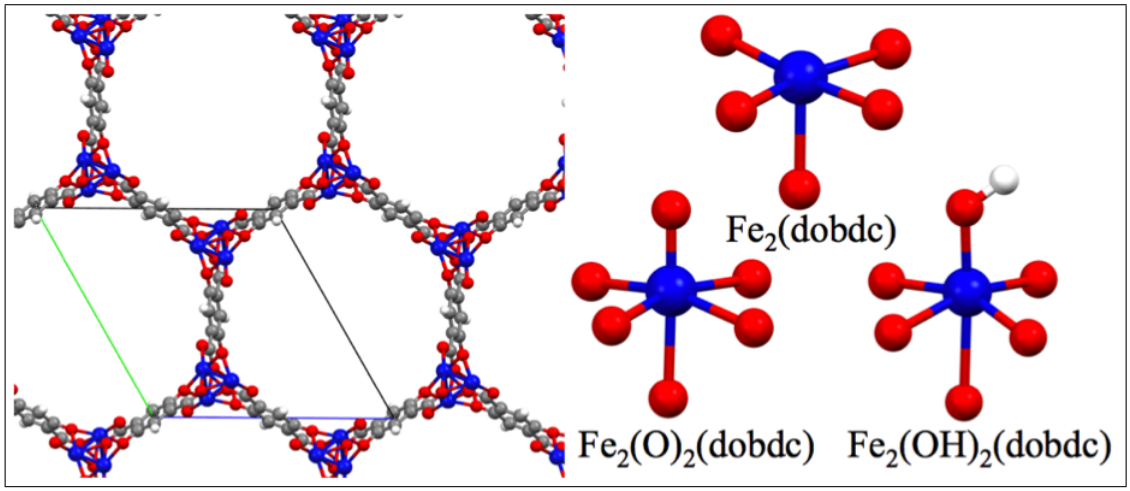

Figure 2.9: The parallelogram on the left is the primitive unit cell[237,238] of Fe_2(dobdc). The figure also shows nearby atoms from other cells. On the right is the first coordination sphere of the metal centers within the three MOFs studied. (Atom legend: blue = Fe, red = O, gray = C, and white = H).

Density functional perturbation theory (DFPT),[239,240,241,242] also called linear response theory (LRT), was employed to compute the infrared spectra in the harmonic approximation. The PBE+U functional was used to compute all frequencies with an energy convergence threshold of 10^6 eV. Only the vibrations of iron, carboxylate carbon, and oxygen atoms were included in the DFPT calculation. The vibrational eigenmodes of each species were determined by the direct force constant approach.[241] The intensities of the infrared active modes were calculated in the dipole approximation by using Born Effective Charges (BECs).[239]

Cluster calculations

All cluster calculations were performed using the *Gaussian09* software package[185], on models similar to the those used in previous research.[159,69] The models contain two or three iron ions. For the model with two iron ions, we can compute nearest-neighbor coupling, and for the models with three iron ions both the nearest-neighbor and the next-nearest-neighbor coupling can be computed (Figure 2.10). The models with two iron ions were cut from the experimental structure of Fe_2(dobdc) and the models with three iron ions were cut from the periodically optimized PBE+U structures of each of the three MOFs. The cut bonds were then capped with hydrogen atoms. In the two-iron model, the Fe−Fe distance and Fe−O_c−Fe angle (Figure 2.13) were frozen to certain values, and the rest of the cluster was optimized using M06-L/def2-TZVP. This was followed by M06//M06-L single-point calculations with ferromagnetic and antiferromagnetic ordering to extract the nearest-neighbor magnetic coupling constant. In the models with three iron ions, the hydrogen positions were optimized with M06-L[212] and the def2-SV(P)[182] basis set. Single-point calculations were then performed with ferromagnetic and antiferromagnetic ordering using the def2-TZVP[182] basis set and the PBE,[70] PBE0,[223,224] M06,[225] HSE06,[73,74,75,76] and B3LYP[219,220,221,222] exchangecorrelation functionals.

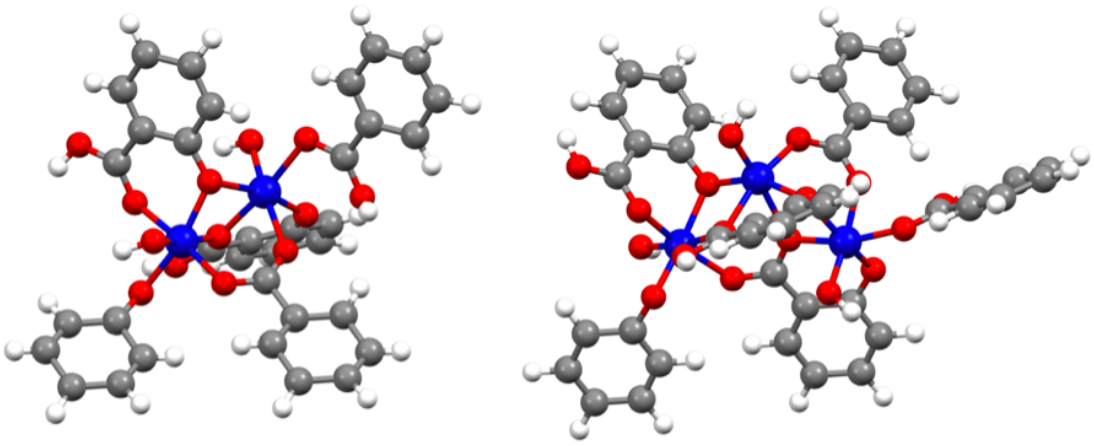

Figure 2.10: Cluster models with both two (left) and three (right) iron ions used for $Fe_2(OH)_2$(dobdc). (Atom legend: blue = Fe, red = O, gray = C, and white = H).

Magnetic coupling parameters

Previous work has demonstrated that the Fe centers in each of the species have high-spin ground states; namely, Fe_2(dobdc) contains quintet Fe(II) centers, $Fe_2(O)_2$(dobdc) contains quintet Fe(IV) centers, and $Fe_2(OH)_2$(dobdc) contains sextet Fe(III) centers.[28,204,10,29,12] Hence, only high-spin metal centers were considered in the magnetic coupling calculations. The periodic DFT calculations for Fe_2(dobdc), $Fe_2(O)_2$(dobdc), and $Fe_2(OH)_2$(dobdc) were performed with the unit cells specified above[237,238] (Figure 2.9). The PBE, PBE+U, PBE+U-D2, HSE06, HSE06-D2, and GAM+U geometries were each fixed to those optimized for the FM spin state, and the plane-wave coefficients were optimized for each of three spin configurations with an energy convergence threshold of 10^6 eV.

The unit cell used in this study contains two vertices of one of the hexagonal channels of Fe_2(dobdc) shown in Figure 2.9 with three iron ions in each of the two vertices. The considered spin alignments of the six high-spin iron ions are provided in Figure 2.11. The broken symmetry approximation[153] allowed us to use the energy differences between these three spin configurations to compute the nearest-neighbor (J_{NN}) and inter-chain (J_{IC}) coupling values with the Heisenberg-Dirac-Van Vleck (HDV) Hamiltonian,[243,173,174]

$$H_{\mathrm{HDV}} = \sum_{j>i} \sum_{i} J_{ij} \hat{S}_i \cdot \hat{S}_j \tag{2.13}$$

where the subscripts i and j represent the Fe sites of the unit cell shown in Figure 2.12, J_{ij} is the isotropic magnetic coupling between magnetic sites i and j, and $\hat{S}_i$ is the spin vector on center i. A positive J_{ij} in eq 2.13 denotes ferromagnetic (FM) coupling between centers i and j, and a negative value indicates antiferromagnetic (AFM) coupling. Note that only matrix elements that contain high-spin Fe sites (i.e., diagonal matrix elements) are eigenfunctions of the HDV Hamiltonian. Also note that the diagonal matrix elements in the HDV Hamiltonian are equivalent to those of the Ising model, which is commonly used for magnetic systems.[28,244] We considered one FM state and two AFM states (AFM1 and AFM2) to be the ones that allow the most direct calculation of the magnetic couplings; note that AFM2 is the ground state configuration of Fe_2(dobdc).

Since all iron sites in Fe_2(dobdc) and its derivatives $Fe_2(O)_2$(dobdc) and

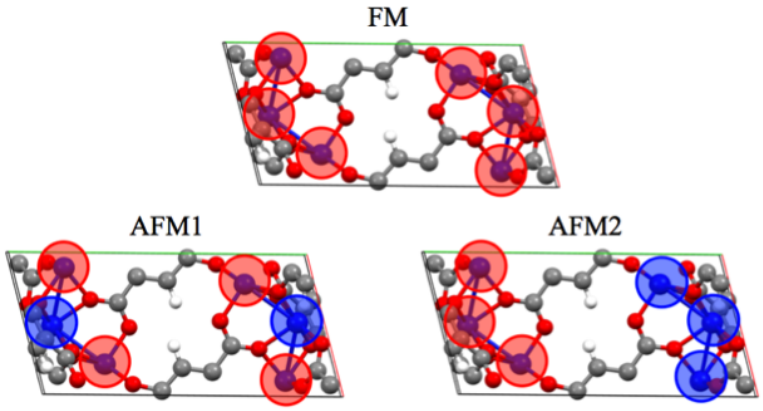

Figure 2.11: Side view of the primitive unit cell of Fe_2(dobdc) (Atom legend: blue = Fe, red = O, gray = C, and white = H). Red and blue circles indicate the upward or downward spin of the high-spin iron ions, respectively. The entirely ferromagnetic (FM), intrachain antiferromagnetic (AFM1), and interchain antiferromagnetic spin states were considered in this work (AFM2). AFM1 is actually ferrimagnetic with this unit cell. Results with a doubled unit cell with strict intrachain AFM coupling are provided in the SI of ref 9.

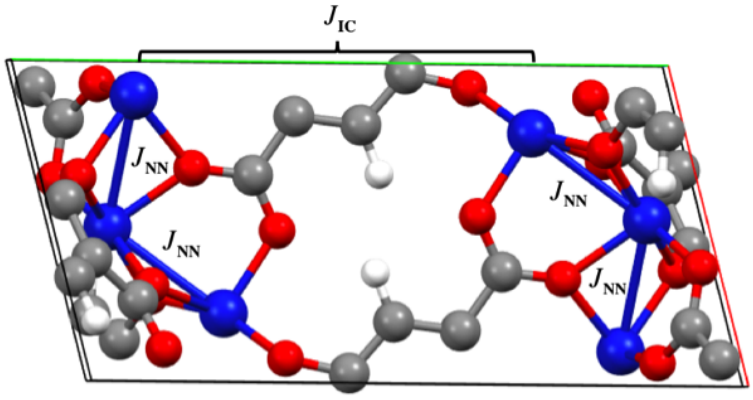

Figure 2.12: Schematic representation of the nearest-neighbor coupling constant, J_{NN}, and the interchain coupling constant, J_{IC}, of the primitive unit cell of Fe_2(dobdc). (Atom legend: blue = Fe, red = O, gray = C, and white = H).

$Fe_2(OH)_2$(dobdc) are equivalent, the four nearest-neighbor interactions represented by J_{NN} in Figure 2.12 are all equivalent. For the atoms at the edge of the unit cell, additional nearest-neighbor interactions arise due to interaction with the periodic image of the unit cell. This accounts for two more J_{NN} values, resulting in a total of six J_{NN} for the primitive cell.

While the treatment described above for nearest-neighbor interactions is unambiguous, the treatment of interchain coupling requires more consideration. Each chain of Fe ions is surrounded by three other chains of Fe ions. Although the three neighboring chains are equally distant, the Fe ions are staggered, so that the smallest interchain Fe$\cdots$Fe distance is not the same for all three neighboring chains of a given Fe ion; in particular, the distance to the nearest Fe ion in each of the three surrounding chains in Fe_2(dobdc) is 7.4, 8.1, and 9.0 Å. If the data were sufficient to accommodate a multiparameter analysis, one would recognize at least three different interchain couplings and also include next-nearest neighbors within a given chain. However, the interchain coupling was found to be small, and the theory might not be good enough to distinguish several different small couplings. Even more significantly, the experiment was interpreted in terms of only two parameters, one intrachain parameter J_{NN} and one interchain parameter zJ_{IC}. Therefore we took the same approach computationally. However, we obtained slightly different results if we assumed the interchain coupling was caused only by the nearest interchain interaction ($z = 1$) or was caused by equal interactions with the nearest neighbors in each of the three surrounding chains ($z = 3$). We will report the equations and the resulting magnetic coupling for the approach in which we computed the magnetic coupling values assuming that each metal center would interact with only the closest metal center of the three neighboring chains, which was reasonable because one of the interchain Fe$\cdots$Fe distances was smaller than the other two. This limited interchain coupling model, corresponding to $z = 1$, leads to a total of six interactions per unit cell. The model with $z = 3$ would lead to 18. We note that the two treatments yield identical values of zJ_{IC} but slightly different values of J_{NN} (SI of ref 9).

Using the energies calculated for the three spin states (FM, AFM1, and AFM2) shown in Figure 2.11, the J_{NN} and J_{IC} values can be extracted for Fe_2(dobdc) and $Fe_2(O)_2$(dobdc) (which have total spin magnitudes ($|M_S|$) of 2 on every iron site) by

solving the following three equations:

$$\begin{aligned}
\langle 222,222|\, H_{HDV}\, |222,222\rangle &= E_{222,222} = [6J_{\mathrm{NN}}2\cdot 2 + 6J_{\mathrm{IC}}2\cdot 2] \\
\langle 2\bar{2}2,2\bar{2}2|\, H_{HDV}\, |2\bar{2}2,2\bar{2}2\rangle &= E_{2\bar{2}2,2\bar{2}2} = [-2J_{\mathrm{NN}}2\cdot 2 + 6J_{\mathrm{IC}}2\cdot 2] \\
\langle 222,\bar{2}\bar{2}\bar{2}|\, H_{HDV}\, |222,\bar{2}\bar{2}\bar{2}\rangle &= E_{222,\bar{2}\bar{2}\bar{2}} = [6J_{\mathrm{NN}}2\cdot 2 - 6J_{\mathrm{IC}}2\cdot 2] \qquad (2.14)
\end{aligned}$$

where H_{HDV} is the HDV Hamiltonian of eq. 2.14, $|222,222\rangle$ and $E_{222,222}$ represent the Slater determinant and total energy of the FM case (Figure 2.11), $|2\bar{2}2,2\bar{2}2\rangle$ and $E_{2\bar{2}2,2\bar{2}2}$ represent the Slater determinant and total energy of the AFM1 case, $|222,\bar{2}\bar{2}\bar{2}\rangle$ and $E_{222,\bar{2}\bar{2}\bar{2}}$ represent the Slater determinant and total energy of the AFM2 case. In the Slater determinants of eq 2.14, the M_S values before the comma are the values for one chain containing three iron centers and the ones after the comma are for the other chain. Solving the equations given by eq 2.14 results in the values of J_{NN} and J_{IC}, which are represented by the following equations:

$$\begin{aligned}
J_{\mathrm{IC}} &= \frac{1}{96}\left[E_{222,\bar{2}\bar{2}\bar{2}} - E_{222,222}\right] \\
J_{\mathrm{NN}} &= \frac{1}{64}\left[E_{2\bar{2}2,2\bar{2}2} - E_{222,222}\right] \qquad (2.15)
\end{aligned}$$

For the unit cell of $Fe_2(OH)_2$(dobdc), each iron ion of which has a spin of 5/2, the J_{NN} and J_{IC} values can be extracted by solving the following three equations:

$$\begin{aligned}
\left\langle \frac{5}{2}\frac{5}{2}\frac{5}{2}, \frac{5}{2}\frac{5}{2}\frac{5}{2}\right|\, H_{HDV}\, \left|\frac{5}{2}\frac{5}{2}\frac{5}{2}, \frac{5}{2}\frac{5}{2}\frac{5}{2}\right\rangle &= E_{\frac{5}{2}\frac{5}{2}\frac{5}{2},\frac{5}{2}\frac{5}{2}\frac{5}{2}} = \left[6J_{\mathrm{NN}}\frac{5}{2}\cdot\frac{5}{2} + 6J_{\mathrm{IC}}\frac{5}{2}\cdot\frac{5}{2}\right] \\
\left\langle \frac{5}{2}\frac{\bar{5}}{2}\frac{5}{2}, \frac{5}{2}\frac{\bar{5}}{2}\frac{5}{2}\right|\, H_{HDV}\, \left|\frac{5}{2}\frac{\bar{5}}{2}\frac{5}{2}, \frac{5}{2}\frac{\bar{5}}{2}\frac{5}{2}\right\rangle &= E_{\frac{5}{2}\frac{\bar{5}}{2}\frac{5}{2},\frac{5}{2}\frac{\bar{5}}{2}\frac{5}{2}} = \left[-2J_{\mathrm{NN}}\frac{5}{2}\cdot\frac{5}{2} + 6J_{\mathrm{IC}}\frac{5}{2}\cdot\frac{5}{2}\right] \\
\left\langle \frac{5}{2}\frac{5}{2}\frac{5}{2}, \frac{\bar{5}}{2}\frac{\bar{5}}{2}\frac{\bar{5}}{2}\right|\, H_{HDV}\, \left|\frac{5}{2}\frac{5}{2}\frac{5}{2}, \frac{\bar{5}}{2}\frac{\bar{5}}{2}\frac{\bar{5}}{2}\right\rangle &= E_{\frac{5}{2}\frac{5}{2}\frac{5}{2},\frac{\bar{5}}{2}\frac{\bar{5}}{2}\frac{\bar{5}}{2}} = \left[6J_{\mathrm{NN}}\frac{5}{2}\cdot\frac{5}{2} - 6J_{\mathrm{IC}}\frac{5}{2}\cdot\frac{5}{2}\right] \qquad (2.16)
\end{aligned}$$

The only difference between the equations for the Fe_2(dobdc) and $Fe_2(O)_2$(dobdc) cases and the $Fe_2(OH)_2$(dobdc) case is the spin state (M_S) of the iron ions. This change results in different prefactors for the J_{NN} and J_{IC} magnetic coupling values. Solving the equations given by eq 2.16 gives the values of J_{NN} and J_{IC} for $Fe_2(OH)_2$(dobdc) which are represented by eq 2.17:

$$\begin{aligned}
J_{\mathrm{IC}} &= \frac{1}{150}\left[E_{\frac{5}{2}\frac{5}{2}\frac{5}{2},\frac{\bar{5}}{2}\frac{\bar{5}}{2}\frac{\bar{5}}{2}} - E_{\frac{5}{2}\frac{5}{2}\frac{5}{2},\frac{5}{2}\frac{5}{2}\frac{5}{2}}\right] \\
J_{\mathrm{NN}} &= \frac{1}{100}\left[E_{\frac{5}{2}\frac{\bar{5}}{2}\frac{5}{2},\frac{5}{2}\frac{\bar{5}}{2}\frac{5}{2}} - E_{\frac{5}{2}\frac{5}{2}\frac{5}{2},\frac{5}{2}\frac{5}{2}\frac{5}{2}}\right] \qquad (2.17)
\end{aligned}$$

Additional considerations in the above two-parameter treatment are the neglect of next-nearest-neighbor interactions in a given chain and the fact that the periodically replicated AFM1 state is not strictly antiferromagnetic down each chain of metals. A more faithful representation of a fully antiferromagnetic chain can be obtained by doubling the size of the primitive cell along the c axis (which runs parallel to the chains) from 54 atoms to 108 atoms for Fe_2(dobdc) (SI of ref 9), from 60 atoms to 120 atoms for $Fe_2(O)_2$(dobdc), and from 66 atoms to 132 atoms for $Fe_2(OH)_2$(dobdc). Single-point calculations were performed on the doubled unit cells with PBE+U to test the validity of utilizing the smaller cells shown in Figures 2.11 and 2.12. We also computed the J_{NN} and J_{NNN} magnetic couplings with cluster models. For the cluster calculations, the Hamiltonian and equations used to compute the magnetic coupling values with the cluster models are described in the SI along with coordinates for each cluster model.

2.2.3 Results and Discussion

Equilibrium structures and Infrared Spectra

The SI of ref 9 compares the equilibrium structures computed with PBE, PBE+U, PBE+U-D2, HSE06, HSE06-D2, and GAM+U. In the case of Fe_2(dobdc) there is a good agreement between the bond distances and angles computed with all the methods and experiment, with the exception of PBE, which significantly underestimates the Fe$\cdots$Fe distances and the Fe$-$O$_c-$Fe angle. Table S2 in the SI of ref 9 shows that, after oxidation to Fe(III), the experimental Fe$\cdots$Fe distance increases by 0.15$-$0.16 Å. If we ignore PBE, because of its underestimation of the Fe$\cdots$Fe distance in Fe_2(dobdc), the density functional calculations predict that there is an increase in the Fe$\cdots$Fe distance of 0.25$-$0.28 Å. Figure 2.13 shows the local environment of a metal center in $Fe_2(OH)_2$(dobdc) and the organic linker.

The experimental infrared (IR) spectra of Fe_2(dobdc) and $Fe_2(OH)_2$(dobdc) in Figure 2.14 provide a good test of the PBE+U computations, which are in Figure 2.15. The theoretical spectra were normalized to match the intensities of the experimental Fe$-$O stretches that occur at $\sim$820 cm^1. The peaks occurring below 500 cm^{-1} are likely due to Fe$-$O bending modes, while those between 600 and 1,000 cm^{-1} are due to Fe$-$O stretches. The PBE+U Fe(III)$-$OH stretching frequencies in $Fe_2(OH)_2$(dobdc)

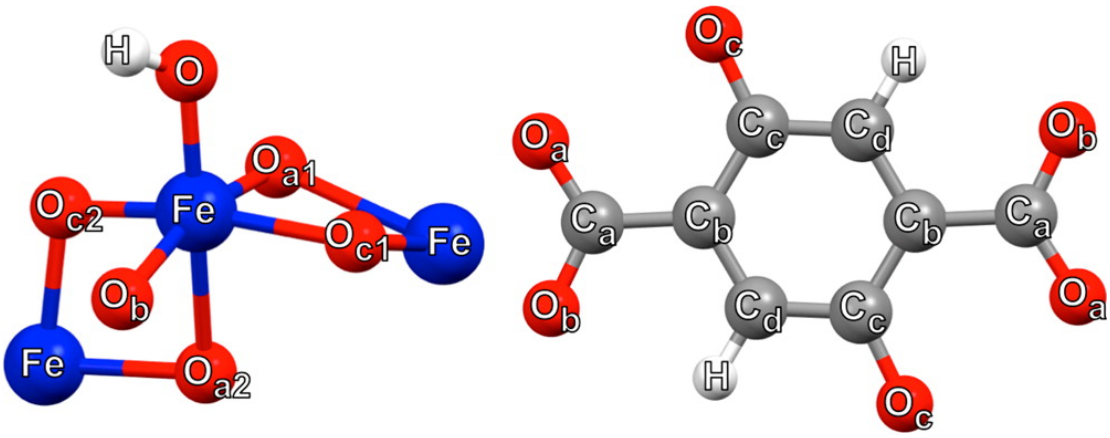

Figure 2.13: (left) The first coordination sphere of the metal center in $Fe_2(OH)_2$(dobdc) and (right) the organic linker. The four unique oxygens, four unique carbons, and two unique hydrogens are shown. Note that the O_{a1}, O_{a2}, O_{c1}, and O_{c2} labeling used here and in Table S2 from the SI of ref 9 distinguish the Fe−O bond positions with respect to the central Fe. The Fe−O_{a1}−Fe and Fe−O_{a2}−Fe bond angles as well as the Fe−O_{c1}−Fe and Fe−O_{c2}−Fe bond angles are equivalent. (Atom legend: blue = Fe, red = O, gray = C, and white = H).

occur between 619 cm^{-1} and 630 cm^{-1}, which is approximately 40 cm^{-1} less than the experimental value of 667 cm^{-1}.[29]

The PBE+U O−H stretching frequency in $Fe_2(OH)_2$(dobdc) is 3,773 cm^{-1} and the experimental value is 3,683 cm^{-1}. The Fe(IV)−oxo stretch is known in other cases to occur between 776 cm^{-1} and 843 cm^{-1}.[245] We find that the PBE+U Fe(IV)−oxo stretches occur here between 888 cm^{-1} and 899 cm^{-1}. Thus theory underestimates the Fe(III)−OH stretching frequency and may overestimate the Fe(IV)−oxo stretching frequency. However, the experimental Fe(IV)−oxo containing material is quite different that the theoretical model. Calculations with the actual experimental composition ($Fe_{0.1}Mg_{1.9}(O)_2$(dobdc)) may yield more accurate frequencies. Molecular DFT calculations are known to systematically overestimate experimental fundamental stretching frequencies, but usually by only 2−5%.[246]

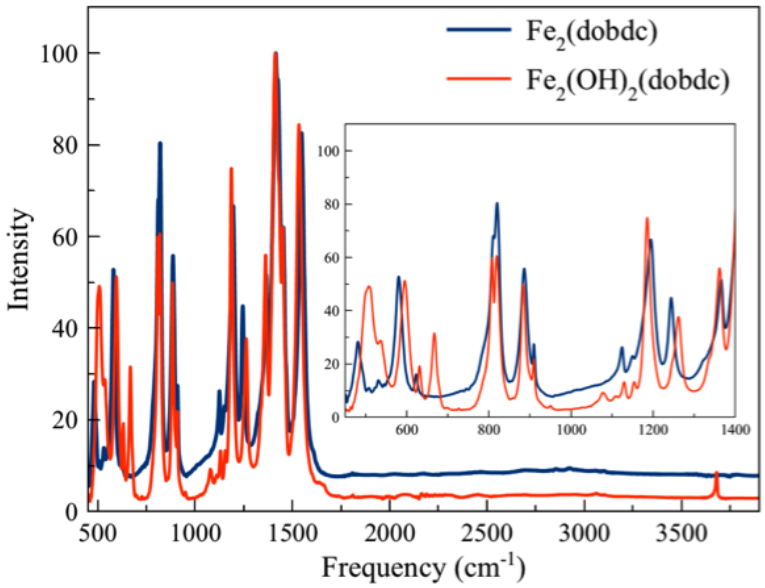

Figure 2.14: Experimental infrared spectra of Fe_2(dobdc) and $Fe_2(OH)_2$(dobdc) (ref 29).

Electronic structure and density of states

To gain insight into the electronic structures, the orbital projected density of states (OP-DOS) is provided for each MOF. The OP-DOS plots were extracted using the default settings for atomic radii in VASP. The atomic radii could be considered tunable parameters that can be improved by computing and comparing to reasonable atomic charges,[247] but the default parameters yielded decent results when compared to experiment. Figures S3 and S4 in the SI of ref 9 show the OP-DOS obtained using PBE+U and HSE06, respectively, for each MOF in its lowest-energy spin state (Table 2.11). We consider only the projections of the DOS on the Fe 3d and O 2p orbitals, since the electrons occupying these orbitals are the ones mainly responsible for the magnetic properties. To identify the bands of the additional oxygen atoms in $Fe_2(O)_2$(dobdc) and $Fe_2(OH)_2$(dobdc), the figures also show projections that include only the 2p orbitals of the added oxygen atoms.

The main consideration in these plots is the band gap, i.e., the difference in energy between the highest occupied orbital and the lowest unoccupied one. PBE+U and HSE06 both predict a sizeable band gap, in particular 1.3 eV and 2.1 eV, respectively,

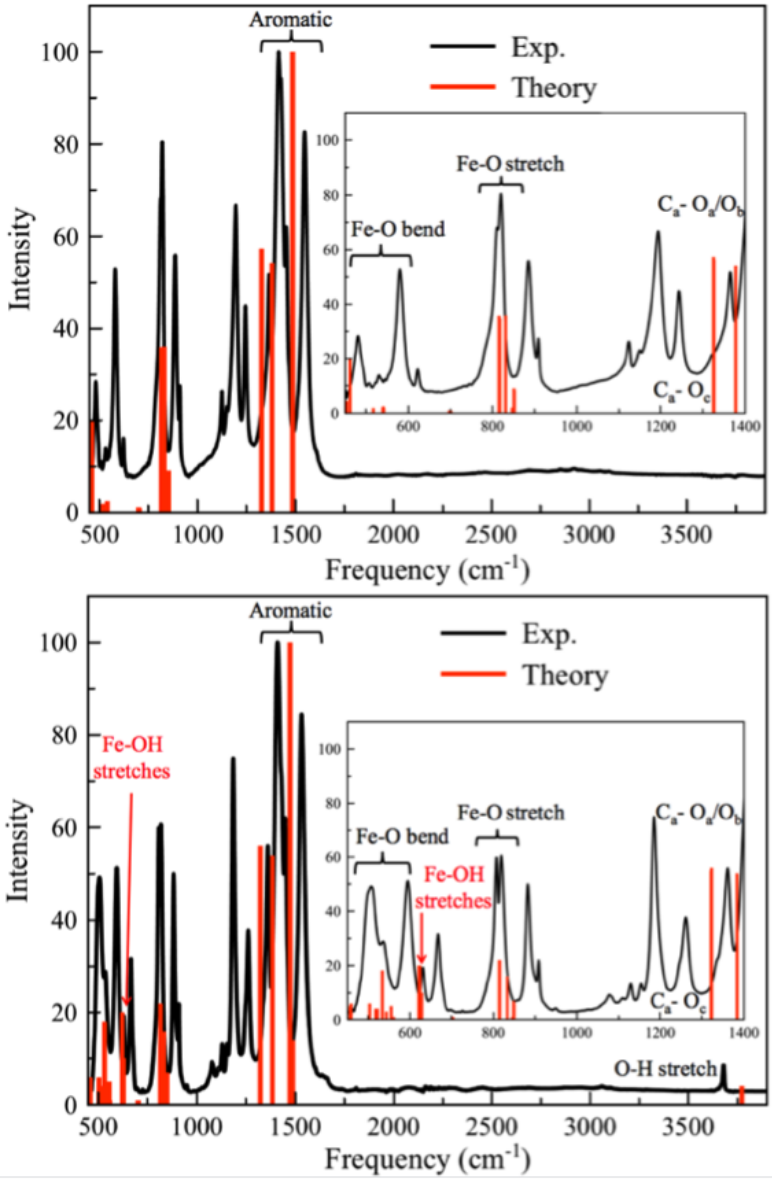

Figure 2.15: Experimental and theoretical (PBE+U) infrared spectra of (top) Fe_2(dobdc) and (bottom) $Fe_2(OH)_2$(dobdc). All spectra were normalized based on the highest peak. The experimental spectra for Fe_2(dobdc) were taken from ref 29. The FeOH stretch theoretical peak intensities (those that are indicated by the red arrow in the range from 619 cm^{-1} to 630 cm^{-1}) were multiplied by 10 for more visible comparison to experiment.

which are substantially larger than the gap of 0.3 eV reported by Zhang et al. (ref 204). We investigated the reason for this discrepancy and found that the band gap decreased as volume increased, but even with a 15% volume fluctuation the band gap remained between 1.1 eV and 0.8 eV. Furthermore, a single-point calculation with the experimental structure gives the same band gap as that obtained from the equilibrium PBE+U structure determined in this work. The trend in the gap upon increasing the oxidation state of iron is different for PBE+U and HSE06. The PBE+U gaps for the Fe(IV) and Fe(III) MOFs are almost identical (0.8 eV), while HSE06 predicts a gap of 1.5 eV for $Fe_2(O)_2$(dobdc), containing Fe(IV), but predicts a larger gap of 1.8 eV for $Fe_2(OH)_2$(dobdc), containing Fe(III).

Magnetic susceptibility measurements

The magnetic susceptibility of $Fe^{II}_{0.26}[Fe^{III}(OH)]_{1.74}(dobdc)(DMF)_{0.15}(THF)_{0.22}$ ($Fe_2(OH)_2$(dobdc)) was measured in the present work. DC magnetic susceptibility measurements were performed under an applied magnetic field of 1,000 Oe across the temperature range 2 to 300 K. The measurements of $Fe_2(OH)_2$(dobdc) revealed a decreasing $\chi_M T$ product with decreasing temperature across the full temperature range measured (Figure 2.16). This trend supports the assignment of both intrachain and interchain magnetic couplings as antiferromagnetic. The $\chi_M T$ value at 300 K and 1,000 Oe is 6.85 emu K/mol, which is much lower than both the expected value for two isotropic S = 5/2 spins (8.75 emu K/mol) and the expected value assuming 0.26 moles (13% of iron sites) of S = 2 Fe(II) per formula unit (8.39 emu K/mol). The low magnetic moment is attributed to the presence of 13% Fe(II), which in addition to simply having a lower magnetic moment than that of Fe(III) may also display enhanced antiferromagnetic coupling with its nearest-neighbor spins. The magnetic susceptibility of Fe_2(dobdc) was measured in ref 10, where the fitting procedure used to compute the experimental coupling values for Fe_2(dobdc) is also described. The fitting procedure is briefly summarized in Section 2.2.2.

It was not feasible to extract the interchain and intrachain magnetic coupling parameters with the Fisher model, as was done for Fe_2(dobdc).[10] The results in Figure 2.16 indicate that Fe_2(dobdc) has ferromagnetic intrachain coupling and antiferromagnetic interchain coupling. The precise coupling parameters for $Fe_2(OH)_2$(dobdc) could

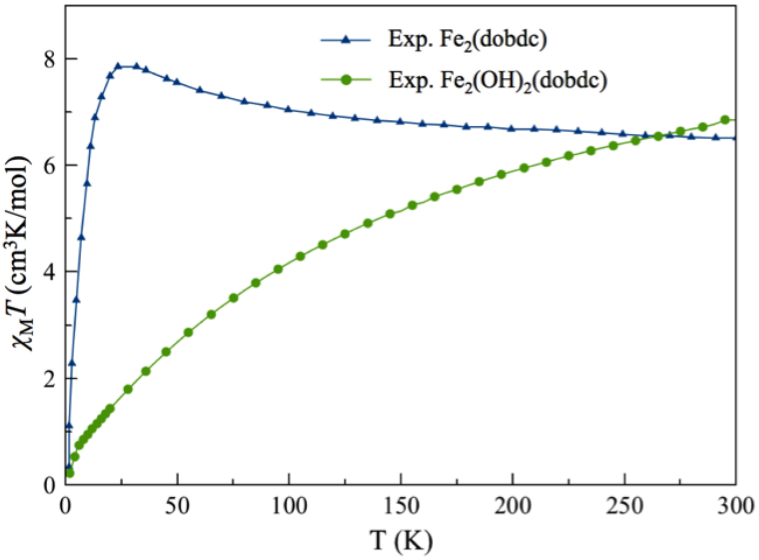

Figure 2.16: Experimental magnetic susceptibility times temperature curves of $Fe_2(dobdc)$[10] (blue) and $Fe_2(OH)_2(dobdc)$ (green). The applied field strength during the susceptibility measurement with each material was 1,000 Oe.

not readily be derived due to the fact that the synthesized MOF was only partially oxidized, with approximately 13% of the iron sites remaining in the Fe(II) state. However, a Curie-Weiss fit to the expression $1/\chi_M = (T-\theta)/C$ for the high temperature regime (50 K to 300 K) of the inverse magnetic susceptibility data for both $Fe_2(dobdc)$ and $Fe_2(OH)_2(dobdc)$ (SI of ref 9) permitted some assessment of the differences in magnetic coupling behaviors for the two frameworks. For $Fe_2(dobdc)$, the Curie-Weiss analysis resulted in a positive Weiss temperature of $\theta = 11$ K, consistent with ferromagnetic interactions being dominant, and a Curie constant of C = 6.3 emu·K/mol. In contrast, the Curie-Weiss analysis for $Fe_2(OH)_2(dobdc)$ resulted in $\theta = -139$ K and C = 10.0 emu·K/mol. The negative sign of the Weiss temperature, θ, for $Fe_2(OH)_2(dobdc)$ indicates that antiferromagnetic interactions are prevalent. Concurrently, the large increase in the magnitude of the Weiss temperature, dependent on the spin states present and the number and strength of the magnetic coupling pathways,[248] suggests that the magnetic interactions are stronger within $Fe_2(OH)_2(dobdc)$, as the iron spins involved only increase from quintet to sextet states, while the number of magnetic coupling pathways

presumably remains unchanged. Thus, we can state qualitatively that adding a hydroxide anion and oxidizing the metal sites of Fe_2(dobdc) switches the nearest-neighbor magnetic coupling behavior from ferromagnetic to antiferromagnetic and increases magnetic coupling strength.

Magnetic coupling parameters

The calculated magnetic coupling parameters for Fe_2(dobdc), $Fe_2(O)_2$(dobdc), and $Fe_2(OH)_2$(dobdc) are provided in Tables 2.11 and 2.12. As mentioned above, the PBE+U calculations were run with both primitive unit cells (54, 60, or 66 atoms) and doubled cells (108, 120, or 132 atoms) as indicated in the second column of Table 2.11. This table shows that there is no significant difference between the PBE+U calculations with 54 and 108 atoms in the unit cell, which indicates that the primitive cell is adequate for these computations. The same is true for couplings in $Fe_2(O)_2$(dobdc) and $Fe_2(OH)_2$(dobdc).

The PBE nearest-neighbor couplings in Fe_2(dobdc) are two orders of magnitude larger both than the experimental ones and than those computed with the other methods tested in Table 2.11. The PBE values are calculated for the PBE geometry, which has short Fe$\cdots$Fe distances. A previous study[28] of magnetic interactions in Fe_2(dobdc) employed the PBE exchange-correlation functional with experimental geometries and obtained a J_{NN} equal to 28 cm^{-1}, which is smaller but still a significant overestimation. They concluded[28] that there is fairly strong ferromagnetic coupling in Fe_2(dobdc). It now appears that such large calculated J_{NN} values are an artifact of the simple gradient approximation used in the PBE functional. This was first shown in previous work,[69] where a calculation with Hartree-Fock exchange gave 3.6 cm^{-1}, in good agreement with the experimental value of 4.1 cm^{-1}.

It was pointed out in Section 2.2.2 that the magnetic coupling constants depend slightly on whether we perform the analysis with z =1 or z = 3. The nearest-neighbor Fe$\cdots$Fe distance is 3.0 Å, and the next-nearest neighbor Fe$\cdots$Fe distance within a chain is 5.0 Å. Thus the next-nearest-neighbor distance is significantly shorter than the shortest interchain Fe$\cdots$Fe separation, and this suggests that the next-nearest-neighbor intrachain coupling should be calculated. The next-nearest neighbor coupling results are shown in Table 2.11, where we report the results with z = 1. (Note that the value

Table 2.11: Periodic DFT exchange and coupling energies (cm^{-1}) of the iron centers.[a]

method	atoms	$E_{\mathrm{AFM1}} - E^c_{FM}$/ $E_{\mathrm{AFM3}} - E^c_{FM}$	$E_{\mathrm{AFM2}} - E^c_{FM}$	$J_{\mathrm{NN}}/J_{\mathrm{NNN}}$	zJ_{IC}
		Fe(II) case: Fe_2(dobdc)			
PBE	54	7287.7	−160.0	113.9	−5.0
PBE+U[b]	108	56.6/92.9	−121.1	0.5/0.3	−1.9
PBE+U	54	41.6	−60.4	0.7	−1.9
PBE+U-D2	54	31.1	−64.6	0.5	−2.0
HSE06	54	171.6	−32.2	2.7	−1.0
HSE06-D2	54	163.2	−47.5	2.6	−1.5
GAM+U	54	145.4	−52.8	2.3	−1.7
Expt.[c]				4.1	−1.1
		Fe(III) case: $Fe_2(OH)_2$(dobdc)			
PBE	66	−2308.1	−2042.3	−23.1	−40.8
PBE+U[b]	132	−3216.0/-2259.0	−630.7	−10.2/−1.1	−6.3
PBE+U	66	−1129.6	−315.9	−11.3	−6.3
PBE+U-D2	66	−1133.9	−311.7	−11.3	−6.2
HSE06	66	−562.0	−169.8	−5.6	−3.4
HSE06-D2	66	−561.4	−170.3	−5.6	−3.4
GAM+U	66	−691.7	−272.7	−6.9	−5.5
		Fe(IV) case: $Fe_2(O)_2$(dobdc)			
PBE	60	−795.8	−164.1	−12.4	−5.1
PBE+U[b]	120	−205.6/−270.2	81.1	−1.2/−0.9	1.3
PBE+U	60	−133.8	40.9	−2.1	1.3
PBE+U-D2	60	−157.6	36.1	−2.5	1.1
HSE06	60	−31.8	17.9	−0.5	0.6
HSE06-D2	60	−43.3	15.8	−0.7	0.5
GAM+U	60	17.5	−42.4	0.3	−1.3

[a]All coupling values were extracted using geometries optimized with the FM spin state. E_{FM} is the electronic energy of the ferromagnetic state, E_{AFM1} is the electronic energy of antiferromagnetic state 1, and E_{AFM2} is the electronic energy of antiferromagnetic state 2 (see Figure 2.11). E_{AFM3} is the electronic energy of antiferromagnetic state 3 of the supercell. J_{NN}, J_{IC}, and J_{NNN} coupling parameters represent the nearest-neighbor, interchain, and next-nearest-neighbor magnetic couplings, respectively (Figure 2.12).
[b]The equations used to calculate the coupling parameters for the doubled cells are in the SI; the spin configurations for the doubled cells are shown in the SI of ref 9.
[c]ref 10

computed for J_{IC} is independent of whether or not J_{NNN} is computed and is also independent of whether we use $z = 1$ or $z = 3$.) Excluding PBE, the nearest-neighbor couplings (J_{NN}) obtained with $z = 3$ are very similar for Fe_2(dobdc), $Fe_2(OH)_2$(dobdc), and $Fe_2(O)_2$(dobdc), whereas the results for zJ_{IC} are unchanged. Table 2.11 shows that the PBE+U and HSE06 calculated values of J_{NN} are smaller than the PBE value and in more reasonable agreement with experiment. For Fe_2(dobdc) the coupling values obtained by HSE06 and HSE06-D2 are identical to each other and are larger than those predicted by PBE+U, whereas for the $Fe_2(O)_2$(dobdc) and $Fe_2(OH)_2$(dobdc) cases, HSE06 and HSE06-D2 yield magnetic couplings that are smaller than the values computed with PBE+U and PBE. PBE+U and HSE06 predict the same signs of the magnetic couplings.

Table 2.11 shows that the periodic calculations of J_{NNN} using PBE+U yield 0.3 cm^{-1}, 0.1 cm^{-1}, and -0.9 cm^{-1} for Fe_2(dobdc), $Fe_2(OH)_2$(dobdc), and $Fe_2(O)_2$(dobdc), respectively. These J_{NNN} values may be compared to the respective J_{IC} coupling values of -0.6 cm^{-1}, -2.1 cm^{-1}, and 0.4 cm^{-1}. The magnitude of the PBE+U J_{IC} coupling values for Fe_2(dobdc) and $Fe_2(O)_2$(dobdc) are smaller than the J_{NNN} values, while the PBE+U J_{IC} value of $Fe_2(OH)_2$(dobdc) is larger than the J_{NNN} value. It is worth noting that the J_{IC} coupling values for $Fe_2(OH)_2$(dobdc) are notably larger than the other two cases with all functionals. This may indicate that, separate from the oxidation of the metal centers, addition of the $(OH)^-$ groups enhances interchain magnetic coupling.

Table 2.12 provides the results of cluster model calculations that may be compared to the periodic calculations in Table 2.11. Because they are very similar to the experimental geometries (Table S2; SI of ref 9), the PBE+U optimized periodic structures were used to make the clusters in most cases. The PBE//PBE J_{NN} value is much larger than the PBE//PBE+U value, in part because the periodic PBE metal-metal bond distances are too small for Fe_2(dobdc) (as noted above in the discussion of Table S2). The PBE//PBE cluster calculation predicts J_{NN} values for Fe_2(dobdc) that are significantly larger than experiment. However, the cluster J_{NN} values obtained by HSE06, M06, PBE0, B3LYP, and GAM+U are all quite reasonable when compared to both the periodic and experimental magnetic coupling parameters.

The results for PBE+U structures in Table 2.12 show that Hartree-Fock exchange, in HSE06, PBE0, M06, and B3LYP, decreases the predicted intrachain coupling values. If

Table 2.12: Isotropic magnetic coupling constants of the iron centers for each studied MOF as obtained by cluster calculations.[a]

method	Fe_2(dobdc)	$Fe_2(OH)_2$(dobdc)	$Fe_2(O)_2$(dobdc)
		J_{NN}/J_{NNN} (cm^{-1})	
PBE//PBE	64.6	−18.2	−9.9
PBE//PBE+U[b]	14.3	−18.7	−9.0
HSE06//PBE+U	2.4/0.4	−3.2/−0.1	0.3−0.2
M06//PBE+U-D2	4.3	−3.9	−0.5
PBE0//PBE+U	2.5	−3.1	−0.1
B3LYP//PBE+U	2.7	−4.1	−0.5
Expt.[b]	4.1	–	–

[a]X//Y indicates a cluster calculation with method X employing a fragment of a MOF optimized by periodic calculations with method Y. Only nearest- and next-nearest-neighbor intrachain coupling values (J_{NN} and J_{NNN}) were computed, and they may be compared with Table 2.11.
[b]Taken from ref 10.

one assumes that the main effect of the U parameter is to mimic Hartree-Fock exchange, this is consistent with the periodic results.

The cluster values of J_{NNN} in Table 2.12 are considerably smaller than the periodic calculations of J_{NNN} in Table 2.11. They do, however, correctly predict the experimentally determined magnetic ordering of Fe_2(dobdc) and $Fe_2(OH)_2$(dobdc). In the case of $Fe_2(O)_2$(dobdc), the magnetic coupling values are likely extremely weak, which is why GAM+U and HSE06//PBE+U predict different magnetic orderings than the other functionals. This demonstrates the difficulty of accurately calculating the small energies of these interactions.

It was suggested by Park et al.[31] that the changes in magnetism within Fe_2(dobdc) upon guest adsorption are due to structural changes within the MOF. When the intrachain Fe$\cdots$Fe distances were less than ∼3.12 Å, the magnetic interactions were interpreted as being dominated by direct exchange between the metal centers and were ferromagnetic; at longer Fe$\cdots$Fe separations, the magnetic interactions were interpreted as dominated by superexchange through the bridging oxygen atoms. In our work, $Fe_2(O)_2$(dobdc) has intrachain Fe$\cdots$Fe distances of ∼3.12 Å(Table S2; SI of ref 9) and the nearest-neighbor AFM coupling is calculated to be very weak (Tables 2.11 and 2.12). For comparison, $Fe_2(OH)_2$(dobdc) has intrachain Fe$\cdots$Fe distances of ∼3.22

Åand shows a larger AFM coupling. But the Fe$\cdots$Fe separation is not the only geometrical parameter that changes. Fe$-$O$_c-$Fe bond angles increase from Fe$_2$(dobdc) to Fe$_2$(O)$_2$(dobdc) to Fe$_2$(OH)$_2$(dobdc) (Table S2; SI of ref 9). Table 2.11 shows that these structural changes are associated with a switch from positive J_{NN} values to negative J_{NN} values i.e., a switch from FM to AFM coupling of the nearest-neighbor metal centers. However, many factors besides geometry may contribute to the changes in magnetic coupling. These factors include electronic effects resulting from (1) the presence of the (OH) and O^{2-} ligands, (2) the change in oxidation state to Fe(III) for $(OH)^-$ and to Fe(IV) for O^{2-}, and (3) the change in spin state of the metal centers from quintet to sextet resulting from the inclusion of the $(OH)^-$ ligands. The magnetic coupling equations for Fe$_2$(OH)$_2$(dobdc) (eq 2.17) take into account the effect of the spin state change (3), but, completely separating all three of these electronic contributions from the geometric contributions required a separate set of calculations, as discussed in the next two paragraphs.

To compute the aforementioned electronic contributions, two approaches were considered. In the first approach, the three-iron cluster model of Fe$_2$(OH)$_2$(dobdc) carved from the PBE+U periodic structure was used. The three $(OH)^-$ groups were removed from this cluster, which changed the Fe(III) centers to Fe(II) centers. While keeping the positions of all atoms in the cluster fixed, magnetic coupling constants were calculated using M06/def2-TZVP. This was done to separate the electronic and geometric contributions to the magnetic coupling. The coupling constant of this new cluster (-1.1 cm^{-1}) should be compared to the M06 magnetic coupling results for Fe$_2$(dobdc) (4.3 cm^{-1}) and Fe$_2$(OH)$_2$(dobdc) (-3.9 cm^{-1}) in Table 2.12. From this comparison, we can see that the magnetic coupling contribution from electronic effects does not match the experimentally observed coupling constant, indicating that geometry also plays an important role in the magnetic couplings studied here.

The second approach was to go in the reverse direction, meaning that we started with the Fe$_2$(dobdc) cluster and then added $(OH)^-$ groups. Three $(OH)^-$ groups were added to the cluster model of Fe$_2$(dobdc) carved from the PBE+U periodic structure, and only these added groups were optimized using M06/def2-TZVP, while the rest of the cluster was kept fixed. The oxidation state and spin state of the metal centers were thus the same as for Fe$_2$(OH)$_2$(dobdc), while the metal coordination geometry was the

same as in Fe_2(dobdc). The magnetic coupling of Fe_2(dobdc) (4.3 cm^{-1}) (Table 2.12) changed to 0.2 cm^{-1} when $(OH)^-$ was added, which is an effect of 4.1 cm^{-1}. The value of 0.2 cm^{-1} can be compared to the M06 magnetic coupling result in Table 2.12 for $Fe_2(OH)_2$(dobdc) of -3.9 cm^{-1}, which also has an effect of 4.1 cm^{-1}. This means that the metal oxidation and addition of $(OH)^-$ and the change in geometry had impacts of similar magnitude. These results show that the presence of the $(OH)^-$ groups (1), the change in oxidation state (2), and the change in spin state (3) all contribute considerably to the magnetic ordering of $Fe_2(OH)_2$(dobdc). We also found that the geometry has an important effect on the magnetic coupling. To examine the overall effect of the geometry, we examined the OP-DOS results from the periodic calculations of each structure. But, we also wanted to understand how distinct geometrical parameters like Fe−Fe distance and Fe−O−Fe angle contribute to the magnetic coupling. We thus designed cluster models to separate the contributions from these parameters.

The periodic calculations on Fe_2(dobdc) (Table 2.11) are in general agreement with previous work.[28,204,10,69] The results for the hydroxylated case in Table 2.11 are consistent with the qualitative inference from experiment in Section 2.2.3 that oxidation of the metal sites of Fe_2(dobdc) and concurrent addition of hydroxide anions to these sites switches the nearest-neighbor magnetic coupling behavior from ferromagnetic to antiferromagnetic and increases its strength. The interactions between the bridging O atoms and the Fe atoms can strongly influence the type and magnitude of the magnetic exchange within a material.[200] The OP-DOS calculations of the Fe 3d and the bridging O 2p orbitals show that overlap between these orbitals is larger for $Fe_2(O)_2$(dobdc) and $Fe_2(OH)_2$(dobdc) than for Fe_2(dobdc). This may indicate that there is more interaction between the metal electrons through the bridging oxygens in $Fe_2(O)_2$(dobdc) and $Fe_2(OH)_2$(dobdc). The increasing Fe−O−Fe bond angle leads to an increase in the magnitude of the AFM coupling because the electrons in the Fe 3d interact more strongly through the bridging oxygen electrons via superexchange (Figure 2.17). The superexchange interaction was developed into a set of semi-empirical rules by Goodenough and Kanamori.7 These rules predict an AFM interaction if the metal-ligand-metal angle is close to 180°, and a weak FM interaction if the angle is close to 90°. The computations performed in this work align reasonably well with these rules, although the actual situation is complicated by the fact that the Fe−O distances and Fe−Fe distances change

along with the change in bond angle. Similar interaction trends have been observed previously within Fe_2(dobdc) when olefins were bound to the metal centers.[10,31]

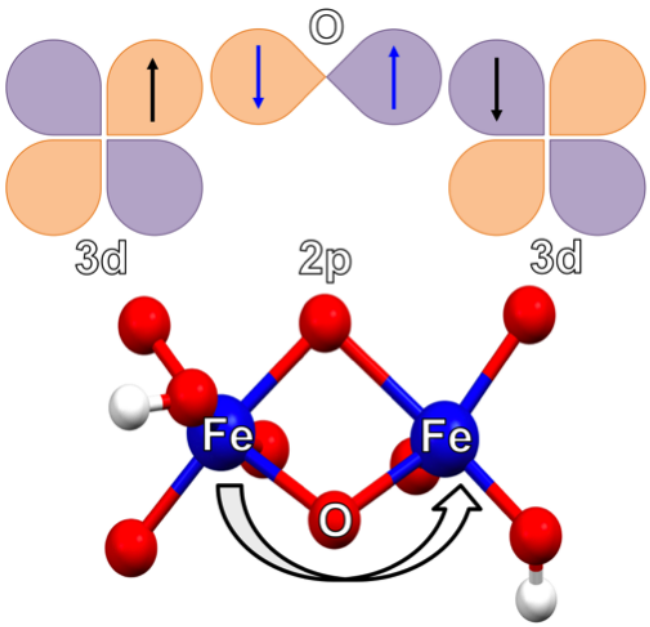

Figure 2.17: Schematic describing the superexchange interaction that takes place within $Fe_2(O)_2$(dobdc) and $Fe_2(OH)_2$(dobdc). (Atom legend: blue = Fe, red = O, and white = H).

In order to somewhat separate changes in intrachain Fe$\cdots$Fe distances and Fe$-$O$-$Fe angles, we performed cluster calculations using the two-iron model, where two degrees of freedom, Fe$\cdots$Fe distance and Fe$-$O$_c-$Fe angle, were set to (2.9 Å, 85°), (2.9 Å, 105°), (3.1 Å, 95°), (3.3 Å, 85°), and (3.3 Å, 105°) to see how the change in either the Fe$\cdots$Fe distance or the Fe$-$O$-$Fe angle affects the magnetic coupling. With these two internal coordinates frozen, all other coordinates were optimized. The J_{NN} values were found to be 10 cm^{-1}, -6.3 cm^{-1}, 1.5 cm^{-1}, 5.0 cm^{-1}, and -1.2 cm^{-1}, respectively. This shows that if the Fe$\cdots$Fe distance is kept fixed to 2.9 Åor 3.3 Åand the Fe$-$O$_c-$Fe angle is increased from 85° to 105°, J_{NN} decreases and becomes negative. On the other hand if the Fe$-$O$_c-$Fe angle is fixed to 85° or 105°, and the Fe$\cdots$Fe distance is increased from 2.9 Åto 3.3 Å, the J_{NN} value again decreases. Hence changing either the Fe$-$Fe distance or the Fe$-$O$_c-$Fe angle has an effect on the magnetic coupling.

2.2.4 Conclusions

In contrast to Fe_2(dobdc), $Fe_2(O)_2$(dobdc) and $Fe_2(OH)_2$(dobdc) feature AFM coupling down each metal chain (Figure 2.18). Previous work by Bloch et al.[10] and calculations performed by Park et al.[31] suggest that the shift from FM to AFM coupling is the result of ligands changing the intrachain Fe$\cdots$Fe distances and Fe$-$O$-$Fe angles. We find here that the effect can also be partially accounted for by the electronic effect of the ligands, the oxidation state of the metal centers, and/or the spin state of the metal centers, even in the absence of geometry changes. This indicates that structural and electronic changes upon framework oxidation likely act in concert to effect magnetic coupling.

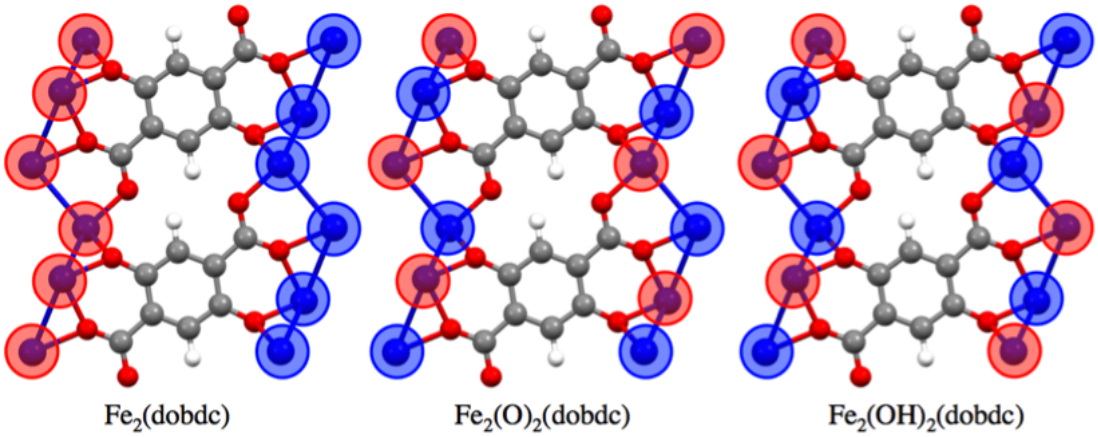

Figure 2.18: Representation of the spin configurations of the studied MOFs. Blue atoms are iron, red atoms are oxygen, grey atoms are carbon, and white atoms are hydrogen. Red circles indicate spin-up Fe spins and blue circles indicate spin-down Fe spins. (Atom legend: blue = Fe, red = O, gray = C, and white = H).

The computationally efficient PBE+U and GAM+U approaches predict structural properties that agree quite well with the values obtained using more expensive hybrid functionals. Inclusion of damped dispersion effects by molecular mechanics does alter equilibrium volumes; however, the effect is minor when compared to inclusion of Hartree-Fock exchange. Thus, rescaling PBE+U or GAM+U unit cells and correcting for the electronic structure with single-point hybrid functional calculations appears to be an efficient approach to calculate magnetic properties of MOFs. Cluster models can be

used to compute J_{NN} coupling values quite accurately, and can be used conveniently with a wider array of computational methods at a lower cost. However, capturing both the J_{NN} and J_{IC} magnetic coupling dependency on the MOF structure does require periodic calculations. Overall, theory can correctly describe the magnetic and electronic properties and their structural dependences for these materials, provided one is aware of the strength and limitations of both periodic and cluster-based modeling. Ongoing research aims at predicting these properties for as yet unsynthesized materials.

Chapter 3

Ab Initio Parameterized Forces Fields for Carbon Dioxide Adsorption in $M_4(O)(bdc)_3$ and $M_2(dobdc)$

3.1 CO_2 Adsorption in M-IRMOF-10 (M = Mg, Ca, Fe, Cu, Zn, Ge, Sr, Cd, Sn, Ba)

3.1.1 Introduction

Recently, substantial research effort has been focused towards separation of CO_2 from other gases, since it is a crucial part of carbon capture and sequestration (CCS), needed for reducing the greenhouse gases produced by consumption of fossil fuels.[249,1] Developing viable strategies to capture CO_2 from flue-gas streams in coal-fired power plants is very challenging. The current technology used for this application, which relies on amine-scrubbing,[250] is energy-intensive and can be cost prohibitive. To this end, it is important to make new materials with the goal of lowering the energy penalty for regeneration after capture of CO_2. New techniques that take advantage of different materials and molecular systems such as zeolites and activated carbons have been studied for this purpose.[251,252] The difficulty in tuning and precisely synthesising some of the aforementioned porous materials has resulted in challenges in their optimization for carbon sequestration. Therefore, we are still seeking new classes of porous materials that can be easily tuned and synthesised.

Metal-organic frameworks (MOFs) represent a class of crystalline porous materials comprised of organic linkers/struts and metal-based nodes.[253,254,255,256] As a consequence of the high porosity, along with chemical diversity and tunability,[257] MOFs have been proposed for a wide range of applications including, but not limited to, gas capture, separation and storage processes,[258,259,260,261,262,263] chemical sensing,[264] drug delivery,[265] catalysis,[124,13,109] and light harvesting.[266,267] Importantly, high-quality computational modeling of interactions between MOFs and potential sorbates can be realized since these materials allow for unequivocal structure determination by X-ray diffraction.[268] Furthermore, MOFs have been shown to be amenable to numerous post-synthetic manipulations to incorporate desired chemical moieties in the pores.[269,5,270]

One particularly powerful post-synthetic manipulation method is transmetalation or cation-exchange.[5] This technique allows synthetic chemists to make materials that are difficult or in some cases, near impossible, to attain via de novo approaches. For example, Brozek and Dincă have used the $Zn_4O(bdc)_3$ (bdc=1,4-benzene-dicarboxylate) topology, also called isoreticular MOF-1 (IRMOF-1) or MOF-5, to make Ti^{3+}, $V^{2+/3+}$,

$Cr^{2+/3+}$, Mn^{2+}, Fe^{2+}, and Ni^{2+} variants via cation-exchange.[4,271] Ni-IRMOF-1 is the only member of this series, apart from the original Zn-IRMOF-1, that has been synthesized successfully by other means.[4] This cation-exchange method is a powerful tool since it allows for a high degree of metal node tunability in MOFs without significantly altering other properties, such as pore volume and catenation, while also allowing for the study of node effects in applications such as gas storage[272] or catalysis.[273] Comparing the effects of cation-exchange on gas storage within an isoreticular series of MOFs is therefore a very worthy study.

Molecular simulations can provide some guidance in distinguishing possible interesting trends upon exchanging metals or linkers within a MOF series. The IRMOF isotopological series has been studied extensively both experimentally[274,275,276] and computationally.[277,278,279,280,281,282] Computations have been performed on the IRMOF series with many different combinations of metals and linkers for a variety of properties.[278,279,280,281,282] Experimental CO_2 adsorption isotherms within this series have been measured with many ligand types,[274,275,283,284] but not for metal-exchanged versions of these MOFs. CO_2 adsorption simulations have been performed for some metals,[277,278,281,282] but a systematic study of the effect of cation-exchange within this series has not been explored.

Typically, isotherms for sorbate loading within MOFs are computed using general force fields like the Universal Force Field (UFF) or DREIDING.[86] Although these force fields can perform reasonably well for some coordinatively-saturated MOFs,[281] they tend to underestimate adsorption in cases where strong guest-host interactions take place.[285,39,286] The accuracy of CO_2 isotherms can be improved by parameterizing the metal$-CO_2$ interactions with quantum mechanical calculations.[285,39,89] Furthermore, using parameters that have been carefully optimized to model the linker environment within a MOF can improve the overall description of the MOF$-CO_2$ interactions. When analyzing binding trends within MOFs containing different metals, it is thus advisable to carefully parameterize the interactions between the metal and guest to make sure that the trends are reflective of the physics of these interactions and not the parameterization sets of the general force fields. The Transferable Potentials for Phase Equilibria (TraPPE) force field[93,87,94,95,96,97,98] parameters have been optimized for various molecules by fitting to experimental vapor-liquid coexistence curves and adsorption

isotherms. Futhermore, the TraPPE linker parameters have been specifically tailored to model a chemical environment similar to the linkers, rather than being optimized from a test set of molecules that are meant to describe many different environments.[84,287,86] Thus, in this work we developed a force field that accurately models CO_2 adsorption within the $M_4O(bpdc)_3$ (bpdc=4,4-biphenyl-dicarboxylic acid), also called M-IRMOF-10, series by combining quantum mechanically optimized M$-CO_2$ interaction parameters with the TraPPE force field (M = Mg, Ca, Fe, Cu, Zn, Ge, Sr, Cd, Sn, Ba). We did so to discover M$-CO_2$ interaction trends and to test the effectiveness of UFF at predicting these trends within the IRMOF topology.

This article is organized as follows: In Section 3.1.2, a description of the ab initio (3.1.2) and classical (3.1.2) methods used in this work is provided. Section 3.1.3 provides the resulting periodic structures (3.1.3), reference energy curves and fitted metal$-CO_2$ interaction parameters (3.1.3), and isotherms (3.1.3). Finally, Section 3.1.4 contains the conclusions that can be drawn from the gathered results.

3.1.2 Methods

Quantum Mechanical Calculations

Periodic Calculations

All geometry optimizations performed in this work were started by replacing the Zn^{2+} ions in the X-ray Powder Diffraction (XRD) structure of Zn-IRMOF-10.[288] The Vienna *Ab Initio* Simulation Package (VASP) was then used to optimize the unit cell, lattice parameters, and atomic positions.[289,290,291,292] Projector-augmented wave[293] potentials that describe the interaction between electrons in the core and valence shells[294] were used in these calculations. The Perdew-Burke-Ernzerhof gradient-corrected, exchange-correlation functional for solids (PBEsol)[295,296] was used for the optimizations, since it has yielded accurate MOF structures in previous work.[297,298] A gamma point optimization of the unit cell was performed with an energy cut-off of 500 eV. The energy and force convergence criteria were set to 1×10^{-5} eV and 0.05 eV/Å, respectively.

Single point calculations were performed with the same settings on these optimized structures to compute the partial charges for each atom type in these MOFs. Density Derived Electrostatic and Chemical (DDEC) partial charges[100] were computed for

each MOF for use in the force-field based simulations. Charge Model 5 (CM5) partial charges[99] were also computed for comparison. The DDEC charge of each atom type was averaged to get the final charges used in the simulations. The CM5 charges were computed with the CM5PAC package[299] by creating 3×3×3 supercells of each member in the M-IRMOF-10 series and averaging the charge of each atom type within the central unit cell to get the final set of charges. Please note that the partial charges of the hydrogen atoms on the phenyl rings were found to be very similar and as such, a single atom type was used for all hydrogen atoms. The atom types present in IRMOF-10 are shown in Figure 3.1.

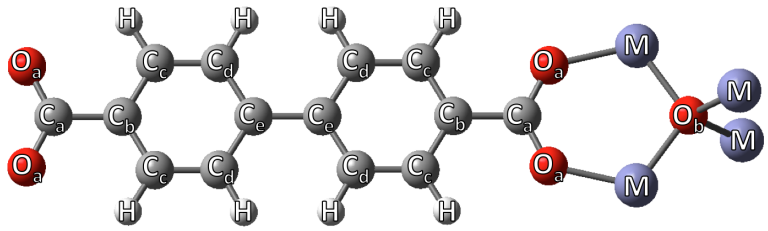

Figure 3.1: Organic linker and metal node present in M-IRMOF-10 labeled with the unique atom types present in this isoreticular series (M = Mg, Ca, Fe, Cu, Zn, Ge, Sr, Cd, Sn, Ba).

Reference Energy Curves

We have demonstrated in previous work[39,285,203] that cluster calculations allow for the computation of accurate M−CO_2 interaction parameters with more expensive functionals for less computational cost than periodic DFT. As such, cluster models were utilized to compute interaction energies with CO_2 by pulling CO_2 away from the cluster along a vector that maximized the M−CO_2 interaction. These energies were then used to fit molecular mechanics force field parameters, which is why they are referred to as reference energy curves. The cluster models, which center around the metal nodes of each member of the M-IRMOF-10 series, were designed by cutting one metal node from each structure at the points where the two phenyl rings meet in the biphenyl-dicarboxylate linkers and capping with 6 hydrogens (Figure 3.2). The 6 capping hydrogens were fixed at the same C−H bond distances as their neighbors. Reference energy curves were

computed with PBE0[104,300,301,302,303,304,305] and the D3 Grimme correction[306] using *Turbomole 6.4*.[301] The def2-TZVP basis set[303,307,308] with effective core potentials that contain scalar relativistic corrections for elements heavier than Kr[309] was used to compute the interaction energy of CO_2 with each MOF. A simplified version of the equation utilized to compute the interaction energies is

$$E_{\text{int}} = E_{\text{MOF-CO}_2} - E_{\text{MOF}} - E_{\text{CO}_2} \tag{3.1}$$

where E_{int} is the electronic interaction energy, $E_{\text{MOF-CO}_2}$ is the energy of the supersystem, E_{MOF} is the energy of the MOF, and E_{CO_2} is the energy of the CO_2 molecule. The counterpoise correction[310] was used to correct for basis set superposition error (BSSE). There is some argument about the validity of this correction when using DFT with triple-zeta basis sets or larger, but we used the counterpoise correction because there is evidence suggesting that it is necessary for describing physisorption.[311,312] The CO_2 configuration was chosen by moving the CO_2 along the metal$-O_b$ vectors that maximizes the distance between CO_2 and all non-metal atoms (Figure 3.2).

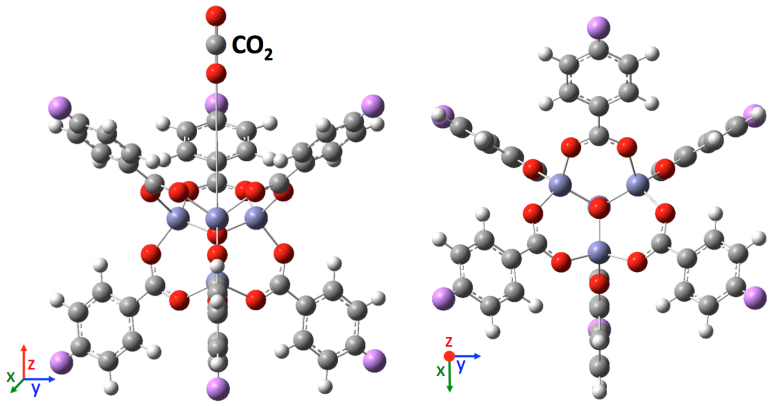

Figure 3.2: On the left, Zn-IRMOF-10 cluster shown along with the CO_2 path used to compute the reference energy curve. On the right, Zn-IRMOF-10 cluster shown along the CO_2 path. Blue atoms represent zinc, red are oxygen, grey are carbon, white are the hydrogens from the PBEsol optimized periodic structure, and purple are the capping hydrogens that were added to the cluster.

Classical Simulations

Force Field

The Transferable Potentials for Phase Equilibria (TraPPE) force field[87,94,95,96,97,98] models the non-bonded interactions between each pair of interaction sites i and j with Lennard-Jones (LJ) and Coulomb potentials in the form

$$E_{ij} = 4\epsilon_{ij}\left[\left(\frac{\sigma_{ij}^{12}}{r_{ij}^{12}}\right) - \left(\frac{\sigma_{ij}^{6}}{r_{ij}^{6}}\right)\right] + \frac{q_i q_j}{4\pi\epsilon_0 r_{ij}} \tag{3.2}$$

where r_{ij} is the distance between the interaction sites, σ_{ij} is the LJ diameter, ϵ_{ij} is the well depth, q_i and q_j are the partial atomic charges for sites i and j, respectively, and ϵ_0 is the vacuum permittivity.

The LJ parameters for the carbon and hydrogen atoms in the framework were obtained from the TraPPE - Explicit Hydrogen (TraPPE-EH) force field[93,87,94,95] for aromatic rings.[94,95] The bpdc oxygen (O_a) ϵ and σ parameters were obtained from geometric and arithmetic means, respectively, of the TraPPE ϵ and σ parameters for ketones and primary alcohols.[96,97] The metal node oxygen (O_b) parameters were taken from the TraPPE - zeolite (TraPPE-zeo) force field,[87] because these parameters should most closely describe the inorganic environment of O_b. The accuracy of the carbon parameters was tested by comparing to CCSD(T) calculations on a CO_2-benzene complex by Witte et al.[313] (Figure S1 in the supporting information (SI) of ref 314). The TraPPE-EH LJ and UFF parameters used to model the framework are shown in Table 3.1. The LJ parameters for the carbon dioxide guest molecules were obtained from the TraPPE force field[98] (Table 3.1). The Lorentz-Berthelot[315,316] combining rules were used for all unlike LJ interactions.

Metal$-CO_2$ LJ parameters were computed by fitting to the PBE0-D3 reference energy curves described in Section 3.1.2. This was done by subtracting all charge interactions between the cluster and CO_2, all non-metal LJ contributions from the cluster, and the LJ contribution from the carbon of CO_2. All that should remain in the reference energy after these subtractions is the LJ interaction between the metal centers and the oxygen atoms of CO_2 (metal$-$O_CO_2), for a total of two LJ parameters (ϵ, σ) to fit for each metal studied. A Boltzmann weighting was applied to ensure accuracy near the minimum energy regions of the potential energy surface. The total electronic,

reference energy and a temperature of 500 K were used to compute the weight, which was then used to multiply the energies during the fitting. This procedure has been used successfully in previous work[203] and resulted in reasonable parameters in this work. The hydrogen charges on the cluster models were altered to neutralize the charge for both DDEC and CM5.

Table 3.1: UFF[84,85] and TraPPE[87,94,98] Lennard-Jones parameters for each atom type present in IRMOF-10 and CO_2 (see Figure 3.1).

Atom	UFF		TraPPE		
Type	σ	ϵ / k_B	σ	ϵ / k_B	Ref
	Å	K	Å	K	
O_a	3.12	30.2	3.04	86	94
O_b	3.12	30.2	3.30	53	87
C_a	3.43	52.8	3.60	30.7	94
C_b	3.43	52.8	3.60	30.7	94
C_c	3.43	52.8	3.60	30.7	94
C_d	3.43	52.8	3.60	30.7	94
C_e	3.43	52.8	3.60	30.7	94
H	2.57	22.2	2.36	25.5	95
$O(CO_2)$	–	–	3.05	79	98
$C(CO_2)$	–	–	2.80	27	98

Isotherms

CO_2 adsorption isotherms were computed using the isobaric-isothermal (NpT) Gibbs Ensemble Monte-Carlo (GEMC)[317] method at a temperature of 298 K. A two box simulation set-up was used, one for the explicit gas reservoir and one for sorbent phase. Using an explicit reservoir allows one to specify the pressure directly as a thermodynamic constraint for the simulations and, hence, an equation of state or additional simulations was not needed to convert between reservoir pressure and chemical potential. Thus, the interactions between CO_2 molecules were treated consistently in the gas and sorbent phases. During the simulation the two phases were allowed to exchange particles while only the volume of the gas reservoir was allowed to change. In order to sample the additional degrees of freedom, translational and rotational moves were carried out on the adsorbate molecules. The final adsorbed loading is equal to the ensemble average of the

number of molecules in the adsorbed phase. An in-house Monte Carlo code for complex chemical systems[318] was used for all the GEMC calculations. Each calculation consisted of 5×10^4 equilibration cycles followed by 5×10^4 production cycles. For each cycle, a number Monte Carlo moves equal to the number of adsorbate molecules in the system was carried out. In these simulations, the number of gas phase CO_2 molecules was increased with increasing pressure. Between 200 and 800 CO_2 molecules were included in all cases. A spherical potential truncation at $r_{\text{cut}} = 14$ Å was used for guest-guest and framework-guest LJ interactions within the adsorbed phase, and a truncation at $r_{\text{cut}} = 40\%$ of the average box lengths for all interactions in the bulk reservoir phase. Analytical tail corrections[88] to estimate the LJ interactions beyond these distances were used within both the bulk and adsorbed phases. Coulomb interactions were calculated using the Ewald summation method[88] with a convergence parameter, κ, of $3.2/r_{\text{cut}}$. The framework atoms were kept fixed at the crystallographic positions determined from the geometry optimization (i.e., slightly different structures are used for the different metal-exchanged IRMOF-10 variants. This is a common assumption[3] for MOFs that do not undergo breathing transitions (e.g. MIL-53[319]). Treating the framework as rigid allows for framework-guest interactions to pre-tabulated and interpolated during the simulation,[320] which results in significant gains in computational efficiency. It should be noted that GEMC simulations can also be used for flexible sorbents.[321]

3.1.3 Results and Discussion

Periodic Calculations

PBEsol,[295,296] which is a slight modification of the PBE functional,[322,323] has been shown to provide reasonable estimates of bond distances and lattice parameters within MOFs[324,325]. However, PBEsol and PBE are not reliable at predicting binding energies of CO_2 within MOFs as they cannot accurately describe dispersion.[326,327] Furthermore, nonlocal exchange is often important for describing guest binding to metals.[328] Hence, PBE0-D3 was used for the interaction energy calculations because in previous work[329] it was demonstrated to provide accurate interaction energies when compared to Coupled Cluster with Single, Double and perturbative Triple excitations (CCSD(T)). PBE0-D3 contains 25% exact exchange and the D3 dispersion correction to correct the tendency

of PBE to underestimate binding energies at both short and long range.[104,300,306]

PBEsol calculations on Zn-IRMOF-1 match very closely with the experimental structure (Table S1). Furthermore, PBEsol has been used on MOFs in the past and has given reliable results.[297,298] Other functionals were not considered given the reliability of PBEsol. The PBEsol calculations for M-IRMOF-10 where M = Mg, Ca, Fe, Cu, Zn, Ge, Sr, Cd, Sn, and Ba demonstrated that the unit cell size of IRMOF-10 increases as the ionic radii of the metals increase. With the exception of Fe^{2+} and Cu^{2+}, all of the metals tested are closed shell. The magnetic ordering between the Fe^{2+} ions within the Fe_4O centers was shown to be antiferromagnetic by the periodic PBEsol calculations, and Mössbauer spectra performed on Fe_4O^{2-} compounds support this finding.[330,331] The PBEsol calculations predict that the Cu^{2+} ions within the Cu_4O centers are ferromagnetically coupled. DDEC and CM5 charges were computed using the PBEsol optimized geometries. For each of the computed structures, the DDEC charges of every atom are larger in magnitude than the corresponding CM5 charges. However, both sets of charges predict relatively similar trends. The main differences between the predictions of DDEC and CM5 will be discussed in Section 3.1.3. Table 3.2 shows the DDEC and CM5 charges of the metal centers, the M−O_a and M−O_b distances, and the lattice parameters of the periodic structures. The M−O_a and M−O_b distances are provided as metrics for the ionic radius, since experimental ionic radii vary wildly based on oxidation number and ligand field. Tables S2 and S3 in the SI contain the charges of every atom type present within every PBEsol optimized MOF.

Reference Curves and Parameter Fitting

The minimum energies along the computed reference energy curves show that the elements that have larger ionic radii have stronger binding with CO_2. Figure 3.3 contains the full interaction energies of the tested CO_2 configuration space and a comparison between the magnitude of the minimum energies along these curves to the M−O_a distance of each cluster. To fit the metal LJ parameters the contributions from the atomic point charges and the interaction with all non-metal atoms was subtracted from the reference energy curves, as shown in Figure 3.3. There are thus four separate sets of curves that will be used to compute the LJ parameters of the metals. These result from the combinations of UFF and TraPPE with CM5 and DDEC charges (UFF-DDEC,

Table 3.2: DDEC and CM5 metal charges, M−O_a and M−O_b distances, and lattice parameters of the primitive cell of the PBEsol M-IRMOF-10 geometries. The lattice angles in this cell are $\alpha = \beta = \gamma = 60°$.

Group	Metal	DDEC charge	CM5 charge	M−O_a Å	M−O_b Å	$a = b = c$ Å	volume Å^3
Alkaline	Mg	1.61	0.89	1.93	1.96	24.35	10212
Earth	Ca	1.54	1.10	2.11	2.17	24.76	10734
Metals	Sr	1.61	1.12	2.36	2.40	26.14	12625
	Ba	1.57	1.15	2.56	2.55	26.88	13732
3d	Fe	1.16	0.74	1.88	1.77	24.18	9992
	Cu	1.11	0.71	1.92	1.87	24.28	10121
	Zn	1.11	0.68	1.93	1.94	24.32	10172
4d	Cd	1.19	0.77	2.18	2.16	25.44	11643
p-block	Ge	1.11	0.50	2.19	2.25	25.45	11684
	Sn	1.14	0.61	2.35	2.33	26.00	12431

UFF-CM5, M-TraPPE-DDEC, M-TraPPE-CM5). UFF-CM5 and UFF-DDEC represent pure UFF parameters with CM5 and DDEC charges, respectively. M-TraPPE-CM5 and M-TraPPE-DDEC represent TraPPE with fitted metal parameters and either CM5 or DDEC charges, respectively. Examples of two representative fitting cases (Ba and Zn) are provided in Figure 3.4. The fitting errors resulting from the other metals are provided in Figure S3. In the copper case, almost all of the attraction between CO_2 and the cluster resulted from interaction with point charges and non-metal atoms, which is why the fit is zero. The mean unsigned error (MUE) for the fit of each metal with respect to the reference energy curves are provided in Table S4. The cases that have the fits with the smallest error (0.2−0.4 kJ/mol) tend to be those that either contain a heavier element with a large ionic radii (Sr, Sn, Ba) or those that have such a weak van der Waals interaction that a fit of zero does not affect the parameters to a significant extent (Cu, Fe). Figure S3 shows that none of the studied systems have particularly large errors (1.2 kJ/mol maximum error for Sn). The energy trends observed in Figure 3.3 indicate that the metals with larger ionic radii interact more strongly with CO_2. Coulomb and dispersion interactions are the main contributors to the binding of CO_2 with these metals as evidenced by the fairly weak binding (15−30 kJ/mol).

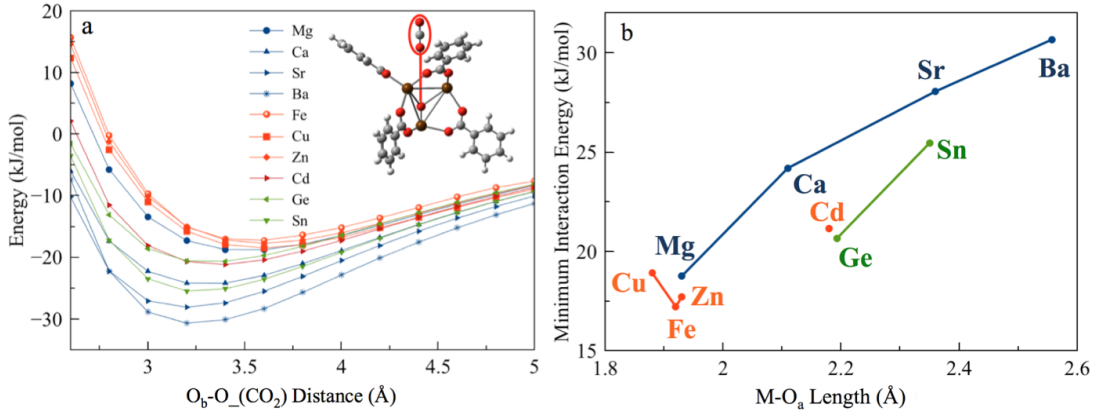

Figure 3.3: (a) Relative PBE0-D3 interaction energies versus the distance between oxygen of CO_2 and the central oxygen (O_b) of the MOF cluster along the CO_2 path shown in red in the inlay, and (b) a comparison between the minimum interaction energy extracted from each curve to the corresponding M−O_a distance computed with PBEsol.

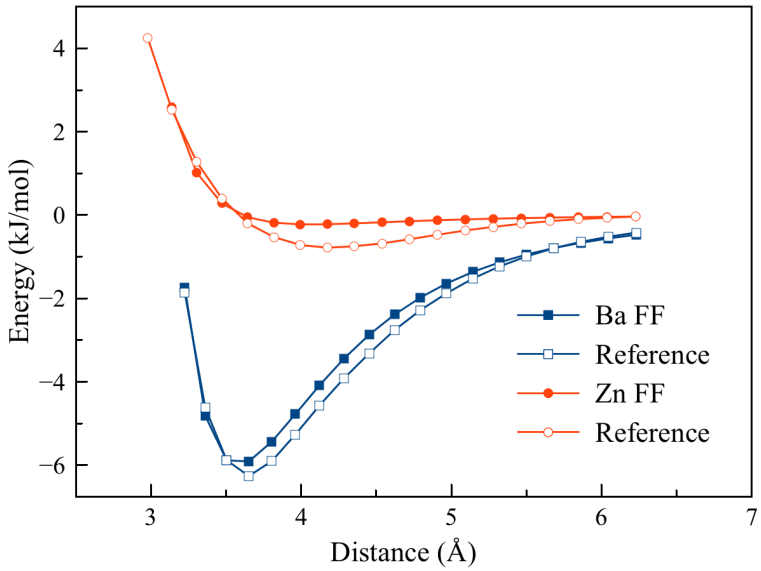

Figure 3.4: Reference metal−O_CO_2 van der Waals interaction energy and the resulting M-TraPPE-CM5 force field prediction along the CO_2 path shown in Figure 3.2 for the Ba-IRMOF-10 (blue) and Zn-IRMOF-10 (orange) cases. The fitting errors for all metals are provided in Figure S3. The reference metal−O_CO_2 van der Waals interaction energy contains only the van der Waals interaction between the oxygen of CO_2 and the metals of each cluster (Figure 3.2).

Isotherms

CO_2 isotherms were simulated only for a subset of the MOFs for which reference curves were computed. The Zn-IRMOF-10 CO_2 isotherms were computed because experimental CO_2 isotherms exist for this structure. Fe- and Ba-IRMOF-10 CO_2 isotherms were computed because they represent the weakest and strongest cases in terms of CO_2 interaction strength, respectively. The Ge-, and Sn-IRMOF-10 CO_2 isotherms were computed to determine if the CO_2 interaction trends would hold when p-block metals, which have significantly smaller charges than the alkali earth metals and larger ionic radii than the 3d metals (Table 3.2), were used.

Table 3.1 contains all of the non-metal TraPPE and UFF parameters. Table 3.3 contains all of the LJ parameters optimized in this work. TraPPE predicts stronger linker-CO_2 attraction than UFF, which is why the values of ϵ for the metals decreased when TraPPE parameters were used (Table 3.3).

Table 3.3: Lennard-Jones parameters for each metal in the M-IRMOF-10 series.

Metal	UFF		M-TraPPE-DDEC		M-TraPPE-CM5	
	σ	ϵ/kB	σ	ϵ/kB	σ	ϵ/kB
	Å	K	Å	K	Å	K
Mg	2.69	55.9	–	–	–	–
Ca	3.03	119.8	–	–	4.12	3.1
Sr	3.24	118.3	3.71	14.3	3.70	18.5
Ba	3.30	183.3	3.52	176.0	3.53	193.0
Fe	2.59	6.5	3.13	10.5	3.18	17.2
Cu	3.11	2.5	–	–	–	–
Zn	2.46	62.4	–	–	4.03	1.1
Cd	2.54	114.8	4.21	1.53	–	–
Ge	3.81	190.8	3.51	21.8	3.13	128.0
Sn	3.91	285.5	3.49	91.3	3.30	233.0

Figure 3.5 contains isotherms for Zn-IRMOF-10 and Zn-IRMOF-1, which are shown alongside existing experimental data.[275,274] Note that the same force fields were used for Zn-IRMOF-10 and Zn-IRMOF-1. For Zn-IRMOF-10, the M-TraPPE-CM5 isotherm provides a closer estimate of the CO_2 adsorption than UFF-CM5 (Figure 3.5), especially below 15 bar. M-TraPPE-CM5 also significantly improves the isotherm of CO_2 adsorption within Zn-IRMOF-1 below 10 bar.[274,275] Therefore, it seems that M-TraPPE-CM5

is a reliable choice for predicting CO_2 adsorption for these systems. This is due to the fact that M-TraPPE-CM5 has several advantages over UFF-CM5: (i) the metal parameters within M-TraPPE-CM5 were specifically tuned for the interaction of CO_2 in the IRMOF series, (ii) the TraPPE benzene carbon parameters result in smaller mean unsigned percentage error (MUPE) values than UFF when interacting with CO_2 (Figure S1), and (iii) the TraPPE oxygen parameters were chosen to model the oxygen types present within the IRMOF series (Section 3.1.2). UFF-CM5 overestimates the loading of CO_2 below 15 bar, and predicts similar CO_2 loadings to M-TraPPE-CM5 near saturation for both Zn-IRMOF-1 and Zn-IRMOF-10. Both UFF-CM5 and M-TraPPE-CM5 overestimate the CO_2 loading at high pressure because the experimental structures likely contain defect sites that result in pore blockage.[203] The CO_2 isotherms simulated with the other metals follow the same trends as presented in Figure 3.5. Ba-IRMOF-10 resulted in the strongest CO_2 binding and Fe, Zn-IRMOF-10 resulted in the weakest. At high pressures, near saturation loading, the number of CO_2 molecules that fit inside of the unit cell is entirely dependent on the free volume, which increases with the unit cell volume in an isoreticular series of MOFs (Table 3.2).

Figure 3.6 contains the remaining CO_2 isotherms simulated in this work for each metal. This plot shows that the isotherms do not shift significantly when the charges are changed. Also, for all metals, the M-TraPPE force fields predicts lower CO_2 loading than UFF, indicating that UFF might be overestimating the interaction of CO_2 with these MOFs based on the comparison to experiment in Figure 3.5. Ba-IRMOF-10 appears to have the highest CO_2 affinity and saturation loading, while Fe-IRMOF-10 has the lowest. All M-TraPPE-CM5 CO_2 isotherms are provided in Figure 3.7. Isotherms were computed only for the strongest and weakest CO_2 binding cases in Figure 3.5. The order of the metals in terms of low pressure CO_2 affinity is Ba > Sn > Ge > Zn > Fe. For all metals the M-TraPPE force fields predict lower CO_2 adsorption than UFF, which is closer to the experimental CO_2 adsorption for both Zn-IRMOF-10 and Zn-IRMOF-1.

Figure 3.8 shows a direct comparison between absolute CO_2 loading in Ba-IRMOF-10 and Zn-IRMOF-10 in both mol/kg and molecules/unit cell. The isotherms are significantly closer in mol/kg due to the difference in atomic mass between Ba and Zn. However, Ba-IRMOF-10 clearly has a higher CO_2 affinity at low pressure than Zn-IRMOF-10 regardless of the units. This demonstrates that the metal centers play a

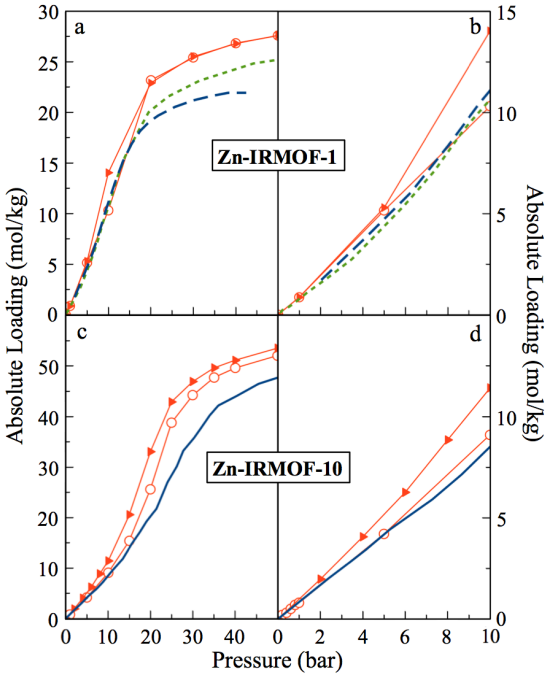

Figure 3.5: (a) Zn-IRMOF-1 experimental (long-dashed blue[274] and short-dashed green lines,[275]) M-TraPPE-CM5 (empty orange circles), and UFF-CM5 (filled orange triangles) isotherms. (b) Zoomed view of the low-pressure region of the Zn-IRMOF-1 isotherms. (c) Zn-IRMOF-10 experimental (solid blue line), M-TraPPE-CM5 (empty orange circles), and UFF-CM5 (filled orange triangles) isotherms. (d) Zoomed view of the low-pressure region of the Zn-IRMOF-10 isotherms.

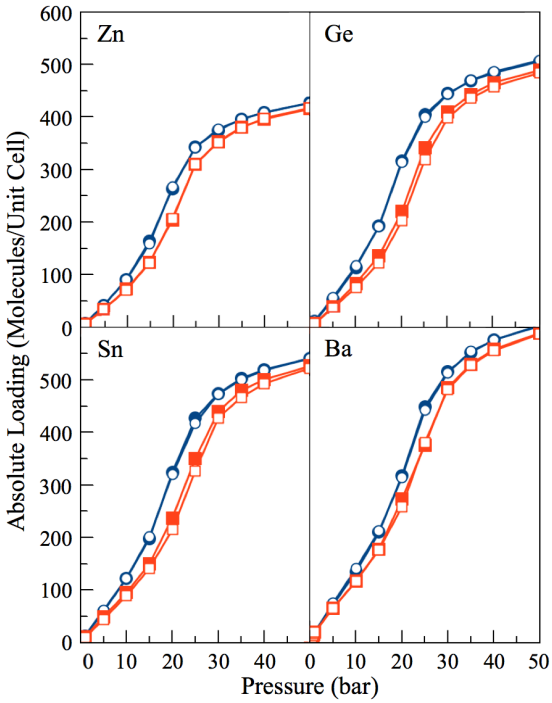

Figure 3.6: CO_2 adsorption isotherms of Zn, Ge, Sn, and Ba-IRMOF-10 with pure UFF (blue circles) and with the fitted metal parameters and TraPPE (orange squares). CM5 (filled) and DDEC (empty) charges were used to compute each isotherm.

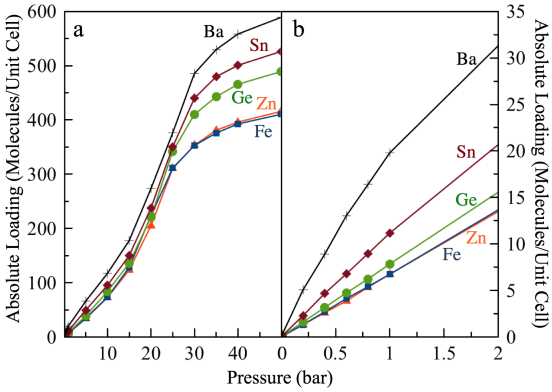

Figure 3.7: CO_2 isotherms simulated with the M-TraPPE-CM5 force field optimized in this work. The complete isotherms are shown in (a) and the low pressure region of the isotherms are shown in (b).

key role in adsorption even in MOFs with coordinatively saturated metal nodes. Simulated[3] CO_2 isotherms for IRMOF-1, IRMOF-7, IRMOF-16, and MOF-200 are provided in Figure 3.8 for comparison. It is clear from Figure 3.8 that Zn-IRMOF-10 has a higher CO_2 affinity than IRMOF-16 and MIL-200 at low pressure, and that changing the metal to Ba^{2+} significantly improves the low pressure CO_2 adsorption relative to the other MOFs. However, the primary goal of this work is to compare the effect of changing the metal center while the MOF topology is fixed, as changing MOF topologies makes it difficult to account for all relevant variables. There are two main reasons why there is an increase in CO_2 binding energy with metal ionic radius: (i) the positive charge of the metals is more exposed to the negative charge of the CO_2 oxygen as the $M-O_a$ distance increases and (ii) there is an increase in the strength of the van der Waals interaction with heavier metals. Based on the computed isotherms the ordering of the metal affinity for CO_2 is Ba > Sn > Ge > Zn > Fe. To determine the proportion of the increased CO_2 interaction that results from (i) and (ii), we computed low pressure (1−10 bar) isotherms for Ba- and Zn-IRMOF-10 with M-TraPPE and assigned zero charge to each of the atoms in the MOF frameworks (Figure 3.9). This plot shows that the main contributor to the increased interaction with CO_2 is the exposed charge of the metal center of Ba. At 10 bar, adding CM5 charges to the framework atoms results in an increase to the absolute loading of 15% for Zn-IRMOF-10 and an increase of 65% for Ba-IRMOF-10.

Recall that at low pressure (below 10 bar), the Zn-TraPPE force fields capture the shape and the magnitude of the CO_2 isotherms much more closely than UFF. This derives from the fact that at low pressure the difference between the force fields is the result of the van der Waals and Coulomb attraction between the metal centers and CO_2, which are better described by the fitted metal−O_CO_2 parameters, and because the TraPPE parameters more accurately describe the linker-CO_2 interactions (Figure S1). At high pressures the cell becomes saturated with CO_2 molecules and the force fields predict similar CO_2 loadings. To test this hypothesis, a simulation was performed wherein the parameters of the Fe-IRMOF-10 PBEsol structure were replaced with the CM5 charges and LJ parameters of the M-TraPPE-CM5 Ba-IRMOF-10 case (Figure 3.21). The resulting isotherm showed a significant increase in the CO_2 loading at low pressures, and the inflection point present in the other isotherms almost disappeared.

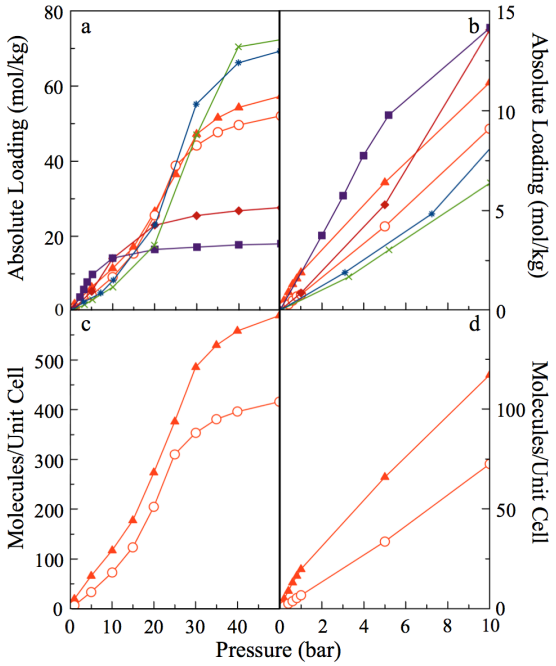

Figure 3.8: (a) Absolute loading of CO_2 in Zn- (filled orange triangles) and Ba-IRMOF-10 (empty orange circles) compared to literature values[3] (computed with DREIDING[86] and Qeq[332] charges) in mol/kg. IRMOF-1 (red diamonds), IRMOF-7 (purple squares), IRMOF-16 (green crosses), and MOF-200 (blue asterisks) are provided.[3] (b) Low pressure region of the Zn- and Ba-IRMOF-10 isotherms in mol/kg. IRMOF-1, IRMOF-7, IRMOF-16, and MOF-200 are also provided here. (c) Zn- and Ba-IRMOF-10 isotherms in Molecules/Unit Cell. (d) Low pressure region of the Zn- and Ba-IRMOF-10 isotherms in Molecules/Unit Cell.

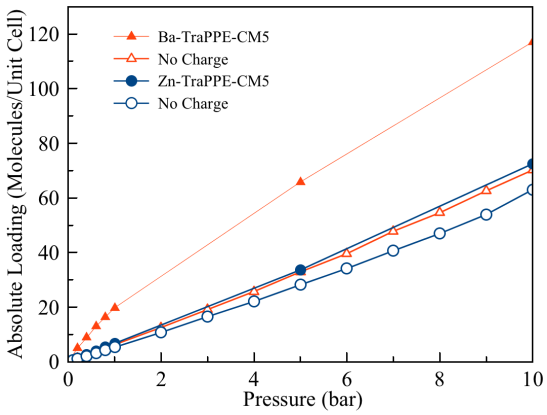

Figure 3.9: Low pressure (1−10 bar) CO_2 isotherms that compare the M-TraPPE results with and without charges assigned to the atoms in the MOF. Ba-TraPPE-CM5 (filled orange triangles) is compared to Ba-TraPPE with no charge (empty orange triangles), Zn-TraPPE-CM5 (filled blue circles), and Zn-TraPPE with no charge (empty blue circles).

This indicates that the metal node was the primary source of attraction within the MOF at low pressures. As the CO_2 loading increased, the less attractive sites around the linker played a greater role and the difference between the isotherms computed with Fe-IRMOF-10 and Ba-IRMOF-10 parameters with the Fe-IRMOF-10 structure decreased until the supercell was close to saturation with CO_2.

To confirm that the location of the primary binding sites within IRMOF-10 is near the metal centers, radial distribution function (RDF) data were generated. The RDFs of the C_CO_2 locations centering around the metal ions for Zn- and Ba-IRMOF-10 are provided in Figure 3.11. Plots of the C_CO_2 positions relative to each atom type with the Zn- and Ba-IRMOF-10 frameworks at 1 bar are provided in Figures S5 and S6. Also, the M−O_CO_2 positions are provided in Figures S7 and S8. The C_CO_2 plots (Figures 3.11, S5, and S6) show that the most prominent binding location for CO_2 in both Ba- and Zn-IRMOF-10 is ∼4 Å from the metal centers. This is because the M−C_CO_2 binding region at ∼4 Å is ∼3 times larger in Ba-IRMOF-10 than in Zn-IRMOF-10 at 1 bar. The C_CO_2 plots also demonstrate that the secondary binding sites at ∼7 Å are the result of the benzene rings in the linker molecules, which is proven by the C_a, C_b, C_c, and C_d curves. The appearance of a peak split at ∼3.5 and ∼5.8 Å in the

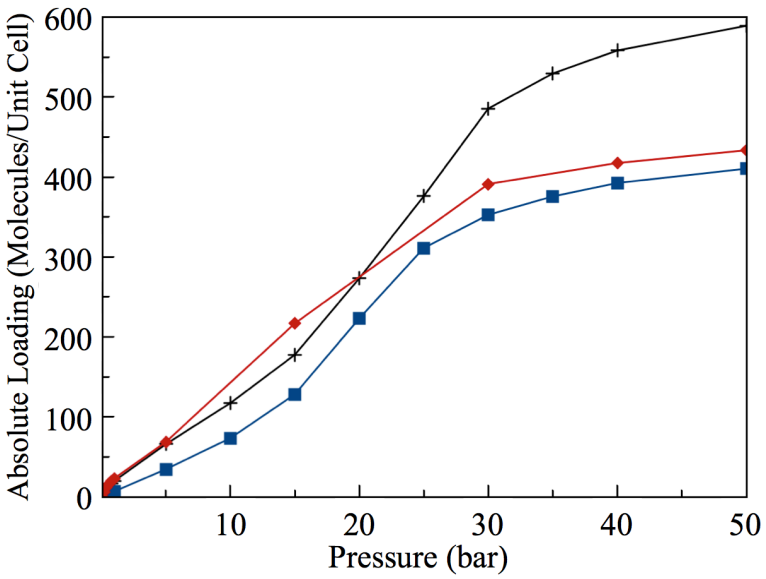

Figure 3.10: Computed CO_2 adsorption isotherms of Fe-IRMOF-10 (blue squares) and Ba-IRMOF-10 (black plus signs) with pure M-TraPPE-CM5, and the isotherm resulting from the combination of the Fe-IRMOF-10 structure with Ba-IRMOF-10 parameters (red diamonds).

M−O_CO_2 plot for Ba-IRMOF-10 (Figure S8) demonstrates that one oxygen of CO_2 tends to be closer to the metal than the other in Ba-IRMOF-10. In Zn-IRMOF-10, the peak split does occur but to a lesser degree (Figure S7). At higher pressures, when more CO_2 molecules are present, the probability of finding a CO_2 in any given location becomes near equivalent.

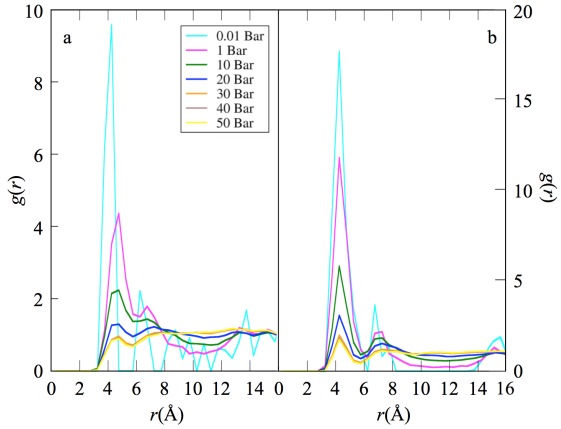

Figure 3.11: Radial distribution function $g(r)$ plots for (a) Zn-IRMOF-10 and (b) Ba-IRMOF-10. *r(Å)* represents the distance between the metal ions and the carbon of CO_2 (M−C_CO_2).

Both DDEC and CM5 charges have been tested extensively[333,334] and demonstrated accuracy with a wide variety of metrics and materials. Despite that fact the metal charges predicted by DDEC are 60-80% larger than those predicted by CM5 (Table 3.2), they do not result in significant differences between the computed isotherms with either UFF or the M-TraPPE force fields (Figure 3.6). This can be attributed to the fact that the increase of the attractive, positive metal charge when using DDEC is accompanied by an increase in the repulsive, negative charge of the O_a oxygens (Tables S2 and S3). The larger negative O_a charge predicted by DDEC results in only a slight difference between the M-TraPPE-CM5 and M-TraPPE-DDEC isotherms (Figure 3.6). The largest differences were for Ge- and Sn-IRMOF-10. For both of these MOFs the CO_2 loading decreased by approximately 10% when DDEC charges were used (Figure 3.6). The reason is that DDEC predicts that the Ge- and Sn-IRMOF-10 cases have larger O_a charges than the 3d-metal-IRMOFs, while CM5 predicts the opposite. Since the negative O_a charges repel the negatively charged oxygens of CO_2, there will be

slightly more repulsion of CO_2 in the Ge- and Sn-IRMOF-10 cases than in the 3d-metal-IRMOF cases when using DDEC. It is difficult to say precisely why CM5 and DDEC predict disparate charge trends for certain metals, since these charge methods have many significant differences.

3.1.4 Conclusions

In this work we simulated CO_2 isotherms within the M-IRMOF-10 series (M = Mg, Ca, Fe, Cu, Zn, Ge, Sr, Cd, Sn, and Ba), and Zn-IRMOF-1, with a force field combining TraPPE and quantum mechanically optimized metal parameters to see if this procedure would improve upon UFF and if there are any interesting CO_2 interaction trends based on the properties of these metal centers. We demonstrated that the interaction between the CO_2 and the metal atoms M_4O nodes is not very strong for any of the tested metals (15−30 kJ/mol), but the interaction energy increases with the bond radius, represented by the M−O_a length, of the metal (Figure 3.5). This increase in CO_2 binding was the result of a decrease in steric hindrance from the linker oxygens (O_a) as they shifted to larger bond distances due to the increasing metal ion radii, and the stronger attraction resulting from the heavier metal ions.

The CO_2 adsorption simulations performed here indicate that the ionic radius of the metal centers within the IRMOF series might be considered as a parameter to increase CO_2 binding, provided that there are no complex electronic interactions taking place. Both the UFF and M-TraPPE force fields predict the same binding trends for each member of the M-IRMOF-10 series. However, TraPPE with fitted metal−O_CO_2 interaction parameters describes the adsorption of CO_2 within Zn-IRMOF-1 and Zn-IRMOF-10 more accurately than UFF (Figure 3.5). Furthermore, the charge models tested in this work do not change the adsorption of CO_2 significantly.

In summary, we have systematically analyzed the effect of changing the metal on CO_2 adsorption within the IRMOF-10 series, and rationalized an explanation as to why certain metals result in larger binding energies. At low pressure (1 bar), we found that CO_2 uptake within the theoretical MOF Ba-IRMOF-10 is more than twice as large as that for Zn-IRMOF-10 (1.9 mol/kg vs. 0.8 mol/kg). Ba- and Zn-IRMOF-10 have similar CO_2 loadings at high pressure (50 bar) when measured in mol/kg (57.3 mol/kg vs. 52.1 mol/kg) (Figure 3.6). However, there is a significant difference between the

CO_2 loadings of Ba- and Zn-IRMOF-10 in units of CO_2/unit cell (589 CO_2/unit cell vs. 416 CO_2/unit cell). This is due to the larger unit cell size caused by the larger ionic radius of Ba^{2+} as demonstrated by the trends in binding energy that we have observed with each metal (Figure 3.3). The increased binding with ionic radii occurs because (i) larger ionic radii increase the bond distance between neighboring oxygen atoms and therefore expose the positive charge of the metals enough to interact with CO_2 and (ii) larger elements have stronger dispersion interactions with CO_2. Figure 3.9 demonstrates that the majority of the increased binding that occurs at low pressure in Ba-IRMOF-10 is due to the electrostatic interactions with CO_2. RDF plots (Figure 3.11) provide further evidence that the main interaction site in IRMOF-10 is near the metal center. Ba-IRMOF-10 has approximately three times more CO_2 molecules near the metal centers than Zn-IRMOF-10. These results may help to guide experimentalists in their design of MOFs for CO_2 adsorption, because they indicate that ionic radii can be selected to increase affinity for CO_2 within MOFs that contain coordinatively saturated metal nodes.

3.2 CO_2 Adsorption in Fe_2(dobdc): A Classical Force Field Parameterized from Quantum Mechanical Calculations

3.2.1 Introduction

Metal-Organic Frameworks (MOFs) are nanoporous materials that consist of metal nodes connected by organic linkers, and can be synthesized with a wide range of topologies, surface areas, and other structural characteristics. These materials can be used to store gasses with different physical and chemical characteristics.[6,335] Experimental characterization of MOFs is necessary for gaining insight into their adsorption ability,[336,337,338,38,339] but experiment alone is not sufficient for the rapid characterization of MOFs due to many possible combinations of metals, linkers, and topologies that could be tested for various applications. Accordingly, one of the reasons that computational approaches play an important role in the screening process is that they can help experimentalists to efficiently screen MOFs that are worth considering for use in gas separations.

Molecular simulations have been widely used to compute macroscopic properties such as adsorption isotherms. These classical simulations require the use of force fields for describing intermolecular interactions. The Grand-Canonical Monte Carlo (GCMC) approach with force fields such as DREIDING[340] and the Universal Force Field (UFF)[341] has been used with some success to study simple molecule adsorption within MOFs.[342,343,344] However, adsorption within MOFs that strongly bind guests, such as those with open-metal sites, cannot be described accurately with these force fields.[345,39] Although it is not possible to accurately compute adsorption isotherms for guests within open-metal site MOFs with general force fields, it is possible to parameterize force fields from quantum mechanical calculations that could be used to simulate these isotherms more accurately.

In previous work, intermolecular potentials were parameterized for the interaction of CO_2 and N_2 with Mg_2(dobdc), Zn_2(dobdc), and $Zn_4O(bdc)_3$ (bdc^{2-} = 1,4-benzenedicarboxylate), also called MOF-5 or IRMOF-1.[39] MOF fragments were used to design clusters to model these extended systems and were used to compute interaction

energy curves with CO_2. This approach yielded parameters that accurately predicted CO_2 and N_2 adsorption in closed shell MOFs. Møller-Plesset second-order perturbation theory (MP2)[102] was used to compute interaction energies for Mg-MOF-74 and Zn-MOF-74 cluster models with CO_2. Cluster models were designed to describe CO_2 interactions with every atom type present in these MOFs. These resulted in accurate force fields, but it was rather expensive. In this study, we simplified this parameterization scheme by computing new parameters only for the interaction between the open-metal site M and the oxygen of CO_2.

It should be noted that there are multiple ways to compute macroscopic characteristics of MOFs. The energy decomposition proposed in this paper is useful both to derive the force field, and also to understand the physics beyond the various terms contributing to the interaction energy, e.g. electrostatics, induction, dispersion, repulsion. This means that the force field will be accurate due to a correct description of the physics of the various terms rather than simply error cancellation. These decomposed terms can then either be used directly as polarizable force fields or can be further simplified to effectively include quantum mechanical effects in calculations with large numbers of atoms. Examples of some of these energy partitioning schemes are the Sum of Interactions Between Fragments *Ab Initio* computed (SIBFA)[346] method, Symmetry Adapted Perturbation Theory (SAPT)[347] which is fully quantum mechanical and has been used on the Fe-MOF-74 before,[348] and the Effective Fragment Potential (EFP) method. The EFP method describes inert interactions with effective potentials, while describing an active region with quantum mechanics. EFPs have been used to compute energies for many types of interactions,[349,350,351] but to our knowledge this method has not been employed to study gas adsorption in MOFs.

In this work we focus on another member of the M_2(dobdc) family, commonly referred to as the M-MOF-74 series, namely Fe-MOF-74 (Figure 3.12), and its ability to bind CO_2. Species containing Fe(II) ions are known to be challenging to describe computationally. In some coordination environments the low-spin and high-spin states of Fe(II) are so close in energy that it is difficult to predict which is the ground state,[352] and within spin states multiconfigurational character has been observed when binding guests to heme.[353,354] Furthermore, complex redox reactions occuring with guests have been observed in Fe-MOF-74 previously.[38] The coordination environment within

Fe-MOF-74 favors the high-spin state for Fe(II) when bare[355] and when binding hydrocarbons.[348] The primary goal of this work was to compute isotherms for CO_2 adsorption within Fe-MOF-74 by extracting force field parameters from an interaction energy curve calculated with Restricted Open-shell Møller-Plesset second-order perturbation theory (ROMP2), while using UFF parameters to describe all non-metal interactions instead of computing new parameters for each of these pairwise interactions.

The isotherms simulated in this work are compared to new experimental Fe-MOF-74/CO_2 adsorption data. The surface area of Fe-MOF-74 was determined at low pressure and temperature by using pure N_2. CO_2 adsorption isotherms were measured at three temperatures by cycling pure CO_2 through an activated sample of Fe-MOF-74 at a constant rate. From these isotherms we can obtain information on the surface area and binding characteristics of MOFs.[356,338,38]

This paper is organized as follows: in Section 3.2.2, the experimental details, the clusters, and the interaction energy calculation method will be described, along with the parameterization method for obtaining the new force field parameters describing the adsorption of CO_2 within Fe-MOF-74. The specific details regarding the classical simulations will be reported in Section 3.2.2. In Section 3.2.3, the simulated CO_2 adsorption isotherms for Fe-MOF-74 and Mg-MOF-74 will be provided and compared to experimental data and previous simulation data. Finally, in Sections 3.2.4 and 3.2.5 there will be a discussion and conclusions.

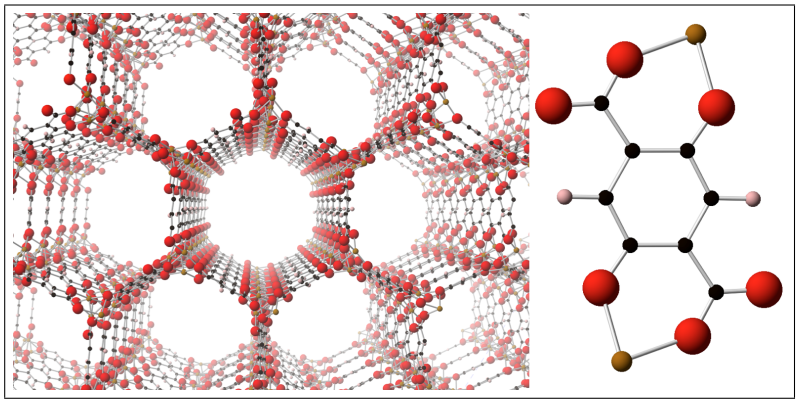

Figure 3.12: Structure of Fe-MOF-74 optimized using periodic density functional theory (DFT) with its stoichiometric unit pictured on the right. The brown atoms are iron, red are oxygen, black are carbon, and pink are hydrogen.

3.2.2 Methods

Gas Adsorption Measurements

Fe-MOF-74 was prepared and activated as reported in ref 38. For the surface area determination and low-pressure CO_2 adsorption experiments 85 mg of Fe-MOF-74 was transferred to a preweighed glass sample tube under an atmosphere of nitrogen and capped with a Transeal. The sample was then transferred to a Micromeritics ASAP 2020 gas adsorption analyzer and heated at a rate of 1 °C/min from room temperature to 160 °C. The sample was considered activated when the outgas rate at 160 °C was less than 2 μbar/min. The evacuated tube containing the activated sample was then weighed and transferred to the analysis port of the instrument where the outgas rate was again determined to be less than 2 μbar/min at 160 °C. High purity N_2 (99.998 %) and CO_2 (99.995 %) were used for the adsorption experiments. Nitrogen adsorption at 77 K indicated a surface area of 1,345 m^2/g (BET). Prior to CO_2 adsorption experiments the sample was reactivated at 160 °C. The measurements at 25, 35, and 45 °C were performed using a recirculating dewar connected to an isothermal bath. The measured experimental data in terms of excess loadings were fit to a dual-site Langmuir-Freundlich model

$$n = \frac{q_{sat,1} b_1 P^{v_1}}{1 + b_1 P^{v_1}} + \frac{q_{sat,2} b_2 P^{v_2}}{1 + b_2 P^{v_2}} \tag{3.3}$$

where n is the excess CO_2 adsorbed in mmol/g, P is the pressure in bar, $q_{sat,i}$ is the saturation capacity in mmol/g, b_i is the Langmuir parameter in bar^{-1}, and v_i is the Freundlich parameter for the two sites indicated by the subscript i. The isotherms measured at 25, 35, and 45 °C were used to compute the isosteric heat of adsorption (Q_{st}) with the Clausius-Clapeyron equation,

$$\ln P = -\frac{Q_{st}}{R}\left(\frac{1}{T}\right) + C \tag{3.4}$$

where P is pressure, n is the amount of CO_2 adsorbed, T is temperature, R is the universal gas constant, and C is a constant. The isosteric heat of adsorption was obtained from the slope of the plots of $(\ln P)_n$ as a function of $1/T$.

Quantum Mechanical Calculations

Model Structures

A neutron powder diffraction structure obtained at 4 K[38] was used as an initial structure for the geometry optimization of Fe-MOF-74 under periodic boundary conditions with the Vienna *Ab Initio* Simulation Package (VASP)[289,290,291,292] Projector-augmented wave[235] potentials that describe the interaction. between electrons in the core and valence shells[294] were used in these calculations. The Perdew-Burke-Ernzerhof (PBE) gradient-corrected, exchange-correlation functional[357] was used with a rotationally invariant, effective Hubbard U correction[358] of 5 eV on the d levels of the Fe(II) centers. This U value was chosen to reproduce the Fe(II)−Fe(II) distances and lattice parameters of the experimental structure. The PBE+U approach was previously shown to give reasonable unit cell volumes, lattice parameters, and metal-metal distances within MOFs[359,360]. The periodic DFT optimization was done using a 54 atom primitive cell of Fe-MOF-74. A gamma point optimization of the unit cell volume, lattice parameters, and atom positions was performed with an energy cut-off of 1,000 eV. The energy and force convergence criteria were set to 1×10^{-6} eV and 0.05 eV/Å, respectively.

A metal centered cluster similar to the one from ref 39 was used to calculate an interaction energy curve of CO_2 with Fe-MOF-74. This reference curve was used to optimize the Fe(II)−O(CO_2) parameters in this force field. The role of the non-central metal atoms was probed by comparing interaction energy curves upon replacement of Fe(II) by Mg(II) and Zn(II). These tests were performed to reveal whether or not the Fe(II)−O(CO_2) interaction within Fe-MOF-74 is sensitive to magnetic couplings between the metal atoms, and to see if calculations could be simplified by replacing some of the open-shell Fe(II) ions with diamagnetic ions of the same charge.

Seven other clusters were designed to model the immediate environments of the other atom types (i.e. O_a, O_b, O_c, C_a, C_b, C_c, and C_d) present in Fe-MOF-74 (see SI of ref 103). These clusters were adopted to compute the charges for these atom types, which were then used in the GCMC simulations. The positions at which the clusters were cut from the periodic DFT structure were capped with hydrogens, and the hydrogen positions were optimized using the PBE[357] functional and def2 basis sets[361,307,308] (def2-TZVP on Fe and O; def2-SV(P) on C and H) with *Turbomole* 6.4.[301]

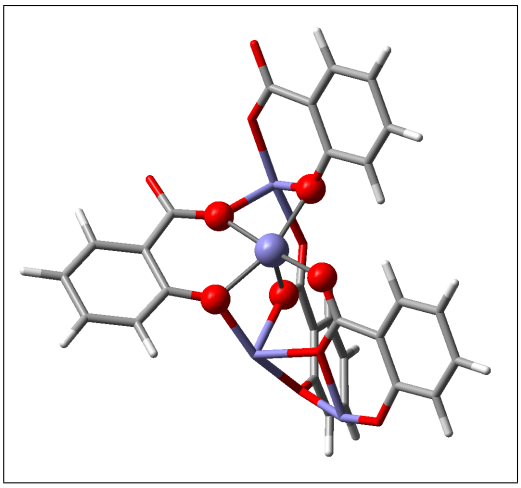

Figure 3.13: Sixty atom cluster used to model the Fe(II) ion and its ligand environment within Fe-MOF-74. Blue atoms represent iron, red are oxygen, grey are carbon, and white are hydrogen.

MOF-CO_2 Interaction Energy Curves

In this work, one of our main goals was to provide a physical description of the Fe(II) interaction with CO_2 in Fe-MOF-74. To accomplish this, we decided to probe a configuration space that contains strong Fe(II)$-$O(CO_2) interactions. The configuration space used to calculate the Potential Energy Curve (PEC) was determined by minimizing the UFF repulsion energy of CO_2 with all atoms present in the cluster except the Fe(II) ions. This was done to ensure that the interaction energies between the CO_2 and the Fe(II) ion of interest was the greatest contributor to the PEC.

The PEC was calculated with the Complete-Active Space second-order Perturbation Theory (CASPT2) formalism[362,363] using *Molcas 7.8*[364]. A quintet spin multiplicity on Fe(II) was specified based on previous experimental and theoretical work[337,38,355,348]. The four singly occupied Fe(II) orbitals for each Fe(II) ion were included in the active space of the Complete-Active Space Self-Consistent Field (CASSCF) calculations. A high-spin (16,16) CASSCF wavefunction is monoconfigurational and is thus isomorphic to a Restricted Open-shell Hartree Fock calculation (ROHF). To justify the accuracy of this active space, a (24,20) CASSCF calculation containing the five d^6 orbitals of each Fe(II) ion was performed. With this active space, the high-spin ground state had

a maximal configuration weight of 0.997 (1 would correspond to a perfect monoconfigurational state). Thus, assuming that the lowest energy d orbital of each of the four Fe(II) ions is strictly doubly occupied was valid. The high-spin (S=8) ground state of the 60-atom cluster is in agreement with previous studies indicating ferromagnetic nearest neighbor[337,38,355,365] and ferromagnetic next-nearest neighbor[355,365] interactions within Fe-MOF-74. The second-order Perturbation Theory (PT2) correction was used to capture more dynamic correlation and an imaginary shift of 0.2 Hartree was applied to prevent the occurrence of intruder states[101]. The Resolution of the Identitity (RI) and Cholesky Decomposition (CD) were used to decrease the computational cost associated with the two-electron integrals[366,367,368]. The Douglas-Kroll-Hess Hamiltonian[369,370] was used in conjunction with Atomic Natural Orbital Relativistic Core Correlated (ANO-RCC) basis sets[371,372] for the ROHF and ROMP2 calculations. The ANO-RCC Valence Double Zeta plus Polarization (ANO-RCC-VDZP) basis set was used for the central atom of each cluster, its nearest neighbor oxygen atoms, and the CO_2 atoms. The ANO-RCC Minimal Basis set (ANO-RCC-MB) was used for all of the remaining atoms. We applied a minimal basis set to the atoms not immediately bound to the central atom to reduce the computational cost, assuming that it does not significantly affect the computed interaction energies.

Basis Set Superposition Error (BSSE) was addressed with the counterpoise correction[310]. A simplified form of the equation used to compute the interaction energies is provided as eq 3.5. The explicit form of the counterpoise corrected interaction energy formula is provided in the Supporting Information (SI) of ref 103. In this work, the Fe(II) cluster pictured in Figure 3.13 was the only one for which the CO_2 interaction energy curve was calculated since in this case the interaction between CO_2 and the open-metal site provides the most important contribution to the adsorption energy.[39] The interaction energy is given by the relation

$$E_{\text{int}} = E_{\text{MOF-CO}_2} - E_{\text{MOF}} - E_{\text{CO}_2} \tag{3.5}$$

where E_{int} is the interaction energy between the MOF and CO_2, $E_{\text{MOF-CO}_2}$ is the energy of the interacting system and E_{MOF} and E_{CO_2} are the energies of the MOF and CO_2, respectively. All energies are computed in the basis of the interacting system (see SI of ref 103).

Partitioning Molecular Properties

The point charge approximation is often used in force fields employed to compute adsorption isotherms of guests interacting with MOFs, because it is computationally convenient and reasonably accurate.[373] The Localization of Properties (LoProp)[374] approach was chosen to compute the point charges. The LoProp approach was also used to extract dipoles, quadrupoles, and polarizabilities. The effects from these were included implicitly in the force field by optimizing parameters against reference data that includes these contributions. The LoProp charges were computed by using the seven clusters analogous to the ones in ref 39 (see SI of ref 103). The charge of the hydrogen atoms was chosen to neutralize the charge of the unit cell by distributing the non-zero charge between the hydrogen atoms equally.

It is often useful to partition interaction energies into multiple terms to try to understand which interactions are predominant and effectively account for more complex electron-electron interactions.[375] The Non-Empirical MOdeling (NEMO) approach[376] was used to decompose the interaction energy of the Fe(II) cluster with CO_2 into electrostatic, induction, dispersion, and repulsion terms, as provided in eq 3.6. The interaction energy was calculated using the procedure described in Section 3.2.2. The NEMO intermolecular interaction energy is decomposed as follows

$$E_{\text{int}} = E_{\text{elect}} + E_{\text{ind}} + \epsilon E_{\text{disp}} + E_{\text{rep}} \tag{3.6}$$

The electrostatic E_{elect}, induction E_{ind}, and dispersion E_{disp} terms were obtained from quantum mechanical reference calculations and the repulsion energy E_{rep} was chosen to reproduce the reference intermolecular interaction energy, as shown in eq 3.7. It is important to note that a scaling parameter ϵ was applied to force the repulsion energy to be positive throughout the configuration space. The scaling parameter on the dispersion term can to some extent be justified by considering the fact that a small basis set, like the one used in this work, does not capture the long range nature of the dispersion interaction.[377] The equations that were used to compute the explicit NEMO terms were taken from ref 378, and are reported in the SI of ref 103. The NEMO terms from eq 3.6 can be reorganized to calculate the repulsion energy as follows

$$E_{\text{rep}} = E_{\text{int}} - (E_{\text{elect}} + E_{\text{ind}} + \epsilon E_{\text{disp}}) \tag{3.7}$$

The partial atomic charges of the CO_2 molecules during the NEMO energy decomposition were set to those used in the Transferable Potentials for Phase Equilibria (TraPPE)[379] force field, since the parameters from this force field are generally considered reliable for the bulk phase of CO_2. The higher-order electrostatic, induction, and dispersion terms in eqs 3.6 and 3.7 were combined into a single attraction energy curve. The attraction and repulsion energy curves were used to optimize the force field parameters for the Fe(II)$-$O(CO_2) interaction. During the fitting of the attraction and repulsion parameters described in Section 3.2.2, the scaling factor was further considered as a tunable constant to provide better fitting agreement.

Force Fields

The effective force field to be used for molecular simulations considers a rigid MOF and rigid CO_2 molecules. We included only pairwise intermolecular interaction terms. These approximations have been used to optimize force field parameters for MOF-guest interactions previously.[375,380] The form of the force field used in this work is

$$\begin{aligned} E_{\text{int}} &= \sum_{i}^{N_A}\sum_{j}^{N_B} \frac{1}{4\pi\epsilon_0}\frac{q_i q_j}{r_{ij}} + E_{\text{attr}}(i,j) + E_{\text{rep}}(i,j) \\ E_{\text{attr}}(i,j) &= \frac{A_{ij}}{r_{ij}^6} \\ E_{\text{rep}}(i,j) &= \begin{cases} \infty & r_{ij} < r_{\text{min}} \\ B_{ij}e^{-C_{ij}r_{ij}} & r_{ij} > r_{\text{min}} \end{cases} \end{aligned} \tag{3.8}$$

where $E_{\text{attr}}(i,j)$ and $E_{\text{rep}}(i,j)$ are the attraction and repulsion energies. The q_i and q_j terms are the charges of atoms i and j. The r_{ij} term represents the distance between atoms i and j within molecules A and B, which contain N_A and N_B atoms, respectively. The vacuum permittivity is provided as ϵ_0, while A_{ij}, B_{ij}, and C_{ij} are parameters to be fitted from the NEMO decomposed, quantum mechanical reference data. The E_{attr} term contains contributions from the dipole, quadrupole, induction, and dispersion interactions. The E_{rep} term was computed by fitting an exponential function to the curve resulting from eq 3.7. The r_{min} value present in this term was chosen to prevent the Buckingham potential from going to negative infinity as r_{ij} approaches zero.

Note that during the parameterization procedure all of the pairwise interactions

besides Fe(II)−O(CO_2) between the cluster atoms and the CO_2 atoms were calculated using a point charge interaction term and a conventional Lennard-Jones potential with standard UFF parameters. To determine the Fe(II)−O(CO_2) parameters in eq 3.8, a simple grid searching method was implemented. A one dimensional array was used to minimize the deviation with respect to the reference attraction energy curve. A two dimensional array containing different ranges for the B_{ij} and C_{ij} parameters was constructed and the pair of parameters that minimized the deviation with respect to the reference repulsion energy curve was chosen. The attractive parameters (A_{ij}) and repulsive parameters (B_{ij},C_{ij}) derived from the PEC were fitted separately.

In summary, three force fields were combined to give the overall force field used in this work. The first and most important van der Waals (vdW) parameters define the vdW interaction between Fe(II) and the oxygen of CO_2. These were the parameters optimized in this work. The second set regards all other pairwise interactions between the MOF and CO_2. These parameters were taken directly from UFF since it often describes organic molecules[85] and non-bonding interactions within closed shell, closed site MOFs quite well.[84] The third set of vdW parameters was used to describe the vdW CO_2-CO_2 interactions. These were taken from the Transferable Potential for Phase Equilibria (TraPPE) force field,[379] which is a reliable and transferable force field for intermolecular interactions of CO_2 molecules. The Lorentz-Berthelot mixing rules were used for the vdW interactions.[315,316] Note that in all cases the MOF atomic point charges were computed with LoProp and the CO_2 atomic point charges were obtained from the TraPPE force field.[379]

GCMC Simulations

Adsorption isotherms of CO_2 were simulated using the GCMC technique. In the grand-canonical ensemble, the chemical potential, the volume, and the temperature are held constant. In these simulations, both the framework and the guest molecules were regarded as rigid. A 1×1×4 supercell (see SI of ref 103) was chosen to ensure that all the potentially relevant vdW interactions are consistently accounted for. The vdW interactions were damped to zero using a switching function at the cut-off radius of 12.8 Å. No tail correction was used. The electrostatic energy was computed using the Ewald summation technique. Several million configurations were sampled in each simulation.

These configurations were generated by random CO_2 translation, rotation, insertion, and deletion to obtain a satisfactory statistical average. Detailed descriptions of the parameters for the vdW interactions and the atomic charges of the framework atoms can be found in Sections 3.2.2 and 3.2.3.

3.2.3 Results

Gas Adsorption Measurements

Table 3.4: Parameters for the dual-site Langmuir-Freundlich fit of the experimental isotherm data.

	$q_{sat,1}$ mmol/g	b_1 bar^{-1}	v_1	$q_{sat,2}$ mmol/g	b_2 bar^{-1}	v_2
25 °C	8.20	4.29	1.07	0.83	0.77	4.26
35 °C	8.20	2.72	1.07	0.83	0.30	4.26
45 °C	8.20	1.77	1.07	0.83	0.21	4.26

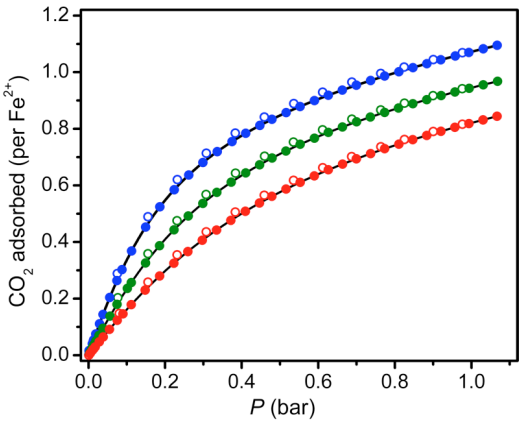

Figure 3.14: CO_2 adsorption isotherms in Fe-MOF-74 at 25 (blue), 35 (green), and 45 (red) °C, closed and open symbols represent adsorption and desorption, respectively. The continuous solid lines are the dual-site Langmuir-Freundlich fits using the parameters specified in Table 3.4.

The optimized parameters for the dual-site Langmuir-Freundlich model (eq 3.3), are reported at three different temperatures in Table 3.4. Excess CO_2 adsorption isotherms in terms of CO_2 per Fe(II) cation are reported in Figure 3.14. The CO_2 loading per

Fe(II) site increases with decreasing temperature. This is because the average kinetic energy of the CO_2 molecules allows a larger proportion of them to escape the binding wells that result from the open sites of the MOF. At a pressure of 1 bar the number of CO_2 molecules per Fe(II) site is approximately 0.80 at 45 °C, 0.95 at 35 °C, and 1.10 at 25 °C. No saturation was observed under the chosen experimental conditions. The adsorption and desorption measurements both fit closely with the dual-site Langmuir Freundlich plot at each temperature.

Structural Analysis

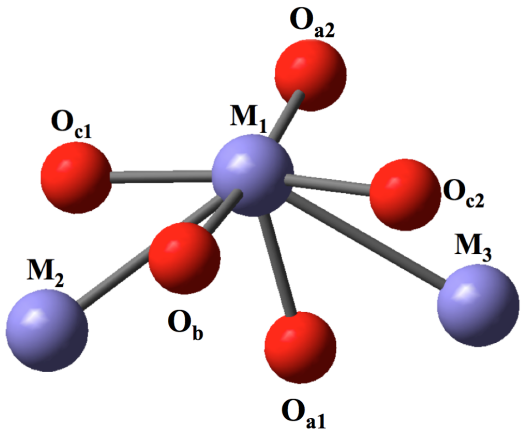

Figure 3.15: A single Fe(II) ion and its nearest neighbors within Fe-MOF-74. The O_a, O_b, and O_c labels correspond to atom types described in Section 3.2.2. M_1, M_2, and M_3 are Fe(II) ions.

The first coordination sphere of Fe-MOF-74 is pictured in Figure 3.15 and the bond distances computed with periodic DFT and the PBE and PBE+U functionals along with the Mg-MOF-74 bond distances optimized with PBE[39] are reported in Table 3.5. Table 3.5 indicates that PBE is not capable of reproducing experimentally determined metal-metal distances for Fe-MOF-74 with the present computational set-up. When a Hubbard U correction of 5 eV was used on the 3d levels of Fe(II), the metal-metal distances within Fe-MOF-74 were closer to those determined by experiment.

Table 3.5: Bond distances for the nearest neighbors of a metal ion in Fe-MOF-74 and Mg-MOF-74 computed using periodic DFT.

Bond	Fe(PBE+U)	Fe(PBE)	Fe(exp)[a]	Mg(PBE)[b]	Mg(exp)[b]
			Length (Å)		
M_1-M_2	3.00	2.80	3.00	2.94	2.94
M_1-M_3	3.00	2.79	3.00	2.94	2.94
M_1-O_{a1}	2.13	2.03	2.13	2.03	2.14
M_1-O_{a2}	2.07	2.06	2.17	2.04	2.01
M_1-O_b	2.11	2.03	2.11	2.08	2.18
M_1-O_{c1}	2.08	2.11	2.07	2.03	1.92
M_1-O_{c2}	2.07	2.04	1.99	2.03	1.86

[a]Taken from ref 38.

[b]Taken from ref 39.

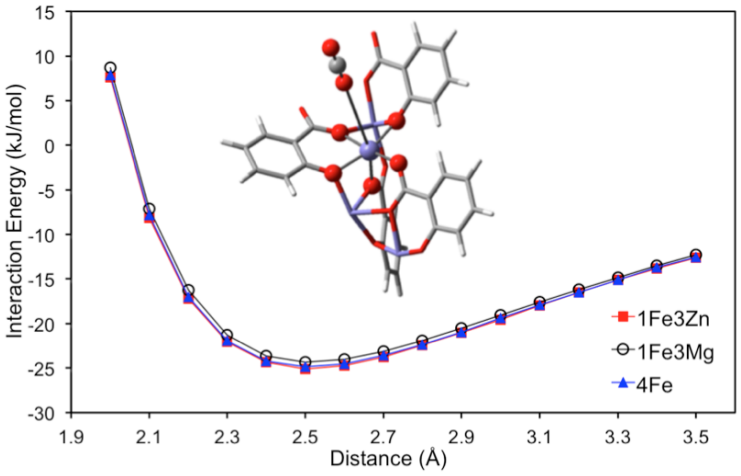

Figure 3.16: ROMP2 interaction energies computed for clusters in which the three non-central metal atoms were modeled by Mg(II) ions (black curve), Zn(II) ions (red curve), and Fe(II) ions (blue curve). A view of the CO_2 path as it approaches the MOF fragment is also provided.

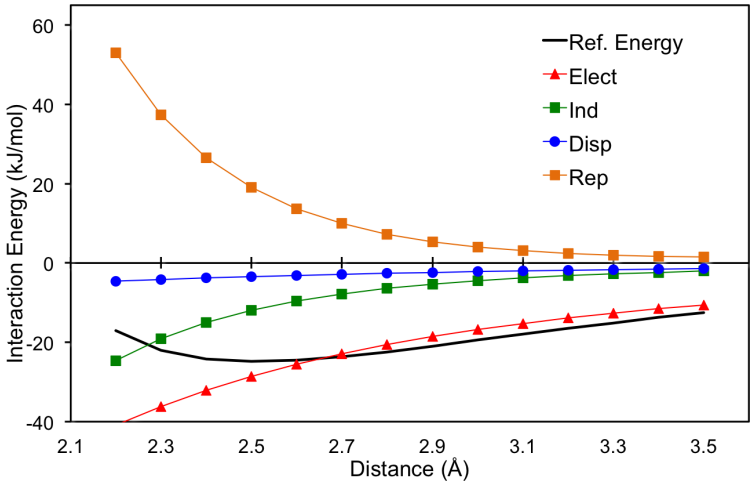

Figure 3.17: NEMO decomposition of the ROMP2 reference curve, including atomic dipole and quadrupole contributions, of the interaction of the 60-atom Fe-MOF-74 cluster with CO_2.

Interaction Energy Curves

Interaction energies for three versions of the 60-atom cluster, differing by the atoms that were used to represent the peripheral Fe(II) centers, are provided in Figure 3.16. These interaction energy curves are within 1 kJ/mol of each other in the considered configuration space. Since this deviation is within the numerical uncertainty of the method, these curves are considered to be in good agreement. We can thus state that the *1Fe3Mg* and *1Fe3Zn* models are good approximations of the *4Fe* cluster when it comes to interaction with CO_2 in the chosen configuration space. The components of the NEMO force field from Figure 3.17 indicate that, with the model and level of theory used, the dispersion contribution to the binding of CO_2 with the Fe(II) ion of interest is quite small when compared to the electrostatic and induction quantities (Figure 3.17). This finding may be ascribed to the small basis set used for the PEC calculations, which was chosen for computational efficiency. Since only the CO_2, the central Fe(II) ion, and the five oxygens coordinated to the Fe(II) had VDZP basis sets, much of the electron correlation energy is missed.

Force Fields

The LoProp charges used in the final force field and those previously used in the Mg-MOF-74 case[39] are reported in Table 3.6, and with more significant numbers in the SI of ref 103. These charges were used in the Coulombic term reported in eq 3.8. The charges obtained for Fe-MOF-74 in Table 3.6 are quite similar to the ones previously obtained for Mg-MOF-74.[39] The ligand charges are all more positive in the Fe-MOF-74 case in part because of the more negative Fe(II) ions present in the model clusters. The large difference between the hydrogen charges is due to the fact that these charges were set to neutralize the charge of the unit cell.

Table 3.6: LoProp charges for Fe-MOF-74 and Mg-MOF-74 computed with ROMP2 using the clusters provided in the SI of ref 103.

Atom	Charge	
	Fe-MOF-74	Mg-MOF-74[a]
Metal	1.51	1.56
O_a	-0.75	-0.77
O_b	-0.70	-0.71
O_c	-0.80	-0.83
C_a	0.61	0.48
C_b	-0.14	-0.14
C_c	0.23	0.19
C_d	-0.16	-0.18
H	0.21	0.39

[a]Taken from ref 39.

The result of the final fitting of the attraction and repulsion curves for the Fe-MOF-74 case is plotted in Figure 3.18. These curves indicate that the Fe(II) ion contributes more to the attraction and repulsion energy than the other atom types within this configuration space. Also, the Fe(II) ion accounts for approximately half of the total attraction energy and a higher proportion of the repulsion energy. The dispersion and repulsion curves that resulted from using other scaling factors on the dispersion energy term are provided in the SI of ref 103.

To validate further this parameterization method we applied the same methodology proposed in this work to the Mg-MOF-74 case. The Mg-MOF-74 fitting results from

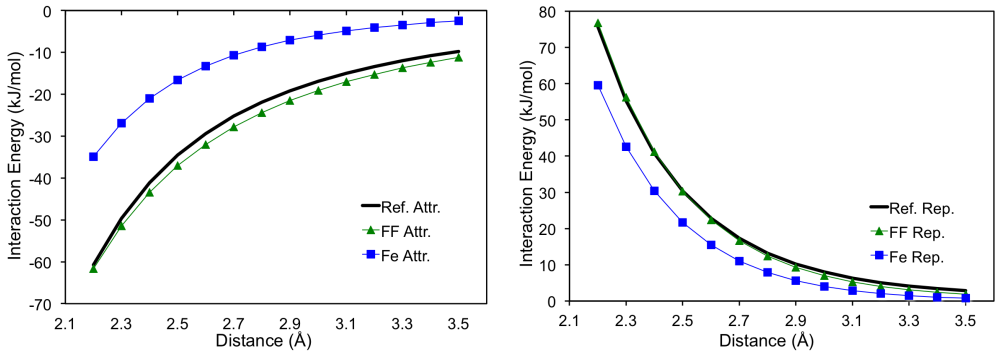

Figure 3.18: Force field fitting results for the ROMP2 interaction energies of CO_2 with the Fe-MOF-74 60-atom cluster. The attraction energy reference curve, force field fitting result, and Fe(II) contribution are reported on the left as *Ref. Attr.*, *FF Attr.*, and *Fe Attr.*, respectively. The same curves are reported on the right for the repulsion energy.

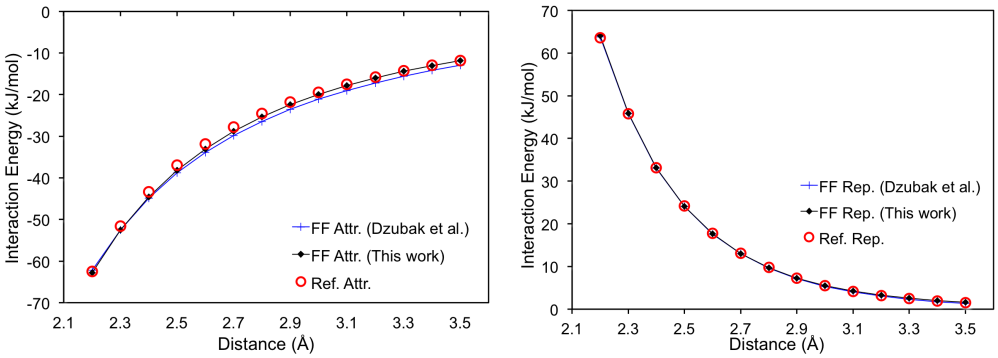

Figure 3.19: Force field fitting results for the MP2 interaction energies of CO_2 with the Mg-MOF-74 60-atom cluster. The result from fitting to the attraction energy is pictured on the left. The *Ref. Attr.* and *Ref. Rep.* lines represent the MP2 interaction energies separated into attractive and repulsive portions by NEMO. The repulsion fitting result from this work is provided on the right as *FF Rep.* along with the repulsion fitting result from Dzubak et al.[39] This fitting procedure was performed with a scaling factor of 2.0 on the dispersion term.

this work match closely previous results from Dzubak et al.[39] The force field parameters for the Fe(II)−O(CO_2) interaction within Fe-MOF-74 are reported in Table 3.7 along with the parameters used for the Mg(II)−O(CO_2) interaction. Note that these new parameters reproduced satisfactorily the reference attraction and repulsion energy curves for both the Fe-MOF-74 and Mg-MOF-74 cases (Figures 3.18 and 3.19).

The vdW interaction energy curves resulting from this work are compared to the UFF curves in Figure 3.20. The vdW contribution to the interaction energy curve of the Fe-MOF-74 cluster and CO_2 obtained with UFF is similar to the one predicted by our new force field. The minimum energy values are less than 1 kJ/mol apart and the CO_2 equilibrium positions are different by approximately 0.1 Å. For Mg-MOF-74 on the other hand, UFF cannot properly capture the strong binding of CO_2 with the Mg(II) open-metal site and thus predicts much weaker binding than the force field fitted by Dzubak et al.[39] DREIDING predicts weaker CO_2 vdW minimum energies and longer minimum energy distances than both UFF and the fitted force field from this work.

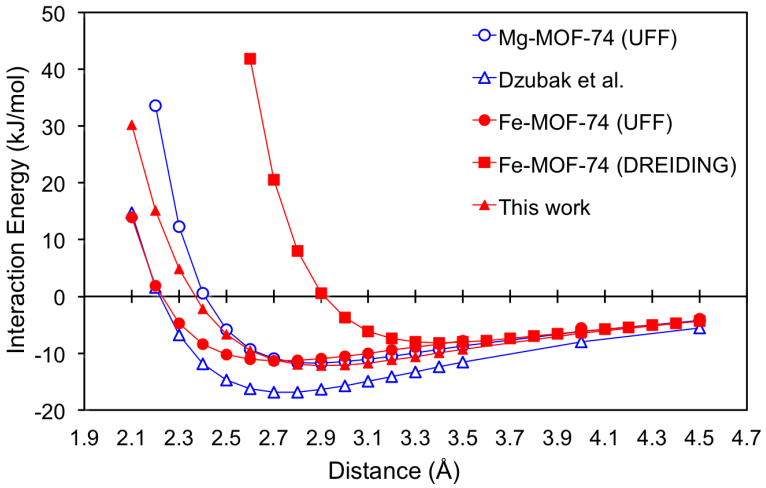

Figure 3.20: The vdW contributions to the interaction energy curves of the Mg-MOF-74 and Fe-MOF-74 cluster models with CO_2. The *Dzubak et al.* curve comes from ref 39.

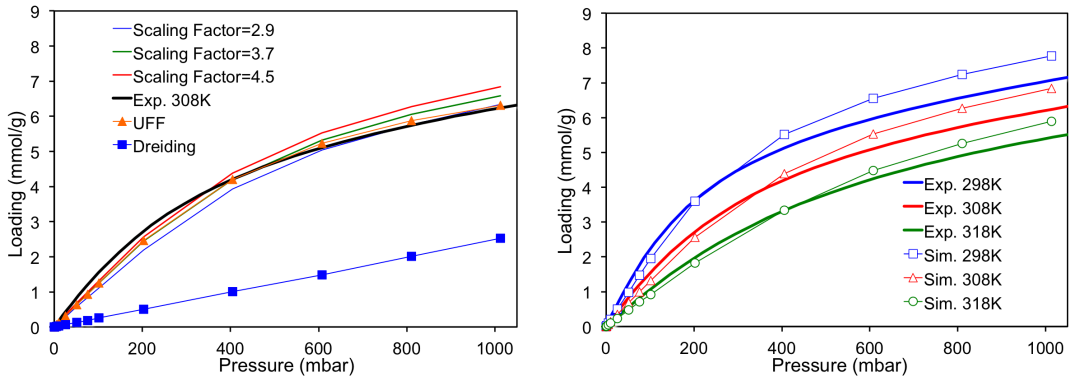

Figure 3.21: Experimental isotherm at 308 K is compared to the isotherm from the newly defined force field and the UFF and DREIDING force fields on the left. The picture on the left includes isotherms computed with different scaling factors on the dispersion term. The isotherms using the force field from this work are compared to experiment for multiple temperatures on the right.

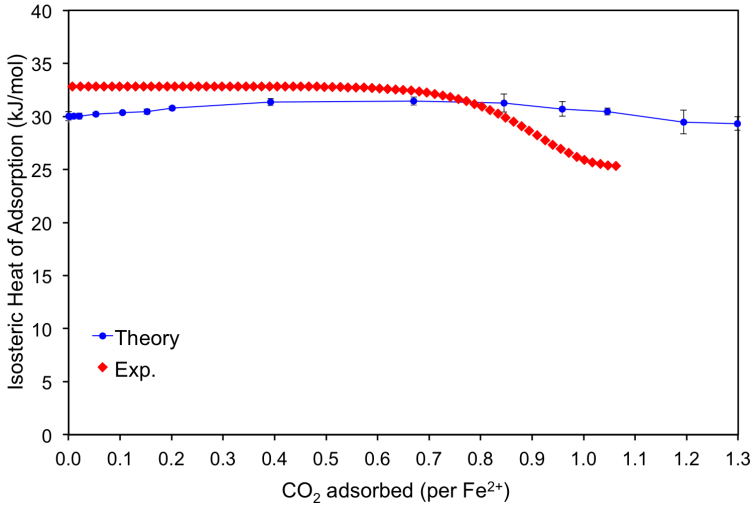

Figure 3.22: Experimental and theoretical Fe-MOF-74/CO_2 isosteric heat of adsorption curves derived in this work.

Simulation of Isotherms

The experimental and theoretical Fe-MOF-74/CO_2 isotherms generated from this work are reported in Figure 3.21 and the isosteric heat of adsorption is provided in Figure 3.22. Isotherms simulated with UFF and DREIDING are shown for comparison. The force field from this work results in isotherms that are in good agreement with the experimental isotherms of Fe-MOF-74 at multiple temperatures. Also, the interaction energy curves between the cluster model and CO_2 (Figure 3.20) agree with findings of the classical simulations. The inflection points in the isosteric heat of adsorption curves predict the point at which open-metal binding sites are saturated with CO_2. This indicates that nearly all of the open-metal sites within Fe-MOF-74 were open for CO_2 binding. There is fairly good agreement between experiment and our force field considering that it is very difficult to exactly predict the Q_{st} inflection point when there is such a small difference in binding energy between the primary and secondary binding sites within Fe-MOF-74. An extended Q_{st} plot can be seen in the SI of ref 103. To test the validity of this parameterization method, isotherms for the adsorption of CO_2 in Mg-MOF-74 were computed using the same approach. The attraction and repulsion fitting curves are reported in Figure 3.19, and are compared to the fittings from Dzubak et al.[39] The reference interaction energy curve was computed with MP2, which is numerically equivalent to the CASPT2 method with no active space. The same ANO-RCC basis sets were used for the calculation of the reference PEC of CO_2 with Fe-MOF-74 were used for the Mg-MOF-74 case. The force field parameters for the Fe(II)$-$O(CO_2) and Mg(II)$-$O(CO_2) interactions are provided in Table 3.7.

Table 3.7: Force field parameters for the Fe(II)$-$O(CO_2) and Mg(II)$-$O(CO_2) from this work in the form of eq 3.8.

Metal		Fe(II)		Mg(II)
ϵ	2.9	3.7	4.5	2.0
A (kJ/mol·Å^6)	2,083	2,932	3,777	3,616
B (kJ/mol)	317,300	164,000	99,500	191,400
C (Å^{-1})	4.040	3.664	3.373	3.815

The fitted force field result from Dzubak et al.[39] is similar to the result obtained in this work. Our force field estimates that the attraction energy between CO_2 and the Mg(II) centered cluster is slightly weaker than does the force field of Dzubak et al.[39]

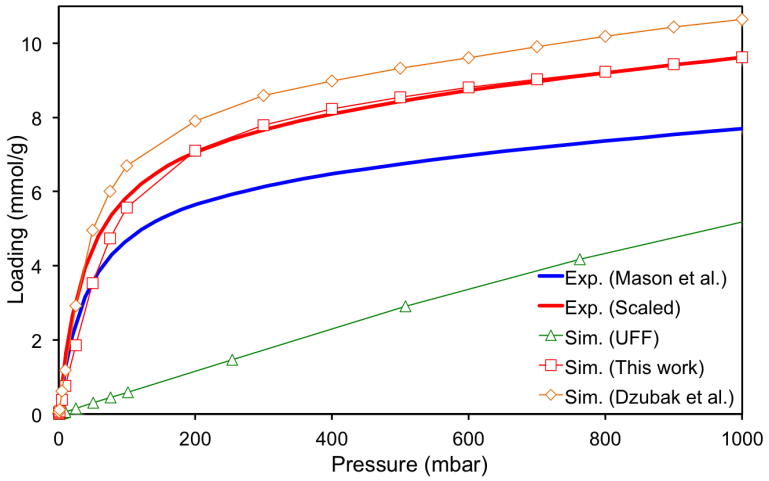

Figure 3.23: Isotherms of CO_2 adsorption in Mg-MOF-74. The experimental data was taken from ref 338 and was scaled assuming that 80 % of the sites within Mg-MOF-74 were available for adsorption of CO_2 as demonstrated by ref 39. The experiment was performed at 313 K, which was the temperature considered in each simulation.

Simulations that used these two force fields are compared to experiment in Figure 3.23. Both force fields result in isotherms that are reasonably close to experiment, while UFF significantly underestimates the loading of CO_2.

3.2.4 Discussion

Figure 3.16 demonstrates that the interaction energy is not significantly affected by the way that the peripheral Fe(II) ions are modeled, provided that the effective charge of these ions is respected. This indicates that if the non-central metals play a role in the adsorption, it is essentially electrostatic. This conclusion is in agreement with recent works that reported that the isotropic couplings between the Fe(II)−Fe(II) centers within this MOF are quite small.[337,355,365,359]

With the PBE functional, the obtained Fe(II)−Fe(II) distances in Fe-MOF-74 were found to be significantly smaller than experiment, while in the Mg-MOF-74 case, satisfactory results were obtained. Since the M(II)-M(II) distances are considered reliable experimental quantities (the positions of heavy atoms being obtained quite accurately), this shows a problem in the description of the Fe-MOF-74 electronic structure with the

PBE exchange-correlation functional. The introduction of a U correction of 5 eV led to the best reproduction of the Fe(II)−Fe(II) distances in Fe-MOF-74. Note that a Hubbard U correction typically leads to the localization of the spin density on the paramagnetic centers, and corrects the unphysical, metallic behavior often obtained with the PBE exchange-correlation functional for open-shell systems, and is thus commonly applied to these systems.[359]

The current force field reproduces experimental findings quite well. The overestimation of CO_2 loading at higher pressures is probably due to imperfections in the experimental sample that are not present in our GCMC simulation. This was the reason cited for the scaling of the experimental isotherm discussed in ref 39. The scaling of the experimental isotherm was not replicated for Fe-MOF-74 since the inflection point from the experimental data occurred at between 0.90 and 0.95 (Figure 3.22), indicating that nearly all of the metal sites within Fe-MOF-74 were open for CO_2 binding. Furthermore, the simulated Q_{st} curve did not have an obvious inflection point. However, imperfections in the experimental sample must be present even in this case, and thus such a good agreement between the two curves was not expected.

In Figures 3.21 and the SI of ref 103, the effect of the dispersion scaling factor ϵ from eqs 3.6 and 3.7 is reported. These plots demonstrate that our force field is not heavily sensitive to changes in the ϵ parameter, once it is large enough to make the repulsion energy positive within the configuration space (ϵ=2.9). Additionally, Figure 3.20 shows that UFF provides reasonable results for Fe-MOF-74 but not for Mg-MOF-74. The UFF and fitted curves are similar for Fe-MOF-74 but are quite different in the Mg-MOF-74 case. UFF clearly overestimates the repulsion energy contribution for the Mg-MOF-74 cluster/CO_2 interaction. Also of note is the large underestimation in Fe-MOF-74 cluster/CO_2 binding predicted by DREIDING. Both DREIDING and UFF use a charge equilibration model. However, the DREIDING vdW parameterization was designed to describe primarily biological molecules, while UFF was meant to be more general. UFF and DREIDING parameters were each optimized with training sets that did not include metal sites similar to those in the MOF-74 series. As such, it was somewhat expected that these force fields would perform inconsistently for these systems, since they are outside of their respective training sets. These findings indicate that commonly used force fields do not yield consistent results for the MOF-74 series.

In contrast, the force fields developed with the parameterization scheme proposed in this work do provide reasonable estimates for adsorption of CO_2 within Mg-MOF-74 and Fe-MOF-74.

The isotherm resulting from this work estimates less CO_2 adsorption than does the isotherm computed by Dzubak et al.[39] (Figure 3.23). The main differences between these two force field parameterizations is that an r^{-5} attraction term was used in the force field of Dzubak et al.[39] to improve the fitting quality, and all eight clusters pictured in the SI of ref 103 were used to compute interaction energy curves with CO_2. NEMO energy decompositions were then performed on each of the resulting PECs and pairwise parameters were optimized for the interaction of each atom type with $O(CO_2)$. In this work, only the metal$-O(CO_2)$ interaction parameters were computed and the other parameters were taken from UFF. The remaining clusters were used only to compute LoProp charges. A comparison of the resulting force field fittings is plotted in Figure 3.19. When the vdW parameters optimized with the Mg-MOF-74 oxygen and carbon atom type clusters were used, the resulting force field did not yield an accurate prediction of CO_2 adsorption within Fe-MOF-74, and it is difficult to rationalize since so many variables are present in this force field parameterization. Since UFF has demonstrated some success in cases where there is not a strong interaction between the guest and an open-metal site, we decided to use these parameters to describe the non-metal, vdW interactions between the MOF and CO_2. In this way, the laborious determination of pairwise parameters from a large number of calculations was avoided. Note that the force fields proposed in this work and those computed by Dzubak et al.[39] are both fairly system specific because the open-metal site within the MOF-74 series is unique and the structural changes that result from switching metals have non-negligible effects on CO_2 binding. These force fields, on the other hand, are less dependent on minor changes to the topology of the MOFs. The important improvement made in this work with respect to the work of Dzubak et al.[39] is the reduction in the number of quantum calculations necessary to simulate new isotherms, and the extension of the method to open-shell MOFs.

The energies computed by our new force field and the one proposed by Dzubak et al.[39] are comparable along the metal$-CO_2$ path. The Mg-MOF-74 study in this work demonstrates that the metal$-CO_2$ interaction is key to improving the prediction of

adsorptive properties within open-metal site MOFs. Furthermore, this result provides validation for the approach proposed in this work for CO_2 adsorption within Fe-MOF-74. By only optimizing the parameters for the interaction of the CO_2 oxygen atoms with an open-metal site, it is possible to provide reasonable descriptions of adsorptive properties.

3.2.5 Conclusions

High purity CO_2 was flowed through activated Fe-MOF-74 and isotherms were measured at 25, 35, and 45 °C. The dual-site Langmuir-Freundlich model provided a fairly precise fit to the experimentally determined adsorption and desorption measurements at three different temperatures. The CO_2 loading increases with decreasing temperature, and no saturation was observed under the chosen experimental conditions.

The simulated isotherms of the adsorption of CO_2 within Fe-MOF-74 using the UFF and DREIDING force fields were not consistently accurate compared with experiment. Additionally, the CO_2 adsorption within Mg-MOF-74 predicted by UFF differed from experiment by approximately one order of magnitude at low pressure. Thus, force field parameters were optimized to better describe the strong open-metal site interaction with CO_2. A CASSCF calculation was used to confirm that the Fe(II) ions within Fe-MOF-74 are in a monoconfigurational quintet state. ROMP2 was then used to compute a reference PEC, and the NEMO approach was used to partition this interaction curve into attractive and repulsive terms. The Fe(II)$-$O(CO_2) Buckingham interaction parameters were fit against these terms. The CO_2-CO_2 interactions were modeled using the TraPPE force field. The remaining vdW parameters were all taken from UFF. This was done based on the success of UFF with MOFs that do not have open-metal sites,[342,343,344] and to simplify the parameterization scheme. With this scheme a force field was derived that can accurately predict CO_2 adsorption for a MOF containing high-spin Fe(II) ions by using LoProp charges and optimizing three vdW parameters describing the Fe(II)$-$O(CO_2) interaction.

To further validate the parameterization scheme proposed in this work, the isotherm of CO_2 within Mg-MOF-74 was computed in a way that was similar to the Fe-MOF-74 case, and compared to experiment and the results of Dzubak et al.[39] The isotherm of CO_2 within Mg-MOF-74 computed in this work is in good agreement with the previously

reported experimental and computational results, suggesting that parameterizing the metal$-$O(CO_2) interactions for these two MOFs was sufficient for the simulation of accurate CO_2 adsorption isotherms. This indicates that force fields for MOFs with dominant metal-guest interactions could be parameterized quickly with this scheme. Furthermore, this method makes the computation of adsorption isotherms involving multiconfigurational states feasible.

3.3 Ab Initio Derived Force Fields for Predicting CO_2 Adsorption and Accessibility of Metal Sites in the Metal−Organic Frameworks M-MOF-74 (M = Mn, Co, Ni, Cu)

3.3.1 Introduction

Metal-organic frameworks (MOFs) together with zeolites and other nanoporous materials have attracted significant interest for various applications due to their versatility and unique properties. A large number of MOFs have been synthesized,[381] and an even greater number have been computationally predicted.[382,383] MOFs are being actively investigated, both experimentally and computationally, in relation to a series of technologically important processes such as adsorption,[384,33] catalysis,[385] and sensing.[386] One important adsorption-based application that could benefit from the use of next generation nanoporous materials, such as MOFs, is carbon capture.[33] With global climate change becoming an increasing threat, the reduction of CO_2 emissions is pivotal.[387]

Currently, the most technologically viable approach is capture of CO_2 at large stationary sources such as coal power plants.[33] One way to carry out this separation is through absorption in aqueous alkanolamine solutions.[250] This process suffers from many limitations, most notably the large energy demands for alkanolamine recovery stemming from the high heat capacity of water. MOFs, having a much lower heat capacity, could become an energy efficient alternative. This trait alone is not enough to warrant the use of MOFs. Other traits, such as thermal stability,[33] are also quite important.

Given the large number of potential materials that could be examined and the time and cost involved in performing the required experiments, integrating computer simulations and experiments offers an attractive solution. The CO_2 adsorption performance of many synthesized MOFs, hypothetical MOFs, and zeolites have been probed through large-scale, high-throughput computational studies.[388,389,390,334,391] To reduce the computational cost, these studies are performed using molecular simulations with effective molecular mechanics force fields. Although capable of identifying potentially high−performance materials, the results of these studies are limited by the quality of

the force fields used. This is a greater problem for MOFs than zeolites, because MOFs are significantly more chemically diverse, which is why generic force fields such as the universal force field (UFF)[83] provide inconsistent results for these materials.

One unique property of MOFs, which is relevant to the application of carbon capture, is that a significant fraction of these frameworks contain unsaturated metal sites. These electron deficient metal atoms can act as strong yet often reversible binding sites of small guest species such as CO_2. An example of a series of MOFs containing open metal sites is M_2(dobdc), also known as M-MOF-74 or CPO-27-M (where dobdc denotes the 2,5-dioxido-1,4-benzenedicarboxylate ligand that carries a formal charge of -4). A series of analogues have been synthesized using various metals which exhibit differences in their CO_2 adsorption performances.[202] M-MOF-74 is comprised of hexagonal, one-dimensional pores that are lined with M^{2+} ions whose open coordination sites point directly into the channel. This topology has one of the highest open metal site densities known. CO_2 interactions with open metal sites in MOFs are often poorly modeled by existing generic molecular mechanics force fields, which stipulates that parameters need to be optimized to correctly describe the unique environments present within these MOFs.[39]

Force field parametrization for nanoporous materials can be based on either experimental results[392] or quantum chemical calculations.[393] There are only a limited number of experimental isotherms throughout the literature, and they often lack reproducibility due to the differences in sample handling and preparation. Parametrization of force fields for adsorption in MOFs from first−principles calculations is therefore preferable.[393,394] There has been a series of studies that developed force fields for adsorption of various gases in MOFs which have been summarized recently in a review article by Fang et al.[393] and one by Odoh et al.[394] Dzubak et al.[39] have developed a force field capable of predicting CO_2 adsorption in Mg-MOF-74 from Møller-Plesset second-order perturbation theory (MP2) calculations. In a subsequent work, Borycz et al.[285] have used a similar approach to predict CO_2 adsorption in Fe-MOF-74. Chen et al.[395] have also successfully derived a force field for the adsorption of CO_2 and CH_4 by using a dispersion−corrected double−hybrid functional (B2PLYP−D2).

In this work we examined four isoreticular M-MOF-74 analogues, where M = Mn,[396] Co,[396,397] Ni,[396,398] and Cu,[399] and developed force fields for CO_2 adsorption in these

systems. To our knowledge, no force field parametrization for CO_2 adsorption in these MOF−74 analogues has been reported in the literature. Based on previous work,[39,285] we used quantum chemical calculations on cluster models of M−MOF−74 to obtain force field parameters for the metal−CO_2 interaction that takes place within the series. In addition, we explored the use of density functional theory (DFT) with two different functionals along with a dispersion correction as an alternative to wave function theory at the MP2 level for the computation of the relevant potential energy curves (PECs). We were able to obtain force fields that yield excellent agreement with experiments for all four materials at low loading. Note that UFF grossly underestimates the isotherms for three out of the four materials (Mn-, Co-, and Ni-MOF-74). At higher pressures, we observe a systematic overestimation for all of the materials, as previously reported for other analogues.[39,285,395] This deviation between predicted and experimentally measured isotherms in M-MOF-74 at higher pressure has been typically attributed to the inaccessibility of the pores due to either crystal defects or incomplete activation,[202,400] i.e., remaining tightly bound solvent molecules. In this work, we examined these two hypotheses by modeling adsorption in the presence of residual solvent molecules as well as blocked pore regions and have quantified the extent of the pore inaccessibility in each of these materials.

The computational details of the quantum chemical calculations, the force field parametrization, and the molecular simulations are described in Section 3.3.2. The results of this study are presented in Section 3.3.3. Section 3.3.4 offers some discussions and comparisons to experimental measurements. Finally, Section 3.3.5 contains our concluding remarks.

3.3.2 Methods

Quantum Chemical Calculations

The periodic M-MOF-74 structures were optimized using the Vienna Ab Initio Simulation Package (VASP).[227,235] The ionic positions, lattice parameters, and cell volumes of each MOF were fully relaxed with an energy cutoff of 520 eV and a 2×2×2 k-point grid. The energy and force convergence criteria were set to 10^{-6} eV and 0.05 eV/Å, respectively. All optimizations were performed with the Perdew-Burke-Ernzerhof (PBE)[70]

gradient-corrected, exchange-correlation functional together with the Grimme D3 dispersion correction (PBE-D3).[401] Density derived electrostatic and chemical (DDEC) charges were computed using these PBE-D3 optimized structures, as well as the theoretical structures computed with PBE and the Hubbard U correction (PBE+U).[358,400] This was done to see how variations of the structure of these MOFs would alter their atomic charges and adsorption capability.

Cluster models were then cut from the PBE+U structures and hydrogen atoms were used as caps, resulting in clusters that contain 60 atoms total. These model structures should be able to capture the local environment of the open metal sites. Similar clusters have been used previously to study the adsorption of CO_2 and N_2 in Mg_2(dobdc)[39] and Fe_2(dobdc).[285] A more detailed description of the cluster design can be found in ref 39.

Complete active space self-consistent field (CASSCF)[362] calculations were performed to identify the ground spin states of the unsaturated metal ions. The results show that all the central atoms are high spin (sextet for Mn, quartet for Co, triplet for Ni, and doublet for Cu), and that they are single-configurational, which is consistent with the literature.[202] Based on these results, restricted open-shell M-Plesset second-order perturbation theory (ROMP2) was used to calculate the interaction energies between CO_2 and the model clusters. This method has been successfully applied in developing a force field for CO_2 adsorption in Fe-MOF-74.[103] The ANO-RCC valence triple-ζ plus polarization (ANO-RCC-VTZP) basis set[371,372] was assigned to the central metal atom, the coordinated five oxygen atoms, and the CO_2 atoms for each cluster-CO_2 configuration. The ANO-RCC minimal basis set (ANO-RCC-MB)[371,372] was assigned for all the other atoms.

In addition to ROMP2, the PECs of CO_2 interacting with the model clusters were also calculated from density functional theory (DFT) using PBE[70] and PBE0[104] functionals. In order to account for dispersion, the D3 correction of Grimme et al.[105] was used together with the Becke-Johnson damping function.[402] It was shown recently[329] that interaction energies of H_2, CO, and CO_2 with coordinatively unsaturated metal ions calculated with the PBE0-D3 functional yield good agreement with coupled-cluster singles, doubles, and noniterative triples (CCSD(T)) energies using nonempirical interference effects.[403] To compare the binding of CO_2, methanol, and water to the M_2(dobdc) series (vide infra), geometry optimizations were performed with the PBE-D3 functional

together with the def2-TZVP[308] (guest molecule, metal atom, and its first coordination sphere) and def2-SV(P)[308] (all other atoms) basis sets. Binding energies were subsequently computed at these geometries using PBE-D3 and the def2-TZVP basis sets for all atoms.

All ROMP2 calculations were performed using the *Molcas 7.8* software package,[364] and all DFT calculations on the cluster models were performed using the *Turbomole 6.4* program package.[404] The basis set superposition error (BSSE) was corrected in both sets of calculations using the counterpoise correction[310] as described in the Supporting Information (SI) of ref 203. The noncentral metal atoms in each 60-atom model were replaced with Zn atoms to simplify the calculations, by exchanging open-shell metals for closed-shell metals that have similar interaction characteristics with CO_2. This decision was justified based on previous results[285] showing that the effect of replacing the noncentral atoms with Zn, in similar Fe-MOF-74 clusters, had a negligible effect on the MOF$-CO_2$ interaction energy.

Force Field Development

It has been demonstrated that a CO_2 molecule interacts predominately with the open metal sites in M-MOF-74. Parametrizing only the CO_2-metal interaction, while using a generic force field for the remaining interactions, is therefore sufficient for obtaining a force field capable of reproducing the experimental results.[285] We thus calculated the interaction energy along a set of configurations such that the CO_2 molecule interacted predominately with the central metal atom of our 60-atom clusters. This minimum-repulsion (MR) path was generated to include CO_2 orientations that minimize the repulsion from all cluster atoms except the central metal.[39,285] For this step the repulsive energy was calculated using Lennard-Jones (LJ) parameters for the framework atoms taken from the universal force field (UFF)[83] and the transferable potentials for phase equilibria (TraPPE) model[405] for CO_2. We sampled 18 points along this path for each M-MOF-74 analogue with distances between the closest oxygen atom in CO_2 and the metal ranging from 2.0 to 4.5 Å.

Since we only parametrized the CO_2-metal interaction versus the quantum chemical reference energies, a set of parameters for the remaining van der Waals (vdW) interactions had to be chosen. The universal force field (UFF)[83] has been extensively used

in the MOF literature and has been shown to reproduce experimental isotherms for MOFs without open metal sites with satisfactory accuracy.[406,407] In this work we have used parameters taken from UFF as well as parameters from the TraPPE force field for molecules with similar chemical environments as the organic linkers in MOF-74. More specifically for the carbon and hydrogen atoms the LJ parameters for the aromatic X(aro)−C(aro)−X(aro) (where X(aro) indicates a neighboring C(aro), N(aro), or O(aro) atom) and H−C(aro) sites from the TraPPE-EH force field[95] were chosen; for all three distinct oxygen atoms the LJ parameters were obtained by averaging the alcohol oxygen[97] and carbonyl oxygen[96] parameters from TraPPE-UA using Lorentz-Berthelot[315,316] combining rules (and rounding to the usual precision of this force field). Head-Gordon and co-workers[313] have recently computed benchmark PECs for the benzene−CO_2 dimer, and the TraPPE force field yields a binding energy of −8.9 kJ/mol; that is in very good agreement with the range of benchmark binding energies of −9.2 to −10.2 kJ/mol including zero-point-energy correction.

CO_2 was modeled as a rigid molecule, maintaining a zero dipole moment while having a considerable quadrupole moment, and LJ parameters and partial charges taken from the TraPPE force field.[405] In order to model the electrostatic interactions between the CO_2 molecules and the framework, atomic point charges were assigned to all the atoms in the system. Two methods were used to assign point charges to the framework atoms, and their effect on the isotherm was investigated. The localization of properties (LoProp)[386] scheme was used to assign point charges with the previously described clusters for the metals as well as seven other clusters centered around one of the eight atom types (excluding hydrogen). These clusters were designed as described in ref 39. In addition we computed charges from periodic DFT (PBE+U) calculations using the PBE+U optimized structures described in ref 400 with the density derived electrostatic and chemical (DDEC) charges method.[408] For both sets of charges the point charges of the hydrogen atoms were adjusted in order to neutralize the total charge of the clusters during the force field parametrization and the periodic structure during the adsorption simulations.

The CO_2-metal interaction was parametrized using the total interaction energy from the quantum chemical calculations. In order to examine the effect of the functional form of the fitted interaction, two different potential functions were tested. As in our

earlier studies,[39,285] a Buckingham exp-6 potential function was used for the CO_2 oxygen interaction with the MOF metals (O_CO_2−metal).

$$U_{\text{Buck}}(r_{ij}) = \begin{cases} A_{ij}e^{-r_{ij}B_{ij}} - \frac{C_{ij}}{r_{ij}^6} & r_{ij} \geq r_{\min} \\ \infty & r_{ij} < r_{\min} \end{cases} \tag{3.9}$$

where A_{ij}, B_{ij}, and C_{ij} are the three parameters of the Buckingham exp-6 potential specific to a pair of interaction-site types; r_{ij} and $r_{\min}$ are the distance between two interaction sites of types i and j and the minimum distance for which the Buckingham exp-6 potential is computed ($r_{\min}$ is set to 1.5 Å in this work). The C_CO_2−metal interaction was not part of the parametrization and was obtained from the TraPPE LJ parameter for the carbon atom and the UFF LJ parameter for the metal atom. In the second approach, the LJ parameters for the CO_2-metal interaction were fit to the quantum mechanical energies (i.e., LJ parameters for the metal atom were determined and the LJ parameters for both O_CO_2−metal and C_CO_2−metal were obtained using the TraPPE CO_2 model and the Lorentz-Berthelot[315,316] mixing rules).

$$U_{\text{LJ}}(r_{ij}) = 4\epsilon_{ij}\left(\frac{\sigma_{ij}^{12}}{r_{ij}^{12}} - \frac{\sigma_{ij}^{6}}{r_{ij}^{6}}\right) \tag{3.10}$$

where ϵ_{ij} and σ_{ij} are the two parameters of the LJ potential specific to a pair of interaction-site types. In both cases, the fit was performed using a grid-based parameter search followed by a least-squares minimization with the Levenberg-Marquardt algorithm as implemented in the scientific Python library SciPy. In order to ensure that the important regions of the PEC are well reproduced by the fitted interaction potential functions, a Boltzmann weighting was applied. A temperature of 500 K and the total quantum chemical reference interaction energies were used to compute this weight, which was used to multiply the energies during the fit. This procedure resulted in a satisfactory fit in all cases with the LJ potential, giving larger errors at O_CO_2−metal distances less than 2.2 Å. This can be attributed to the fact that the LJ potential has only two adjustable parameters, while the Buckingham potential has three.

Molecular Simulations

Once the potential functions for the CO_2-metal interaction were fitted, CO_2 adsorption isotherms were computed using the isobaric-isothermal (NpT) Gibbs ensemble Monte

Carlo (GEMC)[317,409] method. During a GEMC calculation both the gas and adsorbed phases are modeled in two separate boxes. For this reason, there is no need to specify the chemical potential of the sorbates by assuming either the ideal gas law or an empirical equation of state as is commonly done in a grand-canonical Monte Carlo (GCMC) simulation. All GEMC simulations were performed using the MCCCS-MN (Monte Carlo for complex chemical systems-Minnesota) software program.[318] Each calculation consisted of 5 ×104 equilibration cycles followed by 5×104 production cycles. One cycle corresponds to N Monte Carlo moves, where N is the number of molecules in the system. For all calculations, a spherical potential truncation at r_{cut} and tail corrections were used for the LJ interactions. The value of r_{cut} was set to 14 Å for the adsorbed phase and to approximately 40% of the average box length for the gas phase, with the restriction that it be no less than 14 Å. The Ewald summation with a convergence parameter, κ, of $3.2/r_{\text{cut}}$, was used to compute the electrostatic interactions.[410,88]

Throughout the GEMC adsorption calculations the framework atoms were kept rigid following the commonly used assumption that the thermal motion of the framework atoms does not affect adsorption properties. The DFT optimized unit cells were converted from triclinic to orthorhombic, and a 2×2×5 supercell was used for the simulations to ensure that the supercell fully encloses a sphere of radius rcut. For each state point the total number of CO_2 molecules in the system was kept fixed and they were allowed to swap between the bulk and adsorbed phase boxes (swap moves). The volume of the cubic vapor box was allowed to fluctuate using volume moves, and the available degrees of freedom for CO_2 were sampled using translational and rotational moves. The adsorbed loading was computed as the ensemble average of the number of CO_2 molecules in the simulation box representing the MOF. The differential heat of adsorption ΔH_{ad} is defined as the difference between the partial molar enthalpies of the bulk and adsorbed phases. The ΔH_{ad} of CO_2 in each MOF was computed using eq 3.11:[411]

$$\Delta H_{\text{ad}} = \left(\frac{\partial U^a}{\partial n^a}\right)_T - RT \tag{3.11}$$

where U^a and n^a are the internal energy of the adsorbed phase (including guest-host and guest-guest interactions) and the number of absorbed molecules, respectively, and R and T are the ideal gas constant and the absolute temperature. The derivation of eq 3.11 assumes that the molar volume of the adsorbed phase is negligible, that the gas phase is

ideal (which is true for CO_2 at room temperature and subambient pressures), and that there is no change in the sorbates intramolecular energy upon adsorption (which is also true for the rigid CO_2 model used here). The partial derivative in eq 3.11 was computed numerically from a series of GEMC simulations at different pressures. In GCMC simulations, it can also be calculated from the ensemble average of energy/particle fluctuations.[411] The absolute value of ΔH_{ad} is equivalent to the isosteric heat of adsorption obtained experimentally by measuring adsorption isotherms at different temperatures and using the vant Hoff equation.

In addition to performing isotherm calculations for the CO_2-MOF systems, we also performed calculations with solvent molecules bound to some of the open metal sites and hard spheres blocking some of the pores. This was done in order to quantify the inaccessibility of open metal sites in the MOFs we examined. Methanol (MeOH) and water were chosen as the solvent molecules to occupy the open metal sites. We optimized the configuration of a MeOH and a water molecule in the periodic unit cells using PBE-D3 (see SI of ref 203 for the corresponding binding energies). Then we used these configurations to randomly populate the open metal sites in the periodic structure using pymatgen, the open-source python library for materials analysis.[412] The super cell used for the molecular simulations contains 360 open metal sites, and thus our procedure generated 361 structures with the percentage of metal sites occupied by solvent molecules ranging from 0 to 100%. During the isotherm calculations the solvent molecules were considered rigid and fixed at the DFT optimized configurations. The TraPPE united atom model[97] was used for MeOH, and the extended simple point charge model (SPC/E) model was used for water.[413] The choice of keeping the solvent position fixed during the adsorption simulations was made here for computational efficiency and is justified by the exploratory manner of this investigation in which we also studied only one random arrangement for each fractional occupancy of the metal sites. Furthermore, the binding energies for both MeOH and water with the framework were found to be approximately twice as strong as the metal$-CO_2$ interaction and, hence, the motion of the residual solvent molecules should be rather constrained (see SI of ref 203).

We modeled the effect of pore blockage due to structural defects by a distribution of hard spheres equal to the diameter of the pores. From calculations of the isotherms for a limited set of structures containing hard spheres, we concluded that the results

are equivalent to scaling the computed isotherms for fully accessible MOFs by a fixed amount (see SI of ref 203). Therefore, we present only the scaled results here.

The accessible surface areas and volume fractions were computed using the open source code Zeo++.[414,415] A probe with radius of 1.84 Å was used to represent N_2 for the surface area calculations, which are typically used to determine these quantities experimentally, and a point probe (0.0 Å) was used to compute the free volume. Finally, 10000 Monte Carlo steps were used to sample the pore characteristics.

3.3.3 Results

Table 3.8 provides a comparison of the crystal lattice parameters obtained from periodic calculations with PBE-D3 and PBE+U. The largest relative difference between the two DFT approaches is found for r_{CoCo} for which the PBE+U value is 4% larger than the PBE-D3 value. For all four systems, the differences in the lattice parameters are less than 1%, but the unit cell volumes are systematically smaller for PBE-D3 than for PBE+U with an average deviation of 1.5%. Prior studies[285,204] indicate that the PBE+U method provides more accurate geometries and electronic structures for the M-MOF-74 (M = Mn, Co, Ni, Cu) series than PBE. Thus, the PBE+U structures were used to design the 60-atom clusters, calculate the DDEC charges, and compute the CO_2 isotherms.

Table 3.8: Lattice parameters and nearest metal−metal distances of the periodic structures obtained with different flavors of PBE.

			length (Å)			angle (deg)			
method	M	r_{MM}	a	b	c	α	β	γ	V (Å^3)
PBE+U	Mn	3.10	15.51	15.47	15.49	117.5	117.8	117.7	1453
	Co	2.96	15.29	15.28	15.28	117.7	117.8	117.8	1364
	Ni	2.90	15.16	15.16	15.16	117.7	117.8	117.8	1330
	Cu	3.01	15.25	15.25	15.25	118.1	118.1	118.1	1256
PBE-D3	Mn	3.07	15.40	15.36	15.36	117.5	117.8	117.8	1410
	Co	2.84	15.27	15.23	15.25	117.7	118.0	117.8	1345
	Ni	2.90	15.13	15.09	15.11	117.6	117.9	117.8	1315
	Cu	3.04	15.24	15.24	15.24	118.1	118.1	118.1	1250

The CO_2 binding energies, E_{M}, were calculated with ROMP2, PBE0-D3, and PBE-D3 using the 60-atom cluster models. These energies together with the experimental

heats of adsorption measured by Queen et al.[400] are listed in Table 2. All of the binding energy calculations used the PBE-D3 minimum energy configuration for CO_2, and metal-oxygen separations, rMO, for this configuration are also shown in Table 3.9 alongside the experimental values.[400] The agreement in the metal-oxygen separation values is fairly good with the unsigned percentage errors being 3.2, 8.5, 2.6, and 0.3% for Mn-, Co-, Ni-, and Cu-MOF-74, respectively. To directly compare the binding energies with the experimental heats of adsorption, one should technically account for the quantum mechanical zero-point vibrational energies, pressure-volume work, and finite temperature thermal energy corrections. However, these corrections are typically somewhere between 2 and 3 kJ/mol[416,417] and were not included here because the electronic structure calculations using the 60-atom model do not include interactions from the periodic structure. All three methods correctly predict the relative strength of the experimental heats of adsorption of CO_2 in these materials ($E_{\mathrm{Ni}} > E_{\mathrm{Co}} \approx E_{\mathrm{Mn}} > E_{\mathrm{Cu}}$). Comparing the three electronic structure methods to the experimental values, it is immediately obvious that ROMP2 yields significantly more accurate binding energies with a mean signed error (MSE) of -0.5 kJ/mol and a mean unsigned percentage error (MUPE) of 2.1%. The PBE0-D3 binding energies are too favorable for all four systems and yield MSE and MUPE of -3.2 kJ/mol and 10.4%, whereas PBE-D3 underestimates the magnitude of the binding energy in three out of four cases and yields MSE and MUPE of +2.6 kJ/mol and 8.4%. It should be noted that the binding energies are not directly comparable with the experimental heats of adsorption since they lack long-range energetic contributions. However, they are indicative of the agreement between the different levels of theory and experiments. A more direct comparison, using our derived force field, is presented in the Discussion. The CO_2 interaction energies along the MR path used for the force field parametrization are provided in Figure 3.24 for all three methods.

We examined the electron density redistribution of M-MOF-74 (M = Mn, Co, Ni, Cu) interacting with CO_2 (the density redistribution plots are shown in the SI of ref 203) and found that the electron density of CO_2 is significantly shifted when the molecule is adsorbed on the Co^{2+} and Ni^{2+} cations compared to its density when isolated. The effect is smaller on the Mn^{2+} cation, whereas the electron density of CO_2 remains almost unchanged when it is interacting with the Cu^{2+} cation. This behavior is in

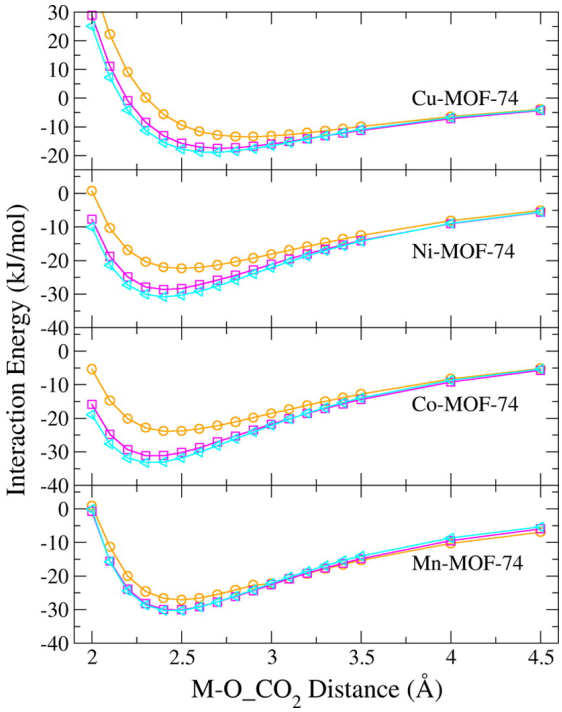

Figure 3.24: Interaction energies along the minimum-repulsion pathway for CO_2 with M-MOF-74 represented by a 60-atom cluster computed using ROMP2 (cyan triangles), PBE0-D3 (magenta squares), and PBE-D3 (orange circles).

Table 3.9: CO_2 binding energies (kJ/mol) calculated with ROMP2, PBE0-D3, and PBE-D3, compared with the experimental heats of adsorption, Q_{st}, M−O separations (Å) calculated only with PBE-D3, and corresponding experimental values.[400]

	E_M			-Qst	r_{MO}	
metal	ROMP2	PBE0-D3	PBE-D3	expt	PBE-D3	expt
Mn	−32.6	−36.3	−32.4	−31.7(1)	2.43	2.51(3)
Co	−32.9	−36.1	−29.5	−33.6(1)	2.42	2.23(4)
Ni	−39.7	−41.9	−32.3	−38.6(6)	2.35	2.29(3)
Cu	−22.5	−24.6	−21.5	−22.1(2)	2.85	2.86(3)

agreement with the calculated interaction energies (Ni > Co ≈ Mn > Cu). A bare, open metal site in MOF-74 has distorted square pyramidal symmetry, and Cu^{2+} has nine d-electrons. In this configuration, Cu^{2+} has two electrons in its d_z^2 orbital. When CO_2 approaches Cu^{2+}, the two electrons in the d_z^2 orbital enter into an antibonding orbital, which weakens the CO_2−M-MOF-74 binding. An analogous explanation for a similar system was proposed previously by Lee et al.[411]

Electron pair bonding is not expected for this range of CO_2 binding energies (≈20-40 kJ/mol); therefore the driving force of this interaction, besides electrostatic and dispersion forces, is either polarization effects or charge transfer. The redistribution of the CO_2 electron density is evidence that polarization plays a role in the stabilization of the adsorbate on the undercoordinated metal cation through ion-induced dipole interactions. Charge transfer on the other hand was not observed by Yu et al.,[202] who performed a natural bond order (NBO) analysis on CO_2 adsorbed to members of the M-MOF-74 series (M = Mn, Fe, Co, Ni, Cu, Zn). The different components of the CO_2 interaction with the framework could be fitted to either an explicitly polarizable force field or an effective potential, which implicitly accounts for these effects while remaining computationally inexpensive. As we will show in the next section, we were able to successfully capture the combination of induction and dispersion interactions by fitting the effective potentials, described under Section 3.3.2, to the quantum chemical potential energy curves, while using point charges for the electrostatic interactions.

Force Fields

The partial point charges obtained from the LoProp and DDEC methods were found to differ considerably (partial charges for all unique framework atoms in the orthorhombic unit cell are provided in the SI of ref 203). Exploratory calculations of the CO_2 adsorption isotherms using UFF parameters for the metal and both sets of charges (see SI of ref 203) were carried out in order to determine whether both of them should be used for the force field derivation. We found that LoProp partial charges resulted in an overestimation of the isotherms for Mn- and Cu-MOF-74 despite the fact that the UFF parameters for the metal likely underestimate the CO_2−M vdW interactions. DDEC partial charges on the other hand are able to model the electrostatic interactions for the M-MOF-74 systems while still allowing for a vdW component that is large enough to

be fitted for all four M-MOF-74 systems. Therefore, DDEC partial charges were used for the rest of this work. The two partial charge assignment approaches used different models for the MOF and different quantum chemical methods (cluster MP2 for LoProp and periodic DFT for DDEC), and hence, there may be multiple factors contributing to this disagreement. All of the point charges and the isotherms used to compare the effect of the charges are shown in the SI of ref 203.

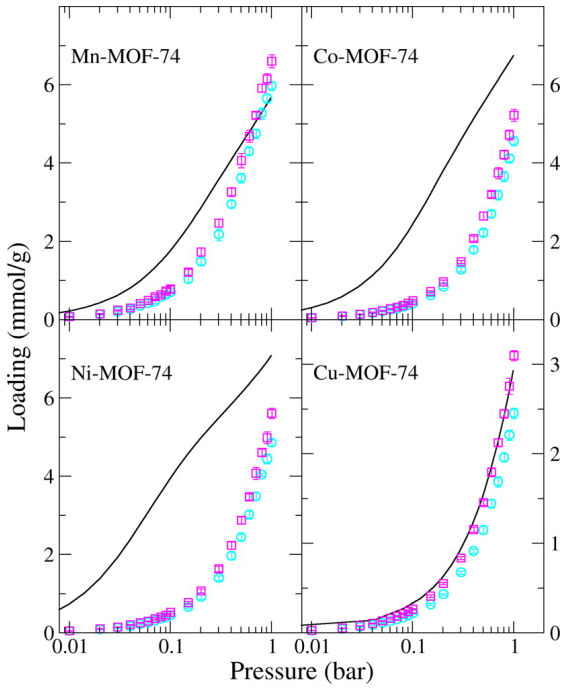

Figure 3.25: CO_2 adsorption isotherms at T = 298 K on Mn-MOF-74 (top left), Co-MOF-74 (top right), Ni-MOF-74 (bottom left), and Cu-MOF-74 (bottom right) computed using UFF (cyan circles) and TraPPE (magenta squares) LJ parameters for the organic linker combined with UFF parameters for the metal and DDEC partial charges. Experimental isotherms measured by Queen et al.[400] are also shown for comparison (black lines).

Next, we compared the effect of the LJ parameters for the organic linker that were not modified in the current parametrization procedure as described in Section 3.3.2. We computed CO_2 isotherms using the UFF and TraPPE LJ parameters combined with DDEC point charges for the organic linkers (see Table 3.10 for a list of the pertinent parameters), whereas CO_2 was represented by the TraPPE model. It should be noted

that for this preliminary investigation the LJ parameters for the metal were taken from the UFF in order to isolate the effect of the interactions with the organic linker on the isotherms. The calculated loadings are compared to the experimental isotherms in Figure 3.25. For all four M-MOF-74 analogues, we observe that use of the TraPPE LJ parameters yields sorbate loadings that are larger and closer to the experimental data than those obtained with the UFF parameters, albeit the difference between the force fields is relatively small. Thus, the TraPPE parameters were used for the remainder of this work.

Table 3.10: List of LJ parameters taken from the UFF[83] and TraPPE[95,97,96] force fields.

	UFF		TraPPE	
	σ (Å)	ϵ/k_B (K)	σ (Å)	ϵ/k_B (K)
O	3.12	30.21	3.04	86.0
C	3.43	52.87	3.6	30.70
H	2.57	22.16	2.36	25.45
Mn	2.64	6.55	–	–
Co	2.56	7.05	–	–
Ni	2.53	7.55	–	–
Cu	3.11	2.52	–	–

The PECs computed using ROMP2 together with the data for the fitted M−O parameters combined with the DDEC partial charges and TraPPE LJ parameters for the organic linker are shown in Figure 3.26. The agreement between the force fields using the Buckingham potential is excellent, whereas using the LJ potential results in a steeper repulsive wall for M−O distances shorter than 2.2 Å and slightly less favorable interactions at intermediate distances (≈3.3 Å). Although small, the inability of the LJ potential form to fully reproduce the interaction curve has a measurable effect on the adsorption isotherm, as discussed later. The fitted parameters for the Buckingham potential resulting from the ROMP2 reference energies of the CO_2−metal interaction are summarized for all four materials in Table 3.11 (and for the LJ potential in the SI of ref 203).

Since the reference energies used to fit the interaction parameters only sample a small part of the potential energy surface, we used an independent set of CO_2 configurations to validate the derived force fields. These configurations were obtained by pulling a CO_2 molecule along its minimum-energy (ME) orientation (i.e., probing the rotation

Table 3.11: List of Buckingham parameters for the M−O_CO_2 interactions, Where M = Mn^{2+}, Co^{2+}, Ni^{2+}, and Cu^{2+}, derived from fitting to ROMP2 reference energies.

interaction	A/k_B	B ($Å^{-1}$)	C/k_B ($K·Å^6$)
Mn−O_CO_2	2.68×107	3.97	2.99×105
Co−O_CO_2	1.62×107	3.81	3.69×105
Ni−O_CO_2	1.25×107	3.79	3.69×105
Cu−O_CO_2	6.44×106	3.38	2.05×105

of the CO_2 molecule) as determined using the 60-atom cluster model and the PBE-D3 method. This path was chosen to represent an energetically important part of the potential energy surface. The force field and reference curves (ROMP2) for all four systems are also shown in Figure 3.26. Again, it is clear that the LJ potential is too repulsive at short separation, but both Buckingham and LJ potentials yield comparable accuracy for the remainder of the PECs.

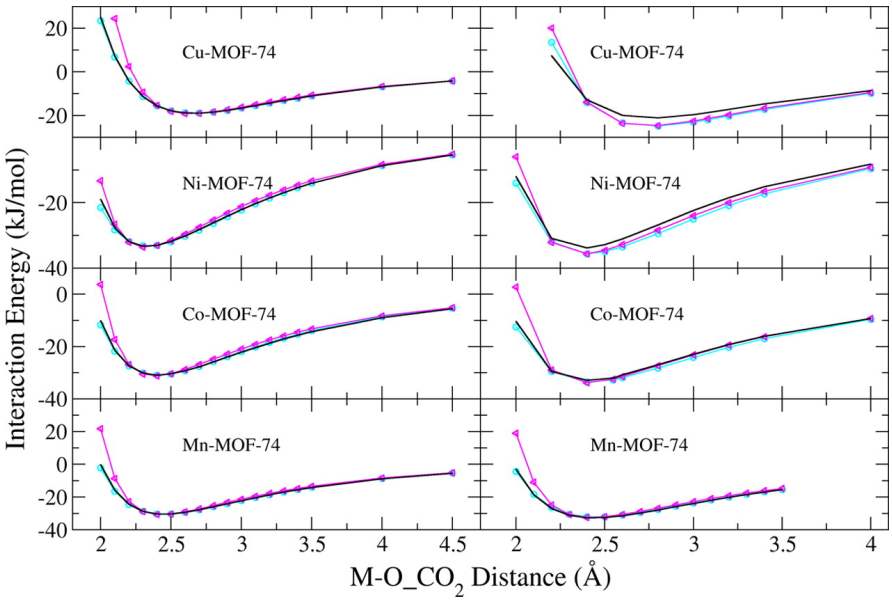

Figure 3.26: Interaction energies along the minimum-repulsion (left column) and minimum-energy (right column) pathways for CO_2 with M-MOF-74 represented by a 60-atom cluster computed using ROMP2 (black lines) together with the corresponding fits using the Buckingham (cyan circles) and LJ (magenta triangles) potentials.

Adsorption Isotherms

We used two independent experimental studies to assess the accuracy of the predicted isotherms. The first study is by Yu et al.[202] and includes CO_2 isotherms for Mn-MOF-74, Co-MOF-74, and Ni-MOF-74. The second is a more recent paper by Queen et al.[400] that provides experimental CO_2 isotherms for all four MOF-74 analogues studied in this work. Overall, the sorbate loadings reported in these two experimental studies are in very good agreement. The most notable disagreement between these studies is found for Mn-MOF-74, with the CO_2 uptake reported by Yu et al. being roughly 15% higher for all pressure points. As we will show later, this discrepancy could be due to different levels of pore accessibility between the two studies.

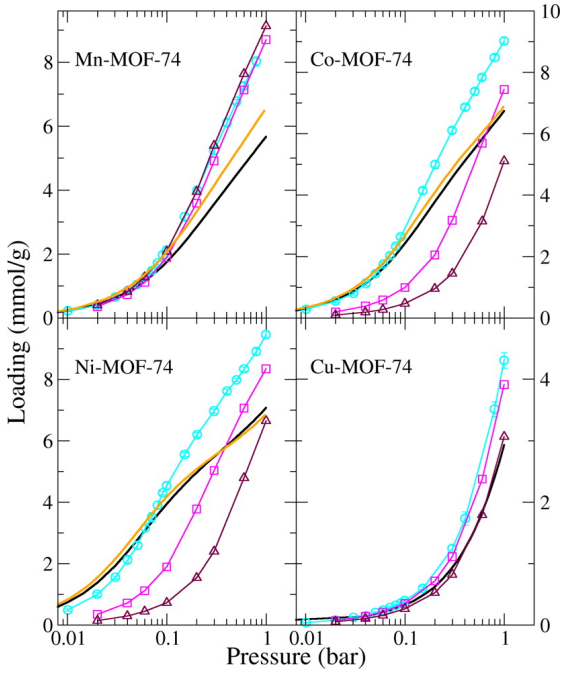

Figure 3.27: CO_2 adsorption isotherms at T = 298 K on Mn-MOF-74 (top left), Co-MOF-74 (top right), Ni-MOF-74 (bottom left), and Cu-MOF-74 (bottom right) computed using DDEC partial charges combined with Buckingham parameters derived from fitting to ROMP2 (cyan circles), PBE0-D3 (magenta squares), and PBE-D3 (maroon up triangles) reference energies. Experimental isotherms measured by Queen et al.[400] (black lines) and Yu et al.[202] (orange lines) are also shown for comparison.

Adsorption isotherms were computed initially using the Buckingham potential derived from the ROMP2, PBE0-D3, and PBE-D3 PECs in order to examine how the CO_2 uptake is affected by the choice of the quantum chemical method. These results are compared to the experimental isotherms in Figure 4. As expected from the interaction curves shown in section 2.2, the CO_2 isotherm is severely underestimated using the PBE-D3 derived force field, for Ni and Co-MOF-74, when compared to those derived from PBE0-D3 and ROMP2 PECs. The PBE0-D3 derived force field on the other hand was found to give comparable isotherms to the one derived from ROMP2 calculations for Mn- and Cu-MOF-74. It does, however, underestimate the adsorption loading considerably for Ni- and Co-MOF-74, where the CO_2-metal interactions are stronger.

Furthermore, we also calculated the CO_2 adsorption isotherms using both the Buckingham and LJ potentials derived from the ROMP2 PECs and the UFF LJ parameters for the metal centers. The resulting isotherms are shown in Figure 5 alongside the experimental results. Both potential functions with ab initio derived parameters yield similar results that are in much better agreement with the experimental data than the predictions using the UFF. In addition, both functional forms result in an overestimation of the sorbate loadings for pressures above 0.1 bar. As we will show in Section 3.3.4, this can be attributed to partial inaccessibility of the open metal sites. Because of this, we computed the mean unsigned percentage errors (MUPEs) between the computed and experimental isotherms only below 0.1 bar to assess the two functional forms, and found that the LJ potential results in systematically larger errors for all four MOFs using both experimental data sets. The MUPE using the LJ potential was found to be as much as 4 times larger for Co-MOF-74 and the experimental data of Yu et al.[202] and as little as 1.5 times larger for Cu-MOF-74 and the experimental data of Queen et al.[400] This indicates that, although small, there is a measurable advantage in employing the Buckingham potential versus the LJ potential for describing the CO_2-metal interactions. Based on these results and those comparing the effect of the quantum chemical methods, the Buckingham potentials derived from the ROMP2 PECs were used for the remainder of this work. As an aside, it should be emphasized here that the same interaction potentials were used here for both oxygen atoms of CO_2, whereas the structures show that CO_2 binds with only one oxygen atom pointing toward the metal site. Thus, another possibility would have been to fit a range-separated potential that

uses a deep but narrow well for the direct M−O interactions and switches to a regular r^{-6} potential at larger distances. However, this would considerably expand the number of parameters.

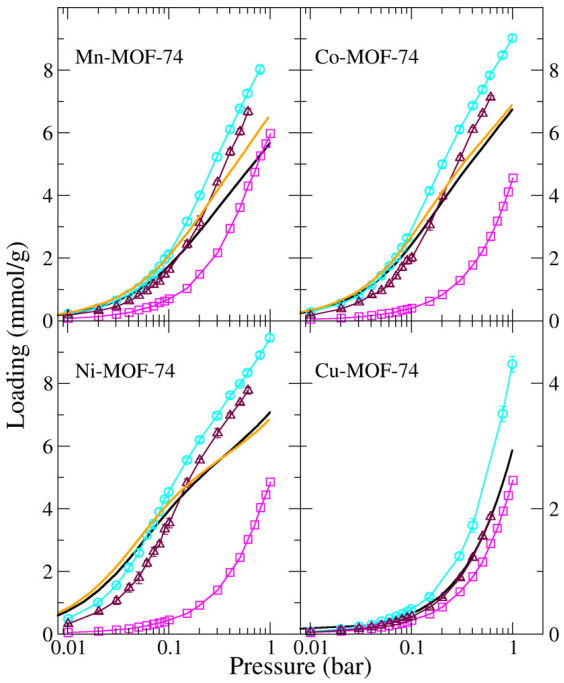

Figure 3.28: CO_2 adsorption isotherms at T = 298 K on Mn-MOF-74 (top left), Co-MOF-74 (top right), Ni-MOF-74 (bottom left), and Cu-MOF-74 (bottom right) computed using DDEC point charges combined with Buckingham parameters (cyan circles) and LJ parameters (maroon up triangles) derived from fitting to ROMP2 reference energies as well as UFF LJ parameters (magenta squares). Experimental isotherms measured by Queen et al.[400] (black lines) and Yu et al.[202] (orange lines) are also shown for comparison.

3.3.4 Discussion

We found that the Buckingham parameters, which were fit to the ROMP2 reference energies, along with the TraPPE parameters for the framework atoms (except for the metal cations) and DDEC point charges yielded the best overall agreement with the experiments, particularly at pressures below 0.1 bar. For all four MOFs, the deviation

between the experimental and computed isotherms starts small and increases with increasing loading, as seen in Figure 3.28. At the infinite dilution limit, a CO_2 molecule is only interacting with the framework atoms. Therefore, the uptake at low loading and low pressure is dictated by the strongest interaction between the framework and CO_2. For the M-MOF-74 series, this interaction is associated with the coordinatively unsaturated metal atoms. The agreement that we obtain, between experiments and simulations, at low loading indicates that we are able to accurately describe these interactions. The fact that the predicted loadings are found to be systematically higher as the pressure increases could be attributed to multiple effects. The isotherms start deviating before the open metal sites are saturated, which indicates that this apparent overestimation is not due to inaccuracies in the treatment of the strongest binding sites but is due to the unavailability of these binding sites at a lower CO_2 loading. One possible explanation could be that not all the open metal sites are accessible to CO_2 molecules during the experimental measurements. This argument has also been made in other computational[39] and experimental[400] studies, but the nature of the inaccessibility remains unclear.

Additional evidence pointing to pore inaccessibility can be deduced from the heats of adsorption. As can be seen from the data presented in Figure 3.29, the agreement between the experimental heats of adsorption and those predicted by the force fields developed here is better than the one found for the UFF. This observation is in accordance with the accurate description of the isotherms at low loading. For Mg-MOF-74, a MOF not examined in this work, a considerable drop in the experimental heat of adsorption with increased CO_2 loading was observed due to the large difference between the interaction strength with the metal site and with the organic part of the MOF.[39] For the four M-MOF-74 analogues considered here, a steep decrease in the heat of adsorption with increasing CO_2 loading is only observed for Ni-MOF-74. In contrast, the decrease is less pronounced for Co- and Mn-MOF-74. This behavior can be attributed to a smaller difference between the interaction strength of CO_2 with the metal sites and the secondary adsorption sites, and hence the two sites can be populated simultaneously. Within the pressure range of the reported isotherm for Cu-MOF-74, the open metal sites remain far from saturation and therefore the heat of adsorption as a function of loading remains flat. If we look at the loading where the heat of adsorption starts

to decline, we can see that it occurs at -0.7 CO_2/Ni^{2+}. If all sites were accessible, we would expect the decline to start after the saturation of the metal sites (1.0 CO_2/Ni^{2+}). This indicates that not all the open metal sites are accessible to the CO_2 molecules during the experimental measurement of the adsorption isotherms.

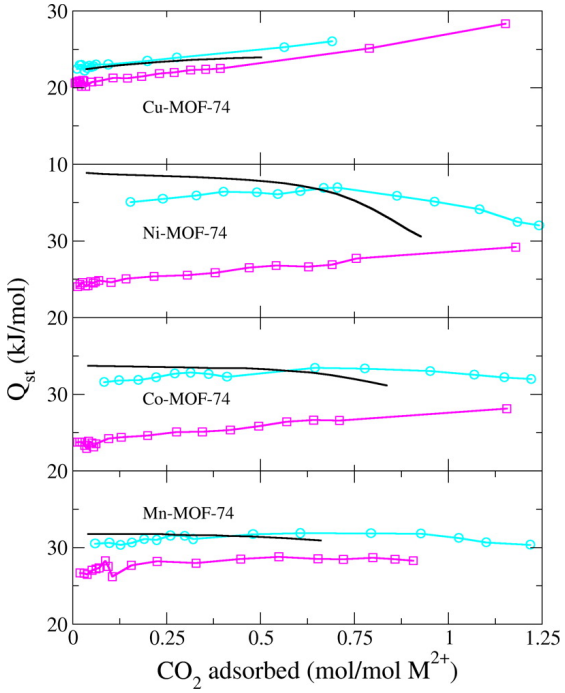

Figure 3.29: CO_2 isosteric heats of adsorption at T = 298 K computed using GEMC simulations for Mn-, Co-, Ni-, and Cu-MOF-74 using the ROMP2 derived force field (cyan circles) and UFF (magenta squares) in combination with DDEC charges. Experimental heats of adsorption taken from Queen et al.[400] are also shown for comparison.

One explanation, suggested in the literature, for the lack of accessibility in M-MOF-74 is that solvent molecules present during synthesis may have not been fully removed during the activation process.[400] Another proposed explanation is that there are structural defects that block a fraction of the pores.[400] We modeled both scenarios in order to identify the extent and nature of the open metal site inaccessibility present in the four M-MOF-74 variants. As described under Methods, we modeled pore inaccessibility due to structural defects by scaling the computed isotherms, after validating that pore blockage using hard spheres had the same effect (see SI of ref 203). For the solvent residue scenario, MeOH and water were used as solvent molecules. MeOH is commonly

used to wash the MOF crystals as the last step of the synthesis,[400] and water is also present during the synthesis[418] and as humidity in ambient air. Other solvents such as DMF and reaction intermediates could also remain in the pores. However, an extensive examination of all potential species that may be present in the pores is beyond the scope of this study.

To this extent, we generated a series of structures containing a varying number of solvent molecules attached to randomly selected open metal sites of the MOFs. An example of such a structure is shown in Figure 3.30, where 100 of the 360 open metal sites in the 2×2×5 supercell of Ni-MOF-74 are occupied by MeOH molecules. We used these solvent-containing structures and computed CO_2 isotherms as a function of solvent content for seven state points (0.01, 0.02, 0.03, 0.1, 0.2, 0.4, and 0.8 bar). These pressures were chosen so that an equal number of points below and above 0.1 bar are included to avoid biasing our conclusions.

In order to understand how the presence of solvent molecules affects the interaction of CO_2 with the MOF structures, we computed the CO_2 heat of adsorption at infinite dilution with no solvent residue and with all of the open metal sites occupied with solvent molecules. The heat of adsorption at infinite dilution is indicative of the strongest interaction between a CO_2 molecule and the framework. For all four MOFs this interaction is reduced when all the sites are occupied with MeOH. On the other hand, it is enhanced when water is the molecule attached to the open metal sites. All the heats of adsorption at infinite dilution with and without solvent molecules in the framework are provided in the SI of ref 203.

Calculated accessible surface areas and experimentally determined Langmuir surface areas have been found to be in good agreement for MOFs.[419] Comparing the two is typically used as a means of measuring pore accessibility.[202,400,256] For this reason we computed the accessible surface area and free volume as a function of residual solvent content. As expected, the effect of water on the accessible surface area and free volume was smaller than that of MeOH due to its smaller size. For example, reducing the free volume of Ni-MOF-74 by 80% requires 57% of the open metal sites to be occupied by MeOH molecules. In the case of water in Ni-MOF-74, the free volume is only reduced to ≈80% even at full occupancy of the open metal sites. Furthermore, we observed that

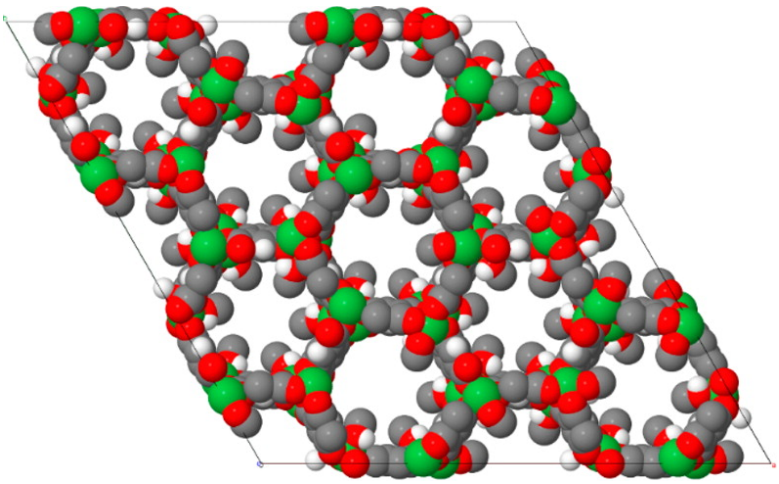

Figure 3.30: Snapshot of the 2×2×5 supercell for Ni-MOF-74 with 100 randomly distributed residual MeOH molecules.

the accessible specific surface area decreases only by about 6% for MeOH in Cu-MOF-74 and less than 3% for the other three MOFs when 30% of the open metal sites are occupied by solvent molecules. This surprisingly small effect is presumably due to a compensation between two effects: the surface area initially increases in absolute terms as the first few solvent molecules protrude into the pores while the additional mass of the solvent molecules reduces the per-gram surface area. The calculated surface areas and free volumes for structures with MeOH or water content in the pores that resulted in the best agreement with the experimental isotherms are comparable to the values derived from N_2 adsorption isotherms by Yu et al.[202] and Queen et al.[400] This result indicates that a considerable amount of residual solvent might not be detectable through surface area measurements. The free volumes and accessible surface areas calculated using Zeo++ are illustrated in Figures S6-S9 in the Supporting Information and are summarized alongside the experimentally derived values in the SI of ref 203.

We used the mean unsigned percentage error between the computed and experimental sorbate loadings as a metric of identifying the extent of the open metal site inaccessibility. Although small, the difference between the two sets of experimental isotherms is not negligible and resulted in different levels of open metal site inaccessibility. However, for generality we used the average of the experimental values from Queen et al.[400] and Yu et al.[202] for all the MOFs except Cu-MOF-74, for which only

data from Queen et al. are available. Our results for each set of experimental data are presented in the SI of ref 203. Using a different metric, such as the absolute error, for minimizing the deviation between the experimental and computed isotherms would result in different levels of pore inaccessibility as the higher pressure part with higher loadings would be given more weight. We prefer to use the percentage error in order to ensure that we strike a balance in the agreement with experiments at both the low- and high-pressure ranges. However, using the absolute error would result in predicted inaccessibility amounts that differ by less than 10%.

We quantified the amount of MeOH required to be present in the pores in order to best reproduce the experimental results. In all three cases, except Cu-MOF-74, we find a fairly broad region of MeOH content that yields statistically indistinguishable fits of the experimental data. Our results, which are illustrated in Supporting Information, Figure S4, indicate that about (34 ± 5)%, (26 ± 4)%, and (24 ± 5)% of the metal sites in Mn-, Co-, and Ni-MOF-74, respectively, may be inaccessible due to residual MeOH molecules (see SI of ref 203). The computed isotherms for the optimal amount of MeOH in the pores are shown in Figure 8, demonstrating that MeOH residue could be a plausible explanation for these MOFs. Specifically, the observation that ≈25% of the open metal sites in Co-MOF-74 are not accessible agrees well with available neutron diffraction data which show a maximum occupancy of 0.73(2) for CO_2 in Co-MOF-74.[400] The occupancy of CO_2 was not determined for the other analogues examined in that work.

The presence of water in the pores creates a more complicated situation with two competing effects acting at the same time. On one hand, the CO_2 interaction with the framework is enhanced by the presence of water in the pores that leads to an enhancement of the CO_2 uptake. On the other hand, the reduction of free volume tends to limit the uptake by reducing the density of highly favorable adsorption sites. In addition, since we are comparing to gravimetric measurements, the adsorption is further reduced due to the additional mass of the water molecules. For Ni-MOF-74, the MUPE can only be reduced down to 22%, for a water content of ≈23%, while the MUPE for the empty framework is 27% (see SI of ref 203). For Mn-MOF-74 and Co-MOF-74 a large fraction of the metal sites needs to be occupied by water for the MUPE between the experimental and calculated data to be minimized, that is, ≈46% for the former

case and ≈88% for the latter case (Supporting Information, Table S4). In both of these cases the minimum MUPEs achieved were larger than the equivalent residual MeOH loadings. Overall, the assumption that water is present in the pores does not appear to be a satisfactory explanation for any of the MOFs considered here.

The available experimental isotherm for Cu-MOF-74 differs from the other isotherms as it remains linear within the pressure range that is reported. This means that the open metal sites do not become saturated, and therefore it is difficult to fully assess the extent of open metal site inaccessibility. Moreover, based on the computed binding energies, neither MeOH nor water molecules are expected to remain in the pores of Cu-MOF-74. The MeOH-Cu^{2+} interaction energy, calculated using PBE-D3, is −46.1 kJ/mol and the water−Cu^{2+} interaction energy is −39.0 kJ/mol (see SI of ref 203), which are ≈30 kJ/mol smaller in magnitude than those for the other M-MOF-74 analogues and comparable to the strongest interaction of CO_2 in these MOFs. MeOH in the pores of Cu-MOF-74 was able to only reduce the MUPE from 27%, for the empty framework, to 20% when approximately 75% of the open metal sites were occupied, which is unlikely based on the relatively weak interaction of MeOH with the framework. In addition, at this MeOH content the CO_2 heat of adsorption is overestimated, resulting in a higher uptake at lower loadings (see SI of ref 203). Any water content in the pores of Cu-MOF-74 resulted in an increase of the uptake. This was because the CO_2−water interaction is considerably larger than the CO_2−Cu^{2+} interaction. The heat of adsorption at infinite dilution is 10 kJ/mol higher for the water containing structure compared to the empty structure (see SI of ref 203).

Assuming pore inaccessibility due to structural defects and using the same procedure as before, we estimated that (22 6)%, (19 2)%, (19 ± 6)%, and (22 ± 7)% of the pores are inaccessible for Mn-, Co-, Ni-, and Cu-MOF-74 (see SI of ref 203). Yu et al.[202] also reported high-pressure CO_2 adsorption isotherms up to 50 bar for Mn-, Co-, and Ni-MOF-74. When extending our computed isotherms using the optimum computed MeOH content and pore blocking, we found the agreement to extend up to the highest pressure range (see SI of ref 203).

It is important to note that MeOH in the pores of Mn-, Co-, and Ni-MOF-74 leads to a better agreement with experiments than assuming pore blockage, with the minimum MUPEs being up to 4 times smaller (see SI of ref 203). The reason for this is that

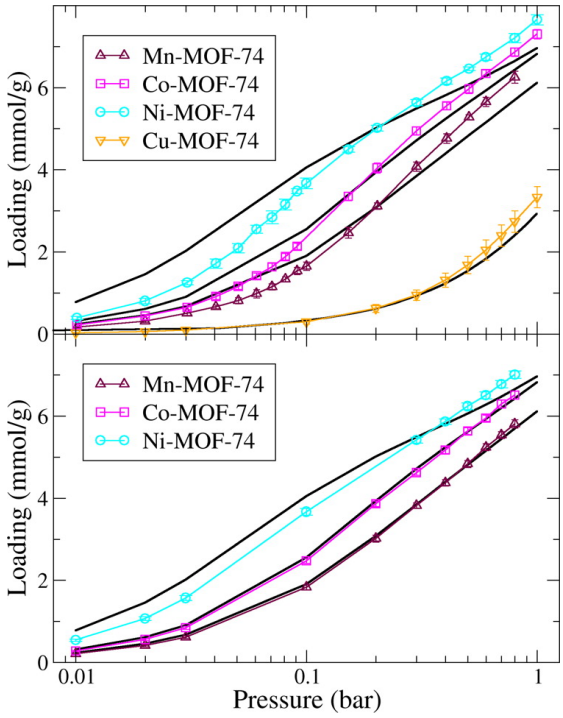

Figure 3.31: CO_2 adsorption isotherms at T = 298 K for Mn (cyan circles), Co (magenta squares), Ni (maroon up triangles), and Cu (orange down triangles) computed with the optimal residual MeOH content in the pores (bottom), or percentage of pores blocked (top). For the case of Cu-MOF-74 only the pore blocking case is shown as no amount of residual MeOH resulted in good agreement with experiments. The experimental isotherm for Cu-MOF-74 from Queen et al.[400] as well as the average value of the experimental isotherms measured by Queen et al.[400] and Yu et al.[202] are also shown for comparison as solid black lines.

the assumption of pore blockage leads to a uniform reduction of the isotherm. This is also the reason that it can be approximated by scaling the isotherm by a fixed amount. On the other hand, MeOH in the pores reduces the higher pressure loading without affecting the lower pressure uptake significantly and therefore a better agreement with experiments can be achieved for both pressure regimes. This effect can be seen in Figure 3.32, where we have plotted the adsorption isotherms normalized by the experimental values. We can see that both the pore blockage and MeOH residue scenarios lead to similar agreement with the experimental results for pressures over 0.1 bar. However, at lower pressures, pore blockage leads to a considerable and systematic underestimation of the experimental isotherms. The improved agreement with experimental results is also reflected in the heat of adsorption when computed for the fraction of residual MeOH molecules or pore blockage that best reproduces the experimental isotherms. The decline of the heat of adsorption with increased loading agrees better with experiments (see SI of ref 203).

It is reasonable to assume that crystalline defects act together with residual solvent to limit the adsorption uptake in these MOFs. We computed the MUPEs, using the average of experimental isotherms,[202,400] as a function of both pore blockage and metal sites being occupied by MeOH for Mn-, Co-, and Ni-MOF-74 (see SI of ref 203). We found that for all cases the deviation is minimized for the case of purely solvent induced inaccessibility. This is due to uniform reduction of the isotherm over the pressure range when pore blockage is assumed. However, there is a series of combinations that result in comparable MUPEs and the difference in the level of agreement obtained for each scenario is small relative to the uncertainty coming from our calculations and the experimental results. A small increase ($\approx$1 kJ/mol) in the CO_2 binding energy with the open metal sites obtained from the electronic structure calculations would significantly increase the loading in the Henrys law region and allow the pore blocking scenario to result in a better agreement with experiments than the residual MeOH scenario. In addition, the predicted residual MeOH content in each MOF is not in accordance with the relative interaction strength of MeOH with the MOFs (see SI of ref 203). For example, at the PBE-D3 level, MeOH is computed to bind more weakly to Co-MOF-74 than to Ni-MOF-74 by about 8 kJ/mol, but comparable amounts of residual MeOH are proposed here for these MOFs. In conclusion, although it is clear from our analysis that

a considerable number of the metal sites in all four MOFs are not accessible to adsorb CO_2, we cannot ascertain which effect or combination of effects acting together is more plausible.

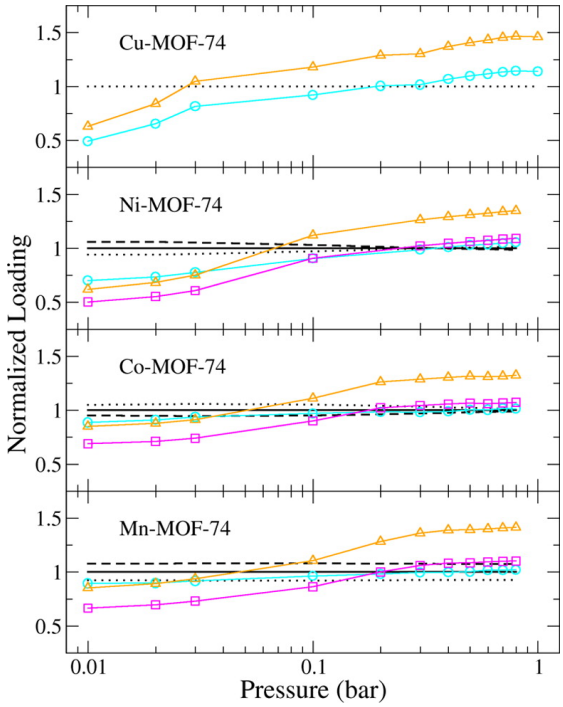

Figure 3.32: Computed CO_2 adsorption isotherms at T = 298 K normalized by their experimental counterparts. Results are shown for Mn-, Co-, Ni-, and Cu-MOF-74 using empty frameworks (orange up triangles), frameworks with optimal number of residual MeOH molecules in the pores (cyan circles), and assuming optimal extent of pore blockage (magenta squares). The normalized experimental results by Queen et al.[400](dotted black line) and Yu et al.[202] (dashed black line) as well as their average value (solid black line) are also shown for comparison.

3.3.5 Conclusions

We extended our previous efforts[39,285] of deriving force fields for CO_2 adsorption from first-principles calculations in MOFs containing open metal sites to four M-MOF-74 analogues, where M = Mn, Co, Ni, and Cu. Using the derived force fields, we computed adsorption isotherms with NpT GEMC simulations and were able to obtain consistently good agreement between our computed isotherms and experimental results. We found

that the best agreement was given when restricted open-shell MP2 calculations were used to parametrize the CO_2−metal interactions, and the DDEC method was used to compute point charges. PBE0-D3 calculations yielded agreement with experiments for Mn- and Cu-MOF-74, whereas PBE-D3 underestimated the isotherms for all four materials.

Our force field appears to capture the CO_2−metal interactions in these four M-MOF-74 analogues based on the agreement between the computed and experimental isotherms at low loadings. At higher loadings, however, a systematic overestimation of the experimental results is observed. We attribute this overestimation to the lack of accessibility of the open metal sites encountered in experimental measurements. In addition, we have used our derived force field to quantify the effect of metal site inaccessibility assuming two possible causes: residual solvent molecules and structural defects causing pore blockage. We used MeOH and water as potential residual solvent molecules based on their availability during synthesis as well as difference in size and interaction strength between these molecules and CO_2. A MeOH content occupying about 25% of the open metal sites results in the best agreement between the computed and experimental adsorption isotherms for all the MOFs except Cu-MOF-74. On the other hand the majority of the open metal sites, and in some cases all the open metal sites, would need to be occupied with water in order to reproduce the experimental isotherms. This indicates that water is an unlikely source of pore inaccessibility in these MOFs. However, the intrusion of water either from incomplete activation or as trace impurity in the adsorbate feed has been suggested in order to explain measurements in cationic zeolites.[420] A pore blockage of roughly 20% for all four MOFs yields good agreement for pressures over 0.1 bar but also leads to a systematic underestimation of the loading at lower pressures. Thus, the overall deviations are higher than those achieved with MeOH molecules attached to the open metal sites. Finally, we have demonstrated that a combination of residual solvent molecules and crystalline defects present in the structures could also explain the lower CO_2 uptake observed in experiments.

Our force field parametrization scheme requires a limited number of quantum chemistry calculations while maintaining a simple form for the potential functions and yields a force field that is able to capture the adsorption behavior in the four MOFs we examined, whereas generic force fields, like UFF, significantly underestimate the loading.

This is accomplished primarily by parametrizing only the CO_2-metal interaction while using a set of parameters taken from the TraPPE force field for the remaining interactions. Although we used cluster calculations to obtain reference energies for the force field parametrization, our approach can be easily extended to periodic DFT calculations. This would obviate the step requiring the generation of cluster models, which is not easy to mechanize, and allow the force field parametrization of open metal containing MOFs at a large scale. On the other hand, cluster models allow for wave function based calculations, which would not be affordable with a periodic model.

Chapter 4

Experimental and Computational Characterization of Zr_6 and Hf_6 Based MOFs for Catalysis

4.1 Defining the Proton Topology of the Zr_6-Based Metal-Organic Framework NU-1000

4.1.1 Introduction

Over the past two decades, considerable attention has been drawn to the powerful attributes of metal-organic frameworks (MOFs) given their structural, as well as chemical, versatility and hence tailorability.[421,254,381] Because of their crystalline nature, unambiguous structural determination is often possible for MOFs; this in turn has facilitated precise mechanistic studies[422,41,423] and in the most favorable cases predictive materials discovery.[424,382] Recently, a new class of MOFs containing octahedral Zr_6 clusters and multitopic carboxylate linkers ($R-(CO_2^-)_n$, $n = 2, 3, 4$) has emerged.[425,110,426] Profiting from strong coordination bonds between the hard acid-hard base interactions of the Zr^{IV} atoms and carboxylate oxygens, Zr_6-based MOFs exhibit exceptional thermal (up to 500 °C),[425] chemical (e.g., from pH 1−pH 11),[427] and even mechanical stability.[425,428] Given these properties, Zr_6-based MOFs have been investigated for several applications including gas sorption,[429,430] catalysis,[431,432,433,434] heavy metal capture,[435,436] sensing,[427] ionic conductivity,[437] toxic industrial chemical capture,[438] and water sorption.[426]

An intriguing subclass of Zr_6-based MOFs are built up from 2D Kagome sheets of eight-connected $[Zr_6(\mu_3\text{-}O)_8(O)_8(H)_16]^{8+}$ nodes bridged by tetra-carboxylate linkers ($R-(CO_2^-)4$); an example of this topology is shown in Figure 4.1.[110,111,439,45] Such a connectivity gives rise to 3D structures with −OH containing (i.e., −OH or $-OH_2$, vide infra) functional groups pointing into exceptionally large 1-D mesoporous channels. As a result, this class of Zr_6-based MOFs has been particularly susceptible to a variety of postsynthesis modification schemes. Examples include metalation at the organic linker,[110] metalation at the nodes via Atomic layer deposition In a Metal-organic framework (AIM),[45] and organic functionalization at the node via Solvent-Assisted Ligand Incorporation (SALI).[108,440] To date, these postsynthesis modified materials have facilitated catalysis,[111,45] enhanced CO_2 adsorption,[108] and been susceptible toward secondary organic functionalization.[440]

Despite the intriguing nature of these frameworks, a less well understood aspect is the precise proton topology of these eight-connected Zr_6 nodes. That is, it has been

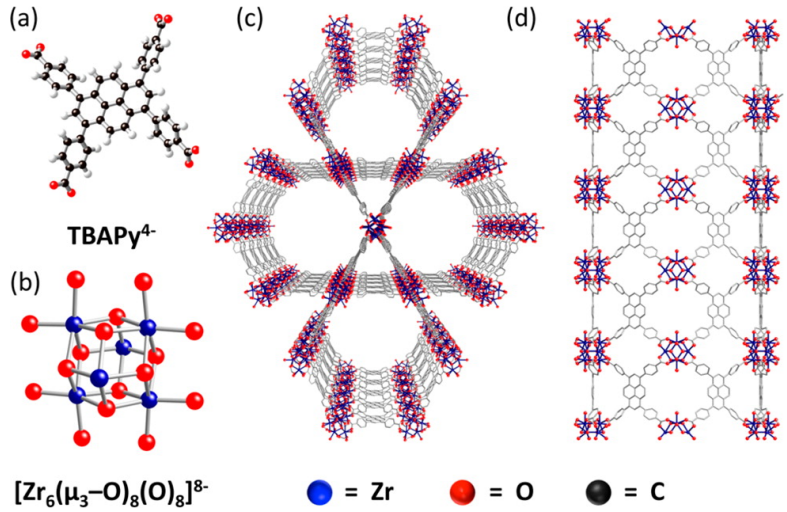

Figure 4.1: 1,3,6,8-Tetrakis(*p*-benzoic acid)pyrene linker, $TBAPy^{4-}$ (a) and the $[Zr_6(\mu_3\text{-}O)_8(O)_8]^{8-}$ node (b) of the Zr_6-based framework NU-1000 (c and d). Note that the linkers are not shown in the representation of the node, and the hydrogens are not shown in the framework representations for clarity.

difficult to assign precisely where the 16 protons (needed for charge balance) reside in the $[Zr_6(\mu_3\text{-}O)_8(O)_8]^{8-}$ node. As an example, both Morris et al. (MOF-545) and Feng et al. (PCN-222) synthesized tetra-carboxylate porphyrin containing Zr_6-based frameworks.[110,111] Based on single-crystal X-ray diffraction, Morris et al. assigned the 16 protons as eight terminal H_2O molecules ($[Zr_6(\mu_3\text{-}O)_8(H_2O)_8]^{8+}$), while Feng et al. assigned the protons as bridging and terminal $-$OH groups[45] ($[Zr_6(\mu_3\text{-}OH)_8(OH)_8]^{8+}$).[a]

Given the ambiguities associated with locating protons in single-crystal structural analysis, we recently utilized IR spectroscopy to obtain data consistent with the presence of both terminal and μ_3-bridging $-$OH groups in tetracarboxylate pyrene-based Zr_6 MOF NU-1000.

Herein we use a combined quantum mechanical and experimental approach to rigorously assign the proton topology of our recently synthesized Zr_6-based framework, NU-1000. We find that the Zr_6-based node of NU-1000 actually comprises a staggered mixed proton topology, namely $[Zr_6(\mu_3\text{-}O)_4(\mu_3\text{-}OH)_4(OH)_4(H_2O)_4]^{8+}$. En route to this

[a] It is worth noting that compared to the fully saturated $Zr_6(O)_8(H)_4(RCO_2)_{12}$ containing nodes such as the UiO series, the $Zr_6(O)_8(O)_8(H)_{16}(RCO_2)_8$ containing nodes in NU-1000 exhibit a significant degree of complexity with respect to their proton topology.

mixed proton topology, we ruled out five additional proton topologies. This is the first time a mixed $-OH$, $-OH_2$ composition has been observed for a symmetric Zr_6-based node, which we suspect will be of paramount importance for understanding the reactivity (e.g., in AIM and SALI), conductivity, and catalytic activity of these unique materials.

4.1.2 Methods

Periodic Systems

Starting from the known experimental single-crystal X-ray structure, the periodic structures for NU-1000-OH, NU-1000-OH_2, and NU-1000-MIX-X (Figure 4.2 where X = S, L, C, and E) were fully optimized using periodic density functional theory as implemented in the Vienna Ab Initio Simulation Package (VASP)[226,290,289,227] employing the generalized gradient approximation exchange-correlation functional PBE.[441,70,104] The VASP calculations use projector-augmented wave potentials to describe the interaction between core and valence electrons. A plane-wave kinetic energy cutoff of 520 eV was used, and the integration over the irreducible Brillouin zone was carried out using the gamma point. The energy convergence cutoff was 1×10^{-6} eV. Atomic positions were relaxed until the forces were lower than 0.05 eV $Å^{-1}$ including accounting for Pulay stress.

Cluster Model

We extracted from the optimized periodic structures of NU-1000-OH, NU-1000-OH_2, and NU-1000-MIX-X (X = S, L, C, and E), corresponding model clusters having the general formula $[Zr_6(\mu_3\text{-}OH)_8(OH)_8(PhCOO)_8]$ (OH-Node), $[Zr_6(\mu_3\text{-}O)_8(OH_2)_8(PhCOO)_8]$ (H_2O-Node) and $[Zr_6(\mu_3\text{-}O)_4(\mu_3\text{-}OH)_4(OH)_4(OH_2)_4(PhCOO)_8]$ (MIX-Node-X; X = S, L, C, and E). These clusters were designed to maintain an overall neutral charge for the model system as well as to preserve a good representation of the first coordination sphere of the Zr_6 oxo-metalate node in the periodic structure. We note that the $TBAPy^{4-}$ linkers (1,3,6,8-tetrakis(*p*-benzoate)pyrene) have been replaced with benzoate ($PhCOO^-$) groups having their carbon atoms constrained to corresponding positions of the $TBAPy^{4-}$ framework.

Two-step constrained geometry optimizations were performed for these clusters. In the first step, all of the aromatic H atom positions were optimized (since one is not present in the periodic structure) while all of the other atoms were held fixed. In the second step, the 6 Zr, 16 O, 16 protonating H^+ nuclei, and the four carboxylic COO^- functionalities were allowed to relax in the presence of the fixed linker fragments so as to mimic the solid-state framework.

Cluster Calculations

DFT cluster calculations used the M06-L[183] density functional as implemented in the *Gaussian 09* software package.[185,442] An ultrafine grid (99 radial nodes and 590 angular nodes) was used to perform numerical integrations. An automatic density-fitting set generated by the Gaussian program was used to reduce the cost for calculations done with the local density functional M06-L. The 6-31G(d,p)[443] basis set was used for H, C, and O, while the Stuttgart [8s7p6d1f | 6s5p3d1f] ECP10MDF contracted effective core potential basis set (SDD)[443,444] was employed for Zr. Single-point calculations were performed with the 6-311+G(df,p)[443] basis set for H, C, and O and the SDD basis set for Zr. The SMD[445] continuum solvent model was employed to account for solvation with water as a solvent. The nature of all stationary points was verified by analytical computation of vibrational frequencies; IR spectra were computed employing a scale factor of 0.939 for fundamentals.

Materials

All compounds and solvents were used as received unless otherwise noted: 1,3,6,8-tetrakis(*p*-benzoic acid)pyrene was synthesized as previously described,[45] acetone (Macron, 98%), benzoic acid (Aldrich, 99.5%), N,N-dimethylformamide (DMF) (Macron, 99.8%), hydrochloric acid (Aldrich, 37%), $ZrOCl_2 \cdot 8H_2O$ (Aldrich, 98%).

Instrumentation

Diffuse reflectance infrared spectra (DRIFTS) were recorded on a Nicolet 7600 FTIR spectrometer equipped with an MCT detector. The detector was cooled with liquid N_2. The spectra were either collected under Ar atmosphere or in a KBr mixture under

N_2 purge. KBr or NU-1000 (difference spectra) were utilized as background spectra. Powder X-ray diffraction (PXRD) measurements were carried out on a Bruker MX $I\mu$S microsource with Cu Kα radiation and an Apex II CCD detector. The samples were mounted in capillaries as powders in a glovebox, sealed with epoxy, brought out of the glovebox and placed on a goniometer head. The data were collected on an area detector with rotation frames over 180° in Φ and at 2θ values of 12, 24, and 36° being exposed for 10 min at each frame. Overlapping sections of data were matched, and the resulting pattern was integrated using Brukers APEX2 phase ID program. The powder patterns were treated for amorphous background scatter. Thermal gravimetric analysis (TGA) was performed on a Mettler Toledo TGA under N_2 flow and heated from room temperature to 700 °C (at 10 °C min^{-1}).

Synthesis of NU-1000

NU-1000 was synthesized as a microcrystalline powder using a slightly modified procedure to that previously published.[45] Briefly, 0.097 g of $ZrOCl_2 \cdot 8H_2O$ (0.30 mmol) was weighed out into a 6-dram vial and 2.7 g of benzoic acid was subsequently added. The solids were dissolved via sonication in 8 mL of DMF and placed in an oven at 80 °C for 1 h. After 1 h the solution was taken out of the oven, allowed to cool, and then 0.040 g of H_4TBAPy was added into the vial and sonicated until a homogeneous yellow suspension was obtained. The yellow suspension was placed in an oven at 100 °C for 24 h and then the mother liquor was decanted. The resultant yellow powder was washed with 10 mL of DMF three times over the course of 24 h. Centrifugation (7000 rpms for 5 min in Eppendorf tubes) was utilized to separate the liquid and solid phases in between washings. The solid was resuspended in 12 mL of DMF and 0.5 mL of 8 M HCl was added to the solution and swirled. The vial was placed in the oven at 100 C for 18 h and then removed. Again the mother liquor was decanted, and the yellow powder was washed three times with 10 mL of DMF over the course of 24 h and then 10 mL of acetone three times over the course of 24 h. Prior to physical measurements the samples were activated under dynamic vacuum at 120 °C until a vacuum level of $\leq$0.002 mmHg min^{-1} was reached. PXRD, TGA, and N_2 adsorption isotherms corroborated many of

the previously reported structural details regarding NU-1000[45] (Figure 4.1).[b]

Diffuse Reflectance Infrared Fourier Transform Spectroscopy (DRIFTS)

For the room temperature measurements approximately 0.5 mg of sample was gently ground and mixed with 20 mg of finely ground KBr. For the temperature-dependent measurements approximately 0.03 g of sample was gently ground and placed in a Harrick praying mantis cell. The cell was cooled in a liquid ice bath. The temperature was increased to the desired temperature, and the spectra were monitored until no further changes were observed. Subsequently, the sample was cooled back down to 25 °C, and the spectra were monitored until no further changes were observed. All reported spectra were collected at 25 °C.

D_2O Exchange Experiments

NU-1000 (0.015 g) was placed in 2 mL of D_2O for 72 h. The solution was decanted and replaced three times over the course of the experiment. Subsequently, the D_2O was exchanged with d_6-acetone (three times over the course of 24 h). Finally the d_6-acetone was removed under dynamic vacuum overnight at 100 °C.

4.1.3 Results and Discussion

Probing the Proton Topology of NU-1000 via Quantum Chemical Calculations

To ensure neutrality of the $[Zr_6(\mu_3\text{-}O)_8(O)_8(RCO_2^-)_8]^{16-}$ node, 16 protons were placed in three distinct oxygen-based environments of NU-1000. The results are schematically summarized in Figure 4.2 (top) and yield the following structural isomers: (i) the −OH

[b] We previously reported the DRIFTS of NU-1000 and tentatively assigned the observed vibrational stretches at 3674 cm^{-1} and 3655 cm^{-1} as terminal and μ_3 bridging −OH stretches. This assignment would be consistent with the NU-1000-OH topology. Re-examination of our DRFTS data in light of the computational and experimental efforts described herein, revealed that the stretch at 3655 cm^{-1} is highly susceptible to trace amounts of weakly bound solvent molecules (likely H_2O, but potentially DMF or acetone molecules that are present as a result of the synthesis NU-1000) that can be removed from the system at 120 °C. A comparison of a NU-1000 DRIFTS spectra taken immediately after activation at 120 °C under dynamic vacuum, to one taken after sitting under ambient atmospheric conditions is shown in the Supporting Information. Clearly the stretch at 3655 cm^{-1} was removed under these activation conditions.

isomer, $[Zr_6(\mu_3\text{-}OH)_8(OH)_8]^{8+}$ (periodic; NU-1000-OH and cluster; OH-node); (ii) the $-$OH2 isomer $[Zr_6(\mu_3\text{-}O)_8(H_2O)_8]^{8+}$ (periodic; NU-1000-OH_2 and cluster; H_2O-Node), and (iii) the -MIX isomer exhibiting the formula $[Zr_6(\mu_3\text{-}O)_4(\mu_3\text{-}OH)_4(OH)_4(H_2O)_4]^{8+}$ (periodic; NU-1000-MIX and cluster; MIX-Node). In the MIX-node case, there are four additional tautomers which have been labeled by referring to the relative position of the four μ_3-OH ligands which could be staggered (MIX-Node-S), eclipsed (MIX-Node-E), lop-sided (MIX-Node-L) or contiguous in opposite corners (MIX-Node-C) as illustrated in Figure 4.2.

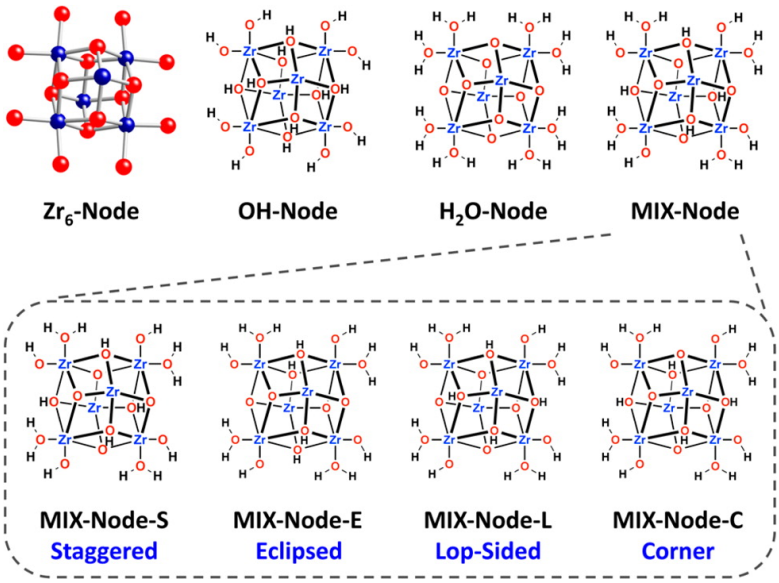

Figure 4.2: Top, schematic representation of the three structural isomers (OH-Node, H_2O-Node, and MIX-Node) considered herein. Bottom, schematic representation of four conformers considered for the MIX-Node isomer. The aromatic carboxylate linkers have been omitted for clarity.

We performed quantum chemical calculations with both periodic and cluster models under different geometry constraints to compute the relative energies for each isomer. The unit cell parameters for NU-1000-OH, NU-1000-OH_2, and NU-1000-MIX-X (X = S, E, L, and C), as well as the parameters from single crystal X-ray diffraction, are listed in the supplementary information (SI) of ref 446. As shown in Table 4.1, the relative energies from the constrained cluster optimizations are in good agreement with the energies from the periodic calculations (average deviation over 7 structures is 10 kJ/mol,

Table 4.1: Relative energies (kJ·mol^{-1}) for the constitutional isomers and conformers studied herein.[a]

NU-1000- or model-node topology	ΔE periodic	ΔE cluster[b,c]	ΔG cluster[b]
-OH	350	334 (214)	299
-OH2	274	274 (218)	236
-MIX-Node-S	0	0 (0)	0
-MIX-L	249	255 (145)	235
-MIX-C	139	154 (105)	150
-MIX-E (30)[d]	122	146 (106)	150
-MIX-E (8)[d]	140	153 (107)	147

[a]Full geometry optimizations were performed by periodic calculations employing PBE and constrained optimizations were performed with cluster models using M06L/SDD(Zr)|6-311+G(df,p)(C,H,O)//M06L/SDD(Zr)|6-31G(d,p)(C,H,O) DFT functional.
[b]Restrained Ph ring positions.
[c]Values in parentheses include continuum aqueous solvation effects.
[d]The E isomers differ with respect to orienting the core protons either into the 30 or 8 Å pores of NU-1000.

which is less than 7% of the typical average energy relative to MIX-Node-S). Notably, when the atomic positions of all atoms in the cluster models were allowed to relax, the agreement between the cluster and periodic calculations for the relative energies of the different isomers was degraded. This highlights the importance of including constraints imposed by the periodicity of the system when analyzing cluster models representing the nodes of MOFs.

Regardless of the chosen computational method or constraints, the MIX-Node-S topology, $[Zr_6(\mu_3\text{-}O)_4(\mu_3\text{-}OH)_4(OH)_4(H_2O)_4]^{8+}$, is predicted to be the thermodynamically most stable structure. For example, in the gas phase (i.e., activated), MIX-Node-S is 299 kJ mol-1 more stable in free energy than the OH-node and 236 kJ·mol^{-1} more stable than the H_2O-node. This structure is also predicted to have the highest density of all computed structures, and its predicted unit cell volume of 22960 Å^3 compares well with the experimental value of 23005 Å^3.

An intriguing feature of the MIX-Node-S conformer is its hydrogen-bonding (H-bonding) motifs, for example the O1−H2$\cdots$O2 motif shown in Figure 3. To assess the degree to which the O1−H2$\cdots$O2 hydrogen bonding confers stability on MIX-Node-S,

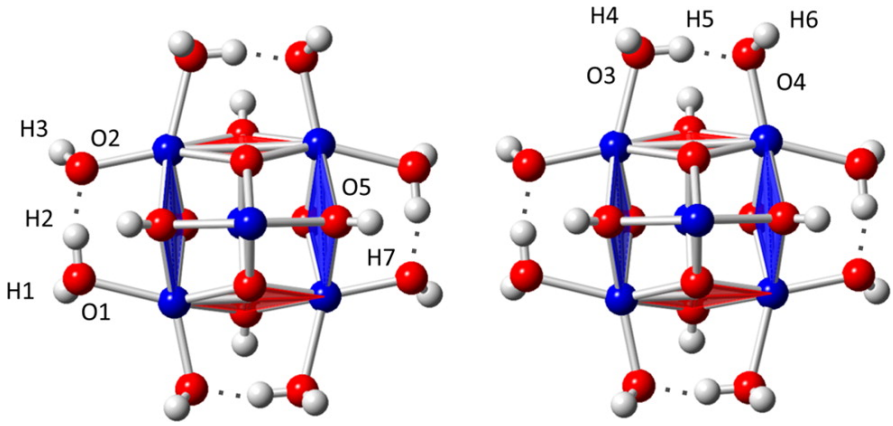

Figure 4.3: Atomic labels for several key stretching frequencies of the MIX-Node-S topology of NU-1000. The blue tetragonal faces point into the large mesoporous channels of NU-1000 (Figure 4.1c), while the red tetragonal faces point into the channels between the Kagome lattices (Figure 4.1d).

the hydrogen bonds were broken through rotation of the aqua ligands about the Zr−O bond. The optimized structure with one such hydrogen bond broken is predicted to be 44 kJ/mol higher in electronic energy than the MIX-Node-S geometry; this difference can be taken as an upper bound for the relevant H-bond strength. Breaking all four H-bonds in this fashion raises the energy by 167 kJ/mol, which is still smaller than the energy difference between the MIX-Node-S and H_2O-Node topologies (i.e., 274 kJ/mol, Table 4.1). Hence, the MIX-Node-S topology with all four H2$\cdots$O2 H-bonds broken is still more stable than the H_2O-Node by about 107 kJ/mol. This quantifies the importance of H-bonding in stabilizing the MIX-Node-S cluster, which we suspect may affect the reactivity, conductivity, and catalytic activity of NU-1000 and potentially other Zr_6-based MOFs. To our knowledge, this is the first mixed $-OH$ and $-OH_2$ ligand motif proposed in the literature for a symmetrical Zr_6-based node. It is notable that mixed proton topologies have been proposed for asymmetric Zr_6-based nodes,[427] although no direct evidence for such a composition has been provided to date.

Considering additional factors that contribute to the stability of the MIX-Node-S topology, we examined oxygen partial charges computed from Charge Model 5[99] (CM5, chosen for its accuracy in reproducing electrical multipole moments, its ready applicability to all atoms in the periodic table, and its insensitivity to basis set). Interestingly,

in the MIX-Node-S isomer, the charges on the O atoms are extremely uniform, being on average 0.667 au with a standard deviation of 0.052 au. By contrast, the O atoms in adjacent μ-oxo bridges in the cores of other MIX isomers have CM5 charges near 0 au (SI of ref 446). The staggered (S) arrangement of protons on the core thus appears to permit optimal polarization of the Zr−O bonds consistent with the different electronegativities of the two atoms. Yang et al. have undertaken similar analyses of bonding and charge densities to rationalize the structures and stability of the Zr_6 MOFs UiO-66, -67, -68, and analogues.[447]

Finally, while gas-phase results are of interest for understanding the properties of the activated MOF, and for comparison to the dry IR spectra described below, it is also informative to consider the effects of aqueous solvation, as estimated from SMD continuum solvent calculations. As the higher energy isomers are less stable owing to electrostatic interactions less favorable than those found in the MIX-Node-S topology, it is unsurprising that solvation levels the energetic landscape (Table 4.1, ΔE values in parentheses in column 3). Nevertheless, the MIX-Node-S topology remains more than 100 kJ/mol more stable than any other.

Computational and Experimental IR Spectra

One attractive method to interrogate the proton topologies of NU-1000 is via IR spectroscopy. Given the agreement between the periodic calculations and the cluster approximations, as well as the significant reduction in computational cost, the vibrational frequencies for the OH-Node, H_2O-Node, and MIX-Node-S proton topologies were calculated utilizing the cluster models in order to compare against experiment. Again, the positions of the atoms in the aromatic rings were kept fixed during geometry optimizations, and therefore their vibrations (arising from the $TBAPy^{4-}$ linker) are not observed in the theoretical IR spectra. The experimental IR spectrum − collected as diffuse reflectance spectra− for NU-1000 is shown in Figure 4.4 (bottom). A noteworthy feature of the experimental spectrum is a series of absorptions that are found below the C−H stretching region between 2400 and 2850 cm^{-1} as illustrated in Figure 4.4 (top).

Considering now results from the theoretical calculations, the key vibrational signatures for the OH and OH2 ligands of the theoretical OH-Node and H_2O-Node topologies are cataloged in Table 4.2 together with several of the key experimental data. In the

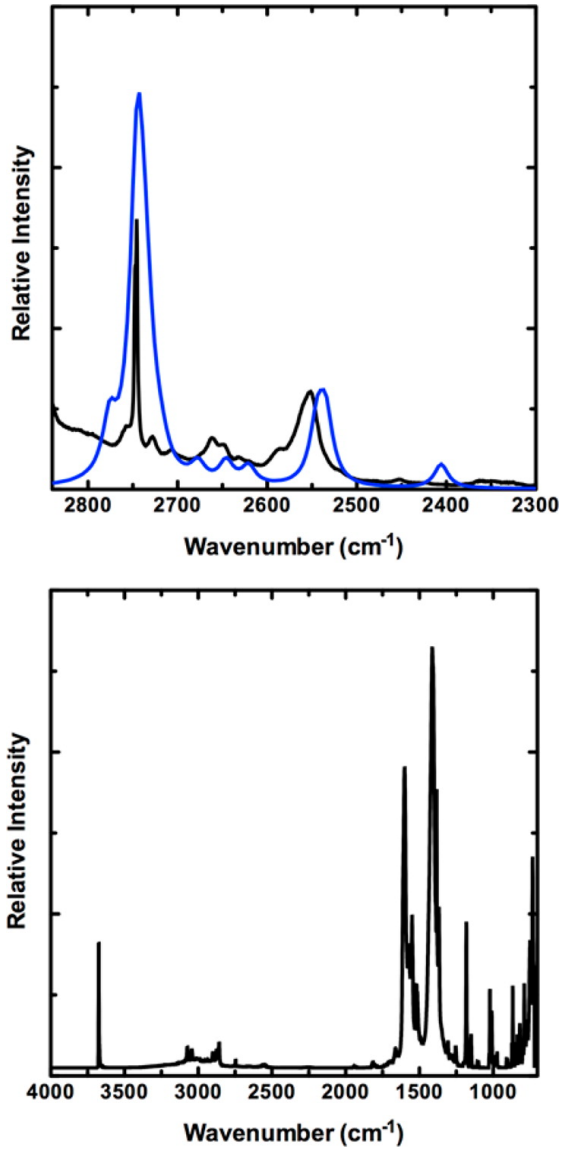

Figure 4.4: Full experimental DRIFTS spectra of NU-1000 (below) and highlights (above) of the H-bonded H_2O and $-OH$ regions from 2300-2850 cm^{-1} for experiment (black) and theory summed over 4 isomers (blue; see text for details).

theoretical spectra for these two nodes, a number of peaks between 3600 and 3800 cm^{-1} are predicted corresponding to the bridging and terminal $-OH$ and $-OH_2$ stretching frequencies for each topology. Any or all of these might reasonably be assigned to correspond to the experimental peaks observed from 3672-3674 cm^{-1}. Importantly, however, no peaks in the region 2400-2900 cm^{-1} are predicted for either the OH-node or H_2O-node topologies.

For the global minimum MIX-Node-S topology shown in Figure 4.3, by contrast (top line in each row of 4 in the MIX-Node-S column of Table 4.2), in addition to high frequency peaks corresponding well with experiment, there are absorptions predicted from 2727 to 2754 cm^{-1}, corresponding to O-H stretches in hydrogen-bonded bridges between aquo and hydroxo ligands, that are in quite reasonable quantitative agreement with the experimental absorptions at 2745 and 2747 cm^{-1}. No peak, however, is predicted at lower frequency that might correspond to the experimentally observed absorption at 2551 cm^{-1}.

This observation led us to consider the possibility that other low energy MIX-Node-S isomers, i.e., MIX-Node-S topologies having alternative arrangements of aquo and hydroxo ligands, might be present at equilibrium such that the experimental spectrum may be a composite of their various individual spectra. By considering proton transfers from aquo to hydroxo ligands, and rotations of aquo ligands to reorient the non-hydrogen bonding proton of the -OH2 unit, we identified 3 other isomers, ranging in energy from 8.4 to 10.0 kJ/mol above the global minimum (details in SI of ref 446), and their predicted IR spectra are included in the additional rows in the MIX-Node-S column in Table 4.2. One of them (the third row) does indeed have absorptions predicted in the range from 2552-2589 cm^{-1}. As we do not expect our DFT calculations to be accurate enough to predict the Boltzmann population of isomers to better than about $\pm$10 kJ/mol accuracy, we have used a direct comparison to the experimental spectrum to estimate the proportions, and Figure 4.4b includes a simulated spectrum assembled as 41% of the global minimum, and 9%, 16%, and 34% of the minor isomers in rows 2, 3, and 4 of the MIX-Node-S column in Table 4.2, respectively. As can be observed, the agreement between theory and experiment is overall quite reasonable.

Thus, qualitative comparison of the experimental DRIFTS spectrum to the theoretical IR spectra effectively rules out the OH-Node and H_2O-Node topologies. The

Table 4.2: Key vibrational modes for the theoretical OH-Node, H_2O-Node, and MIX-Node-S topologies along with the observed experimental vibrational modes for NU-1000 and their corresponding assignments.[a]

	wavenumber (cm^{-1})			vibrational description
OH-Node theory	H_2O-Node theory	MIX-Node-S theory[b]	experimental[c]	
non-H-bonded −OH stretch	3691	not present	3661-3664	3674 (2957[d])
			3658-3663	
			3660, 3662	
			3662-3675	
bridging −OH stretch	3609	not present	3652, 3655	3674 (2957[d])
			3652-3655	
			3653, 3655	
			3652-3667	
non-H-bonded H_2O stretch	not present	3584, 3588	3604-3608	3672 (2957[d])
			3610, 3611, 3626	
			3616-3625	
			3604-3607, 3620	
H-bonded H_2O/OH stretch	3472, 3469	not present	2727, 2743, 2746, 2754	2745, 2747 (2214)
			2406, 2621, 2646, 2676	2625-2660 (2117-2144)
			2515, 2533, 2544, 2551	2551 (2061)
			2727, 2743, 2752, 2784	2745, 2747 (2214)

[a]In some instances the vibrational modes of the four faces of the Zr_6 node are decoupled in two sets; those involving the vibration of the OH/OH_2 ligands pointing inside the large pore within NU-1000 and those corresponding to the analogous mode pointing toward the smaller cavities. In addition, asymmetry in the overall structure may lead to additional peaks. Theoretical data are scaled by a factor of 0.939.
[b]Results for 4 different MIX-Node-S topologies, differing as aquo/hydroxo positional or rotational isomers on the MIX-Node-S core, all predicted to be within 10 kJ/mol of one another in free energy (see SI of 446 for details).
[c]Key peaks that shift on deuterium exchange are reported; deuterated frequencies are in parentheses.
[d]This peak is difficult to assign precisely as it falls in the C−H stretching region.

most striking feature in the experimental spectrum is the combination of (inferred) concerted asymmetric stretches observed at 2551, 2747, and 2745 cm^{-1}, i.e., the stretches predicted for the isomers belonging to the MIX-Node-S topology.

Given the results of our computational effort, and additional IR spectroscopic studies detailed below, we have assigned the experimental peak centered around 3674 cm^{-1} to both the terminal and μ_3 bridging OH groups. There is also a shoulder present at 3672 cm^{-1} (see the Supporting Information for further details), which has been assigned as the terminal H_2O stretching mode. We do also predict terminal and hydrogen-bonded H_2O bending modes at about 1550 and 1060 cm^{-1}, but these peaks fall in regions of the experimental spectrum dominated by absorptions from the organic ligands, so comparisons are not possible. The experimental spectra are also significantly broadened, and this may reflect the influence of trace amounts of solvent molecules of a second-sphere of solvation, the presence of which would be expected to influence the positions and shapes of the stretching frequencies or potentially some small amount of disorder that we observe, for example, in the single crystal X-ray structure of NU-1000. Irrespective of the absolute values of the frequencies, it is clear that only the MIX-Node-S topology is in acceptable agreement with our computational and experimental data.

D_2O Exchange Experiments and Variable Temperature DRIFTS

To further corroborate our proposed IR assignments, we turned to D_2O exchange and variable temperature DRIFTS experiments. NU-1000 was submerged in D_2O and exchanged three times over the course of 72 h. After 72 h, the peak at 3674 cm^{-1} was significantly decreased, while the shoulder at 3672 cm^{-1} was no longer present (Figure 5a). The peaks at 2551, 2745, and 2747 cm^{-1} also disappear almost completely. At the same time, a new peak and shoulder appear at 2216 and 2213 cm^{-1}, and another new peak at 2061 cm^{-1} (Figure 4.5b). Interestingly, a portion of the peak at 3674 cm^{-1} remains in the deuterated spectrum. The results are consistent with both the terminal $-OH$ and hydrogen bonding H_2O ligands being deuterated, but a possibly much slower exchange to deuterate the bridging μ_3-OH ligands, which may be sterically inaccessible.

The isotopic frequency ratios for the pairs of peaks 2747/2216, 2745/2213, and 2551/2061 are all about 1.24. Such a reduction from the harmonic oscillator value of about 1.4 is entirely consistent with the significant anharmonicity associated with

strong hydrogen bonding. With respect to the OH stretch(es) at 3674 cm^{-1}, a similar scaling factor would place the corresponding OD stretch(es) at 2963 cm^{-1}. While this is in the C−H stretching region of the spectrum, and thus hard to assign definitively, nevertheless there does appear to be a new peak in the deuterated spectrum at 2957 cm^{-1} (Supporting Information). It is somewhat surprising that a frequency ratio closer to 1.4 is not observed for this isotope shift, but as no new peaks are observed below the C−H stretching region, we must conclude that the relevant O−D stretches are found there.

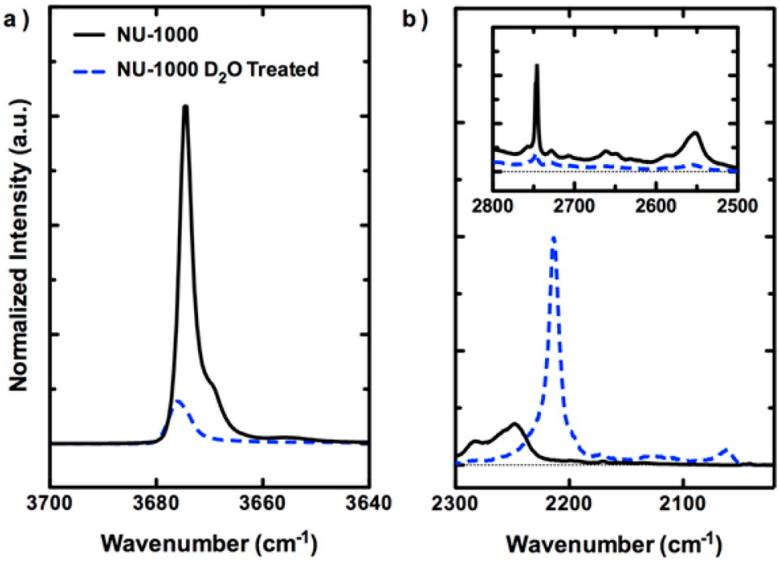

Figure 4.5: (a,b) The terminal and bridging −OH and $-H_2O$ stretching regions of NU-1000 before (solid black line) and after exposure to D_2O (dotted blue line). The inset in panel b shows the H-bonded H_2O stretching features before and after exposure to D_2O.

Next we turned to variable temperature DRIFTS measurements; the hydroxyl and H-bonded H_2O regions are highlighted in Figure 4.6. The symmetric (2747 cm^{-1}) and antisymmetric (2745 cm^{-1}) H-bonded H_2O stretches disappear between 150 and 250 °C presumably via ligand dissociation. Concomitant to the loss of the H-bonded H_2O molecules, the hydroxyl region starts to disappear at 150 °C, and completely disappears by 300 °C. It is well-known that the bridging −OH ligands in UiO-66 (another Zr_6-based MOF node) condense and release water around 300 °C, and we suspect that a similar phenomenon is observed here.[448,449] It is noteworthy that complete dehydration of the

NU-1000 node would correspond to a mass loss of 6.6% and we observe such a mass loss over a similar temperature range (see SI of 446). At high temperature, a peak at 2732 cm^{-1} is observed. While the number of possible dehydrated structures makes it difficult to assess anything computationally, it may be that some dehydration occurs with loss of oxygen atoms in the core, as has been observed for UiO-66,[449] and core rearrangement leads to a local hydrogen bond that persists until still higher temperatures are reached. In any case, the D_2O- and temperature-dependence of the stretches at 2745 and 2747 cm^{-1} excludes the possibility that these are unusually low C−H stretches from the $TBAPy^{4-}$ linker of NU-1000.

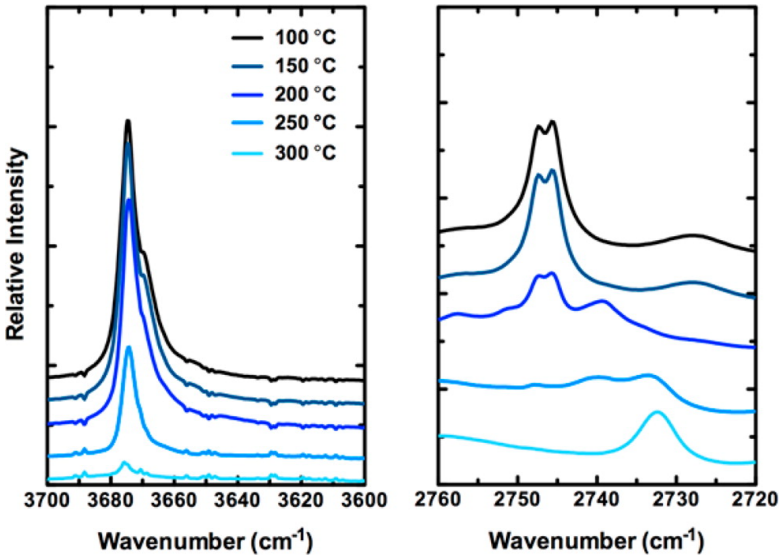

Figure 4.6: Temperature-dependent DRIFTS spectra of the −OH and H-bonded H_2O regions for NU-1000.

Computational Efforts to Address the Loss of the H-Bonded H_2O Molecules and Condensation of −OH Ligands

It is of interest to address and understand the origin of the observed disappearance of the −OH and $-OH_2$ peaks in the IR spectra. Hence we investigated the energetic costs associated with removing the H-bonded H_2O ligands and the condensation of −OH groups to form H_2O. Calculations indicate that the energetic cost to remove one aqua ligand is 145 kJ/mol, while the energy required to remove all four coordinated

water molecules is 565 kJ/mol. (These are constrained electronic energies optimized with the aromatic rings frozen.) This ratio of approximately 4 suggests that there is no special cooperativity associated with addition or removal of individual aqua ligands. Thus, conversion of the MIX-Node-S to the H_2O-Node with subsequent H_2O ligand dissociation can take place upon heating (vide supra). The energy to transfer one proton (H7) from a bridging OH-group to a terminal one is 89 kJ/mol. As such, we speculate that the loss of the $-OH$ and $-OH_2$ stretches in the IR spectra occurs via thermal proton transfer followed by elimination of $-OH_2$ ligands. These benchmarking energies should prove useful for rationalizing the stability and predicting the nodal reactivity of Zr_6-based MOFs.

By employing a combined quantum chemical and experimental approach we have been able to assign a staggered mixed proton topology, $[Zr_6(\mu_3\text{-}O)_4(\mu_3\text{-}OH)_4(OH)_4(H_2O)_4]^{8+}$, to the Zr_6-based MOF NU-1000 while simultaneously ruling out five alternative proton topologies. Within the mixed proton topology, multiple isomers appear to be present at room temperature differing in arrangements of coordinating aquo and hydroxo ligands. This is the first time a mixed node proton topology has been determined for a MOF. We anticipate that this unique H-bonded motif will have wide ranging implications in applications including acid/base chemistry, conductivity, catalysis, and in understanding NU-1000s reactivity toward functionalization (e.g., AIM and SALI). Results from ongoing work in our laboratories consistent with these assessments will be reported in due course.

4.2 A Hafnium-Based Metal-Organic Framework as an Efficient and Multifunctional Catalyst for Facile CO_2 Fixation and Regioselective and Enantioretentive Epoxide Activation

4.2.1 Introduction

Catalysts based on permanently porous frameworks have the potential to unify the best features of homogeneous catalysts (selectivity and ease of modification) and heterogeneous catalysts (ease of purification and recyclability). Metal-organic frameworks (MOFs) represent a special class of porous materials consisting of easily constructed organic linkers and metal clusters.[381] The modular nature and facile tunability of MOFs make them ideal heterogeneous catalysts with uniform active sites through wisely chosen building blocks. In catalysis, MOFs allow for the same level of structural refinement as molecular homogeneous catalysts, while their ultrahigh surface area, pore volume, and heterogeneous nature facilitate good catalytic activity and rapid purification.[385,124,125]

Catalyst-mediated reactions of CO_2 represent one potential positive contributor to climate-relevant carbon capture and storage/sequestration (CCS), albeit a far from sufficient one to satisfy this enormous challenge.[450] Well-designed reactions that utilize waste CO_2 in the production of commercially relevant chemicals are much sought these days. Some of these reactions include the formation of carbonates, where the carbonyl carbon obtained from CO_2 is isohypsic with its starting material and does not require reagent-driven changes in oxidation state.[c] The acid-catalyzed cycloaddition of CO_2 with an epoxide to form a cyclic carbonate, a functionality having various important applications,[452] is a highly atom-economical reaction that might be catalyzed by an appropriately designed MOF. Mechanistically, this reaction is based on an acid catalyst that activates the epoxide, which can then be attacked by a nucleophile cocatalyst to form an alkoxide. This intermediate can then react with carbon dioxide to ultimately

[c] Since CO_2 is the most oxidized state of carbon, thermodynamically carbonates would be the most suitable candidates, as the four chemical bonds of the carbonyl carbon are connected to oxygen. To validate this hypothesis, as a model reaction we calculated ΔG for CO_2 insertion into PO in water at 298 K using multiple functionals and determined that the free energy is approximately $8-15$ kcal/mol in favor of the product (see SI, ref 451).

give the cyclic carbonate.[453] However, on account of the relatively inert nature and low reactivity of CO_2, its activation and incorporation into organic substrates still remains a formidable challenge.[454]

Although some homogeneous catalysts[d] and several types of heterogeneous catalysts,[455,456,457e] such as zeolites,[458] silica-supported salts,[459] metal oxides,[460,461,462,463] titanosilicate,[464] a microporous polymer,[465] and an organic network,[466] have been utilized for the synthesis of cyclic carbonates, most of the processes demand high pressures and temperatures, thus requiring high energy and capital costs.

Recently,[45] we reported a new Zr-based MOF, NU-1000, obtained via the solvothermal reaction of $ZrCl_4$ and 1,3,6,8-tetrakis(*p*-benzoic acid)pyrene (H_4TBAPy) with benzoic acid as a modulator. The parent-framework node consists of an octahedral Zr_6 cluster capped by eight bridging oxygen-containing ligands. The 3D NU-1000 structure can be described as 2D Kagome sheets linked by TBAPy ligands. NU-1000 shares the same topological features as MOF-545[110] and PCN-222,[111] comprising triangular and hexagonal channels. The presence of a high density of acidic sites, the integration of permanent porosity with ultralarge channels, the high surface area, and the extraordinary chemical stability of NU-1000 suggested that it could be an excellent catalyst platform that can overcome the above-mentioned challenges in CO_2 insertion and acid-catalyzed epoxide activation in general.

By comparing the dissociation enthalpies of typical Hf−O versus Zr−O bonds (802 vs 776 kJ·mol^{-1}),[467] we inferred that Hf is more oxophilic (i.e., has stronger M−O bonds) than Zr and should thus function as a stronger Brønsted acid. Therefore, we hypothesized that a Hf-cluster-based NU-1000 would be an even more efficient catalyst than the Zr-cluster-based NU-1000 for acid-catalyzed systems [also see the Supporting Information (SI) of ref 451]. In order to test our hypothesis, we prepared the Hf-based MOF (Hf-NU-1000) with the same topology as NU-1000.[f] To confirm that NU-1000 and Hf-NU-1000 have the same overall crystal structure, periodic density functional

[d] See the SI of ref 451 for an extensive list of references reporting homogeneous catalysts for the synthesis of cyclic carbonates.

[e] See the SI of ref 451 and Table S2 for the complete list of references reporting MOFs as catalysts for the synthesis of cyclic carbonates.

[f] It is not surprising that Hf-NU-1000 and Zr-NU-1000 have similar structures, since Hf^{4+} and Zr^{4+} cations have ionic radii of 0.78 and 0.79 Å, respectively, as well as similar coordination chemistry. (see ref 7)

theory (DFT) within the Vienna ab Initio Simulation Package (VASP)[433] was used to optimize the ionic positions of NU-1000 starting from the validated NU-1000 X-ray diffraction (XRD) data. The Zr^{4+} ions were then replaced with Hf^{4+}, and the simulated Hf-NU-1000 structure was used to optimize the ionic positions. Comparison of the experimental and simulated powder XRD (PXRD) patterns of Hf-NU-1000 and NU-1000 confirmed that the Hf and Zr versions of NU-1000 are indeed isostructural (Figure 4.7; also see the SI of ref 451).

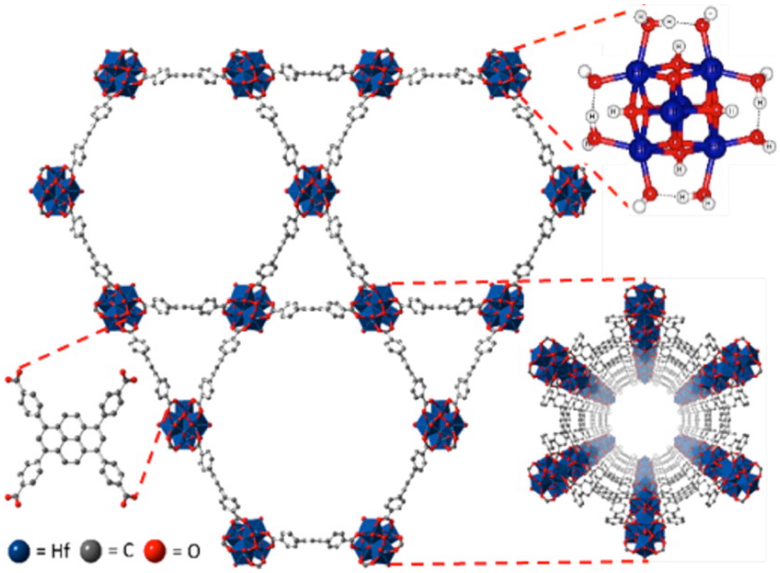

Figure 4.7: Relevant structural features and representations of Hf-NU-1000. For simplicity, H atoms except for the cluster are not shown. For clarity, the carboxylates have been removed from the cluster shown in the top inset.

4.2.2 Results and Discussion

The porosity of Hf-NU-1000 was studied by N_2 adsorption-desorption experiments at 77 K, and the resulting isotherm (type IVc) yielded a Brunauer-Emmett-Teller (BET) surface area of 1780 $m^2\ g^{-1}$ and a total pore volume of 1.14 $cm^3\ g^{-1}$. DFT pore size distribution analysis revealed pore diameters of ca. 13 and 29 Å, assignable to the triangular micropores and hexagonal mesopores, respectively. Thermogravimetric analysis (TGA) of the activated sample showed no major decomposition up to 500 °C (see the SI of ref 451). Diffuse reflectance infrared Fourier transform spectroscopy

(DRIFTS) confirmed the presence of -OH groups and H_2O molecules in the Hf_6 nodes, with peaks at 3679 cm^{-1} assigned to the non-H-bonded -OH and bridging -OH stretches, the peak at 3678 cm^{-1} assigned to the non-H-bonded H_2O stretch, and the peak at 2752 cm^{-1} assigned to the H-bonded H_2O and OH stretches (see the SI or ref 451).[446]

Given the high stability, porosity, and large channels of Hf-NU-1000, we decided to investigate its performance as an acid catalyst in the context of CO_2 fixation through reaction with epoxides to form cyclic carbonates under ambient conditions. Hf-NU-1000 demonstrates highly efficient catalytic activity for the quantitative cycloaddition of styrene oxide using CO_2 at 1 atm gauge pressure to form styrene carbonate at room temperature (r.t.) (Table 4.3, entry 1a). To the best of our knowledge, this is the mildest and the most efficient catalytic system for this type of reaction. Since the conversion of epoxide to carbonate is complete and quantitative, the pure product could be obtained after a simple aqueous extraction, without the need for laborious purification steps such as distillation, which can cause decomposition of the product and the formation of byproducts.[468] Under the same reaction conditions, NU-1000 was not as efficient as Hf-NU-1000 (entry 1b), confirming our hypothesis about their relative catalytic activities. When the same reaction conditions were employed, but in the absence of catalyst, no product was obtained (entry 1c). The same reaction proceeds much faster at elevated temperature (55 °C, 13 h; entry 1d). Hf-NU-1000 was compared with the reported MOFs gea-MOF-1,[457] Cr-MIL-101, MOF-5, ZIF-8, Ni(salphen)-MOF, Co-MOF-74, Mg-MOF-74, $[Cu(Hip)_2(Bpy)]_n$ [CHB(M)], ZIF-68, F-IRMOF-3, and MIL68(In)-NH_2 (Table S2, ref 451, entries 1e-o), which have also been used for the preparation of styrene carbonate, and Hf-NU-1000 clearly stands out in terms of yield and milder conditions.

The industrially important epoxide divinylbenzene dioxide (DVBDO) was also examined, and biscarbonated DVBDO, which could be a useful epoxy resin monomer[469] candidate, was obtained quantitatively after 19 h at 55 °C (Table 4.3, entry 2). Hf-NU-1000 was also compared with other MOF materials for the conversion of propylene oxide (PO) to propylene carbonate (r.t., 26 h; entry 3). Hf-NU-1000 again showed shorter reaction time and higher product yield compared with the previously reported MOFs MMCF-2,[455] PCN-224(Co),[456] gea-MOF-1,[457] HKUST-1, MOF-505, MMPF-9, Cr-MIL-101, MOF-5, Ni(salphen)-MOF, CHB(M), and $Zn_4O(BDC)_x(ABDC)_{3x}$ based on MOF-5 (MIXMOF) (Table S2, ref 451, entries 3b−l). It is worth noting that PO is

Table 4.3: Cycloaddition reactions of CO_2 with epoxides catalyzed by Hf-NU-1000 yielding cyclic carbonates.

Entry	Catalyst	Subs	Prod	T (°C)	P (atm.)	t (h)	Yield (%)
1a[a]	Hf-NU-1000		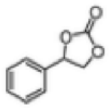	r.t.	1	56	100[c]
1b[a]	NU-1000			r.t.	1	56	46[c]
1c[b]	–			r.t.	1	56	0[c]
1d[a]	Hf-NU-1000			55	1	13	100[c]
2[a]	Hf-NU-1000	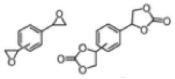		55	1	19	100[c]
3[a]	Hf-NU-1000			r.t.	1	26	100[c]

[a]Reaction conditions: epoxide (0.2 mmol), catalyst (4.0 mol % −OH active sites), and nBu$_4$NBr (10 mol %) under CO_2 (1 atm gauge pressure).
[b] The same conditions as in footnote *a*, but without the catalyst.
[c]Determined by ^{1}H NMR analysis using 1-bromo-3,5-difluorobenzene as the internal standard.

more studied than styrene oxide because of its higher reactivity and ease of isolation. However, its low boiling point could easily lead to mass loss, which can complicate yield calculations; thus, careful handling is required.

To confirm the heterogeneous nature of the reaction, under the same conditions as in Table 4.3, entry 1a, 40 h after the outset of the reaction, the catalyst was removed and the reaction was allowed to continue. As expected, no increase in the formation of carbonate was detected (see the SI or ref 451). At the end of the reaction, inductively coupled plasma (ICP) analysis of the reaction mixture filtrate revealed no Hf leaching, indicating that the catalytic reaction is indeed heterogeneous in nature. Additionally, in the absence of the ammonium salt cocatalyst, no conversion was detected for the model reaction. Furthermore, the catalyst was reused five successive times without a significant decrease in the efficiency of the catalyst or structural deterioration as determined by PXRD analysis (see the SI of ref 451).

After such encouraging results for the cycloaddition reaction of CO_2 with epoxides were obtained, and since mechanistically this reaction occurs via an acid-catalyzed ring-opening step,[453,455] we became interested in investigating the performance of Hf-NU-1000 in the activation of epoxides for the preparation of 1,2-bifuctionalized systems

via acid-catalyzed nucleophilic ring opening. As the initial step, we chose to focus on the synthesis of vicinal azidohydrins, which are important precursors of α-amino alcohols[470] (known as β-blockers). Additionally, vicinal azidohydrins are present in various bioactive natural products[471] and in the chemistry of carbohydrates,[472] nucleosides,[473] lactams,[474] and oxazolines.[475] Although azidohydrins are generally synthesized from epoxides by reaction with alkali azides, this classical method is often accompanied by side reactions such as isomerization, epimerization, and rearrangement.[472,476] To the best of our knowledge, there is no report of highly regioselective azidolysis of epoxides with a high yield and complete conversion of substrate.[477] Tanabe and Cohen[478] and Song et al.[479] studied this reaction using a series of MOFs, but they obtained only moderate conversions and/or required stepwise postsynthetic modifications.

Under the optimized conditions, Hf-NU-1000 catalyzed the solvolytic reaction of trimethylsilyl azide (TMS$-N_3$) with styrene oxide with high regioselectivity for substitution at the benzylic position and complete conversion of substrate (Table S3, ref 451,entry 1). The catalyst was also reused five successive times, and neither a considerable decrease in the efficiency of the catalyst nor structural deterioration as determined by PXRD analysis was observed (see the SI of ref 451). In order to gain a better understanding of the origin of this unique regioselectivity, a few control reactions were conducted. First, hafnium(IV) oxychloride octahydrate was utilized as a Lewis acid catalyst to examine whether the regioselectivity originates from Hf^{IV}; the conversion decreased to 75%, and the co-occurrence of a side-product (30%) was observed (entry 2). When dehydrated Hf-NU-1000 was used, both the conversion (60%) and regioselectivity (85:15) decreased (entry 3). Additionally, aqueous HCl (an alternative homogeneous catalyst) was used to catalyze this reaction, but it showed poor conversion (48%) and the co-occurrence of a side product (26%) (entry 4).

In order to elucidate the mechanism of the reaction, we turned to computational modeling. Quantum-chemical calculations were carried out using DFT at the M06-L/def2-SVP level. The SMD continuum solvent model[480] was employed to account for solvation with TMS$-N_3$ as the solvent. Hf-NU-1000 serves as a proton donor in the ring-opening reaction because of the presence of aqua and OH ligands in the Hf_6 node. Our calculations show that styrene oxide forms an association complex with the Hf_6 node via both hydrogen-bonding and π-stacking interactions (see the SI of ref 451).

The main criteria defining the reaction selectivity are the difference in the activation barriers of the epoxide ring-opening step (kinetic factor) and the relative stability of the products (if the reaction operates under thermodynamic control). The optimized geometries of the transition state (TS) structures **TSa** (azide attack at the benzylic position) and **TSb** (azide attack at the less hindered side) leading to products **A** and **B**, respectively, are depicted in Figure 2. In both TS structures, the aromatic ring of styrene oxide engages in a T-shaped π-stacking interaction with the aromatic rings of the Hf_6 node linker ligands. The calculations show that for the reaction catalyzed by the Hf_6 node, the difference in activation free energies is 3.0 kcal/mol, while in the case of HCl the difference is about 2 kcal/mol. The difference in the free energies of the products $[\Delta_f G^{\circ}_{298}(\mathbf{b'}) - \Delta_f G^{\circ}_{298}(\mathbf{a'})]$ is 0.1 kcal/mol, while with HCl it is -2.3 kcal/mol. These numbers track the variations in the experimental ratios of the products **A** and **B**. To assess the effect of the predicted π-stacking interaction, PO was reacted with TMS$-N_3$ under the same conditions as mentioned in Table S3 from ref 451 for styrene oxide, and a dramatic decrease in regioselectivity was detected. In this case, a 25:75 ratio of the two regioisomers was observed, with the major product resulting from azide attack at the less hindered side (see the SI of ref 451).

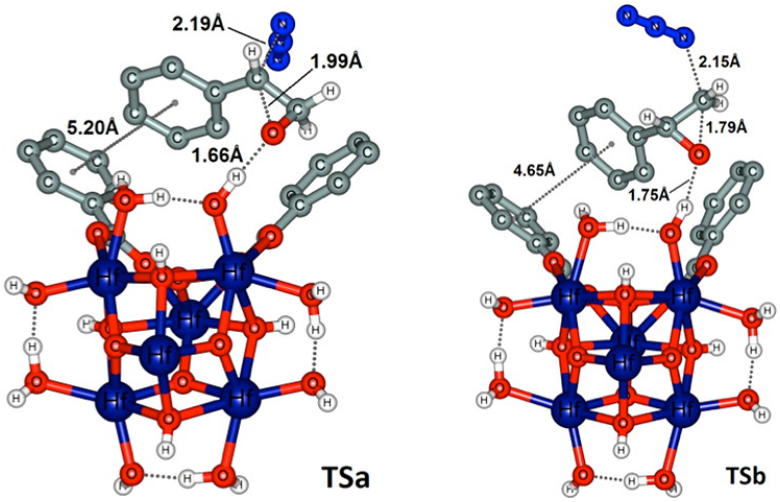

Figure 4.8: Optimized geometries of the TS structures **TSa** and **TSb** for the epoxide ring-opening steps leading to the products **A** and **B**, respectively. H atoms of the phenyl rings have been removed for clarity.

Encouraged by the above results, we employed Hf-NU-1000 to catalyze alcoholytic epoxide ring opening. The opening of epoxides with alcohols is an important transformation in the synthesis of β-alkoxy alcohols.[481] However, the application of such reactions generally is limited because of the poor nucleophilicity of alcohols, which requires harsh and/or strongly acidic conditions, usually leading to the formation of a mixture of regioisomers and polymerization.[482,483] Therefore, the regioselective alcoholysis of epoxides has been the subject of extensive studies.[g] On the basis of the above optimized geometries of the transition states, we speculated that the approach of methanol to hydrogen-bonded epoxide would show good stereoselection. Therefore, under our optimized conditions, (+)-(*R*)-styrene epoxide was reacted with methanol in the presence of Hf-NU-1000 (4.0 mol % of −OH active sites). The regioisomer corresponding to attack at the benzylic position with inversion of the epoxide stereogenic center was obtained selectively and in an enantioretentive fashion (Figure 4.9, top). Additionally, (+)-(*R*)-styrene epoxide was also reacted with TMS−N_3 in the presence of Hf-NU-1000 (4.0 mol % of −OH active sites). Again, the preferred regioisomer was obtained with inversion of the epoxide stereogenic center in an enantioretentive fashion (Figure 4.9, bottom). These selective inversions of the stereogenic center indicate an S_N^2-type mechanism in which the carbocation is not formed as an intermediate. Hf-NU-1000, an achiral catalyst, yielded the enantiomerically pure product, which makes it a promising catalyst in asymmetric catalysis on account of its simple design.

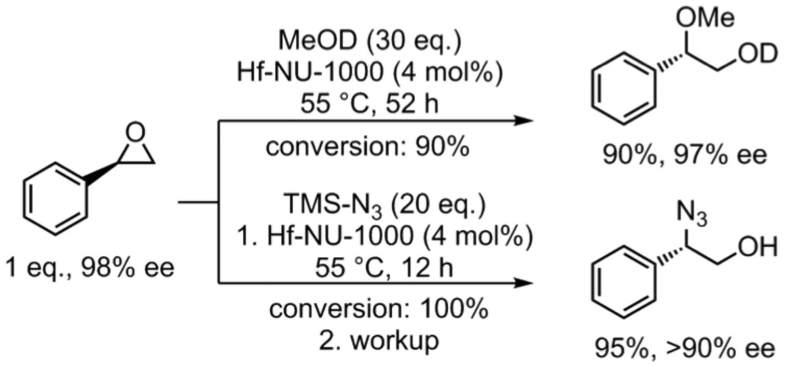

Figure 4.9: Regioselective and enantioretentive methanolysis (top) and azidolysis (bottom) of styrene oxide catalyzed by Hf-NU-1000 to give β-methoxy- and β-azido alcohols.

[g] See the SI of ref 451 for an extensive list of references for the synthesis of β-methoxy alcohols from styrene oxide using different catalysts.

4.2.3 Conclusions

In summary, a new polyoxohafnium-cluster-based MOF isostructural with Zr-based NU-1000 has been prepared and characterized. It demonstrates excellent performance in the context of chemical fixation of CO_2 as an inexpensive, environmentally benign, ubiquitous, and sustainable carbon source for the preparation of cyclic carbonates under ambient conditions. In addition, this multifunctional catalyst is efficient for solvolytic reactions and activates epoxides for the regioselective and enantioretentive synthesis of 1,2-bifunctionalized systems. We have further shown that the catalyst can be recycled and reused for multiple successive runs without considerable loss of activity or structural deterioration. We speculate that this catalyst will be useful for the fixation of CO_2, the regioselective synthesis of enantiomerically enriched β-azidohydrins and β-alkoxy alcohols, and related reactions of epoxides with suppressed formation of byproducts while adhering well to the principles of green chemistry and atom economy.

4.3 Targeted Single-Site MOF Node Modification: Trivalent Metal Loading via Atomic Layer Deposition

4.3.1 Introduction

Metal-organic frameworks (MOFs) are attractive systems for catalytic studies,[124,125] in part because they exhibit uniform mesoscale and/or microscale porosity, generated by periodic and atomically well-defined structures. Importantly, these structures, comprising organic linkers and inorganic, metal-containing nodes, are amenable to full experimental structural characterization and rigorous computational modeling.[422,41,423,394] Although the vast majority of MOF catalysis work focuses on linkers as catalysts[484] for condensed-phase reactions, a few reports of node-based catalysis have also appeared,[485,486,487,488,489,13,490,431,491] including at least one for high temperature (350 °C) heterogeneous catalysis of a gas-phase oxidation reaction.[492] Increasingly popular as nodes for these types of studies are hexa-zirconium(IV)oxo/hydroxo/aqua species and their hafnium(IV) analogues. The lability and reactivity of the nodes oxygen-rich ligandsspecifically, aqua and terminal hydroxo ligands-allows for site-specific functionalization, both with nonstructural organic ligands[108,440,493,494,270] and, in principle, with nonstructural metal ions. We have shown that the latter can be accomplished in reproducible fashion with a suitably porous MOF, NU-1000 (aperture width >3 nm), via chemistry akin to atomic-layer deposition (ALD), a materials synthesis technique typically applied to hydroxyl-presenting surfaces of purely inorganic materials.

Recent advances in both MOF and ALD science make their potential union both feasible and versatile. While the stability ranges of early MOFs and process ranges of early ALD procedures occupied different temperature windows-generally below and above 200 °C, respectively-advances in both fields now permit significant overlap of these ranges. For example, selected MOFs based on Zr_6O_{16} nodes (Figure 4.10), retain their mesoporosity at temperatures above 400 °C, and in some case above 500 °C.[489,45,425] In addition, an ever growing number of ALD processes for oxides, sulfides, nitrides, and pure metals have been identified at temperatures as low as 100 °C.[495,496,497,498,499] Appropriately chosen MOFs exhibit the high porosity and large pore apertures (>3 nm) desirable to minimize the influence of mass transport limitations that would otherwise practically inhibit vapor-phase loading. Such characteristics allow for AIM, where

precise surface chemical control is retained through self-limiting reactions that allow uniform reaction throughout an arbitrarily complex framework. Recently, the platform MOF material NU-1000 has been modified with Al, Zn, and their combination.[45] To provide mechanistic insight and establish universal applicability of the AIM approach, we take trimethylated trivalent metal precursors as model reactants, and examine the extent to which uniform and self-limiting (ALD-like) reactions can be achieved in MOFs. Furthermore, we determine the exact locations of the trivalent metals, obtaining results that are consistent with a mechanism that we derive from first-principles computation. Finally, we assess one of the most chemically aggressive ALD precursors, $AlMe_3$, for compatibility with the MOF framework.

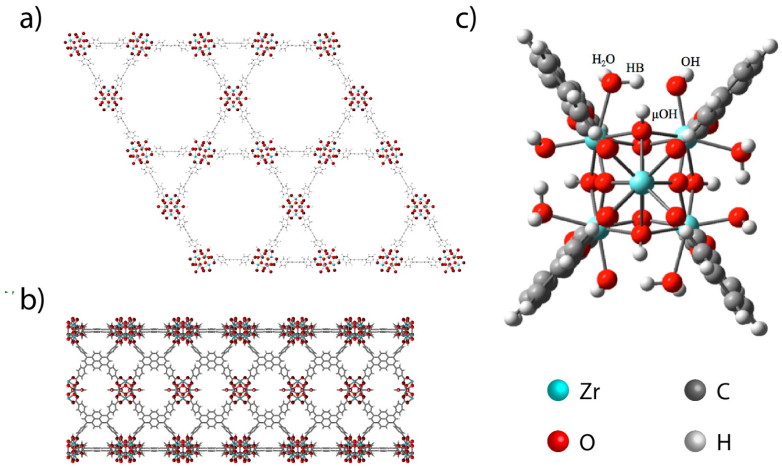

Figure 4.10: (a, b) Zr_6-based framework NU-1000. (c) Cluster used to model the Zr_6-node in NU-1000.

4.3.2 Results and Discussion

A Zr_6-based framework, NU-1000s nodes are octahedral Zr_6 clusters including four each bridging μ-O and μ-OH groups. The 3D structure of the MOF results from bridging of the nodes by tetra-carboxylate linkers (Figure 4.10a, b).[45] Importantly, under ambient conditions, four each aquo and hydroxo groups can occupy remaining open metal coordination sites of the node. The detailed structure of NU-1000 was previously investigated both computationally and experimentally to reveal a staggered mixed proton topology for the $[Zr_6(\mu_3\text{-}O)_4(\mu_3\text{-}OH)_4(OH)_4(H_2O)_4]^{8+}$ cluster (Figure 4.10c) at room

temperature.[446]

The $-OH$ and $-OH_2$ functional groups at the surface of the node present in a manner making them likely to be amenable to many conventional oxide ALD half-reactions. Using density functional theory (DFT) calculations, we have identified highly exothermic reaction pathways for reaction of the node with two trimethylated trivalent metal compounds, $AlMe_3$ and $InMe_3$, as illustrated in Figure 4.11. This chemistry is in close analogy to that previously hypothesized for planar surface modification in traditional thin film ALD growth.[500] On the basis of the reaction pathways, a maximum of 8 metal atoms are predicted to bind to each Zr_6 node with the release of up to 12 methane (CH_4) molecules.

Computational Results

There are four chemically distinct protons on each of the four faces of the Zr_6-node in NU-1000, one that engages in a hydrogen bond between the aquo and hydroxo ligands (HB; see Figure 4.10c), two that are non-hydrogen bonded on the aquo (H_2O) and hydroxo (OH) ligands, respectively, and one that is on the core itself (μOH). To test which of the four protons on each face is most likely to be replaced with either $AlMe_3$ or $InMe_3$, each proton was individually substituted for an $AlMe_2$ or $InMe_2$ group and the structure of the cluster was then optimized with fixed linker positions. Replacement of hydrogen HB with $AlMe_2$ or $InMe_2$ results in the most stable product (Table 4.4). We subsequently located the transition-state (TS) structure leading to this intermediate, and we characterized all of the elementary steps involved in the further reaction of the node face under operating conditions. The full reaction coordinate, shown in Figure 4.11, indicates that each face of the Zr_6-node will react with two ALD precursors to generate four CH_4 product molecules, i.e., our model predicts that every O-H bond on each node will react with $AlMe_3$ and $InMe_3$ to lead to a final structure with eight tetrahedrally coordinated $(RO)_3AlMe$ or $(RO)_3InMe$ groups disposed at the surface.

Experimental Results

To verify the self-limiting nature of the precursor with hydroxyl and water groups, we undertook a full saturation study including exploration of mole-limited and diffusion-time limited variable space (Figure 4.12). In each experiment, 10 mg of microcrystalline

Table 4.4: Relative reaction energies for substitution of $AlMe_2$ and $InMe_2$ (and generation of CH_4) at the positions of the labeled hydrogens in the bare Zr_6 cluster shown in Figure 4.10c.

	relative energy (kcal·mol^{-1})			
	ΔE		ΔG	
	$AlMe_3$	$InMe_3$	$AlMe_3$	$InMe_3$
HB	0.0	0.0	0.0	0.0
H_2O	18.5	15.7	19.2	17.3
OH	22.3	21.6	22.9	23.0
μOH	24.4	22.6	24.9	24.0

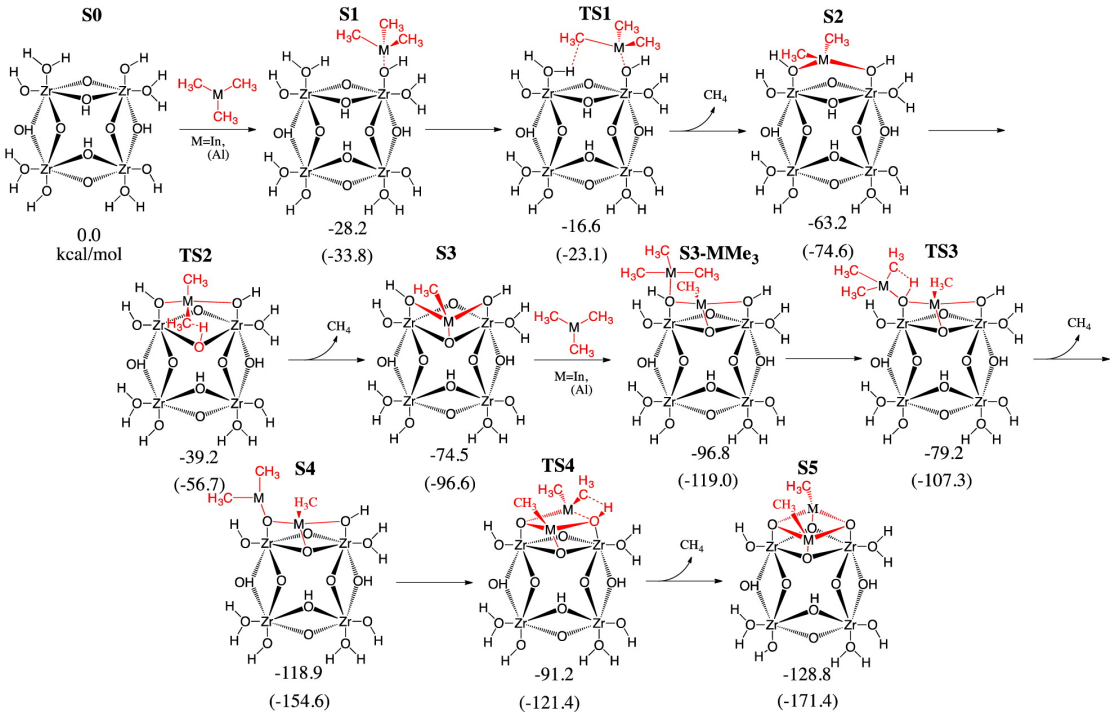

Figure 4.11: M06-L relative enthalpies (kcal·mol^{-1}) for intermediates and TS structures on the reaction coordinate for one face of the NU-1000 node reacting with 2 equivalents of $AlMe_3$ or $InMe_3$ (in parentheses) and liberating 4 equivalents of CH_4. Subsequent reaction coordinates for the remaining faces of the node (not shown) were found to be entirely equivalent, with negligible differences in enthalpies relative to analogous precursors, i.e., there is no significant influence of one face upon another over the course of reaction.

NU-1000 powder was warmed to 125 °C under vacuum with 0.5 Torr of flowing nitrogen for 20 min in order to remove any physisorbed water or solvent. Next, the powder was soaked at the desired temperature (75 and 125 °C for $InMe_3$ and $AlMe_3$, respectively) prior to a 60 s exposure to water vapor. Further soaking under flowing N_2 at temperature establishes an equilibrium $-OH$ and $-OH_2$ population. Finally, the metal precursor ($InMe_3$ or $AlMe_3$) was delivered to the reaction chamber under its own vapor pressure and exposed without pumping (quasi-static mode) for the indicated time for a given number of repetitions. The results of the AIM process with $InMe_3$ (Figure 4.12) reveal many of the characteristics of archetypal ALD surface reactions, albeit with much larger doses and exposures, as predicted for a large surface area powder with high aspect ratio pores. Clearly, a stoichiometric number of precursor molecules must be delivered with respect to the available reaction sites in order to achieve a saturating reaction. The number of sites in 10 mg of powder is estimated to be 3.7×10^{-5} moles based on 8 sites per Zr_6 node. On the basis of the vapor pressure of $InMe_3$, an equal or greater number of moles are expected to be delivered in a single 0.4 s dose. Therefore, under these processing conditions, the reaction is never mole-limited. Still, because of the very high aspect ratio of the channels through which the vapor is required to traverse (-10000), a nontrivial time for precursor diffusion to all points within the microcrystals must also be considered. An empirical formula[501] based on Monte Carlo simulations assuming Knudsen diffusion was used to calculate a total exposure time of at least 20 s required to traverse the long, narrow channels with this aspect ratio. This is roughly consistent with a 600 s exposure time required to achieve the complete loading of the longest crystals. As evidenced by the saturating In ratio in the limit of large dose and long diffusion time, the process shows ideal self-limiting behavior. Based on the saturation studies under these optimized ALD conditions, the number of In per Zr_6 node obtained by inductively coupled plasma-optical emission spectroscopy (ICP-OES) saturates at -6 (In:Zr_6 = 1), in reasonable agreement with the computational prediction. Several factors account for the deviation from the computationally predicted loading of 8 In per Zr_6 node. First, the NU-1000 structure is known to contain a fraction (perhaps 25%) of secondary nodes within the largest pores.[45] This secondary node is connected to the framework through additional linkers, each one of which reduces the potential number of deposition sites on neighboring nodes by 2. Furthermore, the computationally predicted

reaction assumes full initial ligation of the node (4 OH_2, 4 OH, 4 μ-OH), which may be slightly reduced via dehydration under continuous heating (75 °C) in vacuum. Finally, there is the possibility that only a subset of the potential reaction sites are reasonably accessible to $InMe_3$. This possibility, however, was minimized by performing saturation studies in excess of both diffusion time and moles of $InMe_3$ (Figure 4.12). Furthermore, the possibility of a minority of clogged pores, through which the metal precursor will never pass, has not been rigorously excluded.

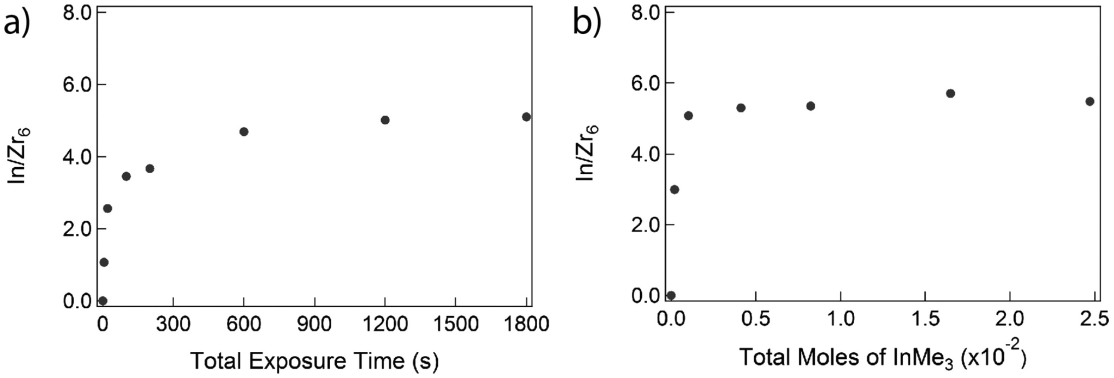

Figure 4.12: In to Zr_6 node ratio as a function of the ALD process conditions. Subsaturating In loading is observed upon delivery of a nonstoichiometric $InMe_3$ dose or insufficient exposure time. In the limit of exceptionally large and long exposures, the process exhibits self-limiting behavior.

Although the AIM process with $AlMe_3$ shows, with moderate exposures, apparent self-limiting behavior with ∼6 Al per Zr_6 (Figure 4.13a), larger exposures reveal non-self-limiting behavior (∼14 metal per Zr_6 node) as shown in Figure 4.13b.

Consistent with its strong Lewis acidity, $AlMe_3$ is known to aggressively react with many functional groups beyond −OH. In extreme cases, for example, $AlMe_3$ preferentially attacks and abstracts oxygen anions from surface oxides of GaAs and $In_{0.2}Ga_{0.8}As$ substrates.[502,503] As such, reaction with components in the MOF framework beyond the hydroxylated node is not extraordinary. The extra-nodal reactivity of this aggressive precursor is further corroborated by the significant loss of sample crystallinity evident in powder X-ray diffraction (PXRD) data obtained following large $AlMe_3$ exposures, Figure S1 in the SI of ref 504. Although $InMe_3$ is also Lewis acidic (albeit not as much as $AlMe_3$), the strong diffraction peaks of the parent MOF are retained even after total

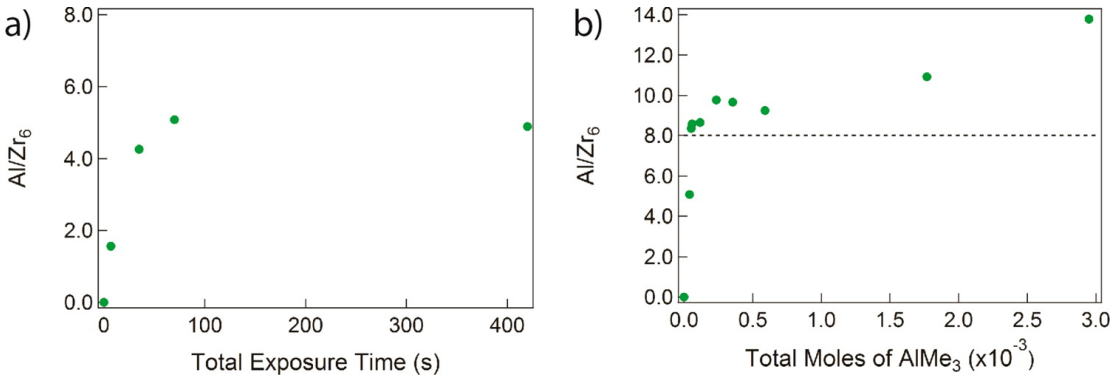

Figure 4.13: ALD metal to Zr_6 node ratio as a function of ALD process conditions. The delivery of a nonstoichiometic $AlMe_3$ dose or insufficient diffusion time produce subsaturating Al loading. In the limit of exceptionally large and long doses, the process does not exhibit self-limiting behavior.

exposures in excess of ∼2 h. Furthermore, the large specific surface area that is associated with the mesoporosity of NU-1000 is significantly degraded upon large $AlMe_3$ exposures, whereas the surface area is retained even after exposure to a 10-fold larger $InMe_3$ dose (see Supporting Information (SI) of ref 504).

The exothermic reaction pathway for trivalent metal binding derived from theory predicts metal atom placement at high-symmetry nodal sites. Each atom is expected to bridge three oxygen atoms, two deriving from previously terminal $-OH_2$ and $-OH$ groups, and one deriving from bridging core oxygen atom functionality ($\mu-O$ or previous $\mu-OH$). Experimental confirmation of ALD metal installation location was obtained from X-ray pair distribution function (PDF) analyses. This method yields atomic scale structural information with crystallographic resolution at a length scale suitable for analysis of few-atom clusters like the Zr_6 node. A differential data plot reveals the new pair correlations present after $InMe_3$ AIM, Figure 4.14.

The experimental differential PDF reflects the new atomatom distances formed upon In-loading; the distances are consistent with those derived from first-principles calculations. The differential PDF is dominated by features at short distances, suggesting that the In-siting is well-defined only locally. Two sharp peaks, centered at 2.12 and 3.33 Å, correspond to the InO bond and In$\cdots$Zr next-nearest neighbor distances, respectively (cf. 2.18 and 3.27 Å from theory, respectively). A broader feature at ∼4 Å reflects

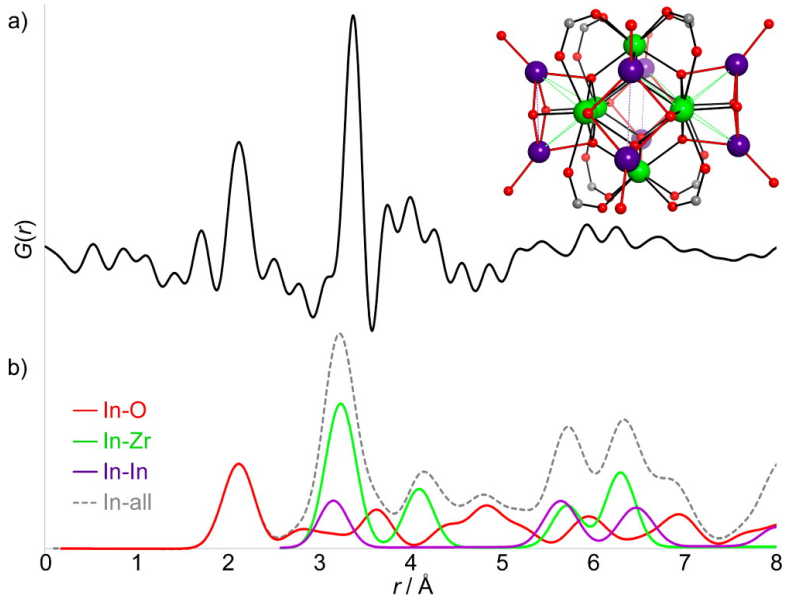

Figure 4.14: (a) Differential PDF corresponding to the new atom-atom distances formed upon $InMe_3$ AIM of NU-1000 at 75 °C following dehydration at 125 °C. (b) Partial pair PDFs calculated based on the model for In-loaded NU-1000 structure predicted by DFT. A representation of the DFT-derived model of the Zr_6 node, highlighting the new In-node distances, is inset.

longer range In$\cdots$Zr distances within the Zr-node, for which a distribution of distances and increased local disorder are evident. Peaks associated with well-defined In$\cdots$In distances are not readily evident in the experimental data, suggesting that the In atoms do not order relative to each other.

Having established the location and bonding environment of In upon exposure to $InMe_3$, we sought to further control the number of metal atoms installed on each node. In principle, the room temperature population of terminal $-$OH, terminal $-OH_2$, and $\mu-$OH on the NU-1000 node support the installation of up to 8 metal atoms. However, under conditions in which the node is dehydrated (e.g., following heating in medium vacuum), a diminished number of presenting functional groups is anticipated to yield a lower degree of metal incorporation under the same AIM conditions. Like many oxide surfaces, the Zr_6O16 node releases water through water desorption and hydroxyl recombination at increased temperatures under vacuum. In situ Fourier transform infrared spectroscopy (conventional FTIR) studies of NU-1000 as a function of temperature clearly reveal dynamics of node dehydration. At elevated temperatures (>125 °C), the intensity of non-hydrogen-bonded $-$OH, $-OH_2$, and $\mu-$OH stretches located at $\sim$3673 cm^{-1} decrease continuously with time and temperature (Figure S3 in the SI of ref 504). On the basis of these findings, we performed node dehydration at elevated temperatures prior to AIM to provide control over the number of metals to be installed on the nodes. Although we do not expect a 1:1 correlation between $-$OH population as inferred from IR and the In:Zr_6 ratio, the integrated intensity of the $-$OH stretches (i.e., a measure of $-$OH population) and the ICP-OES derived ratios of In:Zr_6 do trend together (Figure 4.15). This confirms an ability to control metal loading via node dehydration. Such ability to tune metal loading should allow further customization of node decoration, with the potential for mixed-metal attachment directly to the Zr_6 node in the future through cycles of partial dehydration, deposition, rehydration, and alternative deposition.

4.3.3 Conclusions

We demonstrate that the Zr_6-node present in the NU-1000 framework reacts with the trimethylated trivalent metal compounds $InMe_3$ and $AlMe_3$ to form stable structures with up to eight metals per Zr_6 node. $InMe_3$ exhibits strict self-limiting behavior in the limit of both excess diffusion time and moles without significant loss of crystallinity or

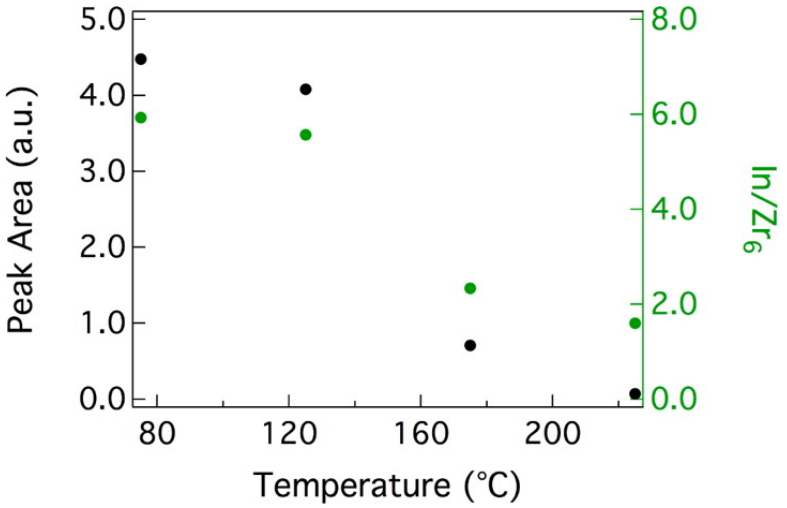

Figure 4.15: In-loading in NU-1000 as a function of node dehydration; temperature is correlated to the integrated intensity of FTIR peaks associated with −OH stretches.

internal surface area. Differential PDF analysis of In-loaded NU-1000 is consistent with theoretical prediction of a highly symmetric structure having two metals deposited on each of four faces of the Zr_6 node; a fully characterized reaction coordinate rationalizes the elementary reaction steps that lead to this structure and confirms that it is highly exothermic. In practice, the number of In per Zr_6 node saturates at a slightly less than 8:1 stoichiometric ratio, which we attribute to the presence of secondary nodes and unintentional dehydration, both of which reduce the total number of reactive sites. In contrast to $InMe_3$, which displays ideal self-limiting behavior, reactions with $AlMe_3$ evidence extra-nodal reactions with NU-1000 for large exposures, as judged by noticeable degradation of crystallinity and loss of internal surface area. These combined results begin to demarcate process variable space for AIM, i.e. temperature and choice of precursors, that must be carefully considered to achieve targeted metal loading while retaining the benefits of mesoporosity and crystallinity. We anticipate reporting soon on using these insights to achieve more ideal functionalization of NU-1000 with Al(III). Importantly, deliberate partial node dehydration at elevated AIM temperatures enables reproducible modulation of the stoichiometry for a single ALD cycle of the saturating reaction of $InMe_3$ with NU-1000, and this control should prove useful for the design of multistep ALD procedures that may involve different metal-containing precursors.

4.3.4 Experimental Section

Computational Methods

The periodic structures were computed with the generalized gradient approximation exchange-correlation functional PBE using the Vienna *ab initio* simulation package (VASP).[441,70,226,227,290,289] The VASP calculations were performed with projector-augmented wave potentials to describe the interaction between the valence and core electrons. A full gamma-point only geometry optimization was performed with a plane-wave kinetic energy cutoff of 520 eV. The energy and force convergence criteria were 1×10^{-6} and 0.05 eV, respectively.

The initial structures for the cluster models were taken from ref 489. The bare Zr_6-node cluster model is provided in Figure 4.10. For the structures shown in the reaction pathway in Figure 4.11, the core zirconium and oxygen atoms were optimized with *Gaussian 09*[185,442] using the M06-L[183] density functional and the 6-31G(d) basis set[443] on Al, O, C, and H, and the Stuttgart/Dresden effective core potential (SDD)[505] on Zr and In, and the linker atoms were fixed. Frequency calculations at 298 K were then performed at the same level of theory. A singlepoint calculation with the 6-311+G(df,p) basis set[443] was then performed to verify the nature of all stationary points. The enthalpies shown in Figure 4.11 were then computed by adding the enthalpy contribution at the 6-31G(d) level to the 6-311+G(df,p) energies ($\Delta H = \Delta E_{\text{6-311+G(df,p)}} + \Delta H_{\text{6-31G(d)}} - \Delta E_{6-31G(d)}$).

NU-1000 Synthesis

$ZrOCl_2{\cdot}8H_2O$ (97 mg, 0.30 mmol) and benzoic acid (2.70 g, 22 mmol) were mixed in 8 mL of DMF (in a 6-dram vial) and dissolved using sonication. The clear solution was incubated in an oven at 80 °C for 1 h. After cooling to room temperature, $\mathbf{H_4TBAPy}$ (40 mg, 0.06 mmol) was added to this solution and the mixture was sonicated for 10 min. The yellow suspension was heated in an oven at 100 °C for 18 h. After cooling to room temperature, yellow **NU-1000** precipitate was collected by centrifuge. (7800 rpm, 5 min) and washed with fresh DMF for two times. As synthesized **NU-1000** was then suspended in 13 mL of DMF and 0.5 mL of 8 M HCl was added to acid-activate the zirconium node. This mixture was heated in an oven at 100 °C for 24 h. After cooling down to room temperature, the supernatant was removed by centrifuge, and

the material was washed twice with fresh DMF. Subsequently the solid materials were washed twice with acetone and soaked in acetone for additional 12 h. Then the acetone was removed by centrifuge, and the solid was briefly dried in an oven at 80 °C. The solid material was activated on a SmartVacPrep station (Micromeritics) under dynamic vacuum at 120 °C until an outgassing rate of $\leq$0.002 mmHg·min^{-1} was reached.

ALD in MOFs (AIM)

AIM process was performed in a Savannah S200 system (Cambridge Nanotech, Cambridge, MA). In-line Entegris Ni filtered nitrogen (N_2) was continuously introduced to the ALD chamber at a flow rate of 20 sccm to maintain a chamber base pressure of ~0.5 Torr. Typically, 10 mg of NU-1000 powder was heated to 125 °C to remove physisorbed water followed by soaking at the desired AIM temperature. All ALD reactions were carried out in quasi-static mode. Standard pulse times for water vapor, $InMe_3$, and $AlMe_3$ were 1, 5, and 0.015 s, respectively.

PDF Analysis

X-ray total scattering data suitable for PDF analysis were collected at beamline 11-ID-B at the Advanced Photon Source (APS). High-energy X-rays (λ = 0.2114 Å) were used in combination with a large amorphous-silicon-based area detector to collect data to high values of momentum transfer (Q).[506] Borosilicate capillary-loaded samples of NU-1000 and $InMe_3$−AIM treated NU-1000 (125 °C dehydration followed by AIM at 75 °C followed by exposure to room ambient) were heated at 125 °C under vacuum in a flow-cell furnace[507] during the measurements. The two-dimensional X-ray scattering images were reduced to one-dimensional diffraction data within *fit2D*. The data were corrected for background, Compton scattering and detector effects within *pdfgetX2*[508] to obtain the structure function $S(Q)$. Fourier transformation of $S(Q)$ to Q_{max} = 24 Å^{-1}, yielded the total PDFs, $G(r)$. Subtraction of the PDF for pristine NU-1000 from that obtained for $InMe_3$−AIM treated NU-1000 yielded the differential PDF.[509] The bond lengths of features of interest were estimated by fitting Gaussian functions to the differential PDF data within *fityk*.[510] For comparison with the experimental differential data, partial pair PDFs for the DFT-optimized model were calculated within *PDFgui*.[511] The partial pair PDFs are given by $G(r) = (1/r)\sum_i \sum_j [((b_i b_j)/(\langle b \rangle^2))\delta(r - r_{ij})] - 4\pi r \rho_0$, where the sum

goes over pairs of atoms i and j within the model separated by r_{ij}. The scattering power of atom i is b_i and $\langle b \rangle$ is the average scattering power of the sample.

4.4 Tuning Zr_6 Metal-Organic Framework (MOF) Nodes as Catalyst Supports: Site Densities and Electron-Donor Properties Influence Molecular Iridium Complexes as Ethylene Conversion Catalysts

4.4.1 Introduction

Thermally stable metal-organic frameworks (MOFs) offer excellent but still little-explored prospects as catalyst supports.[381,421,254,512,124,513,514,515,125,516] Catalysts can be bonded to either the organic MOF linkers[517,518,519] or to the MOF nodes,[520,492,45,48] some of which are essentially small pieces of metal oxides. Such nodes are roughly comparable to conventional metal oxide catalyst supports, but, in contrast to porous metal oxides, they are almost uniform in structure and offer unique opportunities for precise tuning of their properties to influence catalyst performance.

MOF nodes that offer such opportunities include the $[Zr_6(\mu_3{-}O)_4(\mu_3{-}OH)_4(OH)_4(OH_2)_4]^{8+}$ and $[Zr_6(\mu_3{-}O)_4(\mu_3{-}OH)_4]^{12+}$ nodes that occur in NU-1000 and UiO-66, respectively.[45,425] The functional groups (e.g., OH and OH_2 groups) on these nodes provide anchoring sites for metals, and our goals were to determine how to vary the properties of catalysts supported on them and to lay a foundation for design of MOF-supported catalysts. We investigated structurally simple and essentially molecular metal catalysts on a family of MOF nodes and determined how their structures influence metal-support bonding and catalytic properties for a simple test reaction, ethylene conversion in the presence of H_2. We also sought to compare the MOF nodes with conventional catalyst supports. The strategy was to synthesize MOF node-supported metal complex catalysts precisely by using an organometallic precursor and to characterize them with complementary experimental and theoretical approaches. The MOFs UiO-66 and UiO-67 were chosen because they (and their nodes) have been well-characterized[425,521,522] and because they can be used as supports for metal complexes made from precursors such as $Ir(C_2H_4)_2(acac)$ (acac is acetylacetonate) to give catalysts that are suitable for precise characterization.[48,523]

IR spectroscopy and density functional theory (DFT) calculations were used previously in an investigation of the reactions of OH groups on the nodes of the MOFs

NU-1000 and UiO-66. In that work, catalysts bonded to the MOF nodes were made from the precursors $Ir(C_2H_4)_2(acac)$ and $Ir(CO)_2(acac)$.[48] In the work reported here, the MOF syntheses were varied by the choice of modulators to influence the number of node defect sites associated with missing linkers and thereby to vary the properties of the MOFs as catalyst supports. For example, UiO-66 was synthesized with the modulator acetic acid so that the MOF had ∼1 of 12 linkers per node missing.[428] The nodes of UiO-66 modulated by acetic acid incorporate hydrogen-bonded H_2O/OH surface groups (labeled as **site 1** in Figure 4.16) and non-hydrogen-bonded OH groups (labeled as **site 2** in Figure 4.16). We also synthesized UiO-66 and UiO-67 with various numbers of node defect sites (up to ∼4 of 12 missing linkers per node) by also using HCl as a modulator.[522] Moreover, we performed DFT calculations to provide detailed insights into the structure, reactivity, and catalytic properties of iridium catalysts bonded to the nodes of UiO-66 and UiO-67.

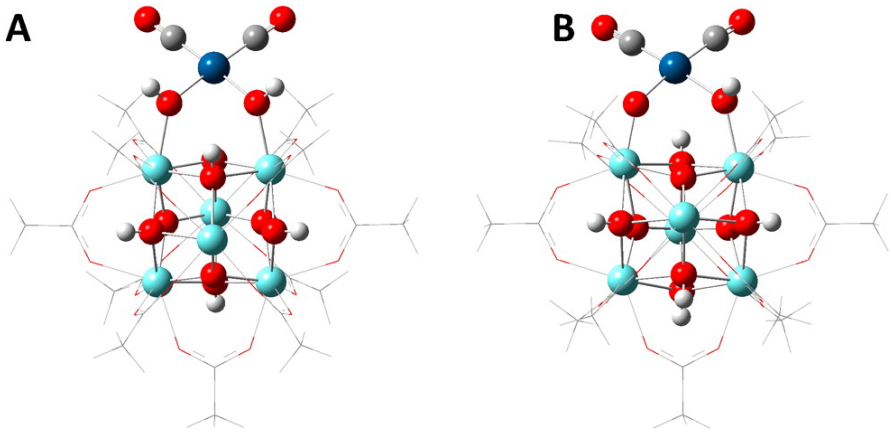

Figure 4.16: Missing linker sites in UiO-66 can be occupied by either (A) a H_2O/OH terminal pair (**site 1**) or by (B) two OH terminal pairs with a migrated proton at another portion of the node (**site 2**). Note that one of the terminal protons is replaced by an Ir(I) dicarbonyl complex.

Our results show that the synthesis conditions can be chosen to generate essentially one type of bonding site on each MOF node − that is, **site 1** on UiO-67 and **site 2** on UiO-66. The DFT calculations show that the influences of the nodes as ligands of the iridium complex catalysts are dictated by their electron-donor properties, which allows comparisons with conventional catalyst supports.

4.4.2 Experimental Methods

Synthesis of UiO-66 with HCl Modulator

$ZrCl_4$ (99.99%, 0.125 g, 0.54 mmol) and 1 mL of concentrated HCl (modulator, 37 wt %) were dissolved in 15 mL of dimethylformamide (DMF) in an 8-dram vial by using ultrasound for 5 min. The linker precursor benzene-1,4-dicarboxylic acid (0.123 g, 0.75 mmol) was then added into the solution and dissolved by ultrasound applied for ∼15 min. The vials were kept in an oven at 353 K under static conditions for 24 h. White precipitates were produced, and they were isolated by centrifugation after cooling to room temperature. The solids were washed with DMF three times to remove unreacted precursors and with methanol six times to remove the DMF. The powder then was dried at room temperature.

Synthesis of UiO-67 with HCl Modulator

ZrCl4 (99.99%, 0.067 g, 0.27 mmol) and 0.5 mL of concentrated HCl (modulator, 37 wt %) were dissolved in 15 mL of DMF in an 8 dram vial by using ultrasound for 5 min. Biphenyl-4,4-dicarboxylic acid (0.09 g, 0.38 mmol) was then added to the solution and dispersed by ultrasound applied for ∼15 min. The vials were kept in an oven at 353 K under static conditions for 24 h. A white precipitate formed, and it was isolated by centrifugation after cooling to room temperature. The solid was washed with DMF three times to remove unreacted precursors and with acetone six times to remove DMF. The powder then was dried at room temperature.

Synthesis of UiO-67 with Acetic Acid Modulator

$ZrCl_4$ (0.12 g, 0.48 mmol) and 1.0 mL of acetic acid (modulator) were dissolved in 20 mL of DMF in an 8 dram vial by using ultrasound for 5 min. Biphenyl-4,4-dicarboxylic acid (0.125 g, 0.53 mmol) was then added to the solution and dispersed by ultrasound applied for ∼15 min. The vials were kept in an oven at 393 K under static conditions for 24 h. A white precipitate formed, and it was isolated by centrifugation after cooling of the sample to room temperature. The solid was washed with DMF three times to remove unreacted precursors and with acetone six times to remove DMF. The powder then was dried at room temperature.

Synthesis of MOF-Supported $Ir(C_2H_4)_2$

Sample synthesis and handling were performed with the exclusion of moisture and air by use of a double-manifold Schlenk vacuum line and an argon-atmosphere glovebox. The precursor $Ir(C_2H_4)_2(acac)$ was synthesized as described elsewhere;[524] it has been characterized by X-ray diffraction (XRD) crystallography and 1H and 13C NMR, Raman, and infrared (IR) spectroscopies.[524]

Each supported iridium complex was prepared by bringing $Ir(C_2H_4)_2(acac)$ (36.2 mg for a 10.0 wt% iridium loading or 3.6 mg for a 1.0 wt% iridium loading) in contact with 200 mg of activated MOF powder (UiO-66 or UiO-67, activated under vacuum (10-7 Torr) at 423 or 393 K, respectively, for 24 h before use) in a Schlenk flask. The mixture was slurried in 30 mL of dried *n*-pentane (Fisher, 99%) at room temperature. After 8 h, the solvent was removed by evacuation for a day, leaving all the iridium bonded to the MOF. The resultant solids (e.g., containing 10.0 wt% iridium, with ∼1 Ir atom per node), was stored in an argon-filled glovebox.

Iridium loadings were inferred from the conditions of the syntheses, whereby all the added iridium remained in the MOF after removal of the solvent. The catalysts with 1.0 wt% iridium loadings were used only for catalytic activity measurements, and those with 10.0 wt% iridium loading were used for all other characterizations.

Synthesis of ZrO_2 and ZrO_2-Supported $Ir(C_2H_4)_2$

The amorphous metal oxide support ZrO_2 was synthesized by a precipitation method. $ZrO(NO_3)_2 \cdot xH_2O$ (99.99%, 3.64 g, 15.74 mmol) and 28.9 mL of concentrated HNO3 (65 wt %) were dissolved in 1 L of deionized water by stirring for 30 min. Ammonium hydroxide solution (100 mL, 28% NH_3 in water) was then added dropwise to the solution with vigorous stirring, and the final pH value was controlled to be $9-10$. The resultant suspension was aged for 4 h by continuous stirring followed by filtration. The precipitate was washed 6 times with deionized water to give a neutral pH value and then dried at 393 K overnight. The powder was calcined at 773 K in O_2 for 2 h and evacuated at 773 K for 12 h.

To prepare the ZrO_2-supported iridium complex, $Ir(C_2H_4)_2(acac)$ (18.1 mg) and the calcined ZrO_2 powder (1.0 g) in a Schlenk flask were combined into a slurry in

dried n-pentane (30 mL) at room temperature. After 24 h, the solvent was removed by evacuation for 24 h so that all of the iridium remained on the support. The resultant solid, containing 1.0 wt% iridium, was stored in the glovebox. Brunauer-Emmett-Teller (BET) Measurements

All N_2 isotherms were measured with a Micromeritics Tristar II instrument. Measurements were performed at 77 K, with the temperature held constant with a liquid nitrogen bath. Consistency criteria were adapted to choose an appropriate pressure range for Brunauer-Emmett-Teller (BET) surface area calculations.

Infrared Spectroscopy

A Bruker IFS 66v/S spectrometer with a spectral resolution of 2 cm^{-1} was used to collect transmission IR spectra of power samples. Approximately 30 mg of solid sample in the glovebox was pressed into a thin wafer and loaded into a cell that was also a flow reactor (In-Situ Research Institute, South Bend, IN). The cell was sealed and connected to a flow system, and spectra were recorded while reactant gases flowed through the cell at various temperatures. Each spectrum is the average of 64 scans.

X-ray Absorption Spectroscopy

X-ray absorption spectra were collected at X-ray beamline 2-2 of the Stanford Synchrotron Radiation Lightsource (SSRL). The storage ring electron energy was 3 GeV, and the ring current was ∼300 mA. A double-crystal Si(220) monochromator was detuned by 20%−25% at the Ir L_{III} edge to minimize the effects of higher harmonics in the X-ray beam. Samples were transferred to the X-ray absorption spectroscopy cells in an inert atmosphere glovebox and sealed before mounting in the X-ray beam.

Catalytic Reaction Experiments

Ethylene hydrogenation catalysis was carried out in a conventional laboratory once-through tubular plug-flow reactor at 298 K and 1 bar. The catalyst (10−50 mg) was mixed with 10 g of inert, nonporous $\alpha-Al_2O_3$ powder and loaded into the reactor in the argon-filled glovebox. The feed partial pressures were 100 mbar of C_2H_4, 200 mbar of H_2, and 700 mbar of helium, with a total flow rate of 100 mL(NTP)/min.

Products were analyzed with an online Agilent Model 6890 gas chromatograph. The ethylene conversions were <5%, and the reactor was well-approximated as differential, determining reaction rates directly.

4.4.3 Computational Methods

We used the same computational models that we previously applied[48] to some of these systems, and which have also been used to predict the structural properties of many other MOFs, as well as their behavior as gas adsorbents, catalysts, catalyst supports, and optical materials.[394] Specifically, periodic DFT calculations were carried out with the PBE[322] exchange-correlation functional augmented with dispersion correction terms, PBE-D3[105] to model the entire materials. For UiO-66/67, one linker was removed from each of the periodic unit cells, in order to describe the terminal H_2O/OH and OH/OH sites crucial for chemisorbing iridium complexes. For NU-1000, there was no need to perform this modification, as its Zr_6 nodes naturally have terminal H_2O/OH groups. The periodic DFT calculations were carried out with the *VASP 5.3.3*[226,227] package using plane wave basis sets, the projector augmented wave (PAW[235]) method for describing electron-ion interactions, an energy cutoff of 550 eV, and 1×1×1 Monkhorst-Pack K-point meshes.

The Zr_6 nodes of NU-1000 and UiO-66/67 were subsequently modeled as finite clusters that were extracted from optimized periodic unit cells to allow investigation of the details of the supported iridium complexes. The cluster models were obtained from the optimized periodic unit cells by truncating the organic linkers to benzoate ($C_6H_5COO^-$) and acetate (CH_3COO^-) groups, for NU-1000 and UiO66/67, respectively. These types of models have been shown to properly describe the nature of the terminal water or hydroxyl groups on the Zr_6 nodes of NU-1000 as well as the catalytic properties of species bonded to the nodes of this MOF.[48,446] The cluster models were optimized using the M06-L[183] density functional, the def2-svp basis set for C, H, and O atoms, and the def2-tzvpp[525,526,182] basis sets with associated effective core potentials for Zr and Ir atoms. In all cases, the positions of all atoms were optimized, except for the C and H atoms of the benzoate groups used in the cluster model of NU-1000. For UiO-66/67, all atoms were allowed to move during geometry optimizations. The optimizations were carried out without symmetry constraints and until tight energy and geometry convergence

criteria were attained; ultrafine grids were used.

For calculations characterizing HY zeolite, we used the same basis sets, grids, and geometry and energy convergence criteria that were used in the calculations characterizing the MOFs. We use a 33T cluster model that consists of 13 interconnected four-ring systems that face the supercage of the zeolite. A sodalite cage and two $SiO_2(OH)_2$ groups were added to complete the ring of the cluster model (Figure 4.17). In all cases, we used protons to cap dangling Si−O bonds. This cluster model was obtained from a periodic structure optimized with the PBE-D3 functional while using plane wave basis sets, as was done for the MOFs.

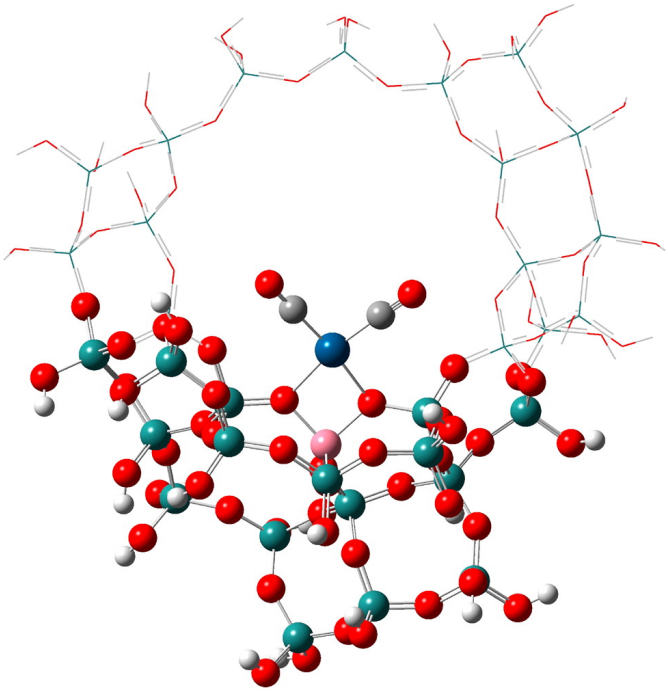

Figure 4.17: 33T Cluster Model Used in Calculations on HY Zeolite. The Zr, Ir, Si, O, C, and H atoms are shown as light blue, dark blue, green, red, gray, and white spheres, respectively. Only the atoms near the anchored $Ir(CO)_2$ complex are shown; the rest are represented by wireframes.

4.4.4 Results

Defect Sites in UiO-66 and UiO-67 Resulting from Modulation of Syntheses by HCl and by Acetic Acid

The sites on MOF nodes for bonding of catalysts are influenced by the number of missing linkers, which is influenced by modulators in the MOF syntheses.[522,428] The quantification of the missing linkers in UiO-66 and UiO-67 samples has been performed by thermogravimetric analysis (TGA) with samples under an O_2 atmosphere.[522] Assuming that the residual mass of the samples corresponds to the zirconium content in the MOFs, one can calculate the theoretical mass loss (from the loss of the linkers) for defect-free samples. The actual mass loss that was measured was compared with this value so the number of missing linkers could be quantified.

The TGA data (Table 4.5) show that ∼1.4 and 1.2 of the 12 node linkers were missing from the HCl-modulated UiO-66 and UiO-67, respectively, and only ∼0.9 and 0.6 of the 12 node linkers were missing from acetic acid-modulated UiO-66 and UiO-67, respectively. Our data are consistent with reported data,[522] showing that MOFs modulated by HCl have almost twice as many missing linker sites as MOFs modulated by acetic acid.

Table 4.5: Comparison of bonding sites on Zr_6 nodes of UiO-66 and UiO-67 synthesized with different modulators and having different types of defect sites generated on the nodes.

MOF	modulator	number of missing linkers per node[a]	bonding sites for metal complexes[b]	ref
UiO-66	acetic acid	0.9	**site 1** and **site 2**	17
	HCl	1.4	**site 2**	this work
UiO-67	acetic acid	0.6	**site 1**	this work
	HCl	1.2	**site 1**	this work

[a]Each Zr_6 node is bonded to 12 linkers at a maximum.
[b]**site 2** is characterized by IR bands at 3780 and 3692 cm^{-1}, **site 1** by a band at 2745 cm^{-1}.

Furthermore, the IR band intensities of the hydroxyl groups at missing linker sites (3780, 3692, and 2745 cm^{-1}) are much greater for the MOFs modulated with HCl than

those modulated with acetic acid (Figure 4.18, as well as Figure S1 in the Supporting Information (SI) of ref 527). The non-hydrogen-bonded OH bands at 3780 and 3692 cm^{-1}, which characterize **site 2** on HCl-modulated UiO-66 (Figure 4.18A), are more intense than previously reported hydroxyl bands characterizing **site 2** of acetic acid-modulated UiO-66,[48] indicating that more bonding sites are generated by using HCl as the modulator rather than acetic acid. The hydrogen-bonded H_2O/OH band characterizing UiO-67 (at 2745 cm^{-1} (**site 1**)) was also found to be more intense when HCl was used as the modulator (Figure 4.18B) rather than acetic acid (Figure S1B in the SI of ref 527).

The samples with various defect site densities provide an essential opportunity to vary the loading of catalytically active iridium complexes on the nodes.

The IR spectra show that the missing linker sites on HCl-modulated UiO-66 were covered by non-hydrogen-bonded OH groups (**site 2**, Figure 4.18A). The lack of a band near 2745 cm^{-1} indicates the absence of hydrogen-bonded OH groups on this MOF.

On the other hand, samples with only **site 1** were generated on the nodes of UiO-67 modulated by either HCl or acetic acid, as evidenced by the sharp band (with HCl modulator, Figure 4.18B) and the weak band (with acetic acid modulator, Figure S1B in the SI of ref 527), each at 2745 cm^{-1}, with both spectra lacking bands at 3780 and 3692 cm^{-1} (Figure 4.18A, as well as Figure S1A in the SI of ref 527); these results indicate the absence of non-hydrogen-bonded OH groups on this MOF.

Thus, UiO-66 and UiO-67 were prepared, each with only one type of site for metal bonding, offering the opportunity for the preparation of unique supported metal complexes, thereby facilitating precise structure determinations and allowing a comparison of the two MOFs as catalyst supports. The key results comparing the MOFs are summarized in Table 4.5.

DFT calculations representing the cluster model of UiO-66/67 predict the O-H stretching of the hydrogen-bonded OH group of **site 1** at 2805.2 cm^{-1}, compared with the experimental value of 2745 cm^{-1}. This comparison suggests that a scaling factor of ∼0.979 is appropriate for hydrogen-bonded OH groups. The other O-H stretching modes (mainly of μ_3-OH groups) were calculated to have frequencies of ∼3872 and 3899 cm^{-1}. These also overestimate the experimental values, 3642 and 3674 cm^{-1}, respectively (Figure 1). This comparison suggests that a scaling factor of ∼0.94-0.98 is

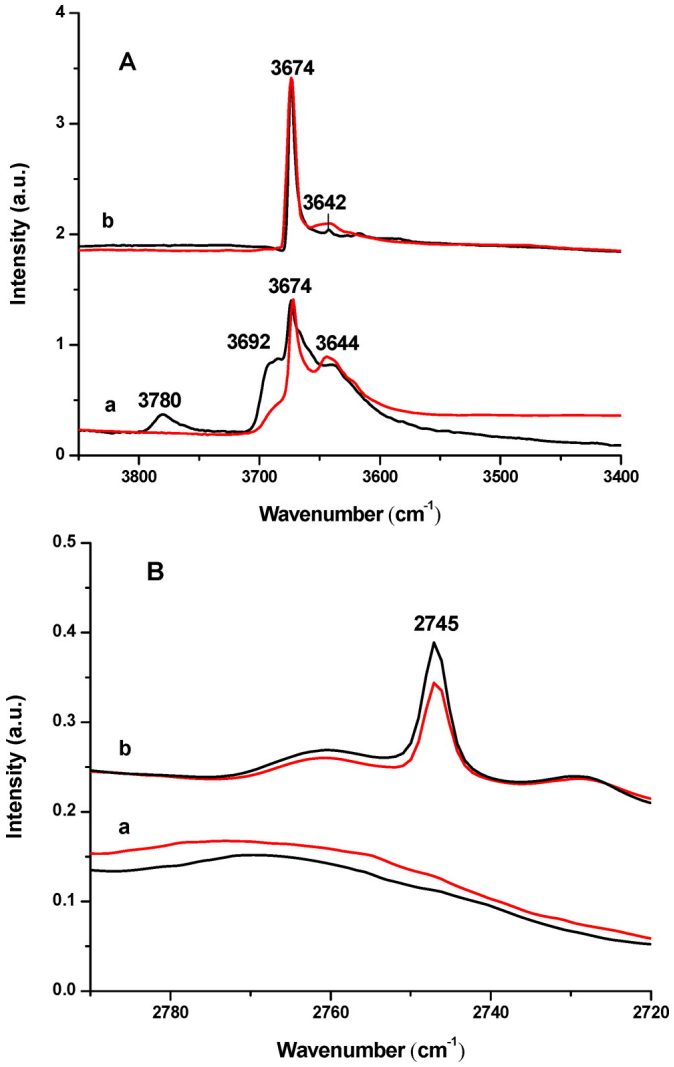

Figure 4.18: IR spectra characterizing the (A) OH region and (B) hydrogen-bonded H_2O and OH regions characterizing (a) bare UiO-66 and (b) bare UiO-67 (black) and the samples formed by adsorption of $Ir(C_2H_4)_2(acac)$ on them (red).

needed for the calculated vibrational frequencies.[48,246] The values of these scaling factors lead us to suggest that a single value might not account satisfactorily for the relative contributions of anharmonic effects in hydrogen-bonded and non-hydrogen-bonded OH groups. Nonetheless, the predicted splitting between the calculated μ_3-OH stretching frequencies at 3872 and 3899 cm^{-1} (27 cm^{-1}) matches the measured splitting well: 3642 and 3674 cm^{-1} (32 cm^{-1}).

The calculations for **site 2** predict the μ_3-OH stretching modes at ∼3869 and 3901 cm^{-1}, similar to the values for **site 1**. However, there is no hydrogen-bonded OH group in the **site 2** structure and, thus, no peak in the region near 2700−2800 cm^{-1}.

Bonding of Iridium Complex to Surface Sites on UiO-66 and UiO-67 Nodes

Samples prepared from $Ir(C_2H_4)_2$(acac) and the MOFs UiO-66 and UiO-67 made with HCl modulation and UiO-67 made with acetic acid modulation were characterized by IR and extended X-ray absorption fine structure (EXAFS) spectroscopies and DFT calculations. The results show that the iridium complexes reacted with hydroxyl groups on the nodes, as shown by the decreased intensities of the O-H bands at 3780 and 3692 cm^{-1} in the IR spectra of Figure 4.18A characterizing UiO-66 made with the HCl modulator, UiO-66(HCl), and the O-H-O band at 2745 cm^{-1} characterizing UiO-67(HCl) in Figure 4.18B and UiO-67(acetic acid) in Figure S1B from the SI of ref 527. The chemisorption reactions were accompanied by the removal of acac ligands from the iridium, as shown by the lack of the shells associated with acac ligands in the EXAFS data (Table 4.6). We infer that acac was converted to Hacac on the basis of reported results characterizing the reaction between the precursor and HY zeolite, which showed that an IR band at 1537 cm^{-1}, assigned as $\nu_{as}(CCC)_{ring}$ of Hacac, appeared after the reaction.[528] However, this band was not distinguishable in the spectra of our MOF samples, because of the strong interfering absorption by the organic linkers. DFT calculations characterizing the NU-1000 cluster model show that the region near 1638-1668 cm^{-1} includes intense vibrations assigned to the asymmetric stretching of the C-O bonds of the carboxylate groups of the organic ligands, ν_{as}(OCO) (see the SI of ref 527). Application of a scaling factor of 0.941, to the region around 1638-1668 cm^{-1} obtained for the non-hydrogen bonded OH groups, brings it near 1541−1570 cm^{-1}, explaining our inability to distinguish the $\nu_{as}(CCC)_{ring}$ of Hacac in our MOF samples.

Table 4.6: EXAFS structural parameters representing $Ir(C_2H_4)_2$ supported on UiO-67 Zr_6 Nodes[a] and $Ir(CO)_2$ supported on NU-1000 Zr_6 Nodes.[b]

	EXAFS				DFT
shell	N	R (Å)	$103\times\Delta\sigma^2$ (Å^2)	ΔE_0 (eV)	R (Å)
			$Ir(C_2H_4)_2$/UiO-67		
Ir−Ir	*c*	*c*	*c*	*c*	n/a
Ir−O_t	2.1	2.15	9.8	6.7	2.13
Ir−C	4.0	2.09	9.9	−4.2	2.09
Ir−O_b	2.1	3.45	11.0	−0.7	3.62
Ir−Zr	1.8	3.62	14.5	−3.5	3.82
			$Ir(CO)_2$/ NU-1000		
Ir−Ir	c	c	c	c	n/a
Ir−O_t	2.0	2.05	5.4	−5.2	2.11
Ir−C_{CO}	2.1	1.97	14.6	−5.9	1.83
Ir−O_{CO}	2.1	2.99	14.5	7.4	2.98
Ir−O_b	1.9	3.13	6.8	−5.6	3.39
Ir−Zr	2.0	3.55	14.2	−0.7	3.72

[a]Notation: O_t, O atoms of terminal OH groups on Zr_6 node; C, ethylene carbon; O_b, O in bridging μ_3−OH or μ_3−O group on Zr_6 node; N, coordination number; R, distance between absorber and back-scatterer atoms; $\Delta\sigma^2$, disorder term; ΔE_0, inner potential correction. Estimated EXAFS error bounds: N, ±20%; R, ±0.02 Å; $\Delta\sigma^2$, ±20%; ΔE_0, ±20% (errors characterizing the Ir−Zr contribution are greater); fit range: $3.85 <$ k (wave vector) < 13.61 $\AA^{-1}$; $0.5 < R < 4$ Å; goodness of fit value = 2.5.
[b]Data for NU-1000 have been obtained from ref 48.
[c]Contribution not detectable. Details of the EXAFS data fitting are as reported previously.[48]

The iridium became bonded to the nodes of UiO-66 and UiO-67, as shown by the EXAFS data indicating an $Ir-O_{support}$ coordination number of nearly 2 (EXAFS data were recorded for UiO-67 and NU-1000, but not UiO-66; see Table 4.6) and consistent with DFT calculations.

The calculated structural properties of $Ir(C_2H_4)_2$ supported at **site 1** of UiO-67 Zr_6 nodes are compared with the EXAFS data in Table 4.6. Overall, the $Ir-O_t$ (O_t represents oxygen in terminal OH groups of a node) and Ir−C bond lengths obtained from DFT calculations agree well with the EXAFS data, to within 0.02 Å. However, the calculations overestimate the Ir−Zr distances by 0.20 Å, consistent with the results reported for $Ir(CO)_2$ supported on NU-1000 (Table 4.6).[48] Moreover, the calculations show that the Ir atom is closer to the O atom of the bridging μ_3-OH (3.092 Å) than to the bridging μ_3-O group (4.156 Å). These results give an average $Ir-O_b$ distance of 3.62 Å, agreeing within error with the EXAFS value of 3.45 Å (Table 4.6) and supporting the value of the coordination number of 2.1 for the $Ir-O_b$ structural parameter determined in the EXAFS data fitting.

Groups on Zr_6 Nodes for Bonding Iridium Complexes

The modulators HCl and acetic acid provide control of the node sites that bond to the iridium complexes. The spectra of Figure 4.18 show that the hydroxyl band of **site 2** on UiO-66 and that of **site 1** on UiO-67 were greater in intensity when the modulator was HCl rather than acetic acid. In earlier work,[48] two types of bonding sites for metal complexes on UiO-66 were observed when the modulator was acetic acid. In contrast, only **site 2** defects were observed when the modulator was HCl. The results thus indicate that the topology of the Zr_6 node is markedly influenced by the modulator.

We infer that the topology of the Zr_6 node is also influenced by the type of solvent used for washing the MOF in the syntheses, because we observed both **site 1** and **site 2** when we used acetone instead of methanol to wash the HCl-modulated UiO-66 (Figure S7 in the SI of ref 527).

Because the HCl-modulated UiO-67 (washed with acetone) and NU-1000 (treated by HCl after synthesis and washed with acetone) are characterized by only **site 1** on their nodes, we further infer that the topology of the Zr_6 node is also influenced by the local structure of the pore and the crystal structure of the MOF.

The MOF nodes were further characterized by probing with reactive iridium complexes. Because the iridium complexes that became bonded to UiO-67(HCl) evidently consist of only one type of species, we took advantage of its simplicity to conduct the experiments described below − complemented by those with iridium complexes on UiO-67(acetic acid), which consisted of mixed species.

Because UiO-67 modulated with acetic acid has far fewer defect sites than that modulated with HCl, adsorption of the same number of iridium complexes on each of these two MOFs (10 wt%) gave iridium complexes that were all chemisorbed on the nodes of UiO-67(HCl) but iridium complexes that were both physisorbed and chemisorbed on UiO-67(acetic acid) with its limited number of missing linker sites, as shown by the IR spectra. The results are consistent with the inference that the bonding sites for the metal complexes were the hydroxyl groups on the missing linker sites of the MOFs nodes.

Comparison of Reactivities of Various MOF Node Sites with $Ir(C_2H_4)_2$(acac)

When $Ir(C_2H_4)_2$(acac) reacted with UiO-66(HCl) having essentially all of the node surface sites present in the form of **site 2**, characterized by IR bands at 3692 and 3780 cm^{-1}, the intensity of the 3692 cm^{-1} band decreased significantly, and the 3780 cm^{-1} band disappeared, showing that the iridium complex reacted with these sites as it was chemisorbed. However, the intensities of the 3674 and 3644 cm^{-1} bands characterizing μ_3−OH groups remained essentially unchanged during the chemisorption, showing that, as the iridium complex reacted with the terminal hydroxyl groups of **site 2** of UiO-66, it did not react with bridging μ_3−OH groups.

In contrast, the reaction between $Ir(C_2H_4)_2$(acac) and UiO-67(HCl) and UiO-67(acetic acid) − with all of the node surface sites being **site 1**, took place at these sites, as indicated by the decrease in intensity of the 2745 cm^{-1} band (Figure 4.18B, as well as Figure S1B from ref 527). The bridging μ_3−OH group (characterized by bands at 3674 and 3642 cm^{-1}, Figure 4.18A) did not react with the organoiridium precursor.

IR spectra in the ν_{CH} region of the UiO-66(HCl)-supported sample (Figure 4.19) demonstrate the presence of ethylene ligands bonded to the iridium, as indicated by the bands at 3061 and 3036 cm^{-1}. These bands are assigned to ν_{CH} of π-bonded ethylene. The frequencies nearly match those of $Ir(C_2H_4)_2$(acac).[524] These observations indicate

that the ethylene ligands remained bonded to the iridium during the chemisorption.

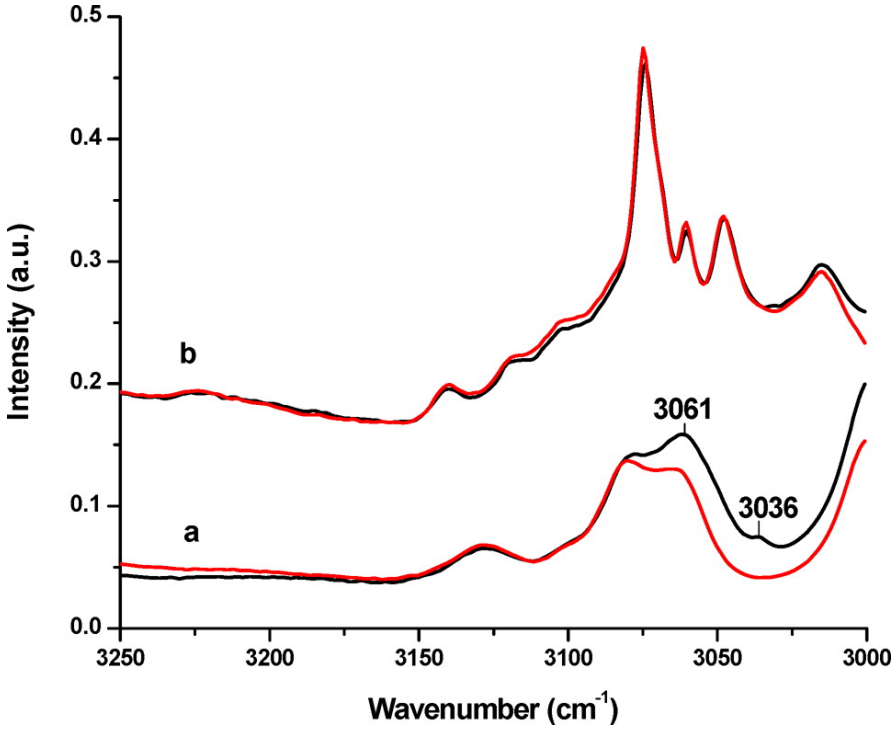

Figure 4.19: IR spectra in the ν_{CH} region characterizing the samples formed by adsorption of $Ir(C_2H_4)_2(acac)$ on (a) UiO-66(HCl) and (b) UiO-67(HCl) (black) after it had been treated with a pulse of CO in helium for 3 min (red).

The DFT calculations predict that the most intense ν_{CH} stretching modes of the ethylene ligands supported at the iridium center of **site 2** appear at ∼3194 and 3172 cm^{-1}. The splitting of these calculated frequencies (22 cm^{-1}) matches the splitting in the experimental frequencies (25 cm^{-1}). Moreover, a scaling factor of 0.957 (close to the 0.956 that was determined in our previous work with $Ir(CO)_2$ species supported on NU-1000) reduces the mean unsigned error of the theoretical calculations to ∼2.0 cm^{-1}.

The comparable IR experiments with the sample formed by adsorption of $Ir(C_2H_4)2(acac)$ on UiO-67(HCl) and UiO-67(acetic acid) provide much less information, because the bands characterizing the organic linkers in the range of 3000-3150 cm^{-1} are so intense that they would have swamped the weak bands characterizing the ethylene ligands; an equivalent statement pertains to UiO-67(acetic acid). The DFT calculations predict only marginal differences between the ν_{CH} stretching modes

of $Ir(C_2H_4)_2$ supported at **site 1** and **site 2** of UiO-66.

EXAFS data characterizing the UiO-67-supported iridium complexes measured at the Ir L_{III} edge show no detectable Ir−Ir contributions, consistent with the inference that the supported iridium species were essentially mononuclear. The best fits of the data (Table 4.5) indicate that each Ir atom was bonded, on average, to two ethylene ligands as well as the two oxygen atoms of the support, as shown by the values of the Ir−C and Ir−O coordination numbers of nearly 4 and nearly 2, respectively. The data include an Ir−O_b and an Ir−Zr contribution with coordination numbers of 2.1 and 1.8 at distances of 3.45 and 3.62 Å, respectively, consistent with the IR data (Figure 1) and the inference that the iridium complexes were bonded at **site 1** of the Zr_6 node where a proton had been removed by the chemisorption.

The aforementioned good agreement between the structural parameters obtained by EXAFS spectroscopy and DFT notwithstanding, there is some disagreement between the corresponding Ir−Zr distances (Table 4.6). A similar situation in which the calculated Ir−Zr distance overestimates the fitted EXAFS data by ∼0.2−0.3 Å was encountered in our reported work on NU-1000,[48] consistent with the results of previous DFT/EXAFS investigations that were previously referenced.[48] (We did not determine EXAFS data for the samples containing mixtures of chemisorbed and physisorbed iridium complexes, because of the challenge of fitting such data for mixtures of species.)

Reaction of MOF Node-Supported $Ir(C_2H_4)_2$ Complexes with CO Experimental Evidence

We used CO and IR spectroscopy to probe the supported iridium species. When the sample of $Ir(C_2H_4)_2$ supported on UiO-66(HCl) or on UiO-67(HCl) or UiO-67(acetic acid) was exposed to a pulse of CO at 298 K and 1 atm (∼80 CO molecules per Ir atom), the initially π-bonded ethylene ligands in the supported $Ir(C_2H_4)_2$ complexes were readily replaced by CO, as shown, for example, by the disappearance of the IR bands at 3061 and 3036 cm^{-1} when the support was UiO-66(HCl) (Figure 4.19). Furthermore, the mass spectra of the effluent gas gave evidence of ethylene formed from each of these supported samples. There was a concomitant growth of ν_{CO} bands at 2074 and 1996 cm^{-1} (characterizing iridium complexes on **site 2**) when the support was UiO-66(HCl) and at 2066 and 1990 cm^{-1} (on **site 1**) when the support was UiO-67(HCl) or

UiO-67(acetic acid) (Figure 4.20, as well as Figure S2 in the SI of ref 527). The spectra indicate chemisorbed iridium *gem*-dicarbonyls[529,530] and demonstrate (with the lack of bridging carbonyl spectra) that the iridium species were mononuclear. The different frequencies of the carbonyl bands are evidence of differences between the various MOF nodes as electron-donor ligands; this point is developed below.

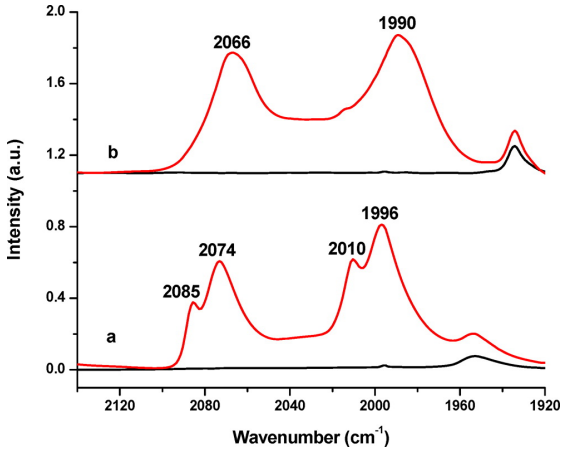

Figure 4.20: Infrared (IR) spectra in the ν_{CO} region characterizing the complexes initially present as $Ir(C_2H_4)_2$ complexes supported on (a) UiO-66(HCl) and (b) UiO-67(HCl) in flowing helium (black) and after contact with a pulse of CO in helium at 298 K and 1 bar for 3 min (red).

We also detected physisorbed $Ir(CO)_2(acac)$ on UiO-66(HCl) and on UiO-67(acetic acid) after the CO treatments. The IR spectra show that, in addition to the anchored iridium complexes, other iridium complexes were present that reacted with CO, as shown by the bands at 2085 and 2010 cm^{-1} (Figure 4.20 and Figure S2 from the SI of ref 527).[48] We infer from the band locations that physisorbed $Ir(C_2H_4)_2(acac)$ was present, and the changes in the spectra show that it was readily converted to $Ir(CO)_2(acac)$ when exposed to CO. The physisorbed species might have resided on the external MOF surfaces and/or been associated with the organic linkers.

Computational Evidence

The reaction of CO with $Ir(C_2H_4)_2$ complexes supported on the Zr_6 nodes of UiO-66/67 and NU-1000 is suggested to proceed stepwise, as shown in reactions 4.1-4.3.

$$Ir(C_2H_4)_2 + CO \rightarrow Ir(C_2H_4)_2(CO) \tag{4.1}$$

$$Ir(C_2H_4)_2(CO) \rightarrow Ir(C_2H_4)(CO) + C_2H_4 \tag{4.2}$$

$$Ir(C_2H_4)(CO) + CO \rightarrow Ir(CO)_2 + C_2H_4 \tag{4.3}$$

and, overall,

$$Ir(C_2H_4)_2 + 2CO \rightarrow Ir(CO)_2 + 2C_2H_4 \tag{4.4}$$

Reactions 4.1-4.3 result in the formation of $Ir(C_2H_4)_2CO$ (A), $Ir(C_2H_4)CO$ (B), and $Ir(CO)_2$ (C). Reaction 4.4 depicts the overall exchange of two ethylene ligands with CO. The calculated free-energy changes (ΔG) associated with these reactions at 298.15 K and 1.000 bar are presented in Table 4.7.

Table 4.7: Calculated free energies of the reactions that occur when supported $Ir(C_2H_4)_2$ species react with CO gas.

	Free Energy (kcal/mol)		
		UiO-66/67	
reaction	NU-1000	**site 1**	**site 2**
(1)	−20.6	−20.1	−19.2
(2)	−0.9	−2.0	−2.6
(3)	−15.8	−15.6	−17.3
(4)	−37.3	−37.7	−39.2

The optimized structures of $Ir(C_2H_4)CO$ and $Ir(C_2H_4)_2$ are shown in Figure 4.21. Our calculations show that the overall reaction depicted in reaction 4.4 is significantly exoergic, which is a result that is not surprising as CO is a stronger σ- and π-donor than C_2H_4.

The calculated frequencies of the C−O stretching vibrations in $Ir(CO)_2$ supported on UiO-66 were found to be 2165 and 2090 cm^{-1} for **site 1**, in contrast to 2173 and 2104 cm^{-1} for **site 2**.[48] The trends in the magnitude of these vibrational frequencies

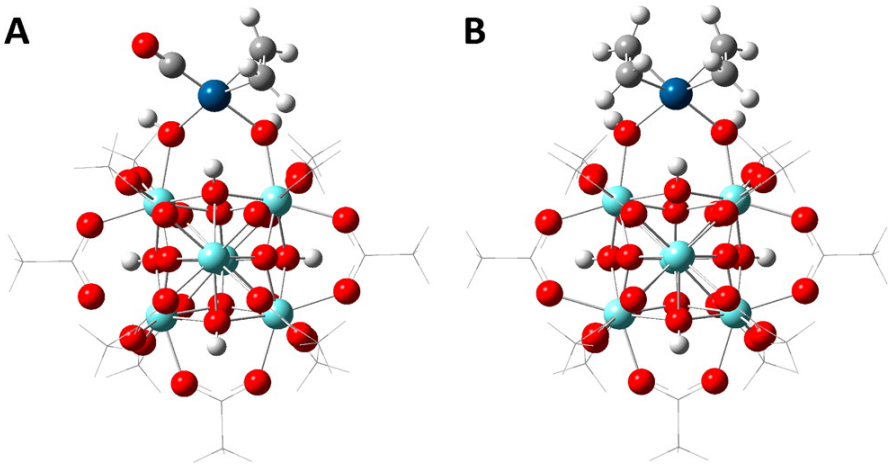

Figure 4.21: Optimized structure of (A) the $Ir(C_2H_4)CO$ aomplex formed after exposure of UiO-66/67 node-supported $Ir(C_2H_4)_2$ complexes to CO and (B) the UiO-66/67 node-supported $Ir(C_2H_4)_2$ complex (color scheme: light blue, Zr; red, O; dark blue,: Ir; gray, C; white, H.)

agree well with the empirical results presented in Figure 4.20. Indeed, application of a scaling factor of 0.956 reduces the mean unsigned error in the calculated values (relative to the experimental values) to $\sim$4.2 cm^{-1}.

Reactivities with Ethylene of $Ir(CO)_2$ Complexes on Nodes of UiO-66 and of UiO-67 Experimental Evidence

Further evidence of the electron-donor properties of the supports was determined in experiments characterizing the replacement of CO ligands on the iridium complexes with ethylene from a stream flowing at 298 K and 1 bar. Changes in the IR spectra in the ν_{CO} region occurred rapidly for both $Ir(CO)_2$ supported on UiO-66(HCl) and that supported on UiO-67(HCl); the initial iridium *gem*-dicarbonyl bands at 2074 and 1996 cm^{-1} characterizing the UiO-66-supported complexes and at 2066 and 1990 cm^{-1} characterizing the UiO-67-supported complexes decreased in intensity with time, with the simultaneous growing in of two bands, at 2038 and 2021 cm^{-1} for UiO-66-supported complexes, and the growing in of a band at 2021 cm^{-1} for the UiO-67-supported complexes.

The bands characterizing the UiO-66-supported species are assigned to $Ir(C_2H_4)_2(CO)$ and to $Ir(C_2H_4)(CO)$, respectively. These assignments are based on the

results of a spectroscopic investigation of the HY zeolite-supported isostructural $Ir(CO)_2$ complexes and products formed from them when they were subjected to the same treatment conditions, whereby the initial ν_{CO} bands of $Ir(CO)_2$ on HY zeolite at 2038 and 2109 cm^{-1} shifted to 2054 and 2087 cm^{-1}; these are assigned to $Ir(C_2H_4)(CO)$ and $Ir(C_2H_4)_2(CO)$, respectively.[531] The band characterizing the UiO-67-supported species is assigned to $Ir(C_2H_4)(CO)$ on the basis of a similar comparison.[531]

Each of these new bands remained unchanged after 20 min of contact with ethylene (Figure 4.22). Estimates based on the band areas indicate that ∼31% of the $Ir(CO)_2$ complexes supported on UiO-66(HCl) were converted to $Ir(C_2H_4)_x(CO)$ complexes, ∼5% of these to $Ir(C_2H_4)_2(CO)$ and ∼95% of these to $Ir(C_2H_4)(CO)$, and ∼50% of the $Ir(CO)_2$ complexes supported on UiO-67(HCl) were converted to $Ir(C_2H_4)(CO)$. We tested the stabilities of the $Ir(C_2H_4)_x(CO)$ species by purging the IR cell with helium for 30 min. Figure 4.22B shows that the 2021 cm^{-1} band characterizing $Ir(C_2H_4)(CO)$ on UiO-67(HCl) decreased in intensity with time, disappearing after 30 min. Concurrently, the 2066 and 1990 cm^{-1} bands of $Ir(CO)_2$ on UiO-67(HCl) increased, indicating the conversion from $Ir(C_2H_4)(CO)$ to $Ir(CO)_2$ under helium.

In contrast, the 2021 cm^{-1} band characterizing $Ir(C_2H_4)(CO)$ on UiO-66 remained unchanged during a 30 min treatment in flowing helium, indicating that this species is quite stable on UiO-66(HCl). The weak band at 2038 cm^{-1}, characterizing $Ir(C_2H_4)_2(CO)$ on UiO-66(HCl), gradually disappeared with the sample in flowing helium.

We emphasize that the physisorbed $Ir(CO)_2(acac)$ species represented by bands at 2085 and 2010 cm^{-1} did not react with ethylene. The reactivities of the iridium complexes anchored to the MOFs are compared in Table 4.8 with those of isostructural iridium complexes on other supports. For example, the $Ir(C_2H_4)_2(CO)$ species on UiO-66 are comparable in their reactivity to these complexes on dealuminated HY zeolite.

Computational Evidence

As reactions 4.1−4.4 were all calculated as being exoergic (Table 4.7), we expect that an excess of ethylene would be required to drive them in the backward direction. Furthermore, we expect that the removal of excess ethylene would result in the conversion of $Ir(C_2H_4)_2(CO)$ and $Ir(C_2H_4)CO$ to $Ir(CO)_2$. These expectations concur with the

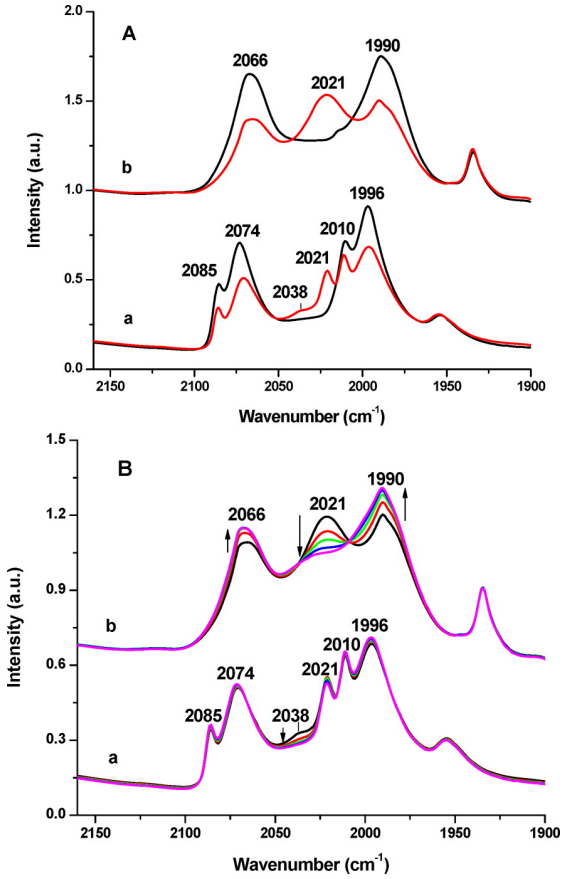

Figure 4.22: IR spectra in ν_{CO} region characterizing changes in the samples initially consisting of $Ir(CO)_2$ on (A) UiO-66(HCl)/UiO-67(HCl), after it had been exposed to flowing ethylene for 20 min at 298 K and 1 bar, (B) followed by flowing helium for 30 min. The $Ir(CO)_2$ complexes were prepared by treating the initial $Ir(C_2H_4)_2$ complexes with CO at 298 K. (For both panels, UiO-66(HCl) (trace a) and UiO-67(HCl) (trace b).)

experimental observations.

There is additional computational evidence for the exchange of CO with C_2H_4. First, the calculated CO stretching vibrational frequencies are 2084 cm^{-1} for $Ir(C_2H_4)(CO)$ and 2105 cm^{-1} for $Ir(C_2H_4)_2(CO)$, when we consider **site 1** of UiO-66/67. The DFT-calculated splitting between the vibrational frequencies of these species (21 cm^{-1}) agrees well with the experimental value (17 cm^{-1}). The theory and experiment also agree, with respect to the trends in the magnitudes of the frequencies. Moreover, the calculated free energies of reaction 4.2 are low (between −0.9 kcal/mol and −2.6 kcal/mol) and within the limits of error of DFT, thus, not inconsistent with $Ir(C_2H_4)(CO)$ being more abundant than $Ir(C_2H_4)_2(CO)$.

Iridium Complexes Supported on ZrO_2

IR spectra of ZrO_2 (Figure S3 in the SI of ref 527) show a weak, sharp peak at 3739 cm^{-1} and a broad peak at 3676 cm^{-1}. These have been assigned to terminal OH and bridging μ_3-OH groups, respectively.[532,533] After the chemisorption of $Ir(C_2H_4)_2(acac)$, the intensities of the 3739 and 3676 cm^{-1} bands decreased markedly, indicating the reaction of this precursor with the OH groups (the terminal OH band was much weaker than the bridging OH band, and thus we infer that most of the reaction was with bridging OH groups). The bands of π-bonded ethylene ligands on iridium in this sample were too weak to discern (data not shown).

When the sample of $Ir(C_2H_4)_2$ supported on ZrO_2 was brought into contact with flowing CO, new ν_{CO} bands appeared, at 2061 and 1981 cm^{-1} (Figure S4 in the SI of ref 527). These bands are characteristic of iridium *gem*-dicarbonyls and indicate that the iridium species were mononuclear.

In contrast to the behavior of the UiO-66(HCl)- and UiO-67(HCl)-supported samples, the isostructural $Ir(CO)_2$ complexes supported on ZrO_2 were not reactive with ethylene under our conditions (Figure S5 in the SI of ref 527).

Comparison of MOF-Supported Iridium Complexes As Catalysts for Ethylene Conversion in the Presence of H_2

The MOF-supported iridium complexes incorporating ethylene ligands were found to be precatalysts for the reactions of ethylene in the presence of H_2. Differential conversion

data were obtained as a function of the time on stream in the flow reactor, with typical data shown in Figure S6 in the SI of ref 527; conversions were determined from the data showing the formation of products. The strategy and details of the experimentation are as described elsewhere.[528]

The conversions were extrapolated to zero time on stream in order to provide measures of the initial activities of the (undeactivated) catalysts. In the catalysis experiments, we used a low loading of iridium on all of the supports (1 wt%) to maximize the simplicity of the catalyst structures and to avoid the physisorbed iridium complexes formed on UiO-66(HCl) at a higher loading. Thus, at this low loading, chemisorbed iridium complexes were initially present solely on **site 2** of UiO-66(HCl), and chemisorbed iridium complexes were initially present solely on **site 1** of UiO-67(HCl) and NU-1000.

The conversion of ethylene in the presence of H_2 has been shown[534] to give the hydrogenation product, ethaneand, in the presence of some catalysts, butene isomers and butane, indicating ethylene dimerization. The ethylene conversion has been investigated with iridium complexes on various supports, and a comparison of previously reported data with ours is given in Table 4.8. The earlier work[534] showed that the performance of catalysts comparable to ours for ethylene hydrogenation is strongly influenced by the support, with the reaction rate being much lower when the support is a good electron donor such as MgO than when it is a weak electron donor, such as dealuminated HY zeolite. The results summarized in Table 4.8 demonstrate that the selectivity for dimerization is also correlated with the electron-donor property of the support.

Table 4.8: Structural characterization and catalyst performance data characterizing samples initially in the form of $Ir(C_2H_4)_2$ complexes on various supports.[a]

	ν_{CO} Band Locations (cm^{-1})							Selectivity in Ethylene Conversion[e] (wt%)				
support[b]	$Ir(CO)_2$		$Ir(C_2H_4)_2$ (CO)	$Ir(C_2H_4)$ (CO)	% Ir complexes converted to $Ir(C_2H_4)$ (CO)[c]	% $Ir(CO)_2$ species converted to $Ir(C_2H_4)_x$ (CO)[c,d]	turnover freq. for C_2H_4 conversion, TOF (s^{-1})	ethane	*n*-butane	trans-2-butene	1-butene	cis-2-butene
HY zeolite	2109 (5)[f]	2038	2087	2054	60	100	0.60	95.0	0.6	2.3	0.8	1.3
UiO-66[g]	2074 (17)	1996	2038	2021	95	31	0.017	98.5	0.4	0.1	0.8	0.1
UiO-67[g]	2066 (33)	1990	n/a	2021	100	53	0.012	99.1	0.1	0.1	0.6	0.1
NU-1000	2066 (33)	1990	n/a	n/a		0	0.01	99.5	0[h]	0	0.5	0
ZrO_2	2061 (33)	1981	n/a	n/a		0	0.008	99.6	0[h]	0	0.4	0
MgO	2051 (26)	1967	n/a	n/a		0	0.003	100	0	0	0	0

[a]The data include characterization of the reaction of supported $Ir(C_2H_4)_2$ complexes to give supported $Ir(CO)_2$ complexes; the reactivities of supported $Ir(CO)_2$ complexes with C_2H_4; and catalytic activities for ethylene conversion in the presence of H_2 at 298 K and 1 bar. There was no detectable catalytic reaction in the absence of the catalyst under our conditions, and the supports alone were catalytically inactive; because some of the data reported previously were not collected under the same conditions as ours, all of the data reported in this table were obtained in this work, and the catalyst preparations were the same as those reported.

[b]Support for catalyst initially incorporating node-anchored $Ir(C_2H_4)_2$.

[c]As determined when treated in flowing C_2H_4.

[d]Fractions of $Ir(C_2H_4)_x(CO)$ (where $x = 1$ or 2) species were estimated on the basis of the area under each peak in the ν_{CO} stretching region, relative to the areas of the two ν_{CO} bands characterizing the respective $Ir(CO)_2$ species.

[e]Turnover frequency (TOF) calculated from differential conversions at zero time on stream and determined from ethylene conversions of $< 5\%$. Conditions: catalyst mass = 30 mg; feed partial pressures = 100 mbar C_2H_4, 200 mbar H_2, and 700 mbar helium; total flow rate = 100 mL(NTP)/min; catalyst iridium content = 1 wt %.

[f]The numbers given in parentheses are the full width at half-maximum (fwhm) values characterizing the carbonyl band.

[g]MOFs were modulated with HCl.

[h]Traces of butane were observed, but too small to quantify.

Our new results extend the observations to a family of supports that now includes metal oxides, zeolites, and MOFs.

4.4.5 Discussion

Effect of MOF Pore Size on the Synthesis of Supported Iridium Complexes

Figure 4.20 shows that the chemisorption of the $Ir(C_2H_4)_2(acac)$ precursor was incomplete when the HCl-modulated UiO-66 was used as the support. The results are contrasted with those for iridium complexes supported on NU-1000 (reported previously[48]) and on HCl-modulated UiO-67, on which all of the iridium complexes were chemisorbed on the nodes. We emphasize that UiO-66(HCl) and UiO-67(HCl) have similar densities of bonding sites (∼1.4 and 1.2 of the 12 sites per node, respectively; see Table 4.5).

The results indicate mass-transfer limitations in the chemisorption of the iridium complex on UiO-66. Comparable results were reported for the adsorption of $Rh(C_2H_4)_2(acac)$ or $Ir(C_2H_4)_2(acac)$ on the small-pore zeolite HSSZ-42 − the pore opening of this zeolite is 6.4 Å× 6.4 Å, which is approximately the same as the critical diameters of the precursors (∼4 Å×6 Å). Substantial adsorption evidently occurred on the outer zeolite surface, forming physisorbed species, and we infer the same for UiO-66.

The ideal structure of UiO-66 has a pore aperture diameter of ∼6 Å. The pore size of the HCl-modulated UiO-66 has been reported to be greater than that of the defect-free UiO-66,[522] because of missing linkers; however, because the defects are randomly distributed in the MOF, the pores are expected to offer a tortuous path for mass transport, with a substantial transport restriction influencing the anchoring of the iridium complex.

In contrast, the pore aperture of UiO-67 is greater than that of UiO-66 (∼8 Å),[425] and the pores of NU-1000 are even wider (with diameters of ∼12 and 30 Å[45]). Thus, we infer that the iridium complexes readily entered the pores of the latter MOFs, without significant transport restrictions and therefore resulting in more nearly uniform distributions of iridium within the pore structures than in UiO-66 − we would expect no gradients of iridium concentration in NU-1000.

Iridium Species Bonded to the Nodes of UiO-66, UiO-67, and NU-1000 Comparison of the Nodes As Electron Donors

The precursor $Ir(C_2H_4)_2(acac)$ reacted with both **site 1** and **site 2** on the Zr_6 nodes of the three MOFs, leading to the dissociation of the acac ligand. The resulting $Ir(C_2H_4)_2$ complexes were found to be anchored to each of the nodes by two $Ir-O_t$ (O_t is terminal oxygen in node **site 1** or **site 2**), as shown by the EXAFS data and DFT calculations (Table 4.6) and consistent with the IR spectra of the iridium *gem*-dicarbonyls formed from the iridium diethylene complexes on each node (Table 4.8).

The frequencies of the ν_{CO} bands are good indicators of the electron densities on the Ir atoms in the supported complexes. The available data (including literature data characterizing various metal oxide and zeolite supports; see Table 4.8) indicate the following order of electron-donor strengths: MgO > ZrO_2 > UiO-67 (= NU-1000) > UiO-66 $\gg$ HY zeolite. The results indicate that **site 2** on UiO-66 has a lower electron-donor strength than **site 1** on UiO-67 or on NU-1000. The sites and nodes in UiO-67 and NU-1000 are essentially the same in structure, and, correspondingly, their electron-donor properties are essentially the same.

The ν_{CO} bands of iridium dicarbonyls on **site 1** or **site 2** of the Zr_6 nodes appeared at exactly the same frequencies, even though the MOFs UiO-66 and UiO-67 modulated with acetic acid or HCl have significantly different numbers of defect sites per node. We thus infer that the electron-donor properties of **site 1** or **site 2** do not change significantly with the number of defect sites on the node.

As shown above, the calculated CO stretching frequencies reproduce the trends in the empirical results for **site 1** or **site 2** (and, when scaled, agree well with the experiment).

Now we focus on another measure of the electron-donor properties of the iridium centers: the calculated partial charges on the iridium centers in the supported $Ir(CO)_2$ species. In our previous work, we found that, for **site 1**, the calculated Mulliken partial charge is 0.36, which is much lower than that of **site 2** (0.51). When we use the Hirshfeld charge analysis method, we find partial charges of 0.17 and 0.29 for **site 1** and **site 2**, respectively. These results support the conclusion that the iridium center at **site 2** has lower electron-donor strength than that at **site 1**. As previously noted, the calculated partial charges of the iridium centers are similar for **site 1** in UiO-66/67 and NU-1000.

To further check whether the density of ligand defects at each metal node affects the

electron-donor strength of the anchored iridium centers, we optimized several structures for UiO-66/67, in which $Ir(CO)_2$ species were supported at 2 or 3 missing linker sites with H_2O/OH (**site 1**) pairs. In both cases (with 2 or 3 missing linkers), the partial atomic (Mulliken and Hirshfeld) charges of the iridium centers were the same within ± 0.04 as those determined when there was only one missing linker. The calculated ν_{CP} bands also remained largely unchanged (± 4.0 cm^{-1}). These results indicate that the facets of the Zr_6 nodes in NU-1000, UiO-66, and UiO-67 are well-separated and, thus, are chemically almost identical, with only little variation in properties, as a result of catalyst loading per node.

Comparison of Reactivities of Iridium Complexes on Various Supports

The iridium dicarbonyl complexes on UiO-66 and on UiO-67 reacted with ethylene, leading to the displacement of one CO ligand per Ir atom and addition of one or two ethylene ligands. The data of Table 4 demonstrate that the reactivity of iridium dicarbonyl complexes with ethylene increased in the order MgO = ZrO_2 = NU-1000 (not reactive) < UiO-66 < UiO-67 $\ll$ HY zeolite, indicating that, for the most part, the reactivity decreased with increasing electron-donor ability of the support. This pattern concurs with the calculated exoergicities of reactions 4.1-4.3 (Table 4.7). $Ir(CO)_2$ supported at **site 2** in UiO-66 is less labile for CO exchange with ethylene than that at **site 1**.

However, significantly, the observed reactivities of $Ir(CO)_2$ complexes on the nodes of UiO-66, UiO-67, and NU-1000 with ethylene do not fall in line with the order of electron-donor properties determined by the frequencies of the aforementioned ν_{CO} bands. We infer that it would be oversimplifying matters to relate the reactivities of the supported iridium complexes just to the electron-donor properties of the supports that provide ligands. We suggest that the pore structures of the MOFs and the distributions of missing linkers on the Zr_6 nodes also influence the reactivity. The DFT calculations represent model clusters and, therefore, are not expected to capture these macroscopic effects.

$Ir(CO)(C_2H_4)_2$ species formed as minority species on UiO-66 but not on UiO-67, suggesting a greater ability of UiO-66 to coordinate multiple ligands and lower electron

densities of the Ir atoms on UiO-66 than on UiO-67 − in other words, a lower electron-donor tendency of UiO-66 than of UiO-67, which is consistent with the deduction from the calculated and empirical vibrational carbonyl stretching frequencies, as well as the calculated atomic partial charges, showing that **site 2** (present only in UiO-66) has a lower electron-donor strength than **site 1** (present in UiO-66, UiO-67, and NU-1000).

Furthermore, the carbonyl band of the $Ir(CO)(C_2H_4)$ species on UiO-67 gradually decreased in intensity when the sample was present in flowing helium, indicating that ethylene ligands (or species formed from them, such as ethane formed in reactions of the ethylene ligands with hydrogen formed by reverse spillover from node OH groups[535]) desorbed. The simultaneous increase in intensity of the carbonyl bands of $Ir(CO)_2$ suggests the transfer of carbonyl ligands from one iridium complex to another. The $Ir(CO)(C_2H_4)$ species on UiO-66 were found to be more stable than those on UiO-67 in flowing helium. The data may indicate that the higher electron-withdrawing tendency of UiO-66 helps to stabilize the weakly bonded ethylene ligands.

Comparison of Catalytic Activities of Iridium Complexes on Various Supports

The data shown in Figure 4.23 indicate that the catalytic activities of the supported iridium complexes initially present as $Ir(C_2H_4)_2$ increasedboth for ethylene hydrogenation and ethylene dimerizationas the iridium complexes became more electron-deficient. The support as a ligand influences the ability of iridium to bond with and activate the ligands formed from both ethylene and H_2.[534,536]

The catalytic activities of $Ir(C_2H_4)_2$/UiO-66(HCl) summarized in Table 4.8 are the same as those of $Ir(C_2H_4)_2$/UiO-66(acetic acid) reported previously,[48] although these two MOFs are characterized by significantly different densities of node defect sites. The results indicate that the catalytic activity measured as a turnover frequency is barely, if at all, influenced by the number of defect sites in the MOF and that turnover frequency is an appropriate measure of catalytic activity. We emphasize that the activities of MOF-supported $Ir(C_2H_4)_2$ are determined by the types of bonding sites on the MOF nodes. Because **site 2** on UiO-66 has a lower electron-donor tendency than **site 1** on NU-1000 or on UiO-67, the iridium complexes on the former sites are more active than on the latter, consistent with the results presented in Table 4.7 and the results of DFT

calculations reported in our previous work.[48]

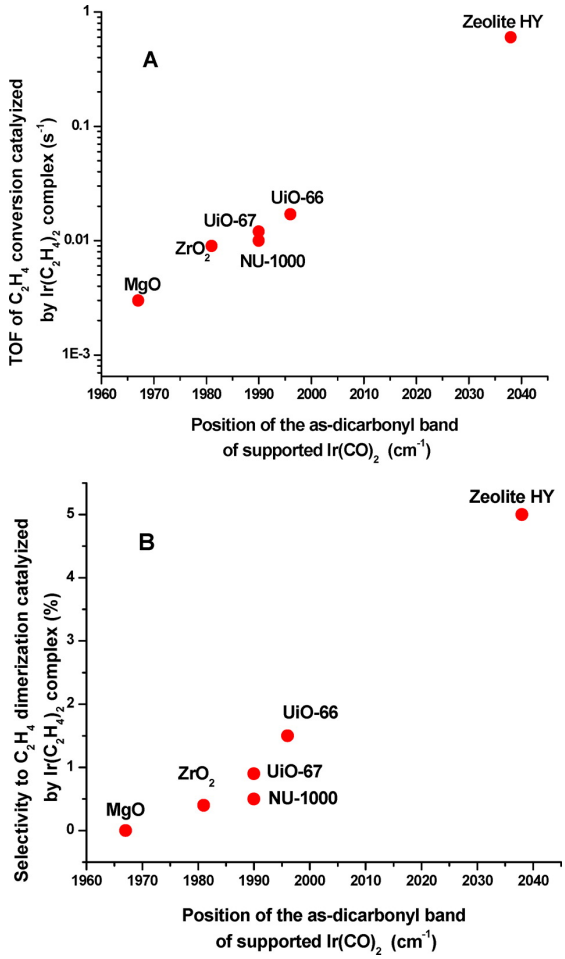

Figure 4.23: Correlation between (A) the turnover frequency (TOF) for ethylene hydrogenation and (B) selectivity for ethylene dimerization catalyzed by iridium complexes initially in the form of supported $Ir(C_2H_4)_2$ and ν_{CO} of the $Ir(CO)_2$ complexes formed from the catalysts (a higher ν_{CO},as frequency indicates that the iridium complex is more electron-deficient).

In contrast, HY zeolite-supported iridium complexes are characterized by much higher activity and selectivity for dimer formation than those supported on the MOFs with Zr_6 nodes. Work[537,538] with supported rhodium complex catalysts for ethylene hydrogenation and dimerization at 298 K and 1 bar also indicated a strong influence of the support on the catalytic activity, showing that the rate of ethylene conversion is an

order of magnitude higher when the support is HY zeolite than when it is MgO. In a further contrast between the electron-withdrawing zeolite and the electron-donating MgO, the selectivity for dimerization at our low conversions was determined to be 80% when the support was HY zeolite, whereas no dimerization was observed when the support was MgO.

We have previously used DFT calculations to show that **site 2** on UiO-66 provides lower transition state barriers for ethylene hydrogenation and dimerization than **site 1** in UiO-66 and NU-1000.(17) Therefore, it is not surprising that UiO-67 and NU-1000 (two MOFs that possess only **site 1**) have indistinguishable activities (Figure 4.23), whereas UiO-66 is more active for hydrogenation and dimerization, as a result of its more electropositive iridium centers at **site 2**.

However, it is informative to consider whether a similar trend emerges from a comparison of the calculated CO band frequencies of metal *gem*-dicarbonyl species as well as the ν_{CH} stretching vibrational frequencies of $Ir(C_2H_4)_2$ species supported on a cluster model of HY zeolite. First, the asymmetric ν_{CH} stretching frequencies of C_2H_4 in HY zeolite-supported $Ir(C_2H_4)_2$ species (3174, 3185, 3213, and 3225 cm^{-1}) are higher than those on **site 1** (3171, 3172, 3194, and 3194 cm^{-1}) or **site 2** (3180, 3182, 3199, and 3201 cm^{-1}) of UiO-66. Correspondingly, the calculated Ir−C bond lengths in the zeolite-supported species (2.08 Å) are slightly less than those in the UiO-66/67- or NU-1000-supported species (2.09 Å). These results would suggest that iridium supported on HY zeolite binds/activates C_2H_4 more strongly than that in the isostructural species on **site 1** and **site 2** on the three MOFs. However, the calculated CO frequencies of $Ir(CO)_2$ supported on the HY zeolite cluster (2174 and 2103 cm^{-1}) are similar to those obtained for $Ir(CO)_2$ on **site 2** of UiO-66 (2174 and 2104 cm^{-1}), which suggests similarities between them.

Degrees of Uniformity of Bonding Sites on Various Supports

The ν_{CO} band of *gem*-dicarbonyls of iridium on ZrO_2, UiO-67, and UiO-66 have full width at half-maximum (fwhm) values of ∼33, 33, and 17 cm^{-1}. A reported value characterizing iridium *gem*-dicarbonyls bonded to the nodes of NU-1000 is 33 cm^{-1}.[48] The fwhm values of iridium *gem*-dicarbonyls on HY zeolite and on MgO have been reported to be 5 and 26 cm^{-1}, respectively.[528,539] These values indicate that the degree

of uniformity of the iridium species on these supports increased in the order of $ZrO_2 \approx$ UiO-67 $\approx$ NU-1000 $<$ MgO $<$ UiO-66 $\ll$ HY zeolite.

The fwhm of the carbonyl band of $Ir(C_2H_4)(CO)$ on UiO-67 is markedly greater than that of the carbonyl band of $Ir(C_2H_4)(CO)$ on UiO-66 (Figure 4.22), indicating that **sites 1** on UiO-67 nodes are less uniform than **sites 2** on UiO-66 nodes. Thus, the node bonding sites vary from one MOF in the family considered here to another, with respect to their degree of uniformity.

Comparison of Nodes of UiO-66, UiO-67, and NU-1000 with ZrO_2

Bulk ZrO_2 calcined at 773 K is represented by a broad IR band centered at 3676 cm^{-1}, assigned to bridging μ_3-OH groups,[532,533] and this frequency is similar to that of the bridging μ_3-OH groups on these Zr_6 nodes. The iridium complexes are observed (Figure S3 in the SI of ref 527) to bond at these μ_3-OH groups on bulk ZrO_2, but instead at the non-hydrogen-bonded terminal OH or hydrogen-bonded H_2O/OH groups of the MOFs that contain Zr_6 nodes– μ_3-OH groups on the MOFs do not react substantially with the organo-iridium precursor under our conditions. DFT calculations confirm that the reaction of iridium complexes with μ_3-OH groups is endoergic by 28 kcal/mol, much more than the value characterizing the reaction of iridium complexes bonding with **site 1** (-4.3 kcal/mol) and **site 2** (1.2 kcal/mol).[48] The frequencies of the ν_{CO} bands of the iridium dicarbonyls bonded to these supports are indicators of the poorer electron-donor tendency of the MOF nodes than of bulk ZrO_2, corresponding to higher reactivities and catalytic activities of the MOF node-supported iridium complexes.

Comparison of UiO-66, UiO-67, and NU-1000 with Zeolites As Ligands and Catalyst Supports

To repeat, the degree of uniformity of the various supported iridium complexes is indicated by the sharpness of the ν_{CO} bands in the IR spectra. Nonuniform bonding sites on the support surfaces give broader ν_{CO} bands in the iridium *gem*-dicarbonyl spectra of the complexes on MOFs than on zeolites, which are characterized by narrow bands, with fwhm values of typically 5 cm^{-1}.[528] Our observations demonstrate that the MOF nodes present more almost-uniform sites than metal oxides, and also that there are

differences from one MOF to another (Table 4.7), but the data show that each of the MOFs offers sites that are much less nearly uniform than the sites on HY zeolite.

The origins of the heterogeneity of the MOF node sites may be a consequence in part of mobility of the hydrogen atoms on the various bonding sites. These hydrogen atoms can bridge two terminals O sites or just be located on one. This variety in bonding of the hydrogen is evidenced by the following observations: after reaction with iridium complexes, **site 1** locations on both UiO-67 and NU-1000 with two hydrogen atoms on each bonding site have similar degrees of uniformity, whereas they are both less uniform than **site 2** on UiO-66, which has only one hydrogen on a bonding site. In contrast, bonding of an iridium complex to the zeolite may remove most of the zeolite protons (which react to form Hacac), contributing to the relatively high degree of uniformity of the zeolite-supported iridium complexes.

These points remain to be clarified. The issues are important for evaluation of the prospects of applying MOF nodes as catalyst supports; because the MOF node structures are almost molecular in character and have relatively high degrees of uniformity, they are good candidates for bonding of catalytic groups guided by theory.[48]

HY zeolite-supported $Ir(C_2H_4)_2$ complexes have been found to provide entry to new chemistry of metal complexes, including activation of H_2 at 298 K leading to formation of iridium hydrides[540] and formation of reactive iridium-dinitrogen complexes.[541] We infer that, at least in part, because the three Zr_6-containing MOF nodes investigated here had weaker electron-withdrawing tendencies than HY zeolite, the rich chemistry occurring on iridium complexes on the zeolite was not observed in this work.

Nonetheless, modified MOF node compositions might be expected to open up more possibilities for new reactivities.[45] Improvement in syntheses may lead to MOF nodes with higher degrees of uniformity than those reported here, and new MOFs might offer improved opportunities for highly selective catalysts associated with highly uniform structures. Many of the reactions observed with zeolite-supported metal complexes take place in association with acidic sites on the zeolites, especially Brønsted acidic sites. The Zr_6-containing MOFs have hydroxyl groups that are Brønsted acids, but they are weakly acidic. Thus, discovery of MOFs with nodes that resemble acidic zeolites or metal oxides may be expected to lead to new opportunities for the application of MOFs in catalysis.

4.4.6 Conclusions

Molecular $Ir(C_2H_4)_2$ complexes bonded to the Zr_6-containing nodes of the MOFs UiO-66, UiO-67, and NU-1000 have been compared with isostructural complexes bonded to metal oxides and zeolites. The UiO-66 used in this work was synthesized to contain only node sites for bonding of iridium complexes that consisted of non-hydrogen bonded terminal OH groups (**site 2**), whereas our UiO-67 and NU-1000 had node sites consisting only of hydrogen-bonded H_2O/OH groups (**site 1**). The data reported here demonstrate that electron-donor tendencies of the MOF nodes and metal oxide and zeolite supports decrease in the order MgO > ZrO_2 > UiO-67 (= NU-1000) > UiO-66 $\gg$ HY zeolite. The supports are ligands for the metal complexes and influence the electron densities of the metals valence orbitals, which affect its ability to coordinate multiple ligands and its reactivity and catalytic activity and selectivity for reactions exemplified by ethylene hydrogenation and ethylene dimerization. The degree of uniformity of **site 2** on UiO-66 is greater than that of **site 1** on UiO-67 or on NU-1000, and the latter MOFs, in this respect, resemble bulk, powder ZrO_2, but all of the MOF node-supported iridium complexes are much less nearly uniform than those on HY zeolite.

As in our previous work, we show that DFT calculations can be used to provide detailed insights into the structure, reactivity, and catalytic properties of iridium catalysts bonded to the nodes of NU-1000, UiO-66, and UiO-67. The calculated ν_{CO} and ν_{CH} stretching frequencies of the iridium *gem*-dicarbonyl, $Ir(CO)_2$, and iridium diethylene species, $Ir(C_2H_4)_2$, are in good agreement with empirical results. The calculated results are crucial for identifying the locations/sites of the iridium catalysts in the MOFs. Our calculations also show that the reactivity of the CO ligands on supported $Ir(CO)_2$ sites with ethylene reflects the electron-donor properties of the iridium sites, which, in turn, are reflected by the calculated (and observed) ν_{CO} stretching frequencies and the calculated partial atomic charges. These relationships between the electronic structures of the supported iridium sites and the catalytic activities for ethylene hydrogenation and dimerization point to the possibilities for designing catalysts in which the metal site is modified by introduction of either additional electron-withdrawing ligands or coadsorbed metal centers. We envisage that the metal sites in such catalysts may be synthesized to be more or less electron-deficient and, consequently, more active and/or selective for target reactions.

4.5 Single-Site Organozirconium Catalyst Embedded in a Metal-Organic Framework

4.5.1 Introduction

Heterogeneous catalysts have many attractions versus their homogeneous counterparts including recyclability, easy separation from product streams, and, often, greater thermal stability.[542] Nevertheless, despite their broad implementation, the design and synthesis of new highly active and selective heterogeneous catalysts remain a challenge. Typically, heterogeneous catalysts are supported on structurally/chemically irregular surfaces, rendering control of reaction selectivity and establishing structure-activity relationships challenging.[543] Such information is crucial for rational catalyst design, and precision methods are needed to prepare heterogeneous catalysts in a controlled, well-defined molecular manner and for their simultaneous computational characterization.

One strategy to access structurally well-defined heterogeneous catalysts is to employ atomically periodic scaffolds. The present approach utilizes a chemically and thermally robust metal-organic framework (MOF) in lieu of a traditional oxide/chalcogenide/nitride or activated carbon platform for supporting molecular complexes.[544,545] MOFs are three-dimensional, sterically/electronically tunable, crystalline, porous materials composed of inorganic nodes and organic linkers.[381,256,254,124] In contrast to the irregular surfaces of classical SiO_2 or Al_2O_3 supports, MOFs have inherently uniform surface structures.

Given the periodicity of MOFs, the potential to precisely determine atomic positions using single crystal X-ray diffraction, and reports of MOF-based catalytic selectivity,[451,516] we consider them promising and underexplored catalytic scaffolds. One class of MOFs that has gained attention for exceptional stability are Zr- and Hf-based MOFs,[426,111,110] such as NU-1000 (Zr) or Hf-NU-1000, which consist of Zr6 or Hf_6 nodes [M6($\mu_3-O)_4(\mu_3-OH)_4(OH)_4(H_2O)_4$, M = Zr, Hf] and the tetra-carboxylate linker 1,3,6,8-tetrakis(*p*-benzoate)pyrene (H_4TBAPy).[451,45] These MOFs have large 29-30 Å hexagonal mesopores that facilitate mass transport of both catalyst precursors and reactants/products, as well as accessible $-OH$ and $-OH_2$ grafting sites, the topologies of which have been established by combined experimental and computational techniques.[446] The node $-OH$ and $-OH_2$ sites are very acidic with the pKa of the most

acidic μ_3-OH proton 3.6. Importantly, these protonolytic sites can be functionalized in many ways.[45,546,48,504,440]

To date, incorporation of catalytic metal centers into MOFs has followed three strategies: (1) inclusion into MOF pores,[547,548,549] (2) covalent attachment via organic linkers,[124,516] and (3) binding to inorganic node groups.[45,546,48,504,492,90] Compared to inclusion complexes, node binding is more likely to afford stable and structurally precise catalysts.[h] Here we report the synthesis, characterization, and preliminary catalytic olefin polymerization properties of a single-component (i.e., not requiring a cocatalyst or activator), single-site, highly electrophilic d^0 organozirconium catalyst embedded in a well-defined Hf-NU-1000 scaffold (Figure 4.24).

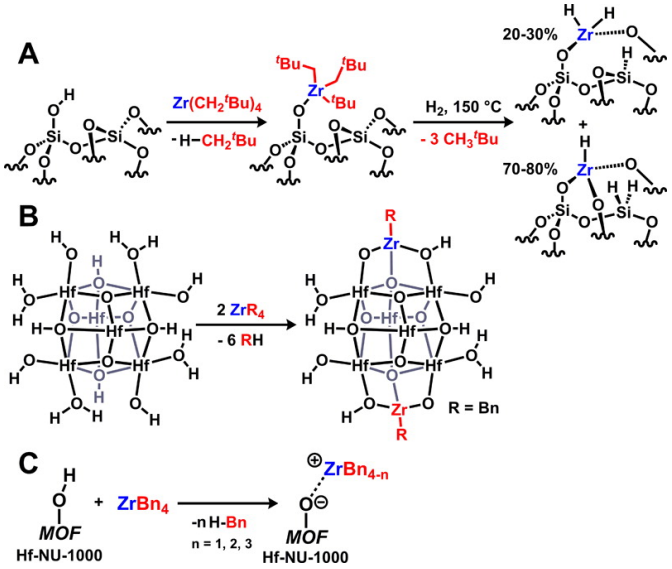

Figure 4.24: Synthesis of supported organozirconium catalysts on (A) silica,[118] (B) Hf-NU-1000, and (C) schematic of proposed chemistry creating highly electrophilic Zr species on a MOF.

4.5.2 Results and Discussion

A benzene solution of tetrabenzylzirconium ($ZrBn_4$) was reacted with a benzene slurry of microcrystalline Hf-NU-1000 at 25 °C for 1 h in an Ar glovebox. The air-sensitive

[h] Node attachment is more likely to afford well-defined periodic species since installing appropriate grafting sites on linkers in a regular and controlled manner is often challenging.

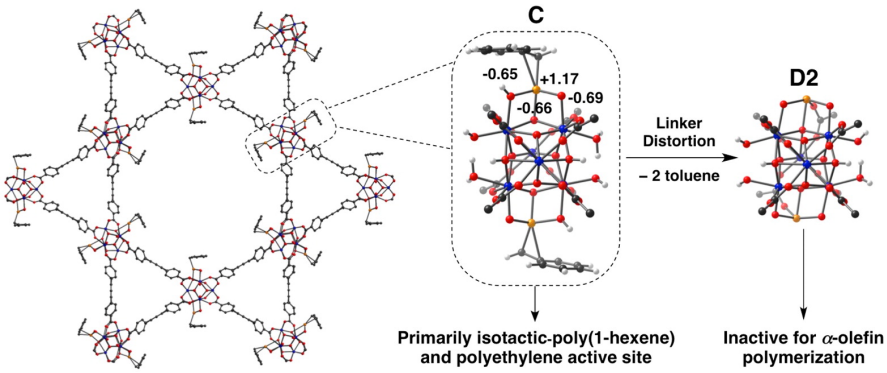

Figure 4.25: Calculated crystal structures showing a hexagonal pore of Hf-NU-1000-ZrBn with two Zr/Hf_6 clusters (left), close-up of Zr MOF component **C** with three Zr−O bonds and one Zr−Bn bond (middle), and close-up of Zr species **D2** with four Zr−O (right) and expected activities of **C** and **D2** with respect to ethylene and 1-hexene. Calculated CM5 charges are shown for Zr and the Hf−O ligands in species **C** (middle).

product was washed repeatedly with benzene to remove residual $ZrBn_4$, and the benzene supernatant exchanged with pentane to facilitate solvent removal from the functionalized MOF. The presence of Zr in Hf-NU-1000-ZrBn (Figures 4.24B,C) was quantified with ICP−atomic emission spectroscopy. On average, 2.4 Zr atoms/Hf_6 node are incorporated (Table S1, supporing information (SI) of ref 550)).[i] SEM−EDX indicates uniform Zr incorporation throughout the MOF crystallites (Figure S1, ref 550).

The powder X-ray diffraction pattern (PXRD) of the Hf-NU-1000-ZrBn indicates that it retains crystallinity after ZrBn incorporation (Figure S3, ref 550). Note also that N_2 adsorption isotherms for Hf-NU-1000-ZrBn reveal that, while the BET surface area decreases versus the parent Hf-NU-1000 material,[j] mesoporosity is maintained (Figure S4, ref 550). Diffuse reflectance FT-IR spectroscopy of Hf-NU-1000-ZrBn confirms metalation via reaction with the node -OH and -OH2 groups (Figure 4.25), evidenced by decreased intensity of the 3678 and 3679 cm^{-1} vibrational modes assigned to terminal −OH and $-OH_2$, respectively (Figure S2, ref 550).

Next, the Hf-NU-1000-ZrBn structure was probed by solid-state ^{13}C CP-MAS NMR

[i] Longer exposure times or reaction at higher temperatures (50 C) do not increase Zr incorporation (Table S1, ref 550).

[j] This is consistent with what is observed by installing other metal ions in NU-1000; see refs 45 and 546.

spectroscopy. The Hf-NU-1000-ZrBn spectrum exhibits aromatic resonances assignable to the carbon atoms of the framework TBAPy linkers, similar to the parent Hf-NU-1000 MOF;[551] however, the spectrum of Hf-NU-1000-ZrBn also exhibits a broad resonance centered at $\delta = \sim$67 ppm, in the chemical shift range expected for a Zr$-CH_2$ carbon (Figure S6, ref 550).[552] The ^{1}H MAS spectrum of Hf-NU-1000-ZrBn likewise reveals peaks at $\delta = 2.9$ and 7.9 ppm, which are assignable to the Zr$-CH_2$ and Zr$-CH_2$Ph protons, respectively (Figure S7, ref 550).[k] These NMR data thus provide evidence for the presence of a Zr$-CH_2$Ph moiety in Hf-NU-1000-ZrBn.

Additional information on the Hf-NU-1000-ZrBn structure is provided by X-ray absorption spectroscopy (XAS, Table S3, ref 550). The XANES Zr K-edge energy of Hf-NU-1000-ZrBn is 18001.5 eV, very similar to that of ZrO_2 and consistent with a Zr(IV) formal oxidation state (Figure S9, ref 550). The Hf-NU-1000-ZrBn EXAFS spectrum was fit by a difference method using reference compounds to determine the individual ligand scattering contributions (details in the SI of ref 550).[553] The optimum fit around Zr was obtained with one Zr$-$Bn ligand and three Zr$-$O ligands. The derived Zr$-$C bond length is identical to that in $ZrBn_4$, 2.29 Å;[554] while the Zr$-$O bonds are slightly shorter than those in ZrO_2, 2.13 and 2.15 Å, respectively.[555]

Organozirconium precursor$-$MOF interactions were next modeled using DFT. Investigating the $ZrBn_4$ reaction with Hf-NU-1000 reveals that a Zr$-$monobenzyl species is the lowest energy product on the reaction pathway, with protonolytic release of the fourth and final benzyl ligand, yielding a purely Zr$-$oxo species, energetically unfavorable (see SI of ref 550 for details, Scheme S1, and Table S4, ref 550). Zr species **C** of Figure 4.25 is thus predicted to be in the 4+ oxidation state and 4-coordinate with three Hf$-$O ligands, originating from the MOF Hf_6 node, and one benzyl ligand, likely coordinated η^2, in good agreement with the EXAFS and NMR data (Figure 4.25, middle, and SI of ref 550). Furthermore, a second potential product is located, resulting from a carboxylate $-CO^{2-}$ group (originating in the TBAPy linker) shifting from the Hf_6 cluster to the Zr of **C** to form species **C2**. **C2** can then react to eliminate toluene and form the product **D2** with no Zr$-$C bond (Scheme S2, ref 550). **D2** is a four-coordinate Zr(IV) species with average Zr$-$O bond lengths of 1.99 Å (Figure 4.25, right, and SI

[k] Such Zr$-CH_2$ protons are sensitive to environment and exhibit resonances over a broad range. The low Zr$-CH_2$ ^{13}C signal intensity precludes 2D ^{1}H$-^1$H DQMAS or 2D ^{1}H-^{13}C HETCOR NMR spectroscopy.

of ref 550).[1] While **D2** is determined to be ∼7 kcal/mol more stable than **C** and is the thermodynamic product of the $ZrBn_4$ reaction with Hf-NU-1000 (Table S4, ref 550), the SS NMR spectroscopy, as well as catalytic results (vide *infra*), suggest that a significant fraction of MOF Zr centers are best represented by kinetic product **C**.

Zr-benzyl species are known catalysts for olefin polymerization, typically requiring a Brønsted or Lewis acid activator/cocatalyst to create coordinatively unsaturated electrophilic centers.[556] Addition of neat 1-hexene to Hf-NU-1000-ZrBn under Ar results in an immediate change of the solution viscosity, without activator/cocatalyst addition. After stirring for 1 h, the supernatant was decanted and the product polymer dried in vacuo. NMR spectroscopy of the resulting colorless highly viscous liquid reveals >95% *isotactic*-poly(1-hexene), consistent with a C^1-symmetric Zr catalytic center (Figures S16 and S17, ref 550).[557,558,559,560] To the best of our knowledge, this is the first report of stereoregular polymerization by a MOF catalyst.[561,562] To obtain better insight into the origin of the regioselectivity, DFT calculations were performed to examine the insertion mechanism of an $\alpha-$olefin into the Zr−Bn bond. At constant elevated [$\alpha-$olefin], the turnover-limiting propagation/insertion step has a low computed barrier of ∼12 kcal/mol, with 1,2-insertion more favorable by ∼3 kcal/mol versus 2,1-insertion (Table S10, ref 550). Note that no polymerization activity is observed upon 1-hexene addition to either the parent MOF Hf-NU-1000 or to solution phase $ZrBn_4$ under identical reaction conditions. Additionally, ICP analysis of the filtered reaction solution after catalysis indicates neither Zr nor Hf particles leached into the solution or into the polymer contained therein.

Furthermore, addition of 100 equiv of methylaluminoxane (MAO; 100 Al/Zr) to the 1-hexene before addition of the MOF-based catalyst yields no polymer.[563] Analysis of poly(1-hexene) by ^{1}H NMR indicates primarily vinylene end groups, consistent with a β-hydride elimination chain transfer pathway.[564] GPC reveals a bimodal mass distribution (Mn = 274000 g/mol, PDI = 1.9 for the higher M_n fraction, and M_n = 570 g/mol, PDI = 1.2 for the lower M_n fraction), likely reflecting activity differences between interior and exterior MOF catalytic sites (Table S9, ref 550).

The Hf-NU-1000-ZrBn 1-hexene polymerization activity is $1.4\times10^2-2.4\times10^3$ g polymer $(\text{mol}\cdot\text{cat})^{-1}$ h^{-1}; the lower range may reflect competitive formation of inactive

[1] The EXAFS first shell data also fit model **D2** with four Zr−O bonds.

species **D2** found in the DFT calculations (Figure 4.25). SEM and PXRD analysis of the MOF after polymerization (Figures S21 and S22 from ref 550, respectively) indicate that the MOF remains crystalline and that the crystallites are largely intact.[m]

Notably, separation of the MOF catalyst from the poly(1-hexene) via filtration and addition of fresh 1-hexene monomer results in further polymerization activity (albeit with a lower activity: 1.2×10^2 g polymer (mol·cat)$^{-1}$ h^{-1}). We expect that the lower activity for the second catalytic run likely results from incomplete separation of the polymer from the MOF, possibly blocking some active site pores. Nonetheless, this result indicates that Hf-NU-1000-ZrBn recyclability is promising.

Under the same catalytic conditions, Hf-NU-1000-ZrBn is also very active for ethylene homopolymerization (Table S9, ref 550). Solution ^{13}C NMR spectroscopy of the product polymer reveals a single resonance at $\delta = 30$ ppm typical of linear high-Mn polyethylene (Figure S24, ref 550). The low polymer solubility precludes separation from the MOF for GPC analysis; however, DSC reveals a melting point (T_m) of 142 °C, suggesting ultrahigh-M_n polyethylene (Figure S25, ref 550).[565] Hf-NU-1000-ZrBn activity for ethylene homopolymerization is 9.3×10^3 g polymer (mol·cat)$^{-1}$ h^{-1}. The higher activity vs 1-hexene likely reflects MOF-Zr steric constraints. Attempts to copolymerize ethylene + 1-hexene under the same conditions result in negligible 1-hexene uptake, again likely reflecting the steric/kinetic constraints imposed by the MOF environment.

Hf-NU-1000-ZrBn single-site catalytic behavior without an activator/cocatalyst implies generation of a cationic/unsaturated Zr center. Indeed, the CM5 and natural population analysis (NPA) calculations on species **C** reveal substantial positive electron density at the Zr center and negative charge density on the surrounding O atoms (Figure 1, middle; Table S6 from ref 550), such that the Zr−MOF interaction is likely more ionic than covalent (Figure 4.24C). This ionicity yields a highly electrophilic d^0 Zr center that enables monomer coordination, insertion, and propagation. In conclusion, a new, structurally well-defined, MOF-based cationic olefin polymerization catalyst was synthesized by incorporation of an organozirconium complex into Hf-NU-1000. Hf-NU-1000-ZrBn is an active single-component catalyst for ethylene and stereospecific 1-hexene homopolymerization.

[m] MOF particles break up to some extent during the reaction due to mechanical stirring. See Figure S19 from ref 550 for a control reaction.

4.6 Thermal Stabilization of Metal−Organic Framework-Derived Single-Site Catalytic Clusters through Nanocasting

4.6.1 Introduction

In the pursuit of highly active heterogeneous catalysts, great emphasis has been placed on the catalyst surface, as mainly the surface atoms are involved in the catalytic reactions. The importance of this active surface has prompted efforts to convert bulk systems to nanoparticles and porous materials, where the reduced size and porosity work to increase the accessible surface area in these materials and thereby enhance reaction rates. Even with these systems, however, the ratio of surface to nonsurface atoms is still small. Structural defects and nonuniformity of the catalyst surface also exist, which can lead to poor selectivity in the reaction products. The need for a catalyst system that combines high catalytic activity and selectivity has thus sparked an interest in single catalytic sites − single atoms or small, well-defined clusters of atoms stabilized as discrete units on a support.[566] Single metal sites arguably maximize catalytic activity per metal compared to their nanoparticle counterparts.[567] Product selectivity can also be expected because these identical, structurally well-defined sites should have similar electronic and spatial interactions with reactant molecules.[568,569,570,571]

A key to promoting the catalytic activity of these single sites is to distribute them at high loadings in a heterogeneous system, which requires porous, high surface area supports. Microporous zeolites have been used as supports for these single sites and have become some of the most important catalyst systems in the industry.[572] Recently, significant focus has been directed to metal-organic frameworks (MOFs),[381,254,421,256] which in comparison with zeolites are a more diverse class of materials in terms of both structure and composition. MOFs are porous materials that consist of metal ions or clusters interconnected via organic linkers. The metal or cluster sites in the MOF themselves can be catalytic,[573,574,124,575,490,576] and these materials can be modified postsynthetically to install other single-site metals.[270,504,45,577,48] Thus, it is possible to tune the reactivity of a MOF-based catalyst by engineering the catalytic metal sites, first with the choice of metal present in the framework itself and then by postsynthetic modification.[578] In

addition, larger pore sizes have been achieved in MOFs than in zeolites, providing easy reactant access to the catalytic sites present in the MOF structure.[579,580]

One drawback of MOFs, however, is their limited thermal stability. Most MOFs can only withstand temperatures of about 150−350 °C in air.[45,51,425,52,581] Above these temperatures, the organic linkers that connect the catalytic metal sites in the MOF structure decompose, leading to the aggregation of the metal sites and loss of their catalytic activity. For this reason, MOFs cannot be used to catalyze reactions that occur only at high temperatures, including a number of industrially important reactions, such as alkane dehydrogenation and water gas shift reactions.[582,583] Faster reaction rates are also attained if catalysts can operate at high temperatures, which makes catalysts with high thermal stability desirable. To take advantage of the highly tunable catalytic metal sites in MOFs for high-temperature catalysis, it is therefore necessary to stabilize the sites so that they remain isolated from each other and accessible even after the linkers are lost at these high temperatures.

Inspired by nanocasting techniques developed extensively for mesoporous materials,[53] we have developed an approach to stabilize the MOF cluster sites by supporting them in a secondary porous skeleton that is maintained at high temperatures. A few examples of nanocasting in MOFs exist in the literature, where the target structure is an inverse replica of the original MOF and all of the original material is removed.[584,54,585,586,55,587] In the product structures described here, only the organic linkers are eliminated, while the catalytic oxometal cluster sites are kept embedded in a thermally stable matrix where they remain isolated from each other and accessible to reactants. In this work, we report the preparation of a silica nanocast of NU-1000,[270] a MOF composed of hexanuclear oxozirconium clusters ($[Zr_6(\mu_3{-}O)4(\mu_3{-}OH)_4(OH)_4(H_2O)_4]^{8+}$) and 1,3,6,8-tetrakis(*p*-benzoate)pyrene linkers ($TBAPy^{4-}$) (Figure 4.26a). When NU-1000 is heated to a temperature at which the oxozirconium clusters lose coordinated water (Figure 4.26b), it becomes a Lewis acid catalyst, showing superior activity, for example, in the catalytic breakdown of known chemical warfare agents.[490] We determined the Lewis acid activity of the oxozirconium clusters experimentally by measuring the catalytic activity and using theory by computing the reaction mechanism of glucose isomerization and analyzing the atomic charges in the clusters throughout the reaction. We demonstrate that the nanocast NU-1000

maintains this activity after the organic linkers have been removed from the structure by high-temperature treatment. We also show that through nanocasting with silica aggregation of the oxozirconium clusters of NU-1000 is prevented after the linkers are removed. Thus, a high concentration of these well-dispersed catalytic sites is maintained in a thermally stable material that is now suitable for catalytic processes that may require high temperatures.

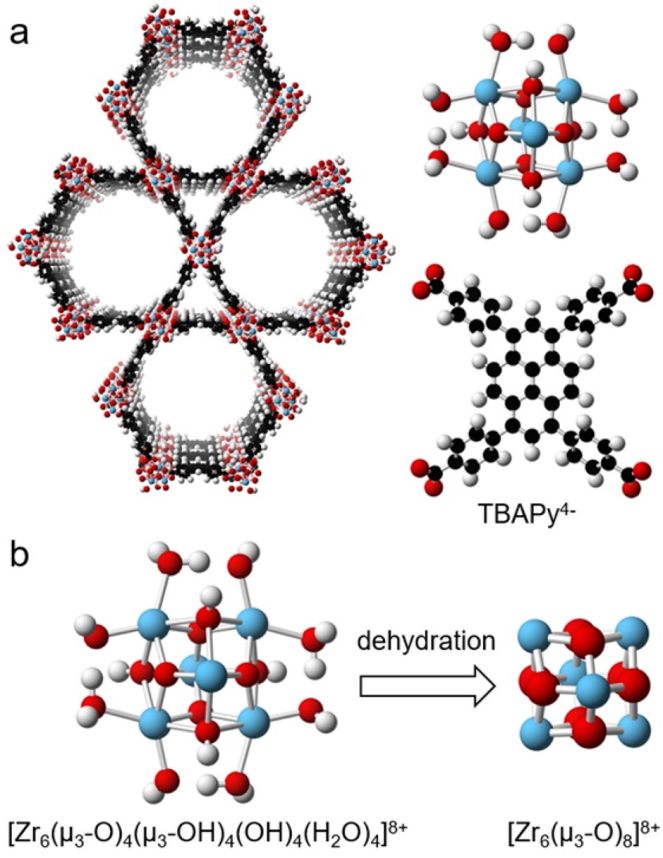

Figure 4.26: (a) Structure of NU-1000 showing the oxozirconium clusters ($[Zr_6(\mu_3{-}O)_4(\mu_3{-}OH)_4(OH)_4(H_2O)_4]^{8+}$) and organic linkers ($TBAPy^{4-}$) that make up the framework. (b) Dehydration of the oxozirconium clusters converts them to the Lewis acidic form ($[Zr_6(\mu_3{-}O)_8]^{8+}$). Color code: Zr (blue); O (red); C (black); H (white).

4.6.2 Experimental Methods

Materials

The following chemicals were used as received: tetramethyl orthosilicate (TMOS, 98%), methanol (99.8%), $ZrOCl_2 \cdot 8H_2O$ (98%), benzoic acid (99.5%), pyridine (99.8%), and *D*-glucose (≥99.5%) from Sigma-Aldrich; acetone (98%) and *N*, *N*-dimethylformamide (DMF, 99.8%) from Macron Fine Chemicals; and hydrochloric acid (36.5-38.0%) from BDH Chemicals. The linker, 1,3,6,8-tetrakis(*p*-benzoic acid)pyrene (H_4TBAPy) was synthesized as previously described.(20) Deionized water produced on-site with a minimum resistivity of 18.2 MΩ·cm was used in all experiments.

Nanocasting NU-1000 with Silica

NU-1000 was synthesized following a previously reported method (details in the Supporting Information (SI) of ref 588).(39) To prepare a silica nanocast of NU-1000, 300 μL of TMOS and 5 μL of H_2O were first sonicated in a vial for 10 min. The mixture was then added to 30 mg of activated NU-1000 and allowed to infiltrate the MOF particles for 24 h. The infiltrated sample was washed with methanol twice to remove the TMOS on the external surface of the NU-1000 particles and then heated at 50 °C for 5 min to dry. To induce polycondensation of TMOS within the sample, the sample was first exposed to HCl vapor for 24 h at room temperature. This was followed by heat treatment in a closed vial at 60 °C for another 24 h. The resulting nanocast material is referred to as SiO_2@NU-1000. This material was heated to 500 °C using a temperature ramp rate of 2 °C/min and maintained at that temperature in air for 1 h to remove the organic linkers from the structure. The resulting product is denoted as Zr_6@SiO_2. To determine the limits of thermal stabilization, SiO_2@NU-1000 was also independently calcined at 600 and 700 °C for 1 h using a ramp rate of 2 °C/min. The resulting samples are denoted as Zr_6@SiO_2 (600 °C) and Zr_6@SiO_2 (700 °C), respectively.

Pyridine Adsorption

The Lewis and Brønsted acid sites on Zr_6@SiO_2 were detected using pyridine as a probe molecule. The sample was placed under dynamic vacuum (<200 mTorr) at 200 °C for 1 h to remove surface-adsorbed water. After cooling to room temperature, the sample

was placed under static vacuum, and excess pyridine was injected through a septum. The reaction with pyridine was allowed to proceed for 1 h. The sample was placed under dynamic vacuum again at 200 °C for 1 h to remove any physisorbed pyridine and then cooled to room temperature. Pyridine adsorption was then analyzed by FT-IR spectroscopy.

Catalyst Testing: Glucose Isomerization

The catalytic performance of Zr_6@SiO_2 was tested using the Lewis-acid-catalyzed isomerization reaction of glucose to fructose as a model reaction. This reaction, carried out at a low temperature (90 °C), allows assessment of the retention of catalytic performance against the original NU-1000 structure which is stable at this temperature. In a typical reaction, 0.03 g of *D*-glucose, 2.97 g of ethanol, and 0.012 g of the catalyst were added into a 20 mL thick-walled glass reactor and sealed with a crimp top (PTFE/silicone septum) from VWR. The reactor was placed in an oil bath at 90 °C at specific reaction times, and the reaction was quenched afterward by placing the reactor in an ice bath. The catalyst was then filtered out, and deionized H_2O (3.87 g) was added to the reaction solution to hydrolyze ethylated sugars at 90 °C for 2 days. All reactants and products were analyzed by HPLC. Aside from NU-1000, the catalytic performance of the nanocast material was tested against other samples including calcined NU-1000 and control samples of oxozirconium clusters in nontemplated silica (see SI of ref 588 for the detailed synthesis of the control samples).

Computational Methods

Density functional theory (DFT) has proven to be helpful for determining the structure[446] and reactivity[504] of NU-1000. To aid in our understanding of the effectiveness of the oxozirconium clusters in NU-1000 and in Zr_6@SiO_2 as Lewis acid catalytic sites, we computed the reaction mechanism of glucose isomerization at these clusters. The free energies (ΔG) of each mechanistic step were computed using the dehydrated oxozirconium cluster model described by Planas et al.[446] with the eight linkers truncated to formic acid groups (Figure S1, ref 588). Each step of the reaction pathway was fully optimized with the M06-L[589] density functional in *Gaussian 09*[185,442] in the gas phase. The optimizations were performed with the 6-31G(d) basis set on C, H, and O and the

Stuttgart/Dresden effective core potential (SDD)[505] on Zr. Frequency calculations at 298 K were also performed at this level to find the transition states. Single-point frequency calculations at the same temperature were then performed on these equilibrium and transition state structures with the def2-TZVP basis set[182] to extract free energies. The relative free energies were computed by subtracting the free energy of glucose bound to the oxozirconium cluster model from the free energy of each reaction step. Mulliken charges were computed for the Zr and O atoms in the cluster as indicators of the change of Lewis acidity along the glucose isomerization reaction path.

Instrumentation

FT-IR spectra were collected on a Nicolet Magna-IR 760 spectrometer. Thermogravimetric analysis (TGA) was carried out using a Netzsch STA 409 PC Luxx instrument. Scanning electron microscopy (SEM) measurements were performed on a JEOL 6700 scanning electron microscope operated using a 3.0 kV accelerating voltage. Prior to SEM analysis, all samples were sputter coated with a conductive thin film (50 Å) of Pt. X-ray diffraction (XRD) patterns were collected using an XPert Pro diffractometer with an XCelerator detector. A Co anode (Kα, $\lambda = 1.789$ Å) operated at 45 kV and 40 μA was used as the radiation source. Simulated XRD patterns of tetragonal ZrO_2 (PDF 50-1089) were generated using Mercury[590] based on Scherrer line widths for different crystallite sizes. Inductively coupled plasma-optical emission spectrometry (ICP-OES) using a Thermo Scientific iCAP 6500 analyzer was employed for the determination of the Zr content in the samples. High-performance liquid chromatography (HPLC) with a Bio-Rad Aminex HPX87C (300×7.8 mm) column and refractive index detector was used for all reactant and product analyses during the catalytic tests. The mobile phase was ultrapure water (pH = 7), and the column temperature was 80 °C. The C, H, and N content in Zr_6@SiO_2 (500 °C) was determined to be 0.2, 1.1, and 0.0 wt %, respectively, using combustion analysis by Atlantic Microlab, Norcross, GA.

N_2 sorption analyses were conducted using a Quantachrome Autosorb iQ2. The NU-1000 and SiO_2@NU-1000 samples were degassed at 120 °C, and the Zr_6@SiO_2 and control samples were degassed at 200 °C, at 1 mTorr for 12 h prior to the analysis. Brunauer-Emmett-Teller (BET) surface areas were evaluated from the adsorption isotherms within the 0.08−0.28 P/P_o range. Pore size distributions and surface area

histograms were obtained using DFT (Quantachrome, N_2 at 77 K on carbon or silica, slit pore) methods.

Transmission electron microscopy (TEM) images were collected on an FEI Tecnai G^2 field-emission S/TEM operating at an accelerating voltage of 300 kV. High-angle annular dark field (HAADF) images were collected on an E. A. Fischione annular detector at a camera length of 120 mm, which yields an inner collection semiangle of 49.8 mrad. Energy-dispersive X-ray spectroscopy (EDS) spectra were collected using an EDAX RTEM thin-window detector. To provide sufficient X-ray intensity for the maps and line-scans, the sample was tilted to the detector takeoff angle of 15°. EDS line scans and maps were collected using a pixel dwell time of 16 s, a beam convergence semiangle of 9.2 mrad, and a probe current of ∼0.5 nA. Data were analyzed using FEI TIA software (version 4.5) and Gatan DigitalMicrograph software (version 1.84).

Synchrotron X-ray Structure Analysis

X-ray scattering data suitable for pair distribution function (PDF) and diffraction analysis were collected at beamline 11-ID-B at the Advanced Photon Source at Argonne National Laboratory. High-energy X-rays (wavelength 0.2114 Å, 58.6 keV) were used in combination with a large amorphous silicon-based area detector. For PDF analysis, total scattering data were collected using a short sample-to-detector distance (∼18 cm) to $Q_{\max} = 23$ Å^{-1}. For diffraction analysis, data with improved angular resolution were collected at longer sample-to-detector distance (∼95 cm). The X-ray scattering images were reduced within QXRD and FIT2D.[591,592]

A difference envelope density (DED) analysis[593,594] was applied to diffraction data to evaluate the distribution of SiO_2 within the crystalline NU-1000 framework. The diffuse contributions to the background were removed by subtracting scattering measured for an empty sample capillary and amorphous SiO_2.[595,596,510] The Bragg peak intensities for pristine and nanocast NU-1000 were determined by performing Le Bail whole pattern fits to the diffraction data within the $P6/mmm$ space group of the parent phase,[45] refining the hexagonal lattice parameters and pseudo-Voigt profile parameters. Structure envelopes were generated based on the low-index reflections, as described previously.[593,597] A difference envelope, reflecting the distribution of silica within the NU-1000 lattice, was generated by taking the difference between the envelopes for SiO_2@NU-1000 and

an unmodified NU-1000 sample.

Pair distribution functions (PDFs) were extracted from the total scattering data within PDFgetX2, correcting for background and Compton scattering.[508] Data were collected for pristine NU-1000, SiO_2@NU1000, Zr_6@SiO_2, TMOS-derived silica, and the control Zr_6@n-t-SiO_2. Differential analyses were applied to separate the contributions from silica from the oxozirconium clusters or NU-1000 lattice. Structure models were refined against the differential PDFs (dPDFs) within PDFgui to evaluate the particle size of the Zr-based clusters following thermal treatment.

4.6.3 Results and Discussion

Silica Nanocasting

Silica nanocasts of NU-1000 were prepared according to the scheme shown in Figure 4.27. The silica precursor, tetramethylorthosilicate (TMOS), is small enough to fit in the 3 nm pores of NU-1000, allowing the precursor to infiltrate these pores. Under hydrolytic conditions, TMOS can then be condensed in the presence of an acid catalyst to form silica within the NU-1000 framework. Our earlier attempts to nanocast NU-1000 with silica used a mixture of TMOS, aqueous HCl, and methanol as the casting fluid (see Supporting Information for details). The added methanol was necessary to slow down the silica formation during infiltration, which could otherwise lead to pore blockage, hindering percolation through the entire NU-1000 particle. However, that method yielded mainly extra-framework silica, with virtually no shift to lower pore size for the 3 nm channels in NU-1000, indicating that only a small amount of silica was present in these pores (Figure S2, ref 588). This could be due to TMOS occupying only 68% of the precursor solution volume. Because both H_2O and HCl as an acid catalyst are present in the precursor solution, TMOS hydrolysis and oligomerization is also possible, yielding short silica chains that could already be too large to infiltrate into the NU-1000 pores. Multiple infiltration steps were carried out using this method, but this did not improve the silica loading in the pores (Figure S2, ref 588).

Instead, to raise the amount of silica in the pores of NU-1000, we increased the fraction of TMOS in the casting fluid to 98% v/v, the balance being water. As TMOS hydrolysis and condensation occur instantaneously when HCl is added to this mixture,

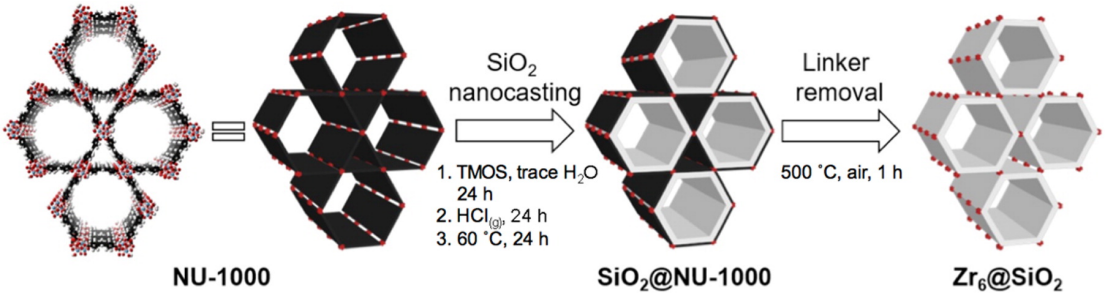

Figure 4.27: Scheme for the process of stabilizing the oxozirconium clusters in NU-1000 by nanocasting with silica. The image on the left represents the NU-1000 structure with cluster nodes (red) and linkers (black). The white layer in the middle image represents silica.

the acid must be introduced (via vapor-phase HCl treatment) only after the mixture has percolated through the NU-1000 pores. The presence of silica in the product obtained after nanocasting was confirmed by the appearance of an intense absorption at 1090 cm^{-1} in the FT-IR spectrum (Figure S3, ref 588) related to the Si−O−Si stretching vibration. While the total amount of silica in this nanocast product is approximately the same as in the sample from the original nanocasting method (TGA data, Figure S4, ref 588), a larger proportion of it is present within the NU-1000 framework as shown by the greater shift in the DFT pore size distribution of the sample (Figure 4.28a). The pore radius decreased by ca. 0.2 nm upon infiltration of the larger hexagonal channels in NU-1000, while the smaller trigonal channels maintained their original dimensions.

The diffraction and pair distribution function (PDF) data demonstrate that the NU-1000 framework structure is maintained through the nanocasting procedure. The presence of Bragg diffraction peaks indicates that the long-range crystalline ordering of the lattice is preserved (Figure S5, ref 588). The differential PDF trace, subtracting the contributions from the new silica phase, shows the same local structures in the pristine and nanocast systems (Figure S6, ref 588), characterized by a feature at ∼1.4 Å associated with the C−C and C−O bonds in the $TBAPy^{4-}$ linker, and features at ∼2.1 and 3.5 Å associated with the Zr−O and Zr$\cdots$Zr atom-atom distances, respectively.

The difference envelope density (DED) analysis, based on the low-index Bragg reflections, provides a map of electron density added to the NU-1000 pores following the silica nanocasting (Figure 4.28b). This analysis shows that the silica is primarily deposited in

a layer on the surface of the 3 nm hexagonal channels close to the oxozirconium nodes and organic linkers, with almost no silica in the smaller 1 nm trigonal pores. This is also reflected in the decrease in intensity of the 010 reflection following nanocasting (Figure S5, ref 588) – this peak corresponds to the 3 nm channel spacing in NU-1000. The reduced electron contrast following silica incorporation into these channels leads to reduced intensity of this 010 peak. As suggested by the nitrogen sorption data (Figure 4.28a), there is no shift in the pore size for the trigonal pores indicating no significant silica electron density within these small pores. The distribution of the silica as a layer on the pore surface of the hexagonal channels provides a secondary skeleton or framework structure that can serve as a scaffold for the oxozirconium clusters following removal of the organic linkers at high temperature.

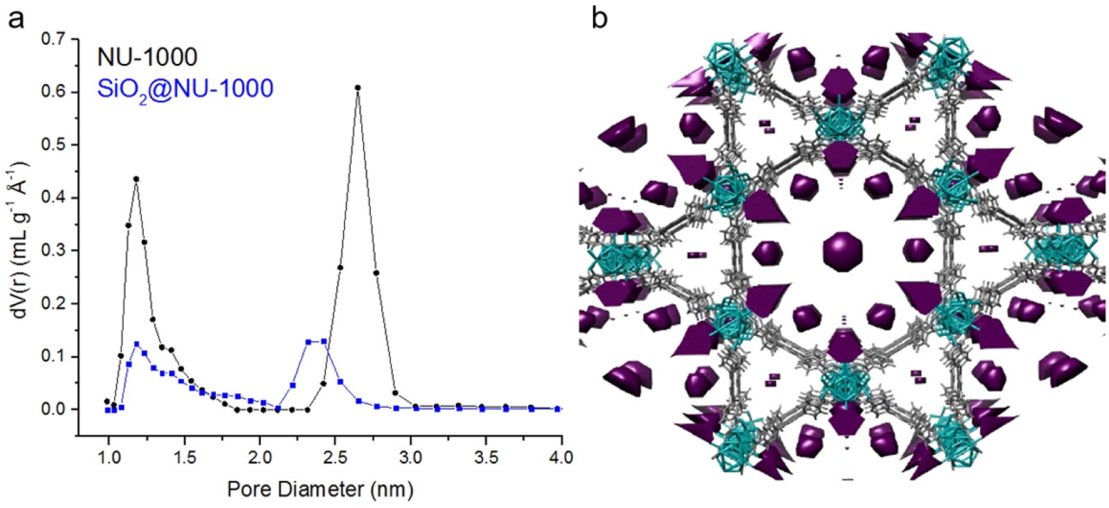

Figure 4.28: (a) DFT pore size distribution of NU-1000 (BET surface area = 2064 m^2 g^{-1}, pore volume = 1.44 cm^3 g^{-1}) before and after nanocasting with SiO_2 (BET surface area = 901 m^2 g^{-1}, pore volume = 0.55 cm^3 g^{-1}). (b) Difference envelope density analysis data showing the new electron density (SiO_2, purple) after nanocasting NU-1000 (oxozirconium clusters in teal, organic linkers in gray).

Cluster Stabilization at High Temperatures An ultimate aim is to use these nanocast products to catalyze reactions at high temperatures. To be useful for high-temperature catalysis, however, the silica backbone in the nanocast materials should be able to serve as a support for the Lewis acidic oxozirconium clusters in place of the organic linkers that are lost at these temperatures. Site isolation and accessibility of these clusters are

necessary to maintain high Lewis acid catalytic activity. To determine whether this high-temperature cluster stabilization was achieved through nanocasting, we removed the organic linkers in the nanocast material (SiO_2@NU-1000) by calcination, which leaves only the oxozirconium clusters and the silica matrix (Zr_6@SiO_2).

The dPDF trace for Zr_6@SiO_2 (Figure 4.29, 0-8 Å region highlighted in Figure S7 of ref 588) shows that the organic linkers were eliminated, with no peaks at ∼1.4 Å from C−C or C−O bonds within the linkers. This is consistent with chemical analysis that detected only 0.2 wt % of carbon in the sample. The dPDF is dominated by peaks at ∼2.14 and ∼3.47 Å associated with Zr−O and Zr$\cdots$Zr correlations within oxozirconium clusters, respectively. Structural models, based on cubic ZrO_2, were refined against the dPDF data, using a spherical particle parameter to estimate the ZrO_2 particle size distribution. The nanocast Zr_6@SiO_2 was dominated by small ∼0.6 nm clusters ZrO_2 (∼95%, a = 4.88 Å) with a minor component of larger ∼3 nm nanoparticles, modeled as cubic ZrO_2 with significant O disorder (∼5%, a = 5.11 Å). The retention of such a large fraction of the small ∼0.6 nm clusters suggests that the nanocasting approach is successful in improving the thermal stability of the clusters. While aggregation was not entirely eliminated in the nanocast system, it may be expected that oxozirconium clusters closer to the outer surface of the particles may be more susceptible to aggregation, and the larger nanoparticles observed in this case may be associated with clusters near the surface. Alternatively, small domains of NU-1000 not penetrated by the silica precursor could account for the minor phase of aggregated ZrO_2 nanoparticles.

Figure 4.30 shows electron micrographs tracking the progression from NU-1000 to the nanocast material SiO_2@NU-1000 and to the final product after removal of the linkers, Zr_6@SiO_2. There is no significant change in morphology after nanocasting (Figure 4.30b), and the lattice fringes from the 3 nm channels are still observable from the high magnification TEM image of the nanocast products (Figure 4.30e). This is consistent with the XRD data which shows a low angle peak at $2\theta = 3°$ that corresponds to structural features on the ∼3 nm scale (Figure S5, ref 588). After the linkers are removed by heating the sample at 500 °C in air, the particles shrink, and the TEM image shows a more disordered structure (Figure 4.30c, 4.30f). This is accompanied by a decrease in BET surface area (from 944 to 444 $m^2\ g^{-1}$) and pore volume (from 0.55 to 0.46 $cm^3\ g^{-1}$) due to the loss of micropores in the structure. Of particular interest is

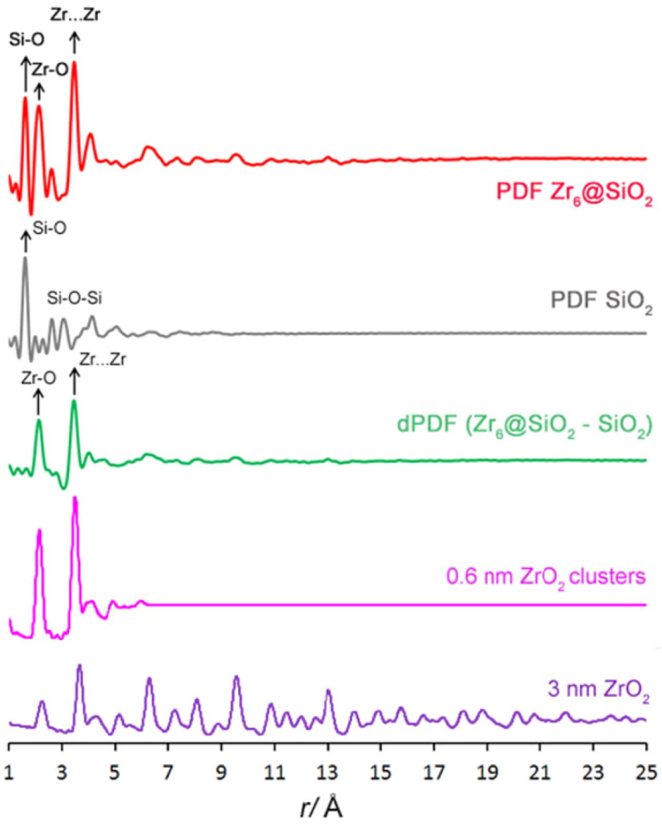

Figure 4.29: PDFs for $Zr_6@SiO_2$ and an amorphous silica sample, dPDF, for $Zr_6@SiO_2$ showing new Zr−O and Zr$\cdots$Zr correlations and PDFs for the oxozirconium clusters (0.6 nm, $Fm\bar{3}m$, a = 4.88 Å) and larger cubic ZrO_2 particles (3 nm, $Fm\bar{3}m$, a = 4.88 Å).

the XRD pattern of this sample, which does not exhibit any notable diffraction peaks (Figure 6, Zr_6@SiO_2 (500 °C)). On the other hand, a noninfiltrated NU-1000 sample that was heated to the same temperature (cal-NU-1000) exhibits diffraction peaks that can be indexed to the tetragonal phase of ZrO_2 (Figure 6, cal-NU-1000 (500 °C)). This difference is also reflected in the selected area electron diffraction (SAED) patterns of the two samples (Figure S8, ref 588), where cal-NU-1000 shows diffraction rings that index to tetragonal ZrO_2, which are absent in the SAED pattern of Zr_6@SiO_2. The presence of the diffraction patterns in the XRD and SAED data indicates that in cal-NU-1000 the oxozirconium clusters have aggregated at the high treatment temperatures to form larger ZrO_2 crystallites (ca. 18 nm calculated from the XRD line broadening using the Scherrer equation), which would cause a loss in catalytic activity because agglomeration reduces the number of exposed Lewis acid sites. The absence of notable diffraction peaks in Zr_6@SiO_2 demonstrates that, by nanocasting with SiO_2, we are able to prevent the oxozirconium clusters from aggregating after the linkers are removed at high temperatures, in agreement with the dPDF data.

The SiO_2@NU-1000 samples were also calcined at 600 and 700 °C to determine the limits of thermal stabilization. As shown in Figure 4.31, the broad features are still maintained at 600 °C, indicating that there is still no significant cluster aggregation at this temperature. At 700 °C, some peaks are visible in the pattern, but these are still not as prominent as in the case of cal-NU-1000. We simulated the Scherrer broadening of the XRD peaks of tetragonal ZrO_2 for different crystallite sizes (Figure S9, ref 588). From this we estimate that for Zr_6@SiO_2 heated to 600 °C the crystallites are still single, isolated clusters (ca. $\sim$ 0.6 nm). The clusters start to aggregate at 700 °C, but the aggregate size is still significantly smaller (<2 nm) compared to the case of cal-NU-1000 (ca. 18 nm) that was heated to only 500 °C.

STEM-EDS elemental maps (Figure 4.32) of the nanocast products after linker removal show a homogeneous distribution of O, Si, and Zr throughout the material. For Si in particular, there is no Si-deficient core, which indicates that uniform infiltration was achieved during nanocasting. This presumably afforded the site isolation of the clusters, as the presence of silica throughout the particle can provide proximal anchor sites for these clusters. Additionally, the EDS map also shows only a very thin outer layer of silica on the sample surface, not a thick crust which would prevent access to

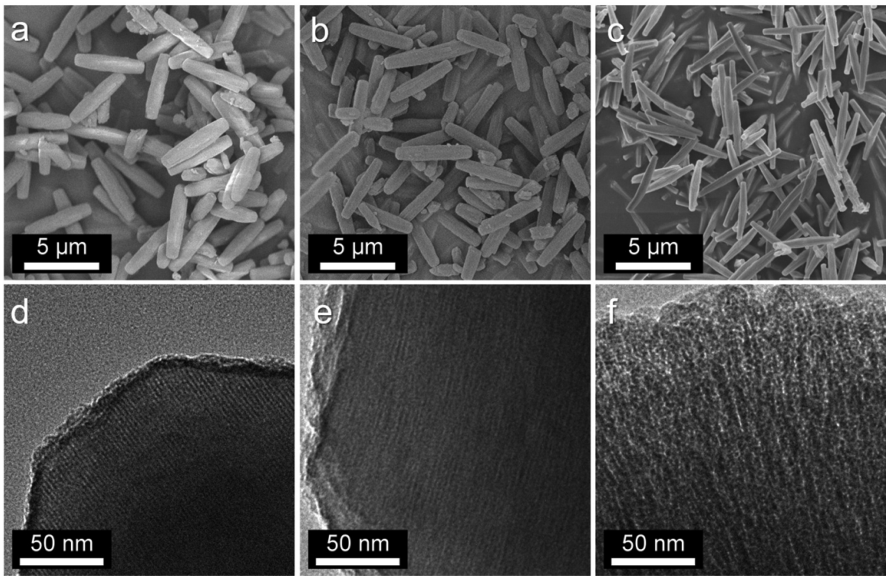

Figure 4.30: SEM (a-c) and TEM (d-f) images of NU-1000 (a, d), SiO_2@NU-1000 (b, e), and Zr_6@SiO_2 (c, f).

the catalytic clusters within the particles.

Lewis Acidity and Catalytic Performance of Nanocast NU-1000

NU-1000 is an excellent Lewis acid catalyst owing to the high concentration of the Lewis acidic oxozirconium clusters in its structure, which are easily accessible through its mesoporous channels.[490] In particular, the Lewis acidity can be enhanced by dehydration of the clusters, which eliminates terminal aquo and hydroxo ligands and converts hydroxo bridges to oxo bridges, thereby reducing the number of oxide-based species that bind to the Zr(IV) centers.[490] Similar cluster dehydration processes are expected during the heat treatment at 500 °C to form Zr_6@SiO_2 and open up Zr(IV) sites. To determine whether the Lewis acidic clusters in the nanocast materials remain accessible, we carried out a pyridine adsorption experiment on Zr_6@SiO_2. Pyridine is a common IR probe for detecting acidic sites in solid acid catalysts. The peaks for the ring vibrations of pyridine, which appear in the region between 1700 and 1400 cm^{-1}, shift depending on whether pyridine is coordinated to a Lewis acid site or is protonated by a Brønsted acid site.[598] After pyridine adsorption, the FT-IR spectrum of Zr_6@SiO_2 shows peaks

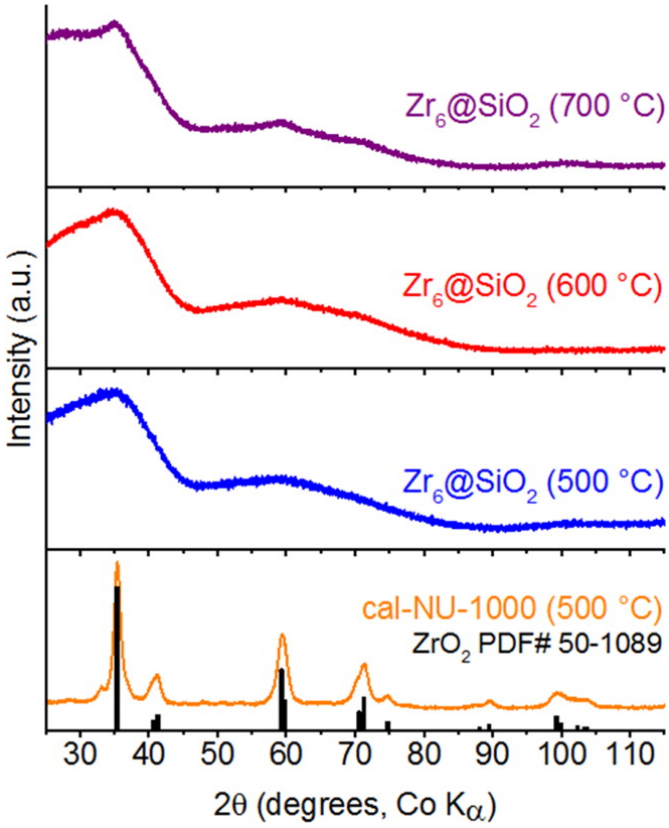

Figure 4.31: XRD patterns of Zr_6@SiO_2 after heat treatment at 500, 600, or 700 °C in air. For comparison, the XRD pattern of NU-1000 calcined at 500 °C in air is also shown. The line pattern corresponds to the published powder diffraction file pattern for tetragonal ZrO_2 (powder diffraction file 50-1089).

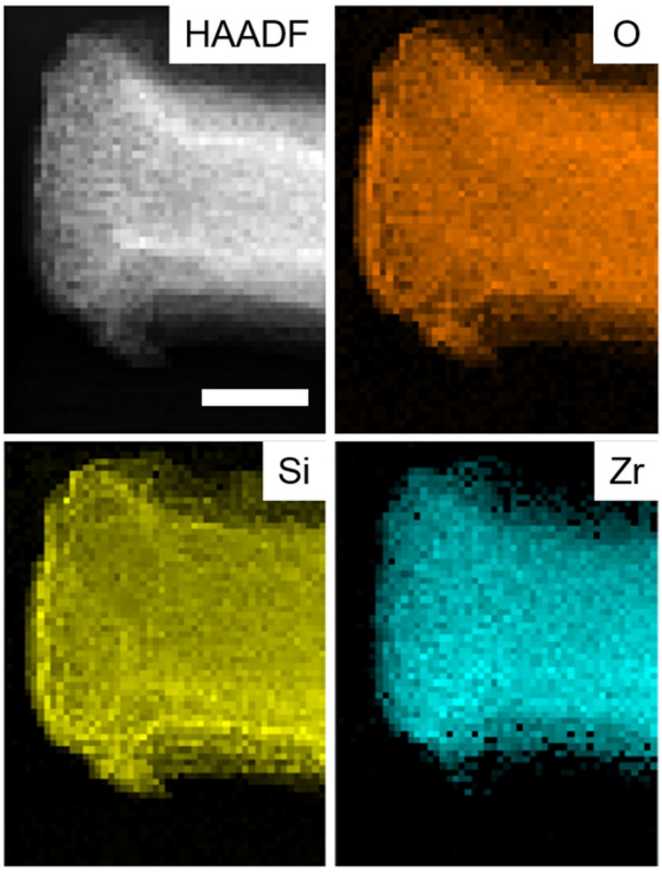

Figure 4.32: High-angle annular dark field (HAADF) image and STEM-EDS elemental maps of Zr_6@SiO_2. The scale bar corresponds to 200 nm.

for pyridine adsorbed on Lewis acid sites (Figure 4.33). These peaks correspond to the normal modes ν_{8a} and ν_{19a} of the ring-breathing (νCCN) vibrations of pyridine with A1 symmetry (1607 and 1490 cm^{-1}, respectively) and the ν_{8b} and ν_{19b} modes with B_2 symmetry (1576 and 1445 cm^{-1}, respectively),[599] all in close agreement with those found for Lewis-site coordinated pyridine on ZrO_2.[600] Similar peaks are observed for pyridine adsorbed on dehydrated NU-1000. It is interesting to note that the pyridine peaks are less well resolved in the case of dehydrated NU-1000, possibly due to additional interactions of the probe molecule with linkers between oxozirconium clusters. Evidence for some Brønsted acidity is also present in both the Zr_6@SiO_2 sample and the dehydrated NU-1000, as indicated by a vibrational band at 1545 cm^{-1} typical for pyridinium ions bonded to Brønsted sites.[600] Amorphous silica prepared from TMOS using the same treatment as for Zr_6@SiO_2 shows no corresponding absorption bands in the FT-IR spectrum. The pyridine adsorption data confirm that the clusters are accessible in the nanocast material, which is facilitated through its high surface area and mesoporous structure (Figure S10, ref 588). We estimated the ratios of Lewis-to-Brønsted acid sites (L:B) in the Zr_6@SiO_2 (500 °C) and dehyd-NU-1000 samples by integrating the peaks at 1445 and 1545 cm^{-1} in Figure 4.33 (see Table S1 from ref 588 for the peak integration values). Absorption coefficients from Rosenberg and Anderson[601] were used to estimate relative acid site concentrations from the peak areas. While the resulting L:B ratios of 0.46 for Zr_6@SiO_2 and 0.24 for dehyd-NU-1000 have some uncertainty due to peak fitting procedures, they show that the relative L:B content did not decrease after nanocasting and probably increased slightly, most likely because removal of the organic linkers exposed more Lewis acid sites on the clusters. More importantly, these data show that both materials contain appreciable amounts of Brønsted and Lewis acid sites, and both sites remain accessible to pyridine molecules.

The catalytic activity of the oxozirconium clusters was tested with the Lewis-acid-catalyzed isomerization of glucose to fructose. As this reaction occurs at low temperatures, the catalytic performance of the clusters in the nanocast Zr_6@SiO_2 and the original NU-1000 structure can be compared. We used DFT calculations to determine the mechanism of glucose isomerization on the clusters (Figure S11, ref 588). The dehydrated, Lewis acidic form of the clusters, $[Zr_6(\mu_3{-}O)_8]^{8+}$, features two Zr and two $\mu_3{-}O$ sites on each face of the cluster structure (Figure 4.26b), which work in tandem to

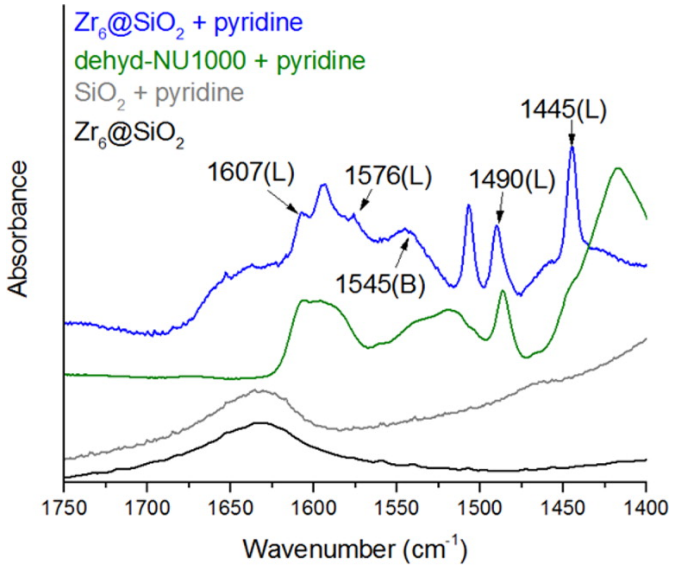

Figure 4.33: FT-IR spectra showing pyridine adsorption data for Zr_6@SiO_2 (500 °C) and dehyd-NU-1000. The peaks indicate the presence of accessible Lewis (L) and Brønsted (B) acid sites in the samples. The spectra of Zr_6@SiO_2 (500 °C) (before pyridine adsorption) and SiO_2 (after pyridine adsorption) are also shown for comparison.

stabilize protonic and oxidic moieties that form during the isomerization reaction. The Mulliken partial charges of the Zr atoms in the bare oxozirconium cluster are ∼1.75. Throughout the reaction, the charges of the two Zr atoms on the reacting face fluctuate between 1.50 and 1.69 (Table S2, ref 588), indicating that both Zr atoms are acting as electron acceptors to stabilize the intermediate species throughout the glucose isomerization. A more detailed description of the mechanism is provided together with the reaction scheme in the SI of ref 588. The largest transition state barrier in the mechanism is 20.6 kcal/mol, which indicates that the clusters are efficient Lewis acid catalysts.

For the catalytic tests, the glucose isomerization reaction was carried out in two steps (Figure 4.34), following the scheme of Saravanamurugan et al.[602,603] In the first step, glucose is isomerized to fructose in the presence of the catalyst. The fructose that is formed immediately reacts with the solvent, ethanol, to form ethyl fructoside. Water is then added in the second step to hydrolyze the fructoside back to fructose. Both steps are carried out at 90 °C. The catalytic performance of the nanocast material was

tested against other samples (Table 4.9), including NU-1000, calcined NU-1000, and control samples of oxozirconium clusters in nontemplated silica supports. As shown in Figure 4.35, both dehyd-NU-1000 (NU-1000 dehydrated at 300 °C under vacuum to make the oxozirconium clusters Lewis acidic) and the nanocast Zr_6@SiO_2 are active. The rate is slower for Zr_6@SiO_2 which could be due to some of the clusters becoming fully coated with SiO_2 during nanocasting or due to the silica scaffold providing some steric hindrance. Despite this, significant catalytic activity was retained in the nanocast material even after it had been heated to 500 °C. In contrast, bare NU-1000 heated to the same temperature (cal-NU-1000) had very low activity. This shows the importance of maintaining the site isolation in the clusters in order to retain catalytic activity, which was made possible by nanocasting. An XRD pattern of the Zr_6@SiO_2 sample collected after the 72 h catalytic reaction (Figure S12, ref 588) shows that the broad diffraction features seen for the original sample (Figure 4.31) are maintained, implying that the clusters remained isolated and did not aggregate during the catalytic reaction. Recycling experiments with Zr_6@SiO_2 show an average loss in glucose conversion of ∼13% per cycle over five cycles (Figure S13, ref 588). The loss in overall activity is more pronounced initially and appears to level off after the third cycle. Interestingly, the fructose yield loss is less pronounced, and as a result, the recycled catalysts become progressively more selective to fructose. It is possible that this is due to reduction of the Brnsted:Lewis acid site ratio with recycling, but further investigations are required to test this hypothesis. Despite these changes, higher catalyst activity is still maintained in recycled Zr_6@SiO_2 as compared to cal-NU-1000. In addition, a higher loading of these site-isolated clusters is also obtained by the nanocasting method than by incorporating oxozirconium clusters in nontemplated silica (Table 4.9). The nontemplated samples Zr_6@n-t-SiO_2 and Zr_6@n-t-SiO_2(High Zr) exhibit cluster aggregation (Figure S14, ref 588) despite having a lower Zr loading. Since only micropores are present in both nontemplated samples (Figure S10, ref 588), the catalytic sites are also less accessible compared to those in the mesoporous nanocast material. This resulted in a significantly lower yield of fructose with Zr_6@n-t-SiO_2 and Zr_6@n-t-SiO_2(High Zr) samples as compared to Zr_6@SiO_2. The ability to retain catalytic activity through site isolation and the templated porosity despite being heated to high temperatures makes nanocasting a useful technique for applying MOF-based catalytic clusters for catalytic

processes that may require high temperatures.

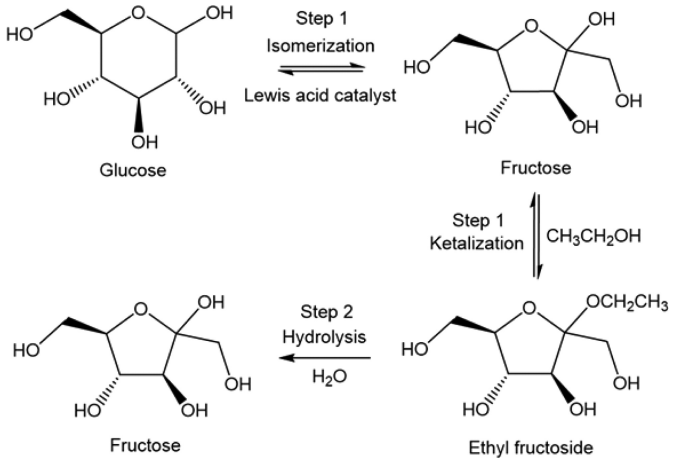

Figure 4.34: Reaction scheme for the isomerization of glucose to fructose. Adapted from Saravanamurugan et al.[602] The computed reaction mechanism is provided in Figure S11 of ref 588.

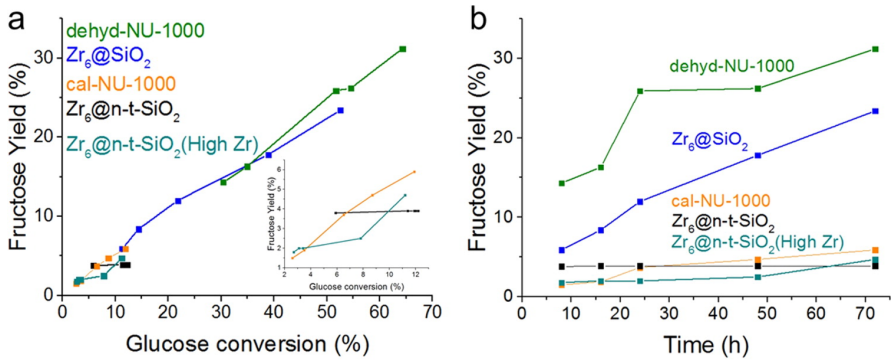

Figure 4.35: (a) Fructose yield versus glucose conversion and (b) fructose yield versus time over different catalysts.

4.6.4 Conclusions

We demonstrated the effectiveness of nanocasting the MOF NU-1000 with silica as a strategy to maintain the catalytic activity of MOF-derived single-site catalytic clusters after high-temperature treatment. Silica coated the larger, 3 nm diameter mesopores, but the precursor did not infiltrate the smaller, 1 nm diameter micropores of NU-1000.

Table 4.9: Properties of catalysts tested for glucose isomerization.

sample	Zr content[a] (% w/w)	maximum synthesis temperature (°C)	BET surface area[b] (m^2 g^{-1})	pore volume (cm^3 g^{-1})[b]
Zr_6@SiO_2	23	500	444	0.46
dehyd-NU-1000	30	300	2100	1.61
cal-NU-1000	74	500	52	0.13
Zr_6@n-t-SiO_2	0.7	500	371	0.32
Zr_6@n-t-SiO_2(High Zr)	9	500	173	0.12

[a]The Zr content of dehyd-NU-1000 and cal-NU-1000 was estimated assuming the formulas $Zr_6(\mu_3{-}O)_8(HTBAPy)_2$ and ZrO_2, respectively. The Zr content of nanocast Zr_6@SiO_2 and the control samples, Zr_6@n-t-SiO_2 and Zr_6@n-t-SiO_2(High Zr), were determined by ICP-MS.
[b]The N_2 sorption isotherms and DFT surface area versus pore size histograms are shown in Figure S10 of ref 588.

Aggregation of oxozirconium clusters to form tetragonal ZrO_2 nanoparticles occurred when NU-1000 was heated to 500 °C in air, but in the nanocast materials no significant cluster agglomeration was observed even after heating to 600 °C in air. The clusters remained accessible to reagents such as pyridine or glucose after these high-temperature treatments. The Lewis acidity of these clusters was demonstrated through the isomerization of glucose to fructose, and the mechanism of this reaction was computed with DFT.

The nanocasting method should also be applicable to other large-pore MOF systems that can accommodate precursors like TMOS in the pores. In addition, other precursors could be used for infiltration to produce other secondary scaffold compositions like metal oxides (e.g. titanium dioxide)[585] or carbon by adapting existing nanocasting methods.[53] This affords another handle for optimizing the catalytic properties of the single-site metals or clusters in the nanocast materials. Multiple nanocasting cycles may be used to control the thickness and stability of the secondary scaffold. Nanocasting, combined with the exceptional tunability of MOFs, may pave the way toward a new generation of highly active and stable catalysts for many transformations.

References

[1] Sumida, K.; Rogow, D. L.; Mason, J. A.; McDonald, T. M.; Bloch, E. D.; Herm, Z. R.; Bae, T.-H.; Long, J. R. *Chem. Rev.* **2012**, *112*, 724–781.

[2] Dechambenoit, P.; Long, J. R. *Chem. Soc. Rev.* **2011**, *40*, 3249–3265.

[3] Han, S. S.; Jung, D.-H.; Heo, J. *J. Phys. Chem. C* **2013**, *117*, 71–77.

[4] Brozek, C. K.; Dincă, M. *J. Am. Chem. Soc.* **2013**, *135*, 12886–12891.

[5] Lalonde, M.; Bury, W.; Karagiaridi, O.; Brown, Z.; Hupp, J. T.; Farha, O. K. *J. Mater. Chem. A* **2013**, *1*, 5453–5468.

[6] Farha, O. K.; Yazaydin, A. O.; Eryazici, L.; Malliakas, C. D.; Hauser, B.; Kanatzidis, M.; Nguyen, S.; Snurr, R.; Hupp, J. *Nat. Chem.* **2010**, *2*, 944–948.

[7] Bon, V.; Senkovskyy, V.; Senkovska, I.; Kaskel, S. *Chem. Commun.* **2012**, *48*, 8407–8409.

[8] Bloch, E. D.; Murray, L. J.; Queen, W. L.; Chavan, S.; Maximoff, S. N.; Bigi, J. P.; Krishna, R.; Peterson, V. K.; Grandjean, F.; Long, G. J.; Smit, B.; Bordiga, S.; Brown, C. M.; Long, J. R. *J. Am. Chem. Soc.* **2011**, *133*, 14814–14822.

[9] Borycz, J.; Paier, J.; Verma, P.; Darago, L. E.; Xiao, D. J.; Truhlar, D. G.; Long, J. R.; ; Gagliardi, L. *Inorg. Chem.* **2016**,

[10] Bloch, E. D.; Queen, W. L.; Krishna, R.; Zadrozny, J. M.; Brown, C. M.; Long, J. R. *Science* **2012**, *335*, 1606–1610.

[11] Geier, S. J.; Mason, J. A.; Bloch, E. D.; Queen, W. L.; Hudson, M. R.; Brown, C. M.; Long, J. R. *Chem. Sci.* **2013**, *4*, 2054–2061.

[12] Verma, P.; Vogiatzis, K. D.; Planas, N.; Borycz, J.; Xiao, D. J.; Long, J. R.; Gagliardi, L.; Truhlar, D. G. *J. Am. Chem. Soc.* **2015**, *137*, 5770–5781.

[13] Katz, M. J.; Mondloch, J. E.; Totten, R. K.; Park, J. K.; Nguyen, S. T.; Farha, O. K.; Hupp, J. T. *Angew. Chem.* **2014**, *126*, 507–511.

[14] Kitagawa, S.; Kitaura, R.; Noro, S.-i. *Angew. Chem.* **2004**, *43*, 2334–2375.

[15] Ferey, G. *Chem. Soc. Rev.* **2008**, *37*, 191–214.

[16] Yaghi, O. M.; Li, G.; Li, H. *Nature* **1995**, *378*, 703–706.

[17] Yaghi, O. M.; Li, H. *J. Am. Chem. Soc.* **1995**, *117*, 10401–10402.

[18] Li, H.; Eddaoudi, M.; O'Keeffe, M.; Yaghi, O. M. *Nature* **1999**, *402*, 276–279.

[19] Keskin, S.; Sholl, D. S. *Ind. Eng. Chem. Res.* **2009**, *48*, 914–922.

[20] Zhao, Z.; Ma, X.; Kasik, A.; Li, Z.; Lin, Y. S. *Ind. Eng. Chem. Res.* **2013**, *52*, 1102–1108.

[21] Zhao, Z.; Li, Z.; Lin, Y. S. *Ind. Eng. Chem. Res.* **2009**, *48*, 10015–10020.

[22] Venkataramanan, N. S.; Sahara, R.; Mizuseki, H.; Kawazoe, Y. *Int. J. Mol. Sci.* **2009**, *10*, 1601–1608.

[23] Rowsell, J. L.; Yaghi, O. M. *Microporous Mesoporous Mater.* **2004**, *73*, 3 – 14, Metal-Organic Open Frameworks.

[24] Wu, X.; Bao, Z.; Yuan, B.; Wang, J.; Sun, Y.; Luo, H.; Deng, S. *Microporous Mesoporous Mater.* **2013**, *180*, 114 – 122.

[25] Chung, Y. G.; Camp, J.; Haranczyk, M.; Sikora, B. J.; Bury, W.; Krungleviciute, V.; Yildirim, T.; Farha, O. K.; Sholl, D. S.; Snurr, R. Q. *Chem. Mater.* **2014**, *26*, 6185–6192.

[26] Wilmer, C. E.; Leaf, M.; Lee, C. Y.; Farha, O. K.; Hauser, B. G.; Hupp, J. T.; Snurr, R. Q. *Nat. Chem.* **2012**, *4*, 83–89.

[27] Civalleri, B.; Napoli, F.; Noel, Y.; Roetti, C.; Dovesi, R. *CrystEngComm* **2006**, *8*, 364–371.

[28] Canepa, P.; Chabal, Y. J.; Thonhauser, T. *Phys. Rev. B* **2013**, *87*, 094407.

[29] Xiao, D. J. et al. *Nat. Chem.* **2014**, *6*, 590.

[30] Schieber, M. M. In *Selected Topics in Solid State Physics Experimental Magnetochemistry*; Wohlfarth, E. P., Ed.; Max Planck Institut für Bioanorganische Chemie: North-Holland, 1967; Vol. VIII.

[31] Park, J.; Kim, H.; Jung, Y. *J. Phys. Chem. Lett.* **2013**, *4*, 2530–2534.

[32] Blanchon le Bouhelec, E.; Mougin, P.; Barreau, A.; Solimando, R. *Energy & Fuels* **2007**, *21*, 2044–2055.

[33] Sumida, K.; Rogow, D. L.; Mason, J. A.; McDonald, T. M.; Bloch, E. D.; Herm, Z. R.; Bae, T.-H.; Long, J. R. *Chem. Rev.* **2012**, *112*, 724–781.

[34] Yeh, J. T.; Resnik, K. P.; Rygle, K.; Pennline, H. W. *Fuel Processing Technology* **2005**, *86*, 1533 – 1546.

[35] Olajire, A. A. *Energy* **2010**, *35*, 2610 – 2628.

[36] Burchell, T.; Rogers, M. *SAE Tech. Pap. Ser.* **2000**,

[37] Getman, R. B.; Bae, Y.-S.; Wilmer, C. E.; Snurr, R. Q. *Chem. Rev.* **2012**, *112*, 703–723.

[38] Bloch, E. D.; Murray, L. J.; Queen, W. L.; Chavan, S.; Maximoff, S. N.; Bigi, J. P.; Krishna, R.; Peterson, V. K.; Grandjean, F.; Long, G. J.; Smit, B.; Bordiga, S.; Brown, C. M.; Long, J. R. *J. Am. Chem. Soc.* **2011**, *133*, 14814–14822.

[39] Dzubak, A. L.; Lin, L.-C.; Kim, J.; Swisher, J. A.; Poloni, R.; Maximoff, S. N.; Smit, B.; Gagliardi, L. *Nat. Chem.* **2012**, *4*, 810–816.

[40] Gándara, F.; Gomez-Lor, B.; Gutiérrez-Puebla, E.; Iglesias, M.; Monge, M. A.; Proserpio, D. M.; Snejko, N. *Chem. Mater.* **2008**, *20*, 72–76.

[41] Planas, N.; Dzubak, A. L.; Poloni, R.; Lin, L.-C.; McManus, A.; McDonald, T. M.; Neaton, J. B.; Long, J. R.; Smit, B.; Gagliardi, L. *J. Am. Chem. Soc.* **2013**, *135*, 7402–7405.

[42] Lu, J.; Serna, P.; Gates, B. C. *ACS Catal.* **2011**, *1*, 1549–1561.

[43] Aydin, C.; Lu, J.; Shirai, M.; Browning, N. D.; Gates, B. C. *ACS Catal.* **2011**, *1*, 1613–1620.

[44] George, S. M. *Chem. Rev.* **2010**, *110*, 111–131.

[45] Mondloch, J. E.; Bury, W.; Fairen-Jimenez, D.; Kwon, S.; DeMarco, E. J.; Weston, M. H.; Sarjeant, A. A.; Nguyen, S. T.; Stair, P. C.; Snurr, R. Q.; Farha, O. K.; Hupp, J. T. *J. Am. Chem. Soc.* **2013**, *135*, 10294–10297.

[46] Li, Z.; Schweitzer, N. M.; League, A. B.; Bernales, V.; Peters, A. W.; Getsoian, A.; Wang, T. C.; Miller, J. T.; Vjunov, A.; Fulton, J. L.; Lercher, J. A.; Cramer, C. J.; Gagliardi, L.; Hupp, J. T.; Farha, O. K. *J. Am. Chem. Soc.* **2016**, *138*, 1977–1982.

[47] Liu, C.; nan Wu, Y.; Morlay, C.; Gu, Y.; Gebremariam, B.; Yuan, X.; Li, F. *ACS Appl. Mater. Interfaces* **2016**, *8*, 2552–2561.

[48] Yang, D.; Odoh, S. O.; Wang, T. C.; Farha, O. K.; Hupp, J. T.; Cramer, C. J.; Gagliardi, L.; Gates, B. C. *J. Am. Chem. Soc.* **2015**, *137*, 7391–7396.

[49] James, D. H.; Castor, W. M. In *Ullmanns Encyclopedia of Industrial Chemistry*; Scuseria, C. E. D., Frenking, G., Kim, K. S., E., G., Eds.; Wiley-VCH: Weinheim, 2005.

[50] Pines, H. *The Chemistry of Catalytic Hydrocarbon Conversions*; Elsevier: Mülheim an der Ruhr, Germany, 2012.

[51] Ma, S.; Wang, X.-S.; Yuan, D.; Zhou, H.-C. *Angew. Chem.* **2008**, *47*, 4130–4133.

[52] Kang, I. J.; Khan, N. A.; Haque, E.; Jhung, S. H. *Chem. Eur. J.* **2011**, *17*, 6437–6442.

[53] Lu, A.-H.; Schueth, F. *Adv. Mater.* **2006**, *18*, 1793–1805.

[54] Sun, J.-K.; Xu, Q. *Energy Environ. Sci.* **2014**, *7*, 2071–2100.

[55] Sabo, M.; Henschel, A.; Froede, H.; Klemm, E.; Kaskel, S. *J. Mater. Chem.* **2007**, *17*, 3827–3832.

[56] na Puertolas, B.; Solsona, B.; Agouram, S.; Murillo, R.; Mastral, A. M.; Aranda, A.; Taylor, S. H.; Garcia, T. *App. Catal. B. Environ.* **2010**, *93*, 395 – 405.

[57] Khirsariya, P.; Mewada, R. K. *Procedia Eng.* **2013**, *51*, 409 – 415.

[58] Neese, F. *J. Am. Chem. Soc.* **2006**, *128*, 10213–10222.

[59] Maurice, R.; Bastardis, R.; de Graaf, C.; Suaud, N.; Mallah, T.; Guihery, N. *J. Chem. Theory Comput.* **2009**, *5*, 2977–2984.

[60] Chibotaru, L. F.; Ungur, L. *J. Chem. Phys.* **2012**, *137*, 64112.

[61] Maurice, R.; Vendier, L.; Costes, J.-P. *Inorg. Chem.* **2011**, *50*, 11075–11081.

[62] Costes, J.-P.; Maurice, R.; Vendier, L. *Chem. Eur. J.* **2012**, *18*, 4031–4040.

[63] Ruamps, R.; Batchelor, L. J.; Maurice, R.; Gogoi, N.; Jimenez-Lozano, P.; Guihery, N.; de Graaf, C.; Barra, A.-L.; Sutter, J.-P.; Mallah, T. *Chem. Eur. J.* **2013**, *19*, 950–956.

[64] Ganyushin, D.; Neese, F. *J. Chem. Phys.* **2006**, *125*.

[65] Duboc, C.; Ganyushin, D.; Sivalingam, K.; Collomb, M.-N.; Neese, F. *J. Phys. Chem. A* **2010**, *114*, 10750–10758.

[66] Kubica, A.; Kowalewski, J.; Kruk, D.; Odelius, M. *J. Chem. Phys.* **2013**, *138*.

[67] Angeli, C.; Cimiraglia, R.; Evangelisti, S.; Leininger, T.; Malrieu, J.-P. *J. Chem. Phys.* **2001**, *114*, 10252–10264.

[68] Xiao, D. J. et al. *Nat. Chem.* **2014**, *6*, 590–595.

[69] Maurice, R.; Verma, P.; Zadrozny, J. M.; Luo, S.; Borycz, J.; Long, J. R.; Truhlar, D. G.; Gagliardi, L. *Inorg. Chem.* **2013**, *52*, 9379–9389.

[70] Perdew, J. P.; Burke, K.; Ernzerhof, M. *Phys. Rev. Lett.* **1996**, *77*, 3865–3868.

[71] Yu, H. Y. S.; Zhang, W. J.; Verma, P.; He, X.; Truhlar, D. G. *Phys. Chem. Chem. Phys.* **2015**, *17*, 12146–12160.

[72] Duanmu, K.; Luo, S.; Truhlar, D. G. **2015**,

[73] Heyd, J.; Scuseria, G. E.; Ernzerhof, M. *J. Chem. Phys.* **2003**, *118*, 8207–8215.

[74] Heyd, J.; Scuseria, G. E. *J. Chem. Phys.* **2004**, *121*, 1187–1192.

[75] Heyd, J.; Scuseria, G. E.; Ernzerhof, M. *J. Chem. Phys.* **2006**, *124*, 219906.

[76] Rivero, P.; Moreira, I. d. P. R.; Illas, F.; Scuseria, G. E. *J. Chem. Phys.* **2008**, *129*, 184110.

[77] Wriedt, M.; Yakovenko, A. A.; Haider, G. J.; Prosvirin, A. V.; Dunbar, K. R.; Zhou, H. C. *J. Am. Chem. Soc.* **2013**, *135*, 4040–4050.

[78] Asmis, K.; Santambrogio, G.; Brmmer, M.; Sauer, J. *Angew. Chem. Int. Ed.* **2005**, *117*, 3182–3185.

[79] Chevrier, V. L.; Ong, S. P.; Armiento, R.; Chan, M. K. Y.; Ceder, G. *Phys. Rev. B* **2010**, *82*, 075122.

[80] Cohen, A. J.; Mori-Sanchez, P.; Yang, W. *J. Chem. Phys.* **2007**, *126*, 191109.

[81] Mori-Sanchez, P.; Cohen, A. J.; Yang, W. *Phys. Rev. Lett.* **2008**, *100*, 146401.

[82] Grimme, S. *J. Comput. Chem.* **2006**, *27*, 1787–1799.

[83] Rappé, A. K.; Casewit, C. J.; Colwell, K. S.; Goddard, W. A., III,; Skiff, W. M. *J. Am. Chem. Soc.* **1992**, *114*, 10024–10035.

[84] Fairen-Jimenez, D.; Lozano-Casal, P.; Dueren, T. In *Characterisation of Porous Solids VIII*; Seaton, N., Reinoso, F. R., Llewellyn, P., Kaskel, S., Eds.; The Royal Society of Chemistry, 2009; Chapter Assessing Generic Force Fields to Describe Adsorption on Metal-Organic Frameworks.

[85] Casewit, C. J.; Colwell, K. S.; Rappé, A. K. *J. Am. Chem. Soc.* **1992**, *114*, 10035–10046.

[86] Mayo, S. L.; Olafson, B. D.; Goddard, W. A. *J. Phys. Chem.* **1990**, *94*, 8897–8909.

[87] Bai, P.; Tsapatsis, M.; Siepmann, J. I. *J. Phys. Chem. C* **2013**, *117*, 24375–24387.

[88] Allen, M. P.; Tildesley, D. J. *Computer Simulation of Liquids*; Oxford University Press: New York, 1987.

[89] Bristow, J. K.; Tiana, D.; Walsh, A. *J. Chem. Theory Comput.* **2014**, *10*, 4644–4652.

[90] Meilikhov, M.; Yusenko, K.; Fischer, R. A. *J. Am. Chem. Soc.* **2009**, *131*, 9644–9645.

[91] Coudert, F.-X.; Ortiz, A. U.; Haigis, V.; Bousquet, D.; Fuchs, A. H.; Ballandras, A.; Weber, G.; Bezverkhyy, I.; Geolfroy, N.; Bellat, J.-P.; Ortiz, G.; Chaplais, G.; Patarin, J.; Boutin, A. *J. Phys. Chem. C* **2014**, *118*, 5397–5405.

[92] Warshel, A.; Kato, M.; Pisliakov, A. V. *J. Chem. Theory Comput.* **2007**, *3*, 2034–2045.

[93] Fetisov, E. O.; Siepmann, J. I. *J. Chem. Eng. Data* **2014**, *59*, 3301–3306.

[94] Rai, N.; Siepmann, J. I. *J. Phys. Chem. B* **2013**, *117*, 273–288.

[95] Rai, N.; Siepmann, J. I. *J. Phys. Chem. B* **2007**, *111*, 10790–10799.

[96] Stubbs, J. M.; Potoff, J. J.; Siepmann, J. I. *J. Phys. Chem. B* **2004**, *108*, 17596–17605.

[97] Chen, B.; Potoff, J. J.; Siepmann, J. I. *J. Phys. Chem. B* **2001**, *105*, 3093–3104.

[98] Potoff, J. J.; Siepmann, J. I. *AIChE J.* **2001**, *47*, 1676–1682.

[99] Marenich, A. V.; Jerome, S. V.; Cramer, C. J.; Truhlar, D. G. *J. Chem. Theory Comput.* **2012**, *8*, 527–541.

[100] Manz, T. A.; Sholl, D. S. *J. Chem. Theory Comput.* **2010**, *6*, 2455–2468.

[101] Forsberg, N.; Malmqvist, P.-Å. *Chem. Phys. Lett.* **1997**, *274*, 196–204.

[102] Gordon, M. S.; Smith, Q. A.; Xu, P.; Slipchenko, L. V. *Ann. Rev. Phys. Chem.* *64*, 553.

[103] Borycz, J.; Lin, L.-C.; Bloch, E. D.; Kim, J.; Dzubak, A. L.; Maurice, R.; Semrouni, D.; Lee, K.; Smit, B.; Gagliardi, L. *J. Phys. Chem. C* **2014**, *118*, 12230.

[104] Perdew, J. P.; Ernzerhof, M.; Burke, K. *J. Chem. Phys.* **1996**, *105*, 9982–9985.

[105] Grimme, S.; Antony, J.; Ehrlich, S.; Krieg, H. *J. Chem. Phys.* **2010**, *132*.

[106] *Solid State Ionics* **2000**, *131*, 175 – 188.

[107] Lu, J.; Serna, P.; Aydin, C.; Browning, N. D.; Gates, B. C. *J. Am. Chem. Soc.* **2011**, *133*, 16186–16195.

[108] Deria, P.; Mondloch, J. E.; Tylianakis, E.; Ghosh, P.; Bury, W.; Snurr, R. Q.; Hupp, J. T.; Farha, O. K. *J. Am. Chem. Soc.* **2013**, *135*, 16801–16804.

[109] Mondloch, J. E.; Katz, M. J.; Isley III, W. C.; Ghosh, P.; Liao, P.; Bury, W.; Wagner, G. W.; Hall, M. G.; DeCoste, J. B.; Peterson, G. W.; Snurr, R. Q.; Cramer, C. J.; Hupp, J. T.; Farha, O. K. *Nat. Mater.* **2015**, *14*, 512–516.

[110] Morris, W.; Volosskiy, B.; Demir, S.; Gandara, F.; McGrier, P. L.; Furukawa, H.; Cascio, D.; Stoddart, J. F.; Yaghi, O. M. *Inorg. Chem.* **2012**, *51*, 6443–6445.

[111] Feng, D.; Gu, Z.-Y.; Li, J.-R.; Jiang, H.-L.; Wei, Z.; Zhou, H.-C. *Angew. Chem.* **2012**, *51*, 10307–10310.

[112] Bosch, R. H. E. C.; Bloksma, F. L.; Huijs, J. M. M.; Verheijen, M. A.; Kessels, W. M. M. *J. Phys. Chem. C* **2016**, *120*, 750–755.

[113] Lu, G. et al. *Nat. Chem.* **2012**, *4*, 310–316.

[114] Moseley, P.; Curtin, W. A. *Nano. Letters.* **2015**, *15*, 4089–4095.

[115] Li, S.; Zhang, W.; Huo, F. *Physica E: Low-dimensional Systems and Nanostructures* **2015**, *69*, 56 – 60.

[116] Li, Z.; Schweitzer, N. M.; League, A. B.; Bernales, V.; Peters, A. W.; Getsoian, A. .; Wang, T. C.; Miller, J. T.; Vjunov, A.; Fulton, J. L.; Lercher, J. A.; Cramer, C. J.; Gagliardi, L.; Hupp, J. T.; Farha, O. K. *J. Am. Chem. Soc.* **2016**, *138*, 1977–1982.

[117] Aydin, C.; Lu, J.; Shirai, M.; Browning, N. D.; Gates, B. C. *ACS Catal.* **2011**, *1*, 1613–1620.

[118] Basset, J.-M.; Coperet, C.; Soulivong, D.; Taoufik, M.; Thivolle Cazat, J. *Acc. Chem. Res.* **2010**, *43*, 323–334.

[119] Leclerc, H.; Vimont, A.; Lavalley, J.-C.; Daturi, M.; Wiersum, A. D.; Llwellyn, P. L.; Horcajada, P.; Ferey, G.; Serre, C. *Phys. Chem. Chem. Phys.* **2011**, *13*, 11748–11756.

[120] Bae, Y.-S.; Lee, C. Y.; Kim, K. C.; Farha, O. K.; Nickias, P.; Hupp, J. T.; Nguyen, S. T.; Snurr, R. Q. *Angew. Chem.* **2012**, *51*, 1857–1860.

[121] Sumida, K.; Rogow, D. L.; Mason, J. A.; McDonald, T. M.; Bloch, E. D.; Herm, Z. R.; Bae, T.-H.; Long, J. R. *Chem. Rev.* **2012**, *112*, 724–781.

[122] Li, J.-R.; Sculley, J.; Zhou, H.-C. *Chem. Rev.* **2012**, *112*, 869–932.

[123] Wu, H.; Gong, Q.; Olson, D. H.; Li, J. *Chem. Rev.* **2012**, *112*, 836–868.

[124] Lee, J.; Farha, O. K.; Roberts, J.; Scheidt, K. A.; Nguyen, S. T.; Hupp, J. T. *Chem. Soc. Rev.* **2009**, *38*, 1450–1459.

[125] Ma, L.; Abney, C.; Lin, W. *Chem. Soc. Rev.* **2009**, *38*, 1248–1256.

[126] Bartolomé, E.; Alonso, P. J.; Arauzo, A.; Luzon, J.; Bartolome, J.; Racles, C.; Turta, C. *Dalton Trans.* **2012**, *41*, 10382–10389.

[127] Senchyk, G. A.; Lysenko, A. B.; Rusanov, E. B.; Chernega, A. N.; Jezierska, J.; Domasevitch, K. V.; Ozarowski, A. *Eur. J. Inorg. Chem.* **2012**, *2012*, 5802–5813.

[128] He, Y.; Krishna, R.; Chen, B. *Ener. Environ. Sci.* **2012**, *5*, 9107–9120.

[129] McWeeny, R. *J. Chem. Phys.* **1965**, *42*, 1717–1725.

[130] Freedman, D. E.; Harman, W. H.; Harris, T. D.; Long, G. J.; Chang, C. J.; Long, J. R. *J. Am. Chem. Soc.* **2010**, *132*, 1224–1225.

[131] Harman, W. H.; Harris, T. D.; Freedman, D. E.; Fong, H.; Chang, A.; Rinehart, J. D.; Ozarowski, A.; Sougrati, M. T.; Grandjean, F.; Long, G. J.; Long, J. R.; Chang, C. J. *J. Am. Chem. Soc.* **2010**, *132*, 18115–18126.

[132] Venkatakrishnan, T. S.; Sahoo, S.; Brefuel, N.; Duhayon, C.; Paulsen, C.; Barra, A.-L.; Ramasesha, S.; Sutter, J.-P. *J. Am. Chem. Soc.* **2010**, *132*, 6047–6056.

[133] Zadrozny, J. M.; Atanasov, M.; Bryan, A. M.; Lin, C.-Y.; Rekken, B. D.; Power, P. P.; Neese, F.; Long, J. R. *Chem. Sci.* **2013**, *4*, 125–138.

[134] Atanasov, M.; Zadrozny, J. M.; Long, J. R.; Neese, F. *Chem. Sci.* **2013**, *4*, 139–156.

[135] Pradipto, A.-M.; Maurice, R.; Guihéry, N.; de Graaf, C.; Broer, R. *Phys. Rev. B* **2012**, *85*, 014409.

[136] Maurice, R.; Pradipto, A.-M.; de Graaf, C.; Broer, R. *Phys. Rev. B* **2012**, *86*, 024411.

[137] Pederson, M. R.; Khanna, S. N. *Phys. Rev. B* **1999**, *60*, 9566–9572.

[138] Aquino, F.; Rodriguez, J. H. *J. Chem. Phys.* **2005**, *123*.

[139] Neese, F. *J. Chem. Phys.* **2007**, *127*.

[140] Schmitt, S.; Jost, P.; van Wllen, C. *J. Chem. Phys.* **2011**, *134*.

[141] de Graaf, C.; Sousa, C. *Int. J. Quant. Chem.* **2006**, *106*, 2470–2478.

[142] Sugisaki, K.; Toyota, K.; Sato, K.; Shiomi, D.; Kitagawa, M.; Takui, T. *Chem. Phys. Lett.* **2009**, *477*, 369–373.

[143] Vancoillie, S.; Pierloot, K. *J. Phys. Chem. A* **2008**, *112*, 4011–4019.

[144] Chibotaru, L. F.; Ungur, L.; Aronica, C.; Elmoll, H.; Pilet, G.; Luneau, D. *J. Am. Chem. Soc.* **2008**, *130*, 12445–12455.

[145] Chibotaru, L. F.; Ungur, L.; Soncini, A. *Angew. Chem.* **2008**, *47*, 4126–4129.

[146] Telser, J.; Ozarowski, A.; Krzystek, J. *Elec. Para. Res.* **2013**, *23*, 209–263.

[147] Ruamps, R.; Maurice, R.; Batchelor, L.; Boggio-Pasqua, M.; Guillot, R.; Barra, A. L.; Liu, J.; Bendeif, E.-E.; Pillet, S.; Hill, S.; Mallah, T.; Guihery, N. *J. Am. Chem. Soc.* **2013**, *135*, 3017–3026.

[148] Abragam, A.; Bleaney, B. *Electron paramagnetic resonance of transition ions*; Dover Publications: New York, 2012.

[149] Telser, J. *J. Braz. Chem. Soc.* **2006**, *17*, 1501–1515.

[150] Maurice, R.; de Graaf, C.; Guihéry, N. *J. Chem. Phys.* **2010**, *133*.

[151] Atanasov, M.; Ganyushin, D.; Pantazis, D. A.; Sivalingam, K.; Neese, F. *Inorg. Chem.* **2011**, *50*, 7460–7477.

[152] McGarvey, B. R.; Telser, J. *Inorg. Chem.* **2012**, *51*, 6000–6010.

[153] Moreira, I. P. R.; Illas, F. *Phys. Chem. Chem. Phys.* **2006**, *8*, 1645–1659.

[154] Calzado, C. J.; Cabrero, J.; Malrieu, J. P.; Caballol, R. *J. Chem. Phys.* **2002**, *116*, 2728–2747.

[155] Calzado, C. J.; Cabrero, J.; Malrieu, J. P.; Caballol, R. *J. Chem. Phys.* **2002**, *116*, 3985–4000.

[156] Calzado, C. J.; Angeli, C.; Taratiel, D.; Caballol, R.; Malrieu, J.-P. *J. Chem. Phys.* **2009**, *131*.

[157] Valero, R.; Costa, R.; de P. R. Moreira, I.; Truhlar, D. G.; Illas, F. *J. Chem. Phys.* **2008**, *128*.

[158] Brain, G. A.; Berry, J. F. *J. Chem. Ed.* **2008**, *85*, 532.

[159] Verma, P.; Xu, X.; Truhlar, D. G. *J. Phys. Chem. C* **2013**, *117*, 12648–12660.

[160] Bogdanov, N. A.; Maurice, R.; Rousochatzakis, I.; van den Brink, J.; Hozoi, L. *Phys. Rev. Lett.* **2013**, *110*, 127206.

[161] Wynn, C. M.; Giryu, M. A.; Brinckerhoff, W. B.; Sugiura, K.-I.; Miller, J. S.; Epstein, A. J. *Chem. Mater.* **1997**, *9*, 2156–2163.

[162] Kar, P.; Biswas, R.; Drew, M. G. B.; Ida, Y.; Ishida, T.; Ghosh, A. *Dalton Trans.* **2011**, *40*, 3295–3304.

[163] Oprea, C. I.; Panait, P.; Cimpoesu, F.; Humelnicu, I.; Ferbinteanu, M.; Gîrţu, M. A. *Theor. Chem. Acc.* **2012**, *131*, 1–13.

[164] Van Vleck, J. H. *Rev. Mod. Phys.* **1951**, *23*, 213–227.

[165] McLachlan, A. D. *Mol. Phys.* **1963**, *6*, 441–444.

[166] Abragam, A.; Pryce, M. H. L. *Proc. Roy. Soc. Lond. A* **1951**, *205*, 135–153.

[167] Gatteschi, D.; Sessoli, R. *Angew. Chem.* **2003**, *42*, 268–297.

[168] Zein, S.; Duboc, C.; Lubitz, W.; Neese, F. *Inorg. Chem.* **2008**, *47*, 134–142.

[169] Zein, S.; Neese, F. *J. Phys. Chem. A* **2008**, *112*, 7976–7983.

[170] Maurice, R.; Sivalingam, K.; Ganyushin, D.; Guihery, N.; de Graaf, C.; Neese, F. *Inorg. Chem.* **2011**, *50*, 6229–6236.

[171] Hendrich, M. P.; Debrunner, P. G. *Biophys. J.* **1989**, *56*, 489–506.

[172] Heisenberg, W. *Z. Physik* **1928**, *49*, 619–636.

[173] Dirac, P. A. M. *Proc. Roy. Sci. Lond.* **1929**, *A123*, 714–733.

[174] Van Vleck, J. H. *Rev. Mod. Phys.* **1945**, *17*, 27–47.

[175] Roos, B. O. In *Theory and Applications of Computational Chemistry*; Scuseria, C. E. D., Frenking, G., Kim, K. S., E., G., Eds.; Elsevier: Amsterdam, 2005; pp 725–764.

[176] Hess, B. A.; Marian, C. M.; Wahlgren, U.; Gropen, O. *Chem. Phys. Lett.* **1996**, *251*, 365–371.

[177] Neese, F. *J. Chem. Phys.* **2005**, *122*.

[178] Malmqvist, P. Å.; Roos, B. O.; Schimmelpfennig, B. *Chem. Phys. Lett.* **2002**, *357*, 230–240.

[179] Roos, B. O.; Malmqvist, P.-Å. *Phys. Chem. Chem. Lett.* **2004**, *6*, 2919–2927.

[180] Neese, F. *ORCA, An ab initio, density functional semiempirical program package, Version 2.9*; Max Planck Institut für Bioanorganische Chemie: Mülheim an der Ruhr, Germany, 2012.

[181] Llusar, R.; Casarrubios, M.; Barandiaran, Z.; Seijo, L. *J. Chem. Phys.* **1996**, *105*, 5321–5330.

[182] Weigend, F.; Ahlrichs, R. *Phys. Chem. Chem. Phys.* **2005**, *7*, 3297–3305.

[183] Zhao, Y.; Truhlar, D. G. *J. Chem. Phys.* **2006**, *125*, 194101.

[184] Zhao, Y.; Truhlar, D. G. *Theor. Chem. Acc.* **2008**, *120*, 215–241.

[185] Frisch, M. J. et al. Gaussian 09. 2009.

[186] Bŏca, R. *Coord. Chem. Rev.* **2004**, *248*, 757–815.

[187] Yamamoto, A. *Organotransition Metal Chemistry*; Wiley: New York, 1986.

[188] Bŏca, R. *Theoretical foundations of molecular magnetism*; Elsevier: Amsterdam: Netherlands, 1999.

[189] Sahoo, S.; Sutter, J.-P.; Ramasesha, S. *J. Stat. Phys.* **2012**, *147*, 181–193.

[190] Dzyaloshinsky, I. *J. Phys. Chem. Solids* **1958**, *4*, 241–255.

[191] Moriya, T. *Phys. Rev.* **1960**, *120*, 91–98.

[192] Plumer, M. L. *Phys. Rev. B* **2007**, *76*, 144411.

[193] Maurice, R.; Guihery, N.; Bastardis, R.; de Graaf, C. *J. Chem. Theory Comput.* **2010**, *6*, 55–65.

[194] Moskvin, A. S. *J. Exp. Theor. Phys.* **2007**, *104*, 913–927.

[195] Maurice, R.; Pradipto, A. M.; Guihery, N.; Broer, R.; De, G. C. *J. Chem. Theory Comput.* **2010**, *6*, 3092–3101.

[196] Kahn, O.; Larionova, J.; Yakhmi, J. V. *Chem. Eur. J.* **1999**, *5*, 3443–3449.

[197] Shen, L.; Yang, S.-W.; Xiang, S.; Liu, T.; Zhao, B.; Ng, M.-F.; Goeettlicher, J.; Yi, J.; Li, S.; Wang, L.; Ding, J.; Chen, B.; Wei, S.-H.; Feng, Y. P. *J. Am. Chem. Soc.* **2012**, *134*, 17286–17290.

[198] Mohapatra, S.; Rajeswaran, B.; Chakraborty, A.; Sundaresan, A.; Maji, T. K. *Chem. Mater. 25*, 1673–1679.

[199] Guha, B. C. *Nature* **1945**, *155*, 364–364.

[200] Goodenough, J. B. *Phys. Rev.* **1960**, *117*, 1442–1451.

[201] Odbadrakh, K.; Lewis, J. P.; Nicholson, D. M.; Petrova, T.; Michalkova, A.; Lesczynski, J. *J. Phys. Chem C* **2010**, *114*, 3732–3736.

[202] Yu, D.; Yazaydin, A. O.; Lane, J. R.; Dietzel, P. D. C.; Snurr, R. Q. *Chem. Sci.* **2013**, *4*, 3544–3556.

[203] Haldoupis, E.; Borycz, J.; Shi, H. L.; Vogiatzis, K. D.; Bai, P.; Queen, W. L.; Gagliardi, L.; Siepmann, J. I. *J. Phys. Chem. C* **2015**, *119*, 16058–16071.

[204] Zhang, Q.; Li, B.; Chen, L. *Inorg. Chem.* **2013**, *52*, 9356–9362.

[205] Liechtenstein, A. I.; Anisimov, V. I.; Zaanen, J. *Phys. Rev. B* **1995**, *52*, R5467–R5470.

[206] Iori, F.; Gatti, M.; Rubio, A. *Phys. Rev. B* **2012**, *85*, 115129.

[207] Grau-Crespo, R.; Wang, H.; Schwingenschloegl, U. *Phys. Rev. B* **2012**, *86*, 081101.

[208] Henderson, T. M.; Paier, J.; Scuseria, G. E. *Phys. Status Solidi B* **2011**, *248*, 767–774.

[209] Bain, G. A.; Berry, J. F. *J. Chem. E.* **2008**, *85*, 532–536.

[210] Kahn, O. *Molecular Magnetism*; Wiley-VCH: New York, 1993; pp 257–258.

[211] Georges, J. J. C. E. C. J. D. M., R.; Borrás-Alemar *Magnetism: Molecules to Materials: Models and Experiments*; Wiley-VCH: Weinheim: Germany, 2002.

[212] Zhao, Y.; Truhlar, D. G. *J. Chem. Phys.* **2006**, *125*.

[213] Zhao, Y.; Truhlar, D. G. *J. Chem. Phys* **2009**, *130*.

[214] Booth, G. H.; Grüneis, A.; Kresse, G.; Alavi, A. *Nature* **2013**, *493*, 365–370.

[215] Paier, J.; Ren, X.; Rinke, P.; Scuseria, G. E.; Grüneis, A.; Kresse, G.; Scheffler, M. *New J. Phys.* **2012**, *14*, 043002.

[216] Cramer, C. J.; Truhlar, D. G. *Phys. Chem. Chem. Phys.* **2009**, *11*, 10757–10816.

[217] Manz, T. A.; Sholl, D. S. *J. Chem. Theory Comput.* **2011**, *7*, 4146–4164.

[218] Krukau, A. V.; Vydrov, O. A.; Izmaylov, A. F.; Scuseria, G. E. *J. Chem. Phys.* **2006**, *125*, 224106.

[219] Becke, A. D. *J. Chem. Phys.* **1993**, *98*, 5648–5652.

[220] Lee, C. T.; Yang, W. T.; Parr, R. G. *Phys. Rev. B* **1988**, *37*, 785–789.

[221] Vosko, S. H.; Wilk, L.; Nusair, M. *Can. J. Phys.* **1980**, *58*, 1200–1211.

[222] Stephens, P. J.; Devlin, F. J.; Chabalowski, C. F.; Frisch, M. J. *J. Phys. Chem.* **1994**, *98*, 11623–11627.

[223] Ernzerhof, M.; Scuseria, G. E. *J. Chem. Phys.* **1999**, *110*, 5029–5036.

[224] Adamo, C.; Barone, V. *J. Chem. Phys.* **1999**, *110*, 6158–6170.

[225] Zhao, Y.; Truhlar, D. G. *Theor. Chem. Acc.* **2007**, *120*, 215–241.

[226] Kresse, G.; Furthmüller, J. *Phys. Rev. B* **1996**, *54*, 11169–11186.

[227] Kresse, G.; Furthmüller, J. *Comput. Mater. Sci* **1996**, *6*, 15–50.

[228] Paier, J.; Marsman, M.; Hummer, K.; Kresse, G.; Gerber, I. C.; Angyan, J. G. *J. Chem. Phys.* **2006**, *124*, 154709.

[229] Gygi, F.; Baldereschi, A. *Phys. Rev. B* **1986**, *34*, 4405–4408.

[230] Onida, G.; Reining, L.; Rubio, A. *Rev. Mod. Phys.* **2002**, *74*, 601–659.

[231] Zhou, J.; Sun, Q. *J. Am. Chem. Soc.* **2011**, *133*, 15113–15119.

[232] Bucko, T.; Hafner, J.; Lebegue, S.; Angyan, J. G. *J. Phys. Chem. A* **2010**, *114*, 11814–11824.

[233] Kerber, T.; Sierka, M.; Sauer, J. *J. Comput. Chem.* **2008**, *29*, 2088–2097.

[234] Penschke, C.; Paier, J.; Sauer, J. *J. Phys. Chem. C* **2013**, *117*, 5274–5285.

[235] Blöchl, P. E. *Phys. Rev. B* **1994**, *50*, 17953–17979.

[236] Kresse, G.; Joubert, D. *Phys. Rev. B* **1999**, *59*, 1758–1775.

[237] Krivy, I.; Gruber, B. *Acta Crystallogr. A* **1976**, *32*, 297–298.

[238] Grosse-Kunstleve, R. W.; Sauter, N. K.; Adams, P. D. *Acta Crysyallogr. A* **2004**, *60*, 1–6.

[239] Gajdos, M.; Hummer, K.; Kresse, G.; Furthmüller, J.; Bechstedt, F. *Phys. Rev. B* **2006**, *73*, 045112.

[240] Baroni, S.; de Gironcoli, S.; Dal Corso, A.; Giannozzi, P. *Rev. Mod. Phys.* **2001**, *73*, 515–562.

[241] Born, M.; Huang, K. *Dynamical Theory of Crystal Lattices*; Oxford University Press: Oxford, 1954.

[242] Pick, R. M.; Cohen, M. H.; Martin, R. M. *Phys. Rev. B* **1970**, *1*, 910.

[243] Heisenberg, W. *Zeit. Fur Phys.* **1928**, *49*, 619–636.

[244] Hamida, Y.; Danilovic, D.; Yuen, T.; Li, K.; Li, J. *J. App. Phys.* **2012**, *111*.

[245] Hohenberger, J.; Ray, K.; Meyer, K. *Nat. Commun.* **2012**, *3*.

[246] Alecu, I. M.; Zheng, J. J.; Zhao, Y.; Truhlar, D. G. *J. Chem. Theory Comput.* **2010**, *6*, 2872–2887.

[247] Huang, S. P.; Wilson, B. E.; Wang, B.; Fang, Y.; Buffington, K.; Stein, A.; Truhlar, D. G. *J. Am. Chem. Soc.* **2015**, *137*, 10992–11003.

[248] Verdaguer, M.; Bleuzen, A.; Marvaud, V.; Vaissermann, J.; Seuleiman, M.; Desplanches, C.; Scuiller, A.; Train, C.; Garde, R.; Gelly, G.; Lomenech, C.; Rosenman, I.; Veillet, P.; Cartier, C.; Villain, F. *Coord. Chem. Rev.* **1999**, *192*, 1023–1047.

[249] Keith, D. W. *Science* **2009**, *325*, 1654–1655.

[250] Rochelle, G. T. *Science* **2009**, *325*, 1652–1654.

[251] Choi, S.; Drese, J.; Jones, C. *ChemSusChem* **2009**, *2*, 796–854.

[252] Wang, J.; Huang, L.; Yang, R.; Zhang, Z.; Wu, J.; Gao, Y.; Wang, Q.; O'Hare, D.; Zhong, Z. *Energy Environ. Sci.* **2014**, *7*, 3478–3518.

[253] Furukawa, H.; Cordova, K. E.; O'Keeffe, M.; Yaghi, O. M. *Science* **2013**, *341*.

[254] Horike, S.; Shimomura, S.; Kitagawa, S. *Nat. Chem.* **2009**, *1*, 695–704.

[255] O'Keeffe, M.; Yaghi, O. M. *Chem. Rev.* **2012**, *112*, 675–702.

[256] Farha, O. K.; Hupp, J. T. *Acc. Chem. Res.* **2010**, *43*, 1166–1175.

[257] Farha, O. K.; Eryazici, I.; Jeong, N. C.; Hauser, B. G.; Wilmer, C. E.; Sarjeant, A. A.; Snurr, R. Q.; Nguyen, S. T.; Yazaydin, A. O.; Hupp, J. T. *J. Am. Chem. Soc.* **2012**, *134*, 15016–15021.

[258] Getman, R. B.; Bae, Y.-S.; Wilmer, C. E.; Snurr, R. Q. *Chem. Rev.* **2012**, *112*, 703–723.

[259] Li, J.-R.; Sculley, J.; Zhou, H.-C. *Chem. Rev.* **2012**, *112*, 869–932.

[260] Peng, Y.; Krungleviciute, V.; Eryazici, I.; Hupp, J. T.; Farha, O. K.; Yildirim, T. *J. Am. Chem. Soc.* **2013**, *135*, 11887–11894.

[261] Suh, M. P.; Park, H. J.; Prasad, T. K.; Lim, D.-W. *Chem. Rev.* **2012**, *112*, 782–835.

[262] Wilmer, C. E.; Farha, O. K.; Yildirim, T.; Eryazici, I.; Krungleviciute, V.; Sarjeant, A. A.; Snurr, R. Q.; Hupp, J. T. *Energy Environ. Sci.* **2013**, *6*, 1158–1163.

[263] Bae, Y.-S.; Hauser, B. G.; Farha, O. K.; Hupp, J. T.; Snurr, R. Q. *Microporous Mesoporous Mater.* **2011**, *141*, 231 – 235.

[264] Kreno, L. E.; Leong, K.; Farha, O. K.; Allendorf, M.; Van Duyne, R. P.; Hupp, J. T. *Chem. Rev.* **2012**, *112*, 1105–1125.

[265] Horcajada, P.; Serre, C.; Vallet-Regí, M.; Sebban, M.; Taulelle, F.; Férey, G. *Angew. Chem. Int. Ed.* **2006**, *45*, 5974–5978.

[266] Lee, C. Y.; Farha, O. K.; Hong, B. J.; Sarjeant, A. A.; Nguyen, S. T.; Hupp, J. T. *J. Am. Chem. Soc.* **2011**, *133*, 15858–15861.

[267] So, M. C.; Wiederrecht, G. P.; Mondloch, J. E.; Hupp, J. T.; Farha, O. K. *Chem. Commun.* **2015**, *51*, 3501–3510.

[268] Lee, K.; Howe, J. D.; Lin, L.-C.; Smit, B.; Neaton, J. B. *Chem. Mater.* **2015**, *27*, 668–678.

[269] Cohen, S. M. *Chem. Rev.* **2012**, *112*, 970–1000.

[270] Deria, P.; Mondloch, J. E.; Karagiaridi, O.; Bury, W.; Hupp, J. T.; Farha, O. K. *Chem. Soc. Rev.* **2014**, *43*, 5896–5912.

[271] Brozek, C. K.; Dincă, M. *Chem. Sci.* **2012**, *3*, 2110–2113.

[272] Liao, J.-H.; Chen, W.-T.; Tsai, C.-S.; Wang, C.-C. *CrystEngComm* **2013**, *15*, 3377–3384.

[273] Li, J.; Li, L.; Hou, H.; Fan, Y. *Cryst. Growth Des.* **2009**, *9*, 4504–4513.

[274] Millward, A. R.; Yaghi, O. M. *J. Am. Chem Soc.* **2005**, *127*, 17998–17999.

[275] Hicks, J. M.; Desgranges, C.; Delhommelle, J. *J. Phys. Chem. C* **2012**, *116*, 22938–22946.

[276] Abdelhameed, R. M.; Carlos, L. D.; Rabu, P.; Santos, S. M.; Silva, A. M. S.; Rocha, J. a. *Eur. J. Inorg. Chem.* **2014**, *2014*, 5285–5295.

[277] Yang, Q.; Zhong, C.; Chen, J.-F. *J. Phys. Chem. C* **2008**, *112*, 1562–1569.

[278] Yang, Q.; Ma, L.; Zhong, C.; An, X.; Liu, D. *J. Phys. Chem. C* **2011**, *115*, 2790–2797.

[279] Yang, L.-M.; Ravindran, P.; Vajeeston, P.; Tilset, M. *RSC Adv.* **2012**, *2*, 1618–1631.

[280] Li, H.; Eddaoudi, M.; O'Keeffe, M.; Yaghi, O. M. *Nature* **1999**, *402*, 276–279.

[281] Hicks, J. M.; Desgranges, C.; Delhommelle, J. *J. Phys. Chem. C* **2012**, *116*, 22938–22946.

[282] Babarao, R.; Jiang, J. *Langmuir* **2008**, *24*, 6270–6278.

[283] Feldblyum, J. I.; Dutta, D.; Wong-Foy, A. G.; Dailly, A.; Imirzian, J.; Gidley, D. W.; Matzger, A. J. *Langmuir* **2013**, *29*, 8146–8153.

[284] Orefuwa, S.; Iriowen, E.; Yang, H.; Wakefield, B.; Goudy, A. *Microporous Mesoporous Mater.* **2013**, *177*, 82 – 90.

[285] Borycz, J.; Lin, L.-C.; Bloch, E. D.; Kim, J.; Dzubak, A. L.; Maurice, R.; Semrouni, D.; Lee, K.; Smit, B.; Gagliardi, L. *J. Phys. Chem. C* **2014**, *118*, 12230–12240.

[286] Li, J.-R.; Ma, Y.; McCarthy, M. C.; Sculley, J.; Yu, J.; Jeong, H.-K.; Balbuena, P. B.; Zhou, H.-C. *Coord. Chem. Rev.* **2011**, *255*, 1791 – 1823.

[287] Addicoat, M. A.; Vankova, N.; Akter, I. F.; Heine, T. *J. Chem. Theory Comput.* **2014**, *10*, 880–891.

[288] Eddaoudi, M.; Kim, J.; Rosi, N.; Vodak, D.; Wachter, J.; O'Keeffe, M.; Yaghi, O. M. *Science* **2002**, *295*, 469–472.

[289] Kresse, G.; Hafner, J. *Phys. Rev. B* **1993**, *47*, 558–561.

[290] Kresse, G.; Hafner, J. *Phys. Rev. B* **1994**, *49*, 14251.

[291] Kresse, G.; Furthmüller, J. *Comput. Mater. Sci.* **1996**, *6*, 15.

[292] Kresse, G.; Furthmüller, J. *Phys. Rev. B* **1996**, *54*, 11169.

[293] Blöchl, P. E. *Phys. Rev. B* **1994**, *50*, 17953–17979.

[294] Kresse, G.; Joubert, D. *Phys. Rev. B* **1999**, *59*, 1758–1775.

[295] Perdew, J. P.; Ruzsinszky, A.; Csonka, G. I.; Vydrov, O. A.; Scuseria, G. E.; Constantin, L. A.; Zhou, X.; Burke, K. *Phys. Rev. Lett.* **2008**, *100*, 136406.

[296] Perdew, J. P.; Ruzsinszky, A.; Csonka, G. I.; Vydrov, O. A.; Scuseria, G. E.; Constantin, L. A.; Zhou, X.; Burke, K. *Phys. Rev. Lett.* **2009**, *102*, 039902.

[297] Hendon, C. H.; Tiana, D.; Walsh, A. *Phys. Chem. Chem. Phys.* **2012**, *14*, 13120–13132.

[298] Hendon, C. H.; Tiana, D.; Fontecave, M.; Sanchez, C.; Dárras, L.; Sassoye, C.; Rozes, L.; Mellot-Draznieks, C.; Walsh, A. *J. Am. Chem. Soc.* **2013**, *135*, 10942–10945.

[299] Marenich, A. V.; Cramer, C. J.; Truhlar, D. G. *University of Minnesota: Minneapolis* **2011**,

[300] Adamo, C.; Barone, V. *J. Chem. Phys.* **1999**, *110*, 6158–6170.

[301] TURBOMOLE V6.4 2012, A Development of University of Karlsruhe and Forschungszentrum Karlsruhe GmbH, 1989-2007, TURBOMOLE GmbH, since 2007; available from
`http://www.turbomole.com`.

[302] Schäfer, A.; Horn, H.; Ahlrichs, R. *J. Chem. Phys.* **1992**, *97*, 2571–2577.

[303] Eichkorn, K.; Weigend, F.; Treutler, O.; Ahlrichs, R. *Theor. Chem. Acc.* **1997**, *97*, 119–124.

[304] Weigend, F.; Häser, M. *Theor. Chem. Acc.* **1997**, *97*, 331–340.

[305] Hattig, C.; Hald, K. *Phys. Chem. Chem. Phys.* **2002**, *4*, 2111–2118.

[306] Grimme, S. *J. Comput. Chem.* **2006**, *27*, 1787–1799.

[307] Schäfer, A.; Horn, H.; Ahlrichs, R. *J. Chem. Phys.* **1992**, *97*, 2571–2577.

[308] Weigend, F.; Ahlrichs, R. *Phys. Chem. Chem. Phys.* **2005**, *7*, 3297–3305.

[309] Armbruster, M. K.; Weigend, F.; van Wullen, C.; Klopper, W. *Phys. Chem. Chem. Phys.* **2008**, *10*, 1748–1756.

[310] Boys, S.; Bernardi, F. *Mol. Phys.* **1970**, *19*, 553–566.

[311] Paizs, B.; Suhai, S. *J. Comput. Chem.* **1998**, *19*, 575–584.

[312] Orestes, E.; Machado Ronconi, C.; Carneiro, J. W. d. M. *Phys. Chem. Chem. Phys.* **2014**, *16*, 17213–17219.

[313] Witte, J.; Neaton, J. B.; Head-Gordon, M. *J. Chem. Phys.* **2014**, *140*.

[314] Borycz, J.; Tiana, D.; Haldoupis, E.; Sung, J. C.; Siepmann, J. I.; Farha, O. K.; Gagliardi, L. *J. Phys. Chem. C* **2016**, submitted.

[315] Lorentz, H. A. *Ann. Phys.* **1881**, *248*, 127–136.

[316] Berthelot, D. *Compt. Rendus,* **1898**, *126*, 1703–1706.

[317] Panagiotopoulos, A. Z. *Mol. Phys.* **1987**, *61*, 813–826.

[318] Monte Carlo for Complex Chemical Systems - Minnesota. http://www.chem.umn.edu/groups/siepmann/software.html, 2015.

[319] Boutin, A.; Coudert, F.-X.; Springuel-Huet, M.-A.; Neimark, A. V.; Frey, G.; Fuchs, A. H. *The Journal of Physical Chemistry C* **2010**, *114*, 22237–22244.

[320] June, R. L.; Bell, A. T.; Theodorou, D. N. *J. Phys. Chem.* **1990**, *94*, 1508–1516.

[321] Zhao, X. S.; Siepmann, J. I.; Xu, W.; Kiang, Y.-H.; Sheth, A. R.; Karaborni, S. *J. Phys. Chem. B* **0**, *0*, null.

[322] Perdew, J.; Burke, K.; Ernzerhof, M. *Phys. Rev. Lett.* **1996**, *77*, 3865–3868.

[323] Perdew, J.; Burke, K.; Ernzerhof, M. *Phys. Rev. Lett.* **1997**, *78*, 1396.

[324] He, L.; Liu, F.; Hautier, G.; Oliveira, M. J. T.; Marques, M. A. L.; Vila, F. D.; Rehr, J. J.; Rignanese, G.-M.; Zhou, A. *Phys. Rev. B* **2014**, *89*, 064305.

[325] Ropo, M.; Kokko, K.; Vitos, L. *Phys. Rev. B* **2008**, *77*, 195445.

[326] Park, J.; Kim, H.; Han, S. S.; Jung, Y. *J. Phys. Chem. Lett.* **2012**, *3*, 826–829.

[327] Grajciar, L.; Wiersum, A. D.; Llewellyn, P. L.; Chang, J.-S.; Nachtigall, P. *J. Phys. Chem. C* **2011**, *115*, 17925–17933.

[328] Verma, P.; Xu, X.; Truhlar, D. G. *J. Phys. Chem. C* **2013**, *117*, 12648–12660.

[329] Mavrandonakis, A.; Vogiatzis, K. D.; Boese, A. D.; Fink, K.; Heine, T.; Klopper, W. *Inorg. Chem.* **2015**, *54*, 8251–8263.

[330] Shinjo, T.; Ichida, T.; Takada, T. *J. Phys. Soc. Jpn.* **1970**, *29*, 111–116.

[331] Dann, S. E.; Weller, M. T.; Currie, D. B.; Thomas, M. F.; Al-Rawwas, A. D. *J. Mater. Chem.* **1993**, *3*, 1231–1237.

[332] Rappe, A. K.; III, W. A. G. *J. Phys. Chem.* **1991**, *95*, 3358–3363.

[333] Wang, B.; Li, S. L.; Truhlar, D. G. *J. Chem. Theory Comput.* **2014**, *10*, 5640–5650.

[334] Colon, Y. J.; Snurr, R. Q. *Chem. Soc. Rev.* **2014**, *43*, 5735–5749.

[335] Lässig, D.; Lincke, J.; Moellmer, J.; Reichenbach, C.; Moeller, A.; Gläser, R.; Kalies, G.; Cychosz, K. A.; Thommes, M.; Staudt, R.; et al., *Angew. Chem. Int. Ed.* **2011**, *50*, 10344–10348.

[336] Chaemchuen, S.; Kabir, N. A.; Zhou, K.; Verpoort, F. *Chem. Soc. Rev.* **2013**, 9304–9332.

[337] Bloch, E. D.; Queen, W. L.; Krishna, R.; Zadrozny, J. M.; Brown, C. M.; Long, J. R. *Science* **2012**, *335*, 1606–1610.

[338] Mason, J. A.; Sumida, K.; Herm, Z. R.; Krishna, R.; Long, J. R. *Energy Environ. Sci.* **2011**, *4*, 3030–3040.

[339] Dietzel, P. D. C.; Besikiotis, V.; Blom, R. *J. Mater. Chem.* **2009**, *19*, 7362–7370.

[340] Mayo, S. L.; Olafson, B. D.; Goddard, W. A., III, *J. Phys. Chem.* **1990**, *94*, 8897–8909.

[341] Rappé, A. K.; Casewit, C. J.; Colwell, K. S.; Goddard, W. A., III,; Skiff, W. M. *J. Am. Chem. Soc.* **1992**, *114*, 10024–10035.

[342] Salles, F.; Kolokolov, D. I.; Jobic, H.; Maurin, G.; Llewellyn, P. L.; Devic, T.; Serre, C.; Ferey, G. *J. Phys. Chem. C* **2009**, *113*, 7802–7812.

[343] Rives, S.; Jobic, H.; Kolokolov, D. I.; Gabrienko, A. A.; Stepanov, A. G.; Ke, Y.; Frick, B.; Devic, T.; Férey, G.; Maurin, G. *J. Phys. Chem. C* **2013**, *117*, 6293–6302.

[344] Atci, E.; Erucar, I.; Keskin, S. *J. Phys. Chem. C* **2011**, *115*, 6833–6840.

[345] Yu, J.; Balbuena, P. B. *J. Phys. Chem. C* **2013**, *117*, 3383–3388.

[346] Gresh, N.; Claverie, P.; Pullman, A. *Theor. Chem. Acc.* **1984**, *66*, 1–20.

[347] Misquitta, A. J.; Podeszwa, R.; Jeziorski, B.; Szalewicz, K. *J. Chem. Phys.* **2005**, *123*, 214103.

[348] Verma, P.; Xu, X.; Truhlar, D. G. *J. Phys. Chem. C* **2013**, *117*, 12648–12660.

[349] Ghosh, D.; Kosenkov, D.; Vanovschi, V.; Williams, C. F.; Herbert, J. M.; Gordon, M. S.; Schmidt, M. W.; Slipchenko, L. V.; Krylov, A. I. *J. Phys. Chem. A* **2010**, *114*, 12739–12754.

[350] Adamovic, I.; Gordon, M. S. *J. Phys. Chem. A* **2006**, *110*, 10267–10273, PMID: 16928117.

[351] Li, H.; Gordon, M. S.; Jensen, J. H. *J. Chem. Phys.* **2006**, *124*.

[352] Bowman, D. N.; Jakubikova, E. *Inorg. Chem* **2012**, *51*, 6011–6019.

[353] Jensen, K. P.; Roos, B. O.; Ryde, U. *J. Inorg. Biochem.* **2005**, *99*, 45 – 54.

[354] Radoń, M.; Pierloot, K. *J. Phys. Chem. A* **2008**, *112*, 11824–11832.

[355] Maurice, R.; Verma, P.; Zadrozny, J. M.; Luo, S.; Borycz, J.; Long, J. R.; Truhlar, D. G.; Gagliardi, L. *Inorg. Chem.* **2013**, *52*, 9379–9389.

[356] Furtado, J. P.; Rahalkar, A. P.; Shanker, S.; Bandyopadhyay, P.; Gadre, S. R. *J. Chem. Phys. Lett.* **2012**, *3*, 2253–2258.

[357] Perdew, J. P.; Burke, K.; Ernzerhof, M. *Phys. Rev. Lett.* **1996**, *77*, 3865–3868.

[358] Dudarev, S. L.; Botton, G. A.; Savrasov, S. Y.; Humphreys, C. J.; Sutton, A. P. *Phys. Rev. B* **1998**, *57*, 1505–1509.

[359] Zhang, Q.; Li, B.; Chen, L. *Inorg. Chem.* **2013**, *52*, 9356–9362.

[360] Manz, T. A.; Sholl, D. S. *J. Chem. Theory Comput.* **2011**, *7*, 4146–4164.

[361] Weigend, F.; Häser, M.; Patzelt, H.; Ahlrichs, R. *Chem. Phys. Lett.* **1998**, *294*, 143–152.

[362] Roos, B. O.; Taylor, P. R.; Siegbahn, P. E. *J. Chem. Phys.* **1980**, *48*, 157–173.

[363] Andersson, K.; Malmqvist, P.-Å.; Roos, B. O. *J. Chem. Phys.* **1992**, *96*, 1218–1226.

[364] Karlström, G.; Lindh, R.; Malmqvist, P.-Å.; Roos, B. O.; Ryde, U.; Veryazov, V.; Widmark, P.-O.; Cossi, M.; Schimmelpfennig, B.; Neogrady, P.; et al., *Comput. Mater. Sci.* **2003**, *28*, 222–239.

[365] Canepa, P.; Chabal, Y. J.; Thonhauser, T. *Phys. Rev. B* **2013**, *87*, 094407.

[366] Aquilante, F.; Malmqvist, P.-Å.; Pedersen, T. B.; Ghosh, A.; Roos, B. O. *J. Chem. Theory Comput.* **2008**, *4*, 694–702.

[367] Aquilante, F.; Pedersen, T. B.; Lindh, R.; Roos, B. O.; de Merás, A. S.; Koch, H. *J. Chem. Phys.* **2008**, *129*, 024113.

[368] Aquilante, F.; Pedersen, T. B.; Lindh, R. *J. Chem. Phys.* **2007**, *126*, 194106.

[369] Douglas, M.; Kroll, N. M. *Ann. Phys.* **1974**, *82*, 89–155.

[370] Hess, B. A. *Phys. Rev. A* **1986**, *33*, 3742–3748.

[371] Roos, B. O.; Lindh, R.; Malmqvist, P.-Å.; Veryazov, V.; Widmark, P.-O. *J. Phys. Chem. A* **2004**, *108*, 2851–2858.

[372] Roos, B. O.; Lindh, R.; Malmqvist, P.-Å.; Veryazov, V.; Widmark, P.-O. *J. Phys. Chem. A* **2005**, *109*, 6575–6579.

[373] Haldoupis, E.; Nair, S.; Sholl, D. S. *J. Am. Chem. Soc.* **2012**, *134*, 4313–4323.

[374] Gagliardi, L.; Lindh, R.; Karlström, G. *J. Chem. Phys.* **2004**, *121*, 4494–4500.

[375] McDaniel, J. G.; Schmidt, J. R. *J. Phys. Chem. A* **2013**, *117*, 2053–2066.

[376] Holt, A.; Boström, J.; Karlström, G.; Lindh, R. *J. Comp. Chem.* **2010**, *31*, 1583–1591.

[377] Holt, A. Modelling of Polarization by Molecular Force Fields: Further Development of the NEMO Potential. Ph.D. thesis, Lund University, 2009.

[378] Stone, A. J. *The Theory of Intermolecular Forces*; Oxford: Clarendon, 1997.

[379] Potoff, J. J.; Siepmann, J. I. *AIChE J.* **2001**, *47*, 1676–1682.

[380] Lin, L.-C.; Kim, J.; Kong, X.; Scott, E.; McDonald, T. M.; Long, J. R.; Reimer, J. A.; Smit, B. *Angew. Chem. Int. Ed.* **2013**, *52*, 4410–4413.

[381] Furukawa, H.; Cordova, K. E.; O'Keeffe, M.; Yaghi, O. M. *Science* **2013**, *341*, 974.

[382] Wilmer, C. E.; Leaf, M.; Lee, C. Y.; Farha, O. K.; Hauser, B. G.; Hupp, J. T.; Snurr, R. Q. *Nat. Chem.* **2012**, *4*, 83–89.

[383] Bao, Y.; Martin, R. L.; Simon, C. M.; Haranczyk, M.; Smit, B.; Deem, M. W. *J. Phys. Chem. C* **2015**, *119*, 186–195.

[384] He, Y.; Zhou, W.; Qian, G.; Chen, B. *Chem. Soc. Rev.* **2014**, *43*, 5657–5678.

[385] Liu, J.; Chen, L.; Cui, H.; Zhang, J.; Zhang, L.; Su, C.-Y. *Chem. Soc. Rev.* **2014**, *43*, 6011–6061.

[386] Hu, Z.; Deibert, B. J.; Li, J. *Chem. Soc. Rev.* **2014**, *43*, 5815–5840.

[387] *Climate Change 2013: The Physical Science Basis; Contribution of Working Group I to the Fifth Assessment Report of the Intergovernmental Panel on Climate Change*; 2013.

[388] Haldoupis, E.; Nair, S.; Sholl, D. S. *J. Am. Chem. Soc.* **2012**, *134*, 4313–4323.

[389] Wilmer, C. E.; Farha, O. K.; Bae, Y.-S.; Hupp, J. T.; Snurr, R. Q. *Energy Environ. Sci.* **2012**, *5*, 9849–9856.

[390] Lin, L.-C.; Berger, A. H.; Martin, R. L.; Kim, J.; Swisher, J. A.; Jariwala, K.; Rycroft, C. H.; Bhown, A. S.; Deem, M. W.; Haranczyk, M.; Smit, B. *Nat. Mater.* **2012**, *11*, 633–641.

[391] Simon, C. M.; Kim, J.; Gomez-Gualdron, D. A.; Camp, J. S.; Chung, Y. G.; Martin, R. L.; Mercado, R.; Deem, M. W.; Gunter, D.; Haranczyk, M.; Sholl, D. S.; Snurr, R. Q.; Smit, B. *Energy Environ. Sci.* **2015**, *8*, 1190–1199.

[392] Bai, P.; Tsapatsis, M.; Siepman, J. I. *J. Phys. Chem. C* **2013**, *117*, 24375–24387.

[393] Fang, H.; Demir, H.; Kamakoti, P.; Sholl, D. S. *J. Mater Chem. A* **2014**, *2*, 274–291.

[394] Odoh, S. O.; Cramer, C. J.; Truhlar, D. G.; Gagliardi, L. *Chem. Rev.* **2015**, *115*, 6051–6111.

[395] Chen, L.; Morrison, C. A.; Düren, T. *J. Phys. Chem. C* **2012**, *116*, 18899–18909.

[396] Zhou, W.; Wu, H.; Yildirim, T. *J. Am. Chem. Soc.* **2008**, *130*, 15268–15269.

[397] Dietzel, P. D. C.; Morita, Y.; Blom, R.; Fjellvaag, H. *Angew. Chem.* **2005**, *44*, 6354–6358.

[398] Dietzel, P. D. C.; Panella, B.; Hirscher, M.; Blom, R.; Fjellvag, H. *Chem. Comm.* **2006**, 959–961.

[399] Sanz, R.; Martinez, F.; Orcajo, G.; Wojtas, L.; Briones, D. *Dalton Trans.* **2013**, *42*, 2392–2398.

[400] Queen, W. L. et al. *Chem. Sci.* **2014**, *5*, 4569–4581.

[401] Moellmann, J.; Grimme, S. *J. Phys. Chem. C* **2014**, *118*, 7615–7621.

[402] Grimme, S.; Ehrlich, S.; Goerigk, L. *Journal of Computational Chemistry* **2011**, *32*, 1456–1465.

[403] Vogiatzis, K. D.; Barnes, E. C.; Klopper, W. *Chem. Phys. Lett.* **2011**, *503*, 157–161.

[404] Ahlrichs, R.; Baer, M.; Haeser, M.; Horn, H.; Koelmel, C. *Chem. Phys. Lett.* **1989**, *162*, 165–169.

[405] Potoff, J. J.; Siepmann, J. I. *Angew. Chem. Int. Ed.* **2001**, *47*, 1676–1682.

[406] Fairen-Jimenez, D.; Lozano-Casal, P.; Düren, T. *Characterization of Porous Solids VIII: Proceedings of the 8th International Symposium on the Characterization of Porous Solids*; The Royal Society of Chemistry: London, 2009.

[407] Getman, R. B.; Bae, Y.-S.; Wilmer, C. E.; Snurr, R. Q. *Chem. Rev.* **2012**, *112*, 703–723.

[408] Manz, T. A.; Sholl, D. S. *J. Chem Theory Comput.* **2010**, *6*, 2455–2468.

[409] Panagiotopoulos, A. Z.; Quirke, N.; Stapleton, M.; Tildesley, D. J. *Mol. Phys.* **1988**, *63*, 527–545.

[410] Ewald, P. P. *Annal. Phys.* **1921**, *369*, 253–287.

[411] Karavias, F.; Myers, A. L. *Langmuir* **1991**, *7*, 3118–3126.

[412] Ong, S. P.; Richards, W. D.; Jain, A.; Hautier, G.; Kocher, M.; Cholia, S.; Gunter, D.; Chevrier, V. L.; Persson, K. A.; Ceder, G. *Comput. Mater. Sci.* **2013**, *68*, 314–319.

[413] Berendsen, H. J. C.; Grigera, J. R.; Straatsma, T. P. *J. Phys. Chem.* **1987**, *91*, 6269–6271.

[414] Willems, T. F.; Rycroft, C. H.; Kazi, M.; Meza, J. C.; Haranczyk, M. *Microporous Mesoporous Mater.* **2012**, *149*, 134–141.

[415] Martin, R. L.; Smit, B.; Haranczyk, M. *J. Chem. Inf. Model.* **2012**, *52*, 308–318.

[416] Valenzano, L.; Civalleri, B.; Sillar, K.; Sauer, J. *J. Phys. Chem. C* **2011**, *115*, 21777–21784.

[417] Poloni, R.; Smit, B.; Neaton, J. B. *J. Phys. Chem. A* **2012**, *116*, 4957–4964.

[418] Dietzel, P. D. C.; Georgiev, P. A.; Eckert, J.; Blom, R.; Straessle, T.; Unruh, T. *Chem. Comm.* **2010**, *46*, 4962–4964.

[419] Walton, K. S.; Snurr, R. Q. *J. Am. Chem. Soc.* **2007**, *129*, 8552–8556.

[420] Bai, P.; Ghosh, P.; Sung, J. C.; Kohen, D.; Siepmann, J. I.; Snurr, R. Q. *Fluid Phase Equilib.* **2014**, *366*, 146–151.

[421] Férey, G. *Chem. Soc. Rev.* **2008**, *37*, 191–214.

[422] Roy, S.; George, C. B.; Ratner, M. A. *J. Phys. Chem. C* **2012**, *116*, 23494–23502.

[423] Oxford, G. A. E.; Dubbeldam, D.; Broadbelt, L. J.; Snurr, R. Q. *J. Molec. Phys. A* **2011**, *334*, 89–97.

[424] Farha, O. K.; Özgür Yazaydin.,; Eryazici, I.; Malliakas, C. D.; Hauser, B. G.; Kanatzidis, M. G.; Nguyen, S. T.; Snurr, R. Q.; Hupp, J. T. *Nat. Chem. 2*, 944–948.

[425] Cavka, J. H.; Jakobsen, S.; Olsbye, U.; Guillou, N.; Lamberti, C.; Bordiga, S.; Lillerud, K. P. *J. Am. Chem. Soc.* **2008**, *130*, 13850–13851.

[426] Furukawa, H.; Gandara, F.; Zhang, Y.-B.; Jiang, J.; Queen, W. L.; Hudson, M. R.; Yaghi, O. M. *J. Am. Chem. Soc.* **2014**, *136*, 4369–4381.

[427] Jiang, H.-L.; Feng, D.; Wang, K.; Gu, Z.-Y.; Wei, Z.; Chen, Y.-P.; Zhou, H.-C. *J. Am. Chem. Soc.* **2013**, *135*, 13934–13938.

[428] Wu, H.; Chua, Y. S.; Krungleviciute, V.; Tyagi, M.; Chen, P.; Yildirim, T.; Zhou, W. *J. Am. Chem. Soc.* **2013**, *135*, 10525–10532.

[429] Chavan, S.; Vitillo, J. G.; Gianolio, D.; Zavorotynska, O.; Civalleri, B.; Jakobsen, S.; Nilsen, M. H.; Valenzano, L.; Lamberti, C.; Lillerud, K. P.; Bordiga, S. *Phys. Chem. Chem. Phys.* **2012**, *14*, 1614–1626.

[430] Yang, Q.; Guillerm, V.; Ragon, F.; Wiersum, A. D.; Llewellyn, P. L.; Zhong, C.; Devic, T.; Serre, C.; Maurin, G. *Chem. Comm.* **2012**, *48*, 9831–9833.

[431] Vermoortele, F.; Vandichel, M.; VandeVoorde, B.; Ameloot, R.; Waroquier, M.; VanSpeybroeck, V.; DeVos, D. E. *Angew. Chem.* **2012**, *51*, 4887–4890.

[432] Siu, P. W.; Brown, Z. J.; Farha, O. K.; Hupp, J. T.; Scheidt, K. A. *Chem. Comm.* **2013**, *49*, 10920–10922.

[433] Vermoortele, F.; Bueken, B.; Le Bars, G.; Van de Voorde, B.; Vandichel, M.; Houthoofd, K.; Vimont, A.; Daturi, M.; Waroquier, M.; Van Speybroeck, V.; Kirschhock, C.; De Vos, D. E. *J. Am. Chem. Soc.* **2013**, *135*, 11465–11468.

[434] Katz, M. J.; Mondloch, J. E.; Totten, R. K.; Park, J. K.; Nguyen, S. T.; Farha, O. K.; Hupp, J. T. *Angew. Chem.* **2014**, *53*, 497–501.

[435] Carboni, M.; Abney, C. W.; Liu, S.; Lin, W. *Chemical Science* **2013**, *4*, 2396–2402.

[436] Yee, K.-K.; Reimer, N.; Liu, J.; Cheng, S.-Y.; Yiu, S.-M.; Weber, J.; Stock, N.; Xu, Z. *J. Am. Chem. Soc.* **2013**, *135*, 7795–7798.

[437] Ameloot, R.; Aubrey, M.; Wiers, B. M.; Gomora-Figueroa, A. P.; Patel, S. N.; Balsara, N. P.; Long, J. R. *Chem. Eur. J.* **2013**, *19*, 5533–5536.

[438] Nickerl, G.; Leistner, M.; Helten, S.; Bon, V.; Senkovska, I.; Kaskel, S. *Inorg. Chem. Front* **2014**, *1*, 325–330.

[439] Chen, Y.; Hoang, T.; Ma, S. *Inorg. Chem.* **2012**, *51*, 12600–12602.

[440] Deria, P.; Bury, W.; Hupp, J. T.; Farha, O. K. *Chem. Commun.* **2014**, *50*, 1965–1968.

[441] Perdew, J. P.; Wang, Y. *Phys. Rev. B* **1992**, *45*, 13244–13249.

[442] Zhao, Y.; Peverari, R.; Yang, K.; Truhlar, D. G. **2012**,

[443] Hehre, W. J.; Radom, L.; Schleyer, P. v. R.; Pople, J. A. *Ab Initio Molecular Orbital Theory*; Wiley: New York, 1986.

[444] Martin, J. M. L.; Sundermann, A. *J. Chem. Phys.* **2001**, *114*, 3408–3420.

[445] Marenich, A. V.; Cramer, C. J.; Truhlar, D. G. *J. Phys. Chem. B* **2009**, *113*, 6378–6396.

[446] Planas, N.; Mondloch, J. E.; Tussupbayev, S.; Borycz, J.; Gagliardi, L.; Hupp, J. T.; Farha, O. K.; Cramer, C. J. *J. Phys. Chem. Lett.* **2014**, *5*, 3716–3723.

[447] Yang, L.-M.; Ganz, E.; Svelle, S.; Tilset, M. *J. Mater. Chem. C* **2014**, *2*, 7111–7125.

[448] Valenzano, L.; Civalleri, B.; Chavan, S.; Bordiga, S.; Nilsen, M. H.; Jakobsen, S.; Lillerud, K. P.; Lamberti, C. *Chemistry of Materials* **2011**, *23*, 1700–1718.

[449] Shearer, G. C.; Forselv, S.; Chavan, S.; Bordiga, S.; Mathisen, K.; Bjorgen, M.; Svelle, S.; Lillerud, K. P. *Top. Catal.* **2013**, *56*, 770–782.

[450] Aresta, M.; Dibenedetto, A. *Dalton Trans.* **2007**, 2975–2992.

[451] Beyzavi, M. H.; Klet, R. C.; Tussupbayev, S.; Borycz, J.; Vermeulen, N. A.; Cramer, C. J.; Stoddart, J. F.; Hupp, J. T.; Farha, O. K. *J. Am. Chem. Soc.* **2014**, *136*, 15861–15864.

[452] Sakakura, T.; Kohno, K. *Chem. Commun.* **2009**, 1312–1330.

[453] North, M.; Pasquale, R. *Angew. Chem.* **2009**, *48*, 2946–2948.

[454] Markewitz, P.; Kuckshinrichs, W.; Leitner, W.; Linssen, J.; Zapp, P.; Bongartz, R.; Schreiber, A.; Muller, T. E. *Energy Environ. Sci.* **2012**, *5*, 7281–7305.

[455] Gao, W.-Y.; Chen, Y.; Niu, Y.; Williams, K.; Cash, L.; Perez, P. J.; Wojtas, L.; Cai, J.; Chen, Y.-S.; Ma, S. *Angew. Chem.* **2014**, *53*, 2615–2619.

[456] Feng, D.; Chung, W.-C.; Wei, Z.; Gu, Z.-Y.; Jiang, H.-L.; Chen, Y.-P.; Darensbourg, D. J.; Zhou, H.-C. *J. Am. Chem. Soc.* **2013**, *135*, 17105–17110.

[457] Guillerm, V.; J., W.; Belmabkhout, Y.; Cairns, A. J.; D'Elia, V.; WojtasŁukasz,; Adil, K.; Eddaoudi, M. *Nat. Chem.* **2014**, *6*, 673–680.

[458] Doskocil, E. J.; Bordawekar, S. V.; Kaye, B. G.; ; Davis*, R. J. *J. Phys. Chem. B* **1999**, *103*, 6277–6282.

[459] Wang, J.-Q.; Kong, D.-L.; Chen, J.-Y.; Cai, F.; He, L.-N. *J. Molec. Catal. A* **2006**, *249*, 143–148.

[460] Yasuda, H.; He, L.-N.; Sakakura, T.; Hu, C. *J. Catal.* **2005**, *233*, 119–122.

[461] Yasuda, H.; He, L.-N.; Sakakura, T. *J. Catal.* **2002**, *209*, 547 – 550.

[462] Yamaguchi, K.; Kohki Ebitani, .; Yoshida, T.; Yoshida, H.; ; Kaneda, K. *J. Am. Chem. Soc.* **1999**, *121*, 4526–4527.

[463] Yano, T.; Matsui, H.; Koike, T.; Ishiguro, H.; Fujihara, H.; Yoshihara, M.; Maeshima, T. *Chem. Commun.* **1997**, 1129–1130.

[464] Srivastava, R.; Srinivas, D.; Ratnasamy, P. *J. Catal* **2005**, *233*, 1–15.

[465] Xie, Y.; Wang, T.-T.; Liu, X.-H.; Zou, K.; Deng, W.-Q. *Nat Commun* **2013**, *4*.

[466] Chun, J.; Kang, S.; Kang, N.; Lee, S. M.; Kim, H. J.; Son, S. U. *J. Mater. Chem. A* **2013**, *1*, 5517–5523.

[467] Kerr, J. A. In *CRC Handbook of Chemistry and Physics, 81st ed.*; Lide, D. R., Ed.; CRC Press: Boca Raton, FL, 2000.

[468] Kruper, W. J.; Dellar, D. D. *J. Org. Chem.* **1995**, *60*, 725–727.

[469] Unnikrishnan, K. P.; Thachil, E. T. *Des. Monomers Polym.* **2006**, *9*, 129–152.

[470] Cho, B. T.; Choi, O. K.; Kim, D. J. *Tetrahedron Asymmetry* **2002**, *13*, 697–703.

[471] Gorzynski Smith, J. *Synthesis* **1984**, *1984*, 629–656.

[472] Scriven, E. F. V.; Turnbull, K. *Chem. Rev.* **1988**, *88*, 297–368.

[473] Coe, D. M.; Myers, P. L.; Parry, D. M.; Roberts, S. M.; Storerb, R. *J. Chem. Soc., Chem. Commun.* **1990**, 151–153.

[474] Smith, B. T.; Gracias, V.; ; Aubé, J. *J. Org. Chem.* **2000**, *65*, 3771–3774.

[475] Badiang, J. G.; Aubé, J. *J. Org. Chem.* **1996**, *61*, 2484–2487.

[476] Treinin, A. *The Azido Group (1971)*; John Wiley Sons, Ltd., 2010; pp 1–55.

[477] Kas'yan, L. I.; Okovityi, S. I.; Kas'yan, A. O. *Russ. J. Org. Chem. 40*, 1–34.

[478] Tanabe, K. K.; Cohen, S. M. *Inorg. Chem.* **2010**, *49*, 6766–6774.

[479] Song, F.; Wang, C.; Lin, W. *Chem. Commun.* **2011**, *47*, 8256–8258.

[480] Marenich, A. V.; Cramer, C. J.; Truhlar, D. G. *J. Phys. Chem. B* **2009**, *113*, 6378–6396.

[481] Baylon, C.; Prestat, G.; Heck, M.-P.; Mioskowski, C. *Tetrahedron Lett.* **2000**, *41*, 3833–3835.

[482] Olah, G. A.; Fung, A. P.; Meidar, D. *Synthesis* **1981**, *1981*, 280–282.

[483] Reeve, W.; Christoffel, I. *J. Am. Chem. Soc.* **1950**, *72*, 1480–1483.

[484] Mondloch, J. E.; Farha, O. K.; Hupp, J. T. *RSC Catalysis Series* **2013**, *12*, 289–309.

[485] Fujita, M.; Kwon, Y. J.; Washizu, S.; Ogura, K. *J. Am. Chem. Soc.* **1994**, *116*, 1151–1152.

[486] Vermoortele, F.; Valvekens, P.; De Vos, D. *RSC Catalysis Series* **2013**, *12*, 268–288.

[487] Corma, A.; Iglesias, M.; Llabres I. Xamena, F. X.; Sanchez, F. *Chem. Eur. J.* **2010**, *16*, 9789–9795.

[488] Henschel, A.; Gedrich, K.; Kraehnert, R.; Kaskel, S. *Chem. Comm.* **2008**, 4192–4194.

[489] Beyzavi, M. H.; Klet, R. C.; Tussupbayev, S.; Borycz, J.; Vermeulen, N. A.; Cramer, C. J.; Stoddart, J. F.; Hupp, J. T.; Farha, O. K. *J. Am. Chem. Soc.* **2014**, *136*, 15861–15864.

[490] Mondloch, J. E.; Katz, M. J.; Isley III, W. C.; Ghosh, P.; Liao, P.; Bury, W.; Wagner, G. W.; Hall, M. G.; De Coste, J. B.; Peterson, G. W.; Snurr, R. Q.; Cramer, C. J.; Hupp, J. T.; Farha, O. K. *Nat. Mater.* **2015**, *14*, 512–516.

[491] Phan, A.; Czaja, A. U.; Gandara, F.; Knobler, C. B.; Yaghi, O. M. *Inorg. Chem.* **2011**, *50*, 7388–7390.

[492] Nguyen, H. G. T.; Schweitzer, N. M.; Chang, C.-Y.; Drake, T. L.; So, M. C.; Stair, P. C.; Farha, O. K.; Hupp, J. T.; Nguyen, S. T. *ACS Catal.* **2014**, *4*, 2496–2500.

[493] Deria, P.; Bury, W.; Hod, I.; Kung, C.-W.; Karagiaridi, O.; Hupp, J. T.; Farha, O. K. *Inorg. Chem.* **2015**, *54*, 2185–2192.

[494] Hod, I.; Bury, W.; Gardner, D. M.; Deria, P.; Roznyatovskiy, V.; Wasielewski, M. R.; Farha, O. K.; Hupp, J. T. *J. Phys. Chem. Letters* **2015**, *6*, 586–591.

[495] Groner, M. D.; Fabreguette, F. H.; Elam, J. W.; George, S. M. *Chem. Mater.* **2004**, *16*, 639–645.

[496] Heil, S. B. S.; Langereis, E.; Roozeboom, F.; van de Sanden, M. C. M.; Kessels, W. M. M. *J. Electrochem. Soc.* **2006**, *153*, G956–G965.

[497] Bakke, J. R.; King, J. S.; Jung, H. J.; Sinclair, R.; Bent, S. F. *Thin Solid Films* **2010**, *518*, 5400–5408.

[498] Ten Eyck, G. A.; Senkevich, J. J.; Tang, F.; Liu, D.; Pimanpang, S.; Karaback, T.; Wang, G.-C.; Lu, T.-M.; Jezewski, C.; Lanford, W. A. *Chem. Vapor Depos.* **2005**, *11*, 60–66.

[499] Miikkulainen, V.; Leskelä, M.; Ritala, M.; Puurunen, R. L. *J. App. Phys.* **2013**, *113*.

[500] Goldstein, D. N.; McCormick, J. A.; George, S. M. *J. Phys. Chem. C* **2008**, *112*, 19530–19539.

[501] Elam, J. W.; Routkevitch, D.; Mardilovich, P. P.; George, S. M. *Chem. Mater.* **2003**, *15*, 3507–3517.

[502] Hinkle, C. L.; Sonnet, A. M.; Vogel, E. M.; McDonnell, S.; Hughes, G. J.; Milojevic, M.; Lee, B.; Aguirre-Tostado, F. S.; Choi, K. J.; Kim, H. C.; Kim, J.; Wallace, R. M. *App. Phys. Lett.* **2008**, *92*.

[503] Milojevic, M.; Aguirre-Tostado, F. S.; Hinkle, C. L.; Kim, H. C.; Vogel, E. M.; Kim, J.; Wallace, R. M. *App. Phys. Lett.* **2008**, *93*.

[504] Kim, I. S.; Borycz, J.; Platero-Prats, A. E.; Tussupbayev, S.; Wang, T. C.; Farha, O. K.; Hupp, J. T.; Gagliardi, L.; Chapman, K. W.; Cramer, C. J.; Martinson, A. B. F. *Chem. Mater.* **2015**, *27*, 4772–4778.

[505] Nicklass, A.; Dolg, M.; Stoll, H.; Preuss, H. *J. Chem. Phys.* **1995**, *102*, 8942–8952.

[506] Chupas, P. J.; Chapman, K. W.; Lee, P. L. *J. Appl. Crystallogr.* **2007**, *40*, 463–470.

[507] Chupas, P. J.; Chapman, K. W.; Kurtz, C.; Hanson, J. C.; Lee, P. L.; Grey, C. P. *J. Appl. Crystallogr.* **2008**, *41*, 822–824.

[508] Qiu, X.; Thompson, J. W.; Billinge, S. J. L. *J. Appl. Crystallogr.* **2004**, *37*, 678.

[509] Chapman, K. W.; Chupas, P. J.; Kepert, C. J. *J. Am. Chem. Soc.* **2005**, *127*, 11232–11233.

[510] Wojdyr, M. *J. Appl. Crystallogr.* **2010**, *43*, 1126–1128.

[511] Farrow, C. L.; Juhas, P.; Liu, J. W.; Bryndin, D.; Bozin, E. S.; Bloch, J.; Proffen, T.; Billinge, S. J. L. *J. Phys. Condens. Matter* **2007**, *19*, 335219.

[512] Corma, A.; Garcia, H.; Llabres I. Xamena, F. X. *Chem. Rev.* **2010**, *110*, 4606–4655.

[513] Gascon, J.; Corma, A.; Kapteijn, F.; Llabres I. Xamena, F. X. *ACS Catal.* **2014**, *4*, 361–378.

[514] Farrusseng, D.; Aguado, S.; Pinel, C. *Angew. Chem.* **2009**, *48*, 7502–7513.

[515] Dhakshinamoorthy, A.; Alvaro, M.; Garcia, H. *Catal. Sci. Tech.* **2011**, *1*, 856–867.

[516] Yoon, M.; Srirambalaji, R.; Kim, K. *Chem. Rev.* **2012**, *112*, 1196–1231.

[517] Manna, K.; Zhang, T.; Carboni, M.; Abney, C. W.; Lin, W. *J. Am. Chem. Soc.* **2014**, *136*, 13182–13185.

[518] Fei, H.; Cohen, S. M. *J. Am. Chem. Soc.* **2015**, *137*, 2191–2194.

[519] Gonzalez, M. I.; Bloch, E. D.; Mason, J. A.; Teat, S. J.; Long, J. R. *Inorg. Chem.* **2015**, *54*, 2995–3005.

[520] Larabi, C.; Quadrelli, E. A. *Eur. J. Inorg. Chem.* **2012**, *2012*, 3014–3022.

[521] Schaate, A.; Roy, P.; Godt, A.; Lippke, J.; Waltz, F.; Wiebcke, M.; Behrens, P. *Chem. Eur. J.* **2011**, *17*, 6643–6651, S6643/1–S6643/11.

[522] Katz, M. J.; Brown, Z. J.; Colon, Y. J.; Siu, P. W.; Scheidt, K. A.; Snurr, R. Q.; Hupp, J. T.; Farha, O. K. *Chem. Comm.* **2013**, *49*, 9449–9451.

[523] Serna, P.; Gates, B. C. *Acc. Chem. Res.* **2014**, *47*, 2612–2620.

[524] Bhirud, V. A.; Uzun, A.; Kletnieks, P. W.; Craciun, R.; Haw, J. F.; Dixon, D. A.; Olmstead, M. M.; Gates, B. C. *J. Organomet. Chem.* **2007**, *692*, 2107–2113.

[525] Metz, B.; Stoll, H.; Dolg, M. *J. Chem. Phys.* **2000**, *113*, 2563–2569.

[526] Weigend, F. *Phys. Chem. Chem. Phys.* **2006**, *8*, 1057–1065.

[527] Yang, D.; Odoh, S. O.; Borycz, J.; Wang, T. C.; Farha, O. K.; Hupp, J. T.; Cramer, C. J.; Gagliardi, L.; Gates, B. C. *ACS Catal.* **2016**, *6*, 235–247.

[528] Uzun, A.; Bhirud, V. A.; Kletnieks, P. W.; Haw, J. F.; Gates, B. C. *J. Phys. Chem. C* **2007**, *111*, 15064–15073.

[529] Mihaylov, M.; Ivanova, E.; Thibault-Starzyk, F.; Daturi, M.; Dimitrov, L.; Hadjiivanov, K. *J. Phys. Chem. B* **2006**, *110*, 10383–10389.

[530] Solymosi, F.; Novak, E.; Molnar, A. *J. Phys. Chem.* **1990**, *94*, 7250–7255.

[531] Lu, J.; Aydin, C.; Liang, A. J.; Chen, C.-Y.; Browning, N. D.; Gates, B. C. *ACS Catal.* **2012**, *2*, 1002–1012.

[532] He, M. Y.; Ekerdt, J. G. *J. Catal.* **1984**, *87*, 381–388.

[533] Ma, Z.-Y.; Yang, C.; Wei, W.; Li, W.-H.; Sun, Y.-H. *J. Molec. Catal. A* **2005**, *227*, 119–124.

[534] Lu, J.; Serna, P.; Aydin, C.; Browning, N. D.; Gates, B. C. *J. Am. Chem. Soc.* **2011**, *133*, 16186–16195.

[535] Uzun, A.; Gates, B. C. *J. Am. Chem. Soc.* **2009**, *131*, 15887–15894.

[536] Lu, J.; Aydin, C.; Browning, N. D.; Gates, B. C. *Langmuir* **2012**, *28*, 12806–12815.

[537] Serna, P.; Gates, B. C. *J. Am. Chem. Soc.* **2011**, *133*, 4714–4717.

[538] Yardimci, D.; Serna, P.; Gates, B. C. *Chem. Eur. J.* **2013**, *19*, 1235–1245.

[539] Uzun, A.; Ortalan, V.; Browning, N. D.; Gates, B. C. *J. Catal.* **2010**, *269*, 318–328.

[540] Lu, J.; Aydin, C.; Browning, N. D.; Gates, B. C. *J. Am. Chem. Soc.* **2012**, *134*, 5022–5025.

[541] Yang, D.; Chen, M.; Martinez-Macias, C.; Dixon, D. A.; Gates, B. C. *Chem. Eur. J.* **2015**, *21*, 631–640.

[542] de Jon, K. P. *Synthesis of Solid Catalysts*; Wiley-VCH: Germany, 2009.

[543] Thomas, J. M.; Thomas, W. J. *Principles and Practice of Heterogeneous Catalysis*; Wiley-VCH: New York, 1997.

[544] Stalzer, M. M.; Delferro, M.; Marks, T. J. *Catal. Lett.* **2015**, *145*, 3–14.

[545] Coperet, C.; Chabanas, M.; Saint-Arroman, R. P.; Basset, J.-M. *Angew. Chem.* **2003**, *42*, 156–181.

[546] Peters, A. W.; Li, Z.; Farha, O. K.; Hupp, J. T. *ACS Nano* **2015**, *9*, 8484–8490.

[547] Li, B.; Zhang, Y.; Ma, D.; Ma, T.; Shi, Z.; Ma, S. *J. Am. Chem. Soc.* **2014**, *136*, 1202–1205.

[548] Kalidindi, S. B.; Yusenko, K.; Fischer, R. A. *Chem. Comm.* **2011**, *47*, 8506–8508.

[549] Zhang, Z.; Zhang, L.; Wojtas, L.; Eddaoudi, M.; Zaworotko, M. J. *J. Am. Chem. Soc.* **2012**, *134*, 928–933.

[550] Klet, R. C.; Tussupbayev, S.; Borycz, J.; Gallagher, J. R.; Stalzer, M. M.; Miller, J. T.; Gagliardi, L.; Hupp, J. T.; Marks, T. J.; Cramer, C. J.; Delferro, M.; Farha, O. K. *J. Am. Chem. Soc.* **2015**, *137*, 15680–15683.

[551] Stylianou, K. C.; Heck, R.; Chong, S. Y.; Bacsa, J.; Jones, J. T. A.; Khimyak, Y. Z.; Bradshaw, D.; Rosseinsky, M. J. *J. Am. Chem. Soc.* **2010**, *132*, 4119–4130.

[552] Popoff, N.; Macqueron, B.; Sayhoun, W.; Espinas, J.; Pelletier, J.; Boyron, O.; Boisson, C.; Merle, N.; Szeto, K. C.; Gauvin, R. M.; De Mallmann, A.; Taoufik, M. *Eur. J. Inorg. Chem.* **2014**, *2014*, 888–895.

[553] Gu, W.; Stalzer, M. M.; Nicholas, C. P.; Bhattacharyya, A.; Motta, A.; Gallagher, J. R.; Zhang, G.; Miller, J. T.; Kobayashi, T.; Pruski, M.; Delferro, M.; Marks, T. J. *J. Am. Chem. Soc.* **2015**, *137*, 6770–6780.

[554] Tedesco, C.; Immirzi, A.; Proto, A. *Acta Crystallogr. B* **1998**, *54*, 431–437.

[555] Howard, C. J.; Hill, R. J.; Reichert, B. E. *Acta Crystallogr. B* **1988**, *44*, 116–120.

[556] Chen, E. Y.-X.; Marks, T. J. *Chem. Rev.* **2000**, *100*, 1391–1434.

[557] Coates, G. W. *Chem. Rev.* **2000**, *100*, 1223–1252.

[558] Collette, J. W.; Tullock, C. W.; MacDonald, R. N.; Buck, W. H.; Su, A. C. L.; Harrell, J. R.; Mulhaupt, R.; Anderson, B. C. *Macromolec.* **1989**, *22*, 3851–3858.

[559] D.D. Eley, H. P., Weisz, P. B., Eds. *One-Component Catalysts for Polymerization of Olefins*; Advances in Catalysis; Academic Press, 1975; Vol. 24; pp 173–219.

[560] Ballard, D. G. H. *Adv. Catal.* **1973**, *23*, 263–325.

[561] Madrahimov, S. T.; Gallagher, J. R.; Zhang, G.; Meinhart, Z.; Garibay, S. J.; Delferro, M.; Miller, J. T.; Farha, O. K.; Hupp, J. T.; Nguyen, S. T. *ACS Catal.* **2015**, *5*, 6713–6718.

[562] Li, H.; Xu, B.; He, J.; Liu, X.; Gao, W.; Mu, Y. *Chem. Comm.* **2015**, *51*, 16703–16706.

[563] Babushkin, D. E.; Brintzinger, H.-H. *J. Am. Chem Soc.* **2002**, *124*, 12869–12873.

[564] Liu, S.; Motta, A.; Delferro, M.; Marks, T. J. *J. Am. Chem. Soc.* **2013**, *135*, 8830–8833.

[565] Romano, D.; Andablo-Reyes, E.; Ronca, S.; Rastogi, S. *Polymer* **2015**, *74*, 76–85.

[566] Thomas, J. M.; Raja, R.; Lewis, D. W. *Angew. Chem.* **2005**, *44*, 6456–6482.

[567] Liang, S.; Hao, C.; Shi, Y. *ChemCatChem* **2015**, *7*, 2559–2567.

[568] Dal Santo, V.; Guidotti, M.; Psaro, R.; Marchese, L.; Carniato, F.; Bisio, C. *Proc. R. Soc. London, Ser.* **2012**, *468*, 1904–1926.

[569] Hu, B.; Schweitzer, N. M.; Zhang, G.; Kraft, S. J.; Childers, D. J.; Lanci, M. P.; Miller, J. T.; Hock, A. S. *ACS Catal.* **2015**, *5*, 3494–3503.

[570] Guo, X. et al. *Science* **2014**, *344*, 616–619.

[571] Vile, G.; Albani, D.; Nachtegaal, M.; Chen, Z.; Dontsova, D.; Antonietti, M.; Lopez, N.; Perez-Ramirez, J. *Angew. Chem.* **2015**, *54*, 11265–11269.

[572] Yilmaz, B.; Mueller, U. *Top. Catal.* **2009**, *52*, 888–895.

[573] Zhang, T.; Lin, W. *Chem. Soc. Rev.* **2014**, *43*, 5982–5993.

[574] Zhao, M.; Ou, S.; Wu, C.-D. *Acc. Chem. Res.* **2014**, *47*, 1199–1207.

[575] Ren, H.-Y.; Yao, R.-X.; Zhang, X.-M. *Inorg. Chem.* **2015**, *54*, 6312–6318.

[576] Junghans, U.; Suttkus, C.; Lincke, J.; Laessig, D.; Krautscheid, H.; Glaeser, R. *Microporous Mesoporous Mater.* **2015**, *216*, 151–160.

[577] Gotthardt, M. A.; Schoch, R.; Brunner, T. S.; Bauer, M.; Kleist, W. *ChemPlusChem* **2015**, *80*, 188–195.

[578] Ranocchiari, M.; Lothschuetz, C.; Grolimund, D.; van Bokhoven, J. A. *Proc. R. Soc. London A* **2012**, *468*, 1985–1999.

[579] Liu, J.; Lukose, B.; Shekhah, O.; Arslan, H. K.; Weidler, P.; Gliemann, H.; Brase, S.; Grosjean, S.; Godt, A.; Feng, X.; Muellen, K.; Magdau, I.-B.; Heine, T.; Woell, C. *Sci. Rep.* **2012**, *2*, srep00921, 5 pp.

[580] Deng, H.; Grunder, S.; Cordova, K. E.; Valente, C.; Furukawa, H.; Hmadeh, M.; Gandara, F.; Whalley, A. C.; Liu, Z.; Asahina, S.; Kazumori, H.; O'Keeffe, M.; Terasaki, O.; Stoddart, J. F.; Yaghi, O. M. *Science* **2012**, *336*, 1018–1023.

[581] Zhang, L.; Hu, Y. H. *J. Phys. Chem. C* **2010**, *114*, 2566–2572.

[582] Sattler, J. J. H. B.; Ruiz-Martinez, J.; Santillan-Jimenez, E.; Weckhuysen, B. M. *Chem. Rev.* **2014**, *114*, 10613–10653.

[583] LeValley, T. L.; Richard, A. R.; Fan, M. *Int. J. Hydrogen* **2014**, *39*, 16983–17000.

[584] Lu, C.; Ben, T.; Xu, S.; Qiu, S. *Angew. Chem.* **2014**, *53*, 6454–6458.

[585] Hall, A. S.; Kondo, A.; Maeda, K.; Mallouk, T. E. *J. Am. Chem. Soc.* **2013**, *135*, 16276–16279.

[586] Leong, K.; Foster, M. E.; Wong, B. M.; Spoerke, E. D.; Van Gough, D.; Deaton, J. C.; Allendorf, M. D. *J. Mater. Chem. A* **2014**, *2*, 3389–3398.

[587] Talin, A. A.; Centrone, A.; Ford, A. C.; Foster, M. E.; Stavila, V.; Haney, P.; Kinney, R. A.; Szalai, V.; El Gabaly, F.; Yoon, H. P.; Leonard, F.; Allendorf, M. D. *Science* **2014**, *343*, 66–69.

[588] Malonzo, C. D. et al. *J. Am. Chem. Soc.* **2016**, *138*, 2739–2748.

[589] Zhao, Y.; Truhlar, D. G. *J. Chem. Phys.* **2006**, *125*, 194101/1–194101/18.

[590] Macrae, C. F.; Edgington, P. R.; McCabe, P.; Pidcock, E.; Shields, G. P.; Taylor, R.; Towler, M.; van de Streek, J. *J. Appl. Crystallogr.* **2006**, *39*, 453–457.

[591] Hammersley, A. P.; Svensson, S. O.; Hanfland, M.; Fitch, A. N.; Hausermann, D. *High Pressure Res.* **1996**, *14*, 235–248.

[592] Jennings, G. *QXRD, version 0.11.10*; Argonne National Laboratory: Lemont, IL, 2015.

[593] Yakovenko, A. A.; Reibenspies, J. H.; Bhuvanesh, N.; Zhou, H.-C. *J. Appl. Crystallogr.* **2013**, *46*, 346–353.

[594] Yakovenko, A. A.; Wei, Z.; Wriedt, M.; Li, J.-R.; Halder, G. J.; Zhou, H.-C. *Cryst. Growth Des.* **2014**, *14*, 5397–5407.

[595] Le Bail, A. *J. Non-Cryst. Solids* **1995**, *183*, 39–42.

[596] Petříček, V.; Dusek, M.; Palatinus, L. *Kristallogr. - Cryst. Mater.* **2014**, *229*, 345–352.

[597] McCusker, L. B.; Baerlocher, C. *Chem. Comm.* **2009**, 1439–1451.

[598] Zaki, M. I.; Hasan, M. A.; Al-Sagheer, F. A.; Pasupulety, L. *Colloids Surf. A* **2001**, *190*, 261–274.

[599] Kline Jr., C. H.; Turkevich, J. *J. Chem. Phys.* **1944**, *12*, 300–309.

[600] Bagshaw, S. A.; Cooney, R. P. *Chem. Mater.* **1993**, *5*, 1101–1109.

[601] Rosenberg, D. J.; Anderson, J. A. *Catal. Lett.* **2002**, *83*, 59–63.

[602] Saravanamurugan, S.; Paniagua, M.; Melero, J. A.; Riisager, A. *J. Am. Chem. Soc.* **2013**, *135*, 5246–5249.

[603] Ren, L.; Guo, Q.; Kumar, P.; Orazov, M.; Xu, D.; Alhassan, S. M.; Mkhoyan, K. A.; Davis, M. E.; Tsapatsis, M. *Angew. Chem.* **2015**, *54*, 10848–10851.

Chapter 5

Appendix A

Care has been taken in this thesis to minimize the use of jargon and acronyms, but this cannot always be achieved. This appendix defines jargon terms in a glossary, and contains a table of acronyms and their meaning.

5.1 Acronyms

Table 5.1: Acronyms

Acronym	Meaning
AC	Alternating Current
AIM	Atomic Layer Deposition in Metal-Organic Frameworks
ALD	Atomic Later Depostion
BEC	Born Effective Charge
BSSE	Basis Set Superposition Error
CASPT2	Complete Active Space 2nd Order Perturbation Theory
CASSCF	Complete Active Space Self-Consistent Field
CM5	Charge Model 5
DC	Direct Currect
DDEC	Density Derived Electrostatic and Chemical Charges

Continued on next page

Table 5.1 – continued from previous page

Acronym	Meaning
DED	Difference Envelope Density
DFPT	Density Functional Perturbation Theory
DFT	Density Functional Theory
DRIFTS	Diffuse Reflectance Infrared Fourier Transform Spectroscopy
DSC	Differential Scanning Calorimetry
EDS	Energy-Dispersive X-ray Spectroscopy
EFP	Effective Fragment Potential
EXAFS	Extended X-ray Adsorption Fine Structure
FWHM	Full-Width Half-Maximum
GCMC	Grand-Conanical Monte Carlo
GEMC	Gibbs Ensemble Monte-Carlo
GGA	Generalized Gradient Approximation
GPC	Gell Permeation Chromatography
HAADF	High-Angle Annular Dark Field
HDV	Heisenberg-Dirac-Van Vleck
HPLC	High-Performance Liquid Chromatography
ICP	Inductively Couple Plasma
ICP-OES	Inductively Coupled Plasma-Optical Emission Spectroscopy
IR	Infrared
IRMOF	Isoreticular Metal-Organic Framework
LJ	Lennard-Jones
LoProp	Localization of Properties
MCCCS-MN	Monte Carlo for Complex Chemical Systems - Minnesota
MEA	Monoethanolamine
MOF	Metal-Organic Framework
MP2	Moller-Plesset 2nd Order Perturbation Theory
MUPE	Mean Unsigned Percentage Error
NEMO	Non-Empirical Modeling
NEVPT2	n-electron Valence State Perturbation Theory

Continued on next page

Table 5.1 – continued from previous page

Acronym	Meaning
NGA	Nonseparable Gradient Approximation
NMR	Nuclear Magnetic Resonance
PDF	Pair Distribution Function
PEC	Potential Energy Curve
PXRD	Powder X-ray Diffraction
ROMP2	Restricted Open-Shell Moller-Plesset 2nd Order Perturbation Theory
SA-CASSCF	State-Averaged Complete Active Space Self-Consistent Field
SALI	Sovlent-Assisted Ligand Incorporation
SAPT	Symmetry Adapyed Perturbation Theory
SCF	Self-Consistent Field
SEM	Scanning Electron Microscopy
SIBFA	Sum of Interaction Between Fragments Ab Initio Computed
SOC	Spin-Orbit Coupling
SPy	Square Pyramid
STEM-EDS	Scanning Tramission Electron Microscopy - Energy Dispersive Electron Microscopy
TGA	Thermogravimetric Analysis
THF	tetrahydrofuran
TMOS	tetramethylorthosilicate
TraPPE	Transferable Potentials for Phase Equilibria
UFF	Universal Force Field
VASP	Vienna Ab Initio Simulation Package
VLE	Vapor-Liquid Equilibrium
WFT	Wave Function Theory
XRD	X-ray Powder Diffraction